

ATOMIC LAYER DEPOSITION OF III-
NITRIDES AND METAL OXIDES; THEIR
APPLICATION IN AREA SELECTIVE ALD

A DISSERTATION SUBMITTED TO
THE GRADUATE SCHOOL OF ENGINEERING AND SCIENCE
OF BILKENT UNIVERSITY
IN PARTIAL FULFILLMENT OF THE REQUIREMENTS FOR
THE DEGREE OF
DOCTOR OF PHILOSOPHY
IN
MATERIALS SCIENCE AND NANOTECHNOLOGY

By
Ali Haider
July, 2017

ATOMIC LAYER DEPOSITION OF III-NITRIDES AND METAL
OXIDES; THEIR APPLICATION IN AREA SELECTIVE ALD

By Ali Haider
July 2017

We certify that we have read this dissertation and that in our opinion it is fully adequate, in scope and in quality, as a thesis for the degree of Doctor of Philosophy.

Ayktulu Dana (Advisor)

Necmi Bıyıklı (Co-Advisor)

Oğuz Gülseren

Ferdi Karadaş

Gökhan Demirel

Adil Denizli

Approved for the Graduate School of Engineering and Science:

Ezhan Karaşan
Director of the Graduate School

ABSTRACT

ATOMIC LAYER DEPOSITION OF III-NITRIDES AND METAL OXIDES; THEIR APPLICATION IN AREA SELECTIVE ALD

ALI HAIDER

PhD in Materials Science and Nanotechnology

Supervisor: Aykutlu Dana

Co-supervisor: Necmi Biyikli

July 2017

III-nitride compound semiconductor materials (GaN, AlN, and InN) and their alloys have generated significant interest in both basic research and commercial applications mainly in the field of photonics, energy storage, nano-sensors, and nano-(opto)electronics. Wurtzite type III-nitrides exhibit direct band gaps, which extend from the ultra-violet (UV) to the mid-IR spectrum with values of 6.2, 3.4 and 0.64 eV for AlN, GaN, and InN, respectively. This feature allows the band gap of III-nitride alloys to be conveniently tuned by precisely controlling the composition for a particular application. Metalorganic chemical vapor deposition (MOCVD) and molecular beam epitaxy (MBE) are the most common successful techniques for achieving high-quality epitaxial III-nitride layers with low impurity concentrations and decent electrical properties. However, both of these methods employ high growth temperatures, which is neither compatible with the existing CMOS technology nor suitable for temperature-sensitive device layers (e.g. In-rich $\text{In}_x\text{Ga}_{1-x}\text{N}$) and substrates (e.g. glass, flexible polymers, etc.). These limitations are the main driving source for a continuous exploration of alternative low temperature processes for the growth of III-nitride layers and their alloys. High aspect ratio III-nitride nanostructures in the form of nanowires and nanorods have been synthesized using different techniques including vapor-liquid-solid crystal growth, electrospinning, template based synthesis, and etching. Critical breakthroughs in fabrication of III-nitrides nanostructures have been achieved by above mentioned techniques but suffer from limited control over properties of nanostructures (shape, orientation, and size) and in some cases high growth-temperature requirement. A recent flurry of interest in developing high quality I-D III-nitride nanostructures derives from

the desire to obtain flexible optoelectronic devices having wider applications. Template-assisted growth technique is one of the most promising approach to fabricate III-nitride nanostructures with precise control over shape, size, position, and distribution.

In the first part of thesis, we have deposited InN and III-nitride alloys using hollow-cathode plasma assisted atomic layer deposition (HCPA-ALD) at low growth temperatures. The aim was to deposit III-nitride materials at lowest growth temperatures with decent crystalline quality and minimum impurity content. Depositions were carried out using group III organometallic precursors along with N_2/H_2 or N_2 plasma as metal and nitrogen source, respectively. Process parameters including precursor pulse time, plasma flow duration, purge time, and deposition temperature are investigated and correlations were developed between process parameters and material properties. Refractive index of the InN film deposited at 200 °C was found to be 2.66 at 650 nm. 48 nm-thick InN films exhibited relatively smooth surfaces with RMS surface roughness values of 0.98 nm, while the film density was extracted as 6.30 g/cm³. The effect of In content on structural, optical, and morphological properties of $In_xGa_{1-x}N$ thin films was investigated. Grazing incidence X-ray diffraction (GIXRD) and transmission electron microscope (TEM) showed that InN and $In_xGa_{1-x}N$ thin films were polycrystalline with hexagonal wurtzite structure. Spectral absorption measurements exhibited an optical band edge of InN around 1.9 eV. X-ray photoelectron spectroscopy (XPS) confirmed the deposition of InN and alloy thin films and revealed the presence of low impurity contents. Higher In concentrations resulted in an increase of refractive indices of $In_xGa_{1-x}N$ ternary alloys from 2.28 to 2.42 at a wavelength of 650 nm. Optical band edge of $In_xGa_{1-x}N$ films red-shifted with increasing In content, confirming the tunability of the band edge with alloy composition. Photoluminescence measurements of $In_xGa_{1-x}N$ exhibited broad spectral features with an In concentration dependent wavelength shift. We have also studied the compositional dependence of structural, optical, and morphological properties of $B_xGa_{1-x}N$ and $B_xIn_{1-x}N$ ternary thin film alloys grown using sequential pulsed CVD. GIXRD measurements showed that boron incorporation in wurtzite lattice of GaN and InN diminishes the crystallinity of $B_xGa_{1-x}N$ and $B_xIn_{1-x}N$ sample. Refractive index decreased from 2.24 to 1.65 as the B concentration of $B_xGa_{1-x}N$ increased from 35 to 88 %. Similarly, refractive index of $B_xIn_{1-x}N$ changed from 1.98 to 1.74 for increase in B concentration value from 32 to 87 %, respectively. Optical

transmission band edge values of the $B_xGa_{1-x}N$ and $B_xIn_{1-x}N$ films shifted to lower wavelengths with increasing boron content, indicating the tunability of energy band gap with alloy composition. Atomic force microscopy measurements revealed an increase in surface roughness with boron concentration of $B_xGa_{1-x}N$, while an opposite trend was observed for $B_xIn_{1-x}N$ thin films.

Moreover, we demonstrate vertical GaN, AlN, and InN hollow nanocylindrical arrays (HNCs) integrated to Si(100) substrates using anodized aluminum oxide (AAO) membrane templated PA-ALD. Our fabrication and Si-integration strategy consists of the following process steps: (i) reactive ion etching (RIE) of Si using AAO membrane as hard mask material to achieve nanoporous Si substrate, (ii) conformal growth of III-nitride films on nanoporous Si via low-temperature PA-ALD, (iii) removal of PA-ALD coated III-nitride material from top surface of Si via plasma etching, and (iv) isotropic dry etching of surrounding Si to attain long-range ordered vertical III-nitride HNCs. The material properties of nanostructured III-nitride materials have been compared with the thin-film counterparts which were also grown using low-temperature PA-ALD. SEM images revealed that long-range ordered arrays of III nitride HNCs were successfully integrated in Si(100) substrates. TEM, GIXRD, and selected area electron diffraction (SAED) cumulatively confirmed that III-nitride HNCs possess hexagonal wurtzite crystalline structure. XPS survey and high-resolution scans detected presence of different elements and peaks at specific binding energies which confirmed the formation of III-nitride HNCs.

The second part of the thesis deals with self-aligned thin film patterning of metal oxides using area selective atomic layer deposition (AS-ALD). Nanoscale process integration demands novel nano-patterning techniques in compliance with the requirements of next generation devices. Conventionally, top-down subtractive (etch) or additive (deposition/lift-off) processes in conjunction with various lithography techniques is employed to achieve film patterning, which become increasingly challenging due to the ever-shrinking misalignment requirements. To reduce the complexity burden of lithographic alignment in critical fabrication steps, self-aligned processes such as selective deposition and selective etching might provide attractive solutions.

We demonstrate a methodology to achieve AS-ALD by using inductively couple plasma (ICP) grown fluorocarbon polymer film as growth inhibition

layer. The fluorocarbon layer was grown using C_4F_8 feed gas in a conventional ICP-etch reactor. Our approach has been tested for metal-oxides including ZnO, Al_2O_3 , TiO_2 , and HfO_2 . Additionally, we investigate the poly(methyl methacrylate) (PMMA) and polyvinylpyrrolidone (PVP) as growth inhibition layers for AS-ALD of TiO_2 . Contact angle, XPS, spectroscopic ellipsometer, energy dispersive X-ray spectroscopy (EDX), and scanning electron microscopy (SEM) measurements were performed to investigate the blocking ability of polymer layers against ALD-grown films. Characterizations carried out revealed that effective blocking on fluorocarbon layer is achieved for ZnO film upto 136 growth cycles. On the other hand, a rather slow nucleation has been observed for HfO_2 growth on fluorocarbon coated surfaces, while TiO_2 and Al_2O_3 growth showed almost no delay with a growth rate equal to the ones on conventional substrate surfaces. For TiO_2 , PMMA revealed successful growth inhibition upto the maximum inspected growth cycles while PVP was able to block TiO_2 growth upto 300 growth cycles. By exploiting this inhibition feature, thin film patterning has been demonstrated by growing ZnO films on photo lithographically patterned fluorocarbon/Si samples. We also demonstrate nanoscale patterned deposition of TiO_2 using a PMMA masking layer that has been patterned using e-beam lithography.

Keywords: Plasma-Enhanced Atomic Layer Deposition, III-Nitrides, Area-Selective Atomic Layer Deposition, Metal Oxides, Thin Films, Nano-Cylinders, Thin-Film Patterning

ÖZET

III-NİTRATLARIN VE METAL OKSİTLERİN ATOMİK KATMAN KAPLAMISI; BUNLARIN ALAN SEÇİCİ ALD'DEKİ UYGULAMALARI

Ali Haider

Malzeme Bilimi ve Nanoteknoloji, Doktora

Tez Danışmanı: Aykutlu Dana

Temmuz 2017

Yarı iletken III-nitrit bileşikleri (GaN, AlN, and InN) ve onların alaşımları, hem temel araştırma alanlarında hem de ticari uygulamalarda, özellikle fotonik, enerji depolaması, nano-sensörler ve nano-(opto) elektronikler alanlarında önemli ilgi uyandırmıştır. Würtzit tipi III-nitritleri, sırasıyla AlN, GaN ve InN için 6,2, 3,4 ve 0,64 eV değerleri ile morötesi (UV) ile orta-IR spektruma uzanan doğrudan bant aralıklarına sahiptir. Bu özellik, belirli uygulamalar için III-nitrit alaşımlarının band aralığını tam bileşim kontrolü ile kolaylıkla ayarlamaya izin veriyor. Metalorganik kimyasal buhar birikimi (MOCVD) ve Moleküler giriş epitaksisi (MBE), düşük safsızlık konsantrasyonlu ve iyi elektriksel özelliğe sahip yüksek kaliteli epitaksiyel III-nitrit tabakalarını elde etmenin en yaygın ve başarılı yöntemleridir. Fakat bununla birlikte, bu yöntemlerin her ikisi de, mevcut CMOS teknolojisi ile uyumlu olmayan ya da sıcaklığa duyarlı aygıt katmanlarına (örneğin In-zengin $In_xGa_{1-x}N$) ve alt tabakalara (örneğin cam, esnek polimerler, vb.) uygun olmayan yüksek büyüme sıcaklıkları kullanılmaktadır. Bu kısıtlamalar, III-nitrit ve alaşımlarının tabakalarını büyütmenin alternatif düşük sıcaklıktaki proseslerin araştırmalarının ana itici kaynağıdır. Nanotel ve nanoçubuk şeklindeki yüksek en-boy oranlı III-nitrit nanoyapıları buhar-sıvı-katı kristal büyümesi, elektrospinning, şablon esaslı sentez ve aşındırma yöntemlerini kapsayan yöntemlerle sentezlenmiştir. III-nitrit nanoyapıların üretiminde kritik gelişmeler yukarıda adı geçen yöntemlerle elde edilmiştir ancak nanoyapılardaki (şekil, yönelim ve boyut)

özelliklerde kısıtlı kontrol ve bazı yüksek sıcaklık gereksinimlerinden muzdarip. Yüksek kalitede I-D III-nitrit nanoyapıların geliştirilmesine yönelik yeni bir ilgi, daha geniş uygulamalara sahip esnek optoelektronik aygıtlar elde etme isteğinden kaynaklanmaktadır. Şablon destekli büyütme tekniği, III- nitrit nanoyapılarının şekli, boyutu, konumu ve dağılımı üzerinde hassas kontrolü olan en umut verici üretim yöntemlerinden bir tanesidir.

Tezin ilk bölümünde, düşük büyüme sıcaklıklarında içi boş katot plazma yardımcı atomik katman çökeltme (HCPA-ALD) kullanarak InN ve III-nitritür alaşımları tevdi ettik. Amaç, III-nitritür materyallerin, uygun kristal kalitesi ve minimum safsızlık içeriği ile en düşük büyüme sıcaklıklarında depolanmasıydı. Depozisyonlar N_2/H_2 ve N_2 plazması ile birlikte grup III organometalik öncülleri kullanılarak gerçekleştirildi. Prekürsör darbe süresi, plazma akış süresi, boşaltma süresi ve çökeltme sıcaklığı gibi proses parametreleri araştırılmış ve proses parametreleri ile malzeme özellikleri arasında korelasyonlar geliştirilmiştir. 200 °C'de biriken InN filminin refraktif indeksi 650 nm'de 2.66 bulundu. 48 nm kalınlığında InN filmleri 0.98 nm RMS yüzey pürüzlülüğü değerlerine sahip nispeten pürüzsüz yüzeyler sergilerken film yoğunluğu 6.30 g / cm^3 olarak çıkarıldı. In içeriğinin yapısal, optik ve $In_xGa_{1-x}N$ ince filmlerin morfolojik özelliklerine etkisi araştırıldı. Grazing insidansı X-ışını kırınımı (GIXRD) ve transmisyon elektron mikroskobu (TEM). InN ve $In_xGa_{1-x}N$ ince filmlerin altıgen würzit yapıya sahip polikristalin olduğunu gösterdi. Spektral absorpsiyon ölçümleri, 1.9 eV civarında InN'nin bir optik bant kenarını sergiledi. X-ışını fotoelektron spektroskopisi (XPS) InN ve alaşım ince filmlerin birikimini doğruladı ve düşük safsızlık içeriğinin varlığını ortaya koydu. Dahası, anodize edilmiş alüminyum oksit (AAO) membran kalıplı PA-ALD kullanarak Si(100) alttaşa üzerine dikey GaN, AlN ve InN oyuk nano-silindir dizisinin etegrasyonu gösterildi. Bizim fabrikasonumuz ve Si-etegrasyonu takip eden işlemleri içerir: (i) Nano-pürüzlü Si alttaşa sahip olmak için, AAO membranı sert maske malzemesi olarak kullanarak Si rekatif iyon oyma (RIE), (ii) düşük sıcaklıklı PA-ALD ile nano-pürüzlü Si üzerinde III-Nitrat filmlerin konformal olarak büyütülmesi, (iii) PA-ALD kaplamalı III-nitrat malzemelerin Silikon yüzeyinden plazma oyma kullanarak kaldırılması, ve (iv) uzun mesafeli dizili dikey III-nitrat HNC'lere sahip olmak için Silikonun çevresinin izotropik kuru oyulması. Nano-işlenmiş III-Nitrat malzemelerin malzeme özellikleri, benzer şekilde düşük sıcaklıklı PA-ALD'de büyütülmüş ince film emsalleri ile karşılaştırıldı. SEM resimleri, uzun sıralı dizilmiş III-Nitrat HNC dizisi başarılı

bir şekilde Si(100) alttaşa entegre edildiğini ortaya koymuştur. TEM, GIXRD ve seçili alan electron difraksiyon (SAED) sonuçları III-Nitrat HNC'lerin hegzagonal wurtzite kristal yapıya sahip olduğunu kümülatif olarak gösterdi. XPS analizi ve yüksek çözünürlüklü taramalar III-Nitrat HNC'lerin farmasyonunun doğrulayan spesifik bağlanma enerjilerinde farklı elementler tespit etti.

Tezin ikinci bölümü,alan seçmeli atomik katman birikimini kullanarak metal oksitlerin ince filmde kendi dizilişine değinmektedir(AS-ALD).Nanoölçüm süreç entegrasyonu yeni nesil cihazların gereksinimlerine uygun olarak nanodiziliş tekniklerini talep eder.Genellikle, çeşitli litografi teknikleri ile birlikte yukarıdan aşağıya eksiltici(etch) ya da katkı maddesi(biriktirme/kaldırma) prosesleri filmin desenleme işlemini elde etmek için kullanılır,bu, sürekli küçülen yanlış hizalama gereksinimleri nedeniyle gittikçe zorlaşır.Kritik üretim aşamalarında litografik hizalamanın karmaşıklık yükünü azaltmak için, seçici biriktirme ve seçici aşındırma gibi kendi kendine hizalı işlemler cazip çözümler sağlayabilir.

Artımlı inhibisyon tabakası olarak indükte çift plazma (ICP) yetiştirilmiş florokarbon polimer filmi kullanarak AS-ALD'yi gerçekleştirmek için bir metodoloji gösteriyoruz.Florokarbon tabakası, alışılmış bir ICP-etch reaktöründe C₄F₈ besleme gazı kullanılarak büyütüldü. Yaklaşımımız ZnO, Al₂O₃, TiO₂ ve HfO₂ gibi metal oksitler için test edilmiştir. Ayrıca, TiO₂'nin AS-ALD için büyüme önleyici tabakalar olarak poli (metil metakrilat) (PMMA) ve polivinilpirolidonu (PVP) araştırdık.ALD ile üretilen filmlere karşı polimer katmanlarının bloke edici özelliklerini araştırmak için temas açısı, XPS, spektroskopik elipsometre, enerji dağılımlı X-ışını spektroskopisi (EDX) ve taramalı elektron mikroskobu (SEM) ölçümleri yapıldı. Yapılan karakterizasyonlar, ZnO filmi 136 büyüme çevrimine kadar florokarbon tabakasında etkili bir blokajın gerçekleştirildiğini ortaya koydu.Diğer yandan,TiO₂ ve Al₂O₃ büyümesi, geleneksel substrat yüzeylerindeki büyüme hızına eşit bir büyüme oranı ile neredeyse hiç gecikme göstermezken,florokarbon kaplı yüzeylerde HfO₂ büyümesinde oldukça yavaş bir çekirdeklenme gözlemlendi. TiO₂ için, PMMA maksimum incelenen büyüme döngüsüne kadar başarılı büyüme inhibisyonu ortaya koyarken, PVP ,TiO₂ büyümesini 300 büyüme döngüsüne kadar bloke edebildi. Bu inhibisyon özelliğinden yararlanılarak ince film şekillenmesi, foto litografik olarak desenli florokarbon/Si numuneleri üzerinde ZnO filmlerinin büyütülmesi ile

gösterildi.e-ışınli litografi kullanılarak desenlendirilmiş bir PMMA maskeleme katmanı kullanarak TiO₂'nin nano ölçekli desenli birikimini ayrıca kanıtlamış olduk.

Anahtar kelimeler: Plazma Arttırılmış Atomik Katmanlı Depozit, III-Nitrürler, Alan Seçici Atomik Katmanlı Kalınım, Metal Oksitler, İnce Filmler, Nano-Silindirler, İnce Film Desenlendirme

Acknowledgement

I would like to express my sincere gratitude to my advisors, Dr. Necmi Biyikli and Dr. Aykutlu Dana for their valuable guidance and endless support during my PhD research. I want to express my gratitude to Cagla Ozgit-Akgun, Sevde Altuntas, Petro Deminskyi, and Seda Kizir for their continued support and help in my research work.

I would like to express my deepest appreciation to my lovely parents and siblings for their love and care throughout my PhD studies. They were always very kind and supportive through highs and lows during my doctorate. They encouraged me to strive for the best research work and gave me the belief to always remain positive throughout the course of my PhD.

I would like to say a very special thanks to all my friends at Bilkent University and in Turkey who made my life really wonderful in past few years. Especially, I want to mention Jamoliddin Khanifaev, Talha Masood Khan, Naveed Mehmood, Berrera Maqbool, Murat Serhatlioglu, Haydarali Sayfiddinov, Hamit Eren, Ziya Işıksaçan, Begimai Adilbekova, Naveed ul Mustafa, Umar Raza, and Ali Kalantarifard for their support, kind advices, and amazing times spend together.

Finally, I would also like to say thanks to all engineers especially Semih Yasar, Mustafa Guler, and Enver Kahveci who contributed to my research experience and always helped me in enhancing my learning towards research equipment's.

To my family and friends

Contents

ABSTRACT	ii
ÖZET	vi
Acknowledgement	x
Contents.....	xii
List of Figures	xv
List of Tables.....	xxii
Chapter 1.....	1
Introduction	1
1.1 Historical Background of the Technique Used	1
1.2 Motivation	3
1.2.1 InN and III-Nitride Alloy Thin Films Deposition Using HCPA-ALD	3
1.2.2 Template Assisted Fabrication of III-nitride Hollow Nanocylinders via HCPA-ALD	4
1.2.3 Area Selective Atomic Layer Deposition of Metal Oxides Using Polymer Growth Inhibition Layers.....	6
1.3 Objectives	8
1.4 Thesis Overview	11
Chapter 2.....	12
Theoretical Background and Literature Overview.....	12
2.1 An Overview on Atomic Layer Deposition	12
2.1.1 Mechanism	13
2.1.2 Factors Causing Saturation and Growth of Less than Monolayer per Cycle.....	14
2.1.3 ALD Window	14
2.1.4 Merits and Demerits of ALD and Comparison with Other Deposition Techniques.....	16
2.1.5 Plasma vs. Thermal ALD	17
2.2 InN and III-Nitride Alloy Thin Film Deposition Using HCPA-ALD reactor.....	17

2.3 Template Assisted Fabrication of III-Nitride Nanocylinders.....	19
2.4 Area-Selective ALD of Metal Oxides Using Polymer Growth Inhibition Layers	21
Chapter 3.....	23
Experimental Details	23
3.1 Hollow Cathode Plasma Assisted Atomic Layer Deposition of InN	23
3.2 Hollow Cathode Plasma Assisted Atomic Layer Deposition of $\text{In}_x\text{Ga}_{1-x}\text{N}$ Thin Films	25
3.3 Sequential Pulsed Chemical Vapor Deposition of Ternary $\text{B}_x\text{Ga}_{1-x}\text{N}$ and $\text{B}_x\text{In}_{1-x}\text{N}$ Thin Film Alloys	26
3.4 Template Assisted Fabrication of III-Nitride Nano-Cylinder Arrays via Plasma-Assisted Atomic Layer Deposition.....	27
3.4.1 AAO Foils Preparation.....	27
3.4.2 Vertical III-nitride Hollow Nano-cylinder Array Fabrication.....	28
3.5 Area Selective Atomic Layer Deposition of Metal Oxides Using Polymer Growth Inhibition Layers	30
3.6 Characterization Methods.....	31
Chapter 4.....	34
InN and III-Nitride Alloy Thin Films Deposition Using HCPA-ALD.....	34
4.1 Hollow Cathode Plasma Assisted Atomic Layer Deposition of InN Thin Films.....	34
4.1.1 Optimization of Growth Parameters.....	35
4.1.2 Material Characterization of InN Thin Films.....	39
4.2 Hollow Cathode Plasma Assisted Atomic Layer Deposition of $\text{In}_x\text{Ga}_{1-x}\text{N}$ Thin Films	51
4.3 Low-temperature Sequential Pulsed Chemical Vapor Deposition of Ternary $\text{B}_x\text{Ga}_{1-x}\text{N}$ and $\text{B}_x\text{In}_{1-x}\text{N}$ Thin Film Alloys.....	68
Chapter 5.....	77
Template Assisted Atomic Layer Deposition of III-nitride Nanostructures	77
5.1 GaN Hollow Nanocylinder Arrays.....	79
5.2 AlN Hollow Nanocylinder Arrays	88
5.3 InN Hollow Nanocylinder Arrays	96

Chapter 6.....	106
Area Selective Atomic Layer Deposition of Metal Oxides Using Polymer Growth Inhibition Layers.....	106
6.1 AS-ALD of ZnO, HfO ₂ , and Al ₂ O ₃ Using Plasma Polymerized Fluorocarbon Growth Inhibition Layer	106
6.2 Nanoscale Selective Area Atomic Layer Deposition of TiO ₂ Using E- beam Patterned Polymers	124
Chapter 7.....	141
Conclusion and Future Prospects	141
Bibliography.....	146

List of Figures

Figure 2.1: Schematic representation of an ALD cycle consisting of four steps.	14
Figure 2.2: Effect of deposition temperature on the ALD growth rate.	15
Figure 3.1: Details regarding specific parts and their features of ALD system .	24
Figure 3.2: A schematic showing growth process sequence of $\text{In}_x\text{Ga}_{1-x}\text{N}$ thin film with single sub cycle of InN and GaN.....	26
Figure 3.3: The schematic showing step-by-step fabrication of vertically aligned III-nitride HNCs: (a) AAO membrane placement on Si(100), (b and c) Si patterning with Ar/ CHF_3 based reactive ion etching (RIE) using AAO membrane as hard mask material to achieve nanoporous Si substrate, (d) conformal coating of III-nitride materials, (e) Ar based RIE of PA-ALD coated III-nitride material from top surface of Si, (f) SF_6 based selective etching of Si to obtain III-nitride HNCs.	29
Figure 4.1: Effect of precursor doses on growth rate at 200 °C: TMI pulse length was kept constant at 0.7 s for the N_2 plasma saturation curve, N_2 plasma dose was kept constant at 100 s for the TMI saturation curve. (Inset) N_2 plasma dose vs. carbon at. % present in the bulk of the film.....	36
Figure 4.2: InN film thickness vs. number of deposition cycles. (Inset) Deposition rate as a function of purge time: TMI dose and N_2 plasma exposure time were constant at 0.7 and 100 s, respectively.	37
Figure 4.3: Growth rate and In/N ratio (evaluated by XPS) of InN deposited at different substrate temperatures.	39
Figure 4.4: Compositional depth profile of InN thin film deposited on Si(100) at 200 °C.....	42

Figure 4.5: High resolution XPS scans of (a) In3d and (b) N1s obtained from InN thin film deposited on Si(100) at 200 °C.	43
Figure 4.6: Valence band spectra of InN sample deposited on Si(100) at 200 °C. Inset shows the position of spectra near valence band maximum region.	44
Figure 4.7: (a) SEM images of InN thin film deposited on Si(100) substrate at 200 °C, (b) Surface morphology of same sample revealed by AFM.	45
Figure 4.8: GIXRD pattern of InN film deposited on Si(100) substrate at 200 °C.	46
Figure 4.9: (a) Cross-sectional TEM image of AlN capped InN film showing the interface of InN and SiO ₂ /Si deposited at 200 °C on Si (100) substrate. Inset Colorized elemental map of same sample. (b) Cross-sectional TEM image of same InN sample. (c) SAED pattern of the same sample.	48
.....	49
Figure 4.10: (a) Optical constants (refractive index and extinction coefficient) of InN thin film deposited on Si (100) at 200 °C, (b) Absorption spectrum of same InN sample deposited on Si (100). (Inset) Optical transmission spectrum of the InN film deposited on double-side polished quartz.....	49
Figure 4.11: GIXRD patterns of GaN, InN, and In _x Ga _{1-x} N thin films deposited on Si(100) substrates.	52
Figure 4.12: Indium concentration values obtained from EDX, XPS, and GIXRD for In _x Ga _{1-x} N films having different RS values.....	57
Figure 4.13: Compositional depth profile of ~33 nm thick In _{0.33} Ga _{0.67} N thin film deposited on a Si(100) substrate.....	58
Figure 4.14: Ga 3d, In 3d, and N 1s HR-XPS scans of In _{0.25} Ga _{0.75} N (a, b and c), In _{0.33} Ga _{0.67} N (d, e and f), and In _{0.64} Ga _{0.36} N (g, h and i) thin films deposited on Si(100).	60
Figure 4.15: (a) Optical transmission spectra of GaN, InN, and In _x Ga _{1-x} N thin films deposited on double-side polished quartz substrates. (b) (αE) ² vs. E plots, indicating the optical band gaps of GaN, InN, and In _x Ga _{1-x} N thin films.	62
Figure 4.16: Spectral refractive indices of GaN, InN, and In _x Ga _{1-x} N thin films with different In fractions.....	63

Figure 4.17: (a) Cross-sectional TEM image of the AlN-capped $\text{In}_{0.33}\text{Ga}_{0.67}\text{N}$ thin film deposited on the Si(100) substrate. (b) Cross-sectional HR-TEM image of the same sample.	64
Figure 4.18: (a) Elemental map of the AlN-capped $\text{In}_{0.33}\text{Ga}_{0.67}\text{N}$ thin film deposited on Si(100) substrate	65
Figure 4.19: Room temperature PL spectra of (a) $\text{In}_{0.25}\text{Ga}_{0.75}\text{N}$, (b) $\text{In}_{0.33}\text{Ga}_{0.67}\text{N}$, and (c) $\text{In}_{0.64}\text{Ga}_{0.36}\text{N}$ thin films deposited on Si(100) substrates.	66
Figure 4.20: Surface morphologies of (a) $\text{In}_{0.25}\text{Ga}_{0.75}\text{N}$, (b) $\text{In}_{0.33}\text{Ga}_{0.67}\text{N}$, and (c) $\text{In}_{0.64}\text{Ga}_{0.36}\text{N}$ thin films deposited on Si(100) substrates.	67
Figure 4.21: GIXRD pattern of (a) GaN and $\text{B}_x\text{Ga}_{1-x}\text{N}$ with different compositions, (b) InN and $\text{B}_x\text{In}_{1-x}\text{N}$ with different compositions.	72
Figure 4.22: Refractive indices of (a) BN, GaN, and $\text{B}_x\text{Ga}_{1-x}\text{N}$ with different compositions, (b) BN, InN and $\text{B}_x\text{In}_{1-x}\text{N}$ with different compositions.	73
Fig. 4.23: Transmission spectra of (a) BN, GaN, and $\text{B}_x\text{Ga}_{1-x}\text{N}$ with different compositions, (b) BN, InN and $\text{B}_x\text{In}_{1-x}\text{N}$ with different compositions.	75
Fig. 4.24: AFM images of (a) $\text{B}_{0.35}\text{Ga}_{0.65}\text{N}$, (b) $\text{B}_{0.76}\text{Ga}_{0.24}\text{N}$, (c) $\text{B}_{0.88}\text{Ga}_{0.12}\text{N}$, (d) $\text{B}_{0.32}\text{In}_{0.67}\text{N}$, (e) $\text{B}_{0.75}\text{In}_{0.25}\text{N}$, and (f) $\text{B}_{0.87}\text{In}_{0.13}\text{N}$	76
Figure 5.1: SEM image of (a) top side of AAO membrane with partially blocked pores, (b) bottom side of AAO membrane with dominantly open nanopores, (c) cross-section of AAO membrane after substrate attachment showing the total height of AAO membrane and the rough top portion, (d) porous Si surface with AAO membrane on top, (e) nanoporous Si revealing pore-widening effect and uniformly aligned hexagonal pores, and (f) angled-view image of nanoporous Si indicating the depth of etched pores.	78
Figure 5.2: (a) Top view SEM image obtained from PA-ALD (1500 cycle) grown GaN on nanoporous Si substrate, (b) Angled-view SEM image of the same sample showing the rather conformal filling of GaN into the Si nanopores, (c) Top-view SEM image of GaN HNCs revealing their morphology and dimensions, and (d) Angled-view SEM image of GaN HNCs showing the total height of nano-cylinders.	81

Figure 5.3: (a) Top view and (b) cross-sectional view SEM images obtained after 2 minutes of Ar plasma exposure successfully removed GaN from top of nano-pores leaving GaN integrated inside Si(100).	82
Figure 5.4: (a) TEM image of several individual and bundled GaN HNCs, (b) TEM image of GaN HNCs revealing their wall thickness and total length, (c) HR-TEM image of a GaN HNC displaying the polycrystalline structure of PA-ALD grown GaN, (d) SAED pattern of GaN HNCs, and (e) EDX elemental mapping of the same GaN HNC sample.	84
Figure 5.5: GIXRD pattern obtained from (a) GaN HNCs grown on nanoporous Si substrates, (b) ~50 nm thick GaN deposited on planar Si via HCPA-ALD...	86
Figure 5.6: HR-XPS scans of (a) Ga 3d and (b) N 1s obtained from GaN HNCs revealing presence of various bonding schemes.	87
Figure 5.7: PL spectra of GaN HNCs and ~60 nm thick GaN thin film gathered at room temperature.....	88
Figure 5.8: (a) Top view SEM image obtained from HCPA-ALD (500-cycle) grown AlN on nanoporous Si substrates, (b) Angled-view SEM image of the same sample, (c) Top-view SEM image of AlN HNCs revealing their morphology and dimensions, (d) angled-view SEM image of AlN HNCs depicting the total height of nanocylinders.	89
Figure 5.9: (a) Top view and (b) cross-sectional view SEM images obtained after 3 minutes of Ar plasma exposure successfully removed AlN from top of nano-pores leaving AlN integrated inside Si(100).	90
Figure 5.10: (a) Top view SEM image of AlN HNCs obtained after 5 sec of SF ₆ based Si(100) etching revealing their morphology and dimensions, (b) cross-sectional image of same AlN HNCs showing the total height of nano-cylinders.	91
Figure 5.11: (a) TEM image of AlN HNCs, (b) TEM image of an individual AlN HNC revealing thickness and total length, (c) HR-TEM image of AlN HNC displaying internal crystal structure of AlN, (d) EDX elemental map of aluminum, (e) EDX elemental map of nitrogen, and (f) SAED pattern of AlN HNC samples.....	93

Figure 5.12: GIXRD pattern obtained from (a) ~173 nm long AlN HNCs, (b) ~50 nm thick AlN deposited on Si via HCPA-ALD.	94
Figure 5.13: HR-XPS scans of (a) Al 2p and (b) N 1s obtained from ~173 nm long AlN HNCs revealing presence of different bonding schemes.	95
Figure 5.14: (a) Top view SEM image obtained from PA-ALD (700-cycle) grown InN on nanoporous Si substrate, (b) Angled-view SEM image of the same sample, (c) Top view SEM image of InN HNCs revealing their morphology and dimensions, and (d) Angled-view SEM image of InN HNCs showing the free-standing height of InN nanocylinders.	96
Figure 5.15: (a) Top view and (b) cross-sectional view SEM images obtained after 3 minutes of Ar plasma exposure successfully removed InN from top of nano-pores leaving InN integrated inside Si(100).	98
Figure 5.16: (a) Top view SEM image of InN HNCs obtained after 6 sec of SF6 based Si(100) etching revealing their morphology and dimensions, (b) cross-sectional image of same InN HNCs showing the total height of nano-cylinders.	100
Figure 5.17: (a) TEM image of InN bundled HNCs, (b) TEM image of InN HNCs revealing their wall thickness and total length, (c) HR-TEM image of InN HNC displaying internal crystal structure and confirming the polycrystalline nature, (a) SAED pattern of InN HNCs, and (b) EDX elemental mapping of same sample.	101
Figure 5.18: GIXRD pattern obtained from (a) ~210 nm long InN HNCs, (b) ~47 nm thick InN deposited on Si via HCPA-ALD.	103
Figure 5.19: HR-XPS scans of (a) In 3d and (b) N 1s obtained from ~210 nm long InN HNCs revealing presence of different bonding schemes.	104
Figure 6.1: (a) XPS survey scan obtained from a ~32 nm thick plasma polymerized fluorocarbon thin film deposited on Si(100). High resolution XPS scans of (b) F 1s and (c) C 1s obtained from the same film.	109
Figure 6.2: Variation in contact angle (a) and thickness (b) of ZnO with the increase in number of growth cycles on Si (100) and fluorocarbon/Si.	110

Figure 6.3: XPS survey scans of ZnO grown with different number of ALD cycles on (a) Si(100) and (b) fluorocarbon/Si revealing presence of different elements.....	111
Figure 6.4: HR-XPS scans of Zn 2p _{3/2} obtained from ZnO grown on fluorocarbon/Si as a function of ALD growth cycles.....	112
Figure 6.5: SEM images of (a) bare fluorocarbon/Si sample, (b) ZnO coated on fluorocarbon/Si sample with 68 number of growth cycles.....	114
Figure 6.6: Plan view SEM images of 102 cycles ALD grown ZnO on (a) fluorocarbon/Si and (b) Si (100); 136 cycles ALD grown ZnO on (c) fluorocarbon/Si and (d) Si (100) (all scale bars = 50 nm).....	115
Figure 6.7: Variation in (a) contact angle and (b) thickness of HfO ₂ as a function of ALD growth cycles on Si(100) and fluorocarbon/Si.	117
Figure 6.8: XPS survey scans of HfO ₂ grown with different number of growth cycles on (a) Si (100) and (b) fluorocarbon/Si revealing presence of different elements.....	118
Figure 6.9: Variation in (a) contact angle and (b) thickness of Al ₂ O ₃ with the increase in number of growth cycles on Si(100) and fluorocarbon/Si.	120
Figure 6.10: XPS survey scans of Al ₂ O ₃ grown with different number of growth cycles on (a) Si (100) and (b) fluorocarbon/Si revealing presence of different elements.....	121
Figure 6.11: (a) Plan-view SEM image of 102 cycle ZnO ALD grown on fluorocarbon line patterns (scale bar = 10 μm) (inset) HR-SEM image from the interface of ZnO and fluorocarbon layer (scale bar = 50 nm). (b) Plan-view SEM image of 102 cycle ZnO ALD grown on fluorocarbon checker board patterns (scale bar = 150 μm) (inset) HR-SEM image from the interface of ZnO and fluorocarbon layer (scale bar = 100 nm). (c) XPS line scan obtained from patterned ZnO substrate.....	123
Figure 6.12: Variation in (a) contact angle and (b) thickness of TiO ₂ with number of growth cycles on PMMA, PVP, C ₄ F ₈ coatings, and reference Si(100) substrate.....	125

Figure 6.13: XPS survey scans of TiO ₂ grown with different number of ALD cycles on (a) PMMA and (b) PVP surface, confirming the effective inhibition/blocking of these layers up to more than 1200 and 300 cycles, respectively.....	127
Figure 6.14: XPS survey scans of TiO ₂ grown with different number of ALD cycles on (a) CF _x /Si and (b) Si(100) revealing the presence of similar elemental composition almost independent of film growth stage, confirming a non-delayed TiO ₂ deposition on both surfaces.	128
Figure 6.15: HR-XPS survey scans of Ti2p obtained from TiO ₂ at different stages of ALD-growth on (a) PMMA/Si(100) and (b) PVP/Si(100).	131
Figure 6.16: SEM images of PMMA/Si surface after 1200-cycle TiO ₂ growth (a) Si(100) substrate surface (b) the interface of Si(100) and PMMA showing the effective inhibition at the PMMA side.	132
Figure 6.17: XPS survey scans from sample surface after acetone treatment of PMMA layer subsequent to TiO ₂ ALD cycles, confirming the facile and complete removal of polymeric blocking layer even for 1200 growth cycles at a substrate temperature of 150 °C.	133
Figure 6.18: SEM images of (a) ebeam exposed and post developed PMMA, (b) and (c) TiO ₂ patterns grown on patterned PMMA/Si(100) surface after the removal of PMMA, (d) interface between TiO ₂ pattern and Si(100).....	136
Figure 6.19: (a) XPS Ti2p line scan obtained from mm-scale patterned TiO ₂ grown via AS-ALD recipe on PMMA/Si(100) samples, (b) EDX Ti K line scan obtained from nm-scale TiO ₂ line features produced via AS-ALD on e-beam lithography patterned samples.....	137
Figure 6.20: SEM image of (a) TiO ₂ pattern, (b) Ti K EDX elemental map, (c) O K EDX elemental map.	138
Figure 6.21: TEM image of (a) TiO ₂ patterned PMMA free region, (b) patterned TiO ₂ region revealing the thickness uniformity of pattern.....	139

List of Tables

Table 1.1: Alternative names of ALD	2
Table 2.1: Merits and demerits of ALD	16
Table 2.2: Comparison of ALD with other thin film deposition techniques.....	16
Table 4.1: Summary of studied growth parameters range and established value.	39
Table 4.2: Summary of studied growth parameters range and established value.	41
Table 4.3: SAED pattern analysis of InN thin film deposited on Si(100) substrate at 200 °C: comparison between measured and theoretical values of interplanar spacing (d_{hkl}) with corresponding crystallographic planes.	49
Table 4.4: Lattice parameters and alloy compositions (as determined by Vegard's law) for GaN, $\text{In}_x\text{Ga}_{1-x}\text{N}$, and InN films.	53
Table 4.5: Crystallite size values estimated using Scherrer formula for GaN, $\text{In}_x\text{Ga}_{1-x}\text{N}$, and InN films.	54
Table 4.6: Elemental composition, Ga/N ratio, and In fractions for $\text{In}_x\text{Ga}_{1-x}\text{N}$ films having different RS values.	55
Table 4.7: Calculation of number of sub-cycles of BN and GaN to deposit ~ 40 nm of $\text{B}_x\text{Ga}_{1-x}\text{N}$	70
Table 4.8: Calculation of number of sub-cycles of BN and InN to deposit ~ 40 nm of $\text{B}_x\text{In}_{1-x}\text{N}$	70
Table 4.9: $\text{B}_x\text{In}_{1-x}\text{N}$ and $\text{B}_x\text{Ga}_{1-x}\text{N}$ alloy compositions calculated from XPS measurements.	71
Table 5.1: SAED Results, Theoretical Values, and Corresponding Crystallographic Planes.....	84

Table 5.2: SAED pattern analysis of AlN HNCs: comparison between measured and theoretical values of interplanar spacing (d_{hkl}) with corresponding crystallographic planes.	93
Table 5.3: SAED pattern analysis of InN HNCs: comparison between measured and theoretical values of interplanar spacing (d_{hkl}) with corresponding crystallographic planes.	102
Table 6.1: Variation in Zn at. % with the increase in number of ZnO growth cycles on Si(100) and fluorocarbon/Si.	112
Table 6.2: Variation in Hf at. % with the increase in number of HfO ₂ growth cycles on Si (100) and fluorocarbon/Si	118
Table 6.3: Variation in Al at. % with the increase in number of Al ₂ O ₃ growth cycles on Si (100) and fluorocarbon/Si	121
Table 6.4: Variation in Ti at. % with the increase in number of TiO ₂ ALD-growth cycles.	128
Table 6.5: Decrease in thickness of PMMA with the increase in number of TiO ₂ growth cycles.	130

Chapter 1

Introduction

1.1 Historical Background of the Technique Used

Atomic layer deposition (ALD) is a low-temperature vapor phase growth technique, in which ultra-thin film growth is carried out by exposing the substrate to alternate pulsing of two precursors featuring surface chemisorption and ligand exchange reactions. Major advantages of ALD include large area uniformity, excellent three-dimensional (3D) conformality, and un-paralleled sub-angstrom level thickness control.[1], [2]

Origin of ALD dates back to 1970s where credit of realizing the principles of ALD for the first time is given to two different research groups i-e one Finnish and other Soviet-union. First patent of ALD was published in 1970s by a Finnish Professor Tuomo Suntola with the demonstration of following processes: growth of SnO_2 by Sn/O_2 precursors, growth of ZnS by Zn/S precursors, and growth of GaP by Ga/P precursors. The first commercial application of ALD has been realized in manufacturing of thin film electroluminescent displays in 1980s.[1], [2]

Less acknowledged pioneer of ALD is a research group in Soviet Union headed by Professor Aleskovskii. Shevjakov who first demonstrated the $\text{TiCl}_4/\text{H}_2\text{O}$ process to deposit layers of TiO_2 and $\text{GeCl}_4/\text{H}_2\text{O}$ process to grow films of GeO_2 in the proceedings of a conference, organized in 1965, and

published in 1967. The Soviet Union researchers described this technique as "molecular layering".

Partly because of its history, and partly because of its distinct properties, this technique has been referred with many different names. The current most commonly used name is ALD, which dates back to early 1990s. Plasma-enhanced atomic layer epitaxy (ALE) was first demonstrated in 1991 by De Keijser and Van Oordorp from Philips research laboratories in Eindhoven, Netherlands. In their work, remote microwave-induced plasma was utilized to generate hydrogen radicals which were then used for the deposition of gallium arsenide. A major driving force for ALD is in the prospective observed in continuous scaling down of microelectronic devices by using ALD. Table 1.1 represents the alternative names and abbreviations of ALD which have been utilized in history instead of ALD.[1], [2]

Table 1.1: Alternative names of ALD

Name	Abbreviation
Atomic layer chemical vapor deposition	ALCVD
Atomic layer deposition	ALD
Atomic layer epitaxy	ALE
Atomic layer evaporation	ALE
Atomic layer growth	ALG
Chemical assembly	
Digital layer epitaxy	DLE
Molecular deposition	
Molecular lamination	
Molecular layer epitaxy	MLE
Molecular layering	ML

1.2 Motivation

This thesis mainly consists of three sections: 1. InN and III-Nitride alloy thin films deposition using hollow cathode plasma assisted atomic layer deposition (HCPA-ALD), 2. Template assisted fabrication of III-nitride hollow nanocylinders via HCPA-ALD, and 3. Area selective ALD of metal oxides using polymer growth inhibition layers. The motivation for this thesis work is described in three separate following subsections.

1.2.1 InN and III-Nitride Alloy Thin Films Deposition Using HCPA-ALD

Among the III-nitride compound semiconductor materials family, indium nitride (InN) has attracted much attention due to its largest electron saturation velocity, highest mobility, smallest direct band gap, and smallest electron effective mass. InN has a relatively low decomposition temperature and possesses high nitrogen equilibrium vapor pressure.[3] The challenge of low dissociation temperature and high nitrogen vapor pressure necessitates lower temperature growth techniques and recipes for InN. Moreover, growth techniques which operate at high temperatures pose incompatibilities with temperature-sensitive substrates (*e.g.* glass, flexible polymers). Experimental efforts for enabling low temperature growth of InN are imperative to widen its perspective for applications in flexible (opto)electronics as well.

Small band gap value of InN has widened the spectral range covered by nitrides, from the ultraviolet for AlN to the near infrared for InN. With the last-decade discovery of the lower band gap of InN,[4], [5] $\text{In}_x\text{Ga}_{1-x}\text{N}$ can potentially cover the whole spectral range from ultraviolet to near-infrared. This provides a significant advantage to III-nitride family for the optoelectronic device applications such as full-color light-emitting diodes and highly efficient multi-junction solar cells.[6], [7] Commonly used epitaxy growth methods employ

high deposition temperatures, which is a critical limitation in growing indium-rich $\text{In}_x\text{Ga}_{1-x}\text{N}$ thin films. In addition, growth techniques which require high temperatures pose incompatibilities with temperature sensitive substrates (*e.g.* glass, flexible polymers). These limitations are the main driving source for a continuous exploration of alternative low temperature processes for the growth of $\text{In}_x\text{Ga}_{1-x}\text{N}$ alloys. Furthermore, an alternative growth method in which indium content can be precisely controlled with relative ease for tunable band gap engineering is highly imperative. With the same rationale, a low temperature growth method is necessary to control boron concentration in $\text{B}_x\text{Ga}_{1-x}\text{N}$ and $\text{B}_x\text{In}_{1-x}\text{N}$ alloys.

Unlike other chemical vapor deposition (CVD) methods, ALD is based on the saturative surface reactions, which results in a self-limiting growth mechanism. The growth temperatures can also be kept low, which makes ALD attractive and applicable for a wide range of substrates including transparent and flexible polymers. Alloy thin films can be deposited via PA-ALD either by regulating the vapor pressures of simultaneously exposed precursors or by composing a growth cycle that consists of subcycles of the constituent materials. The latter is termed as “digital alloying” which is a unique and straight forward method of accurately controlling the composition of thin film alloys.

1.2.2 Template Assisted Fabrication of III-nitride Hollow Nanocylinders via HCPA-ALD

By virtue of significant material properties and wide-spread device applications, nanostructures of III-nitride materials have been thoroughly explored [8]–[14] via either template-assisted or template-free fabrication methodologies.

A major limitation associated with template-free synthesis strategy is the lower degree of control over the properties of resulting structures. There may either exist additional unwanted morphologies or impurities in the final product which result in poor optical and electronic properties. It is of great significance

to fabricate ordered nanostructures with superior regularity and large-area uniformity for tailoring semiconductor characteristics in a way to enhance the performance of nanostructured materials. Template-based methods are advantageous in the sense that a well-defined and long-range ordered sacrificial template can be used to guide the morphology of the nanostructures which lead to their synthesis with controlled properties and large-area uniformity. Moreover, commonly used methods (metal organic chemical vapor deposition (MOCVD) and molecular beam epitaxy (MBE)) for the fabrication of III-nitride nanostructures employ high growth temperatures which can be lowered considerably by alternative low-temperature growth techniques.

Variety of sacrificial templates can be employed as growth temperature decreases. Polymeric materials are famous sacrificial templates due to their design flexibility, availability, simple synthesis, and low cost. In one prominent strategy, polymeric electrospun nanofibers have been utilized as templates for subsequent ALD growth to fabricate long and uniform metal-oxide and nitrides nanofibers with conformal and precise wall thickness control.[15]–[18]

The main drawback of electrospun nanofibrous templates is the randomness in the nanotemplate pattern: nanofibers are randomly oriented without any alignment. On the other hand, AAO membranes are another well-known class of templates that can be used to synthesize long-range ordered/aligned nanostructures with high degree of regularity and uniformity.[19]–[25] AAO membranes are advantageous since they can be utilized to produce free-standing nanostructures as well as nanostructures attached/integrated to the host substrate. AAO membranes have been used as templates to produce GaN nanodot arrays, nanotubular materials, and porous GaN films where GaN growth is carried out via MOCVD.²¹⁵⁻²¹⁸ Using such a non-lithographic approach to fabricate arrays of nanostructures provides an attractive solution for large-area nano-patterning with relative process simplicity, high throughput, and low cost. Nevertheless, reliability of nanostructures obtained using high aspect ratio templates are determined by the conformability of the thin film deposition process. On that note, ALD stands out as an ideal process that can be utilized to build

nanostructures with very high aspect ratio templates owing to its superior conformality, uniformity, and atomic-scale thickness control.

1.2.3 Area Selective Atomic Layer Deposition of Metal Oxides Using Polymer Growth Inhibition Layers

Controlling the lateral dimensions of thin films by patterning is pivotal in microelectronics industry due to ever-increasing trend towards further miniaturization of device feature sizes. Conventionally, thin film patterning is achieved by photolithography which includes several processing steps such as resist spinning, UV exposure, resist development, and film etching. ALD processes, in which film nucleation is critically dependent on the surface chemistry between gaseous precursors and the solid surface, provide an attractive opportunity for performing area-selective deposition by chemically modifying the substrate surface. Local modification of substrate surface opens up possibilities to achieve lateral control over film growth in addition to robust thickness control during ALD process. Area-selective ALD (AS-ALD) might pave the way for low-temperature self-aligned nanoscale device fabrication by reducing or eliminating lithography/etch process steps and minimizing hazardous reagent use. Taking these significant advantages into consideration, the efforts of developing reliable and effective AS-ALD recipes have attracted considerable interest in recent years. ALD-enabled nano-patterning has been classified under two broad categories, one with area-activated agents and the other with area-deactivated blocking/inhibition layers. So far, majority of the AS-ALD studies have been performed using area-deactivated approach where mostly self-assembled monolayers (SAMs) are utilized as the growth-blocking layers by covering the chemically reactive sites on the substrate and exposing non-reactive groups.[26]–[30]

Nevertheless, several constraints are associated with the AS-ALD processes relying on SAMs. It is essential to have large-area defect-free coverage of SAMs for effective deactivation. Formation of a high-quality SAM with almost no

defects is challenging and usually takes more than 24 hours to obtain relatively densely packed hydrophobic SAM coverage without microscopic pin holes.[26]–[30] Samples are immersed in a SAM solution for such a long time to enhance the packing density. Additionally, head groups must be chemically bonded to the surface of the substrate and it introduces a limitation for selection of substrates for which such bonding will occur. Controlling the dimensions of patterning is yet another issue for AS-ALD processes involving SAMs. As a typical SAM is only ~2 nm thick, it is quite challenging to fabricate thicker features more than a few nanometers.[28] Once the film thickness increases above the height of SAM, lateral film over-growth might start. On the other hand, polymer films are usually deposited using spin coating, which is a rather in-efficient and low throughput coating technique. Moreover, both SAMs and polymers are solution-based processes which implies that their applicability with patterning on 3D nanostructures will not be straightforward. Finally, solution-based processes also limit integrability of SAMs and polymers with the thin film processes carried out in vacuum reactors.

These restrictions pose serious limitations for successful integration of area-selective ALD processes for nanoscale device fabrication. Overcoming these issues require alternate approaches featuring significantly less process complexity. Only then AS-ALD might attain as serious process alternative for high-volume manufacturing.

Overcoming the limitations associated with SAM-based mask layers require the production of easily patterned, non-reactive, and defect-free blocking layer materials. Polymer films present an alternative way to prepare defect free masking layers which physically screen the active sites on the substrate and enable AS-ALD process. Indeed, polymer films with several critical advantages including quick and easy coating, defect free film quality, and ease of patterning have been implemented in majority of the lithographic patterning processes.

We demonstrate a new strategy to achieve selective deposition by using inductively coupled plasma (ICP) polymerized CF_x deactivation layer against metal-oxide ALD processes. Plasma polymerized CF_x layer was grown in an

ICP reactor using C_4F_8 feed gas. The relatively fast and conformal deposition of the CF_x layer (~30-35 nm/min) provides a strong advantage against SAMs and spin-coated polymer blocking layers. This strategy provides another distinct advantage; as the growth of CF_x blocking layer is performed in a vacuum reactor, it allows for easy integration with ALD reactors. A relatively easy thickness control of CF_x layer would possibly solve the issue of lateral broadening. An additional merit of such an approach would be to achieve topographical selectivity due to relatively conformal growth of CF_x layer which might enable patterning on 3D structures. All these advantages combined with the efficient gaseous precursor (C_4F_8) usage in vapor phase deposition process make this approach attractive to explore. Moreover, we also investigate poly(methyl methacrylate) (PMMA) and polyvinylpyrrolidone (PVP) polymer films as growth inhibition layers to demonstrate AS-ALD process of TiO_2 .

1.3 Objectives

The first part of the thesis focuses on growth recipe development and material characterization of InN and III-nitride alloy thin films via HCPA-ALD. Following are the main objectives of this section.

- Self-limiting, low-temperature (200 °C) growth of crystalline InN films exhibiting crystalline wurtzite structure and low impurity concentrations via HCPA-ALD.
- Detailed optimization of critical growth parameters including both indium and nitrogen precursor exposure dose and deposition temperature.
- Impact of HCPA-ALD process parameters on InN film quality.
- Evaluation of the structural, chemical, surface, and optical properties of the HCPA-ALD-grown InN samples.

- Self-limiting, low-temperature (200 °C) growth of crystalline $\text{In}_x\text{Ga}_{1-x}\text{N}$ films exhibiting crystalline wurtzite structure and low impurity concentrations via HCPA-ALD
- $\text{In}_x\text{Ga}_{1-x}\text{N}$ bandgap engineering studies via digital alloying and successful tuning of the bandgap towards near-infrared regime
- Low-temperature sequential pulsed chemical vapor deposition of ternary $\text{B}_x\text{Ga}_{1-x}\text{N}$ and $\text{B}_x\text{In}_{1-x}\text{N}$ thin film alloys.
- Successful band gap engineering of $\text{B}_x\text{Ga}_{1-x}\text{N}$ and $\text{B}_x\text{In}_{1-x}\text{N}$ demonstrated via digital alloying, resulting in continuous tunability from BN to GaN/InN.
- Compositional dependent structural, optical, and morphological properties of $\text{B}_x\text{Ga}_{1-x}\text{N}$ and $\text{B}_x\text{In}_{1-x}\text{N}$ ternary thin film alloys.

The second part focuses on demonstrating controlled fabrication of vertical GaN, AlN, and InN hollow nano-cylinders (HNCs) integrated to Si(100) substrates via template assisted HCPA-ALD. Towards this goal, we have utilized anodized alumina (AAO) membranes which function as the the three-dimensional nanotemplate for PA-ALD materials growth. Using the conformality of ALD in conjunction with subsequent processing steps, long-range ordered vertical III-nitride nanostructures with atomic-scale precision control have been obtained on Si substrates. In this regard, following were the main objectives.

- Fabrication of long-range ordered III-nitride nano-cylinders integrated inside Si(100) via combination of AAO templates and PA-ALD
- An in-depth materials characterization of PA-ALD grown III-nitride hollow nano-cylinders using scanning electron microscopy (SEM), energy dispersive X-ray analysis (EDX), transmission electron microscopy (TEM), selected area electron diffraction (SAED), grazing incidence X-ray diffraction (GIXRD), X-ray photoelectron spectroscopy (XPS), and photoluminescence (PL).

- Comparative analysis of material properties between nanostructured III-nitride materials and their thin-film counterparts both grown using low-temperature PA-ALD.
- Conformality analysis and comparison between different III-nitride nano-cylinders.

Another goal of this thesis was to demonstrate the AS-ALD of metal oxides and metals using polymers as growth inhibition layers. To achieve this goal, fluorocarbons, PMMA, and PVP were utilized as inert growth inhibition layers. After demonstrating the effectiveness of AS-ALD process, these polymers were patterned via either photolithography or e-beam lithography for subsequent patterning of metal oxides. Following were the major objectives of this section.

- Using ICP-polymerized fluorocarbon coating as hydrophobic blocking/inhibition layers for area-selective deposition
- Investigation of AS-ALD of metal-oxide materials including ZnO, Al₂O₃, TiO₂, and HfO₂ using plasma polymerized fluorocarbon as growth inhibition layer.
- An in-depth materials characterization using contact angle, XPS, spectroscopic ellipsometer, and SEM measurements to determine the extent of growth selectivity for the set of metal oxide materials.
- Patterning of metal-oxide using AS-ALD on lithographically defined patterns of CF_x layer.
- A comparative study of different polymeric materials including PMMA, PVP, and CF_x for demonstrating AS-ALD of TiO₂. An in-depth materials characterization to determine the extent of growth selectivity of TiO₂ using these polymer layers.
- Self-aligned growth of nano-scale TiO₂ using a PMMA masking layer that has been patterned using e-beam lithography. Also, the successful facile removal of PMMA after selective deposition has been an objective of this work.

1.4 Thesis Overview

In this part, a brief outline of the thesis is given. Chapter 2 presents a review of ALD and literature overview for the work presented in this thesis. Chapter 3 explains the experimental procedure together with the characterization techniques used. Chapter 4 presents the experimental results on growth of InN and III-nitride alloy thin films deposition using HCPA-ALD. Details regarding the template assisted fabrication of III-nitride hollow nanocylinders via HCPA-ALD are summarized in chapter 5. Chapter 6 presents the experimental results on AS-ALD of metal oxides using polymer growth inhibition layers. Finally, chapter 7 concludes the thesis.

Chapter 2

Theoretical Background and Literature Overview

In this chapter, a brief overview on ALD process will be presented first, which will include basic characteristics of ALD and thin-film growth mechanism. Moreover, advantages and disadvantages of ALD and comparison of ALD with other thin film deposition methods will be presented. After that, a brief literature overview on InN and III-Nitride alloy thin film deposition, template assisted fabrication of III-nitride nanocylinders, and area-selective ALD of metal oxides will be presented.

2.1 An Overview on Atomic Layer Deposition

Atomic layer deposition (ALD) is a special type of vapor phase material deposition scheme that enables the conformal coating of thin films with sub-nanometer thickness control and excellent large-area uniformity. A unit ALD cycle consists of four steps: (i) exposure of metal-containing precursor, (ii) purge or evacuation, (iii) exposure of second precursor, and (iv) purge or evacuation. During the introduction of each precursor, surface reactions take place only at the available reactive sites, self-limiting the film growth to a

certain sub-monolayer thickness within a single ALD cycle. Evacuation/purging of excess precursor molecules and reaction by-products eliminates gas phase reactions and thus CVD-growth mode. Besides being ligand-preserving low temperature growth technique, its self-limiting characteristic offers precision thickness control at sub-angstrom level with superior conformality and uniformity over arbitrary topography, large areas, and complex structures. In this regard, ALD becomes an attractive low-temperature material growth method to be used for template-assisted fabrication of various nanostructured materials.[1], [2]

2.1.1 Mechanism

Figure 2.1 shows a schematic representation of a typical ALD cycle. Layer by layer material growth consists of following four steps:

- (1) First precursor exposure, precursor chemisorbs on reactive sites with formation of reaction products.
- (2) Unreacted excess precursor and reaction byproducts removal by purging the reactor with an inert gas.
- (3) Second precursor exposure, precursor reacts with the 1st precursor which was chemisorbed on reactive sites with formation of reaction products.
- (4) Unreacted excess precursor and reaction byproducts removal by purging the reactor with an inert gas.

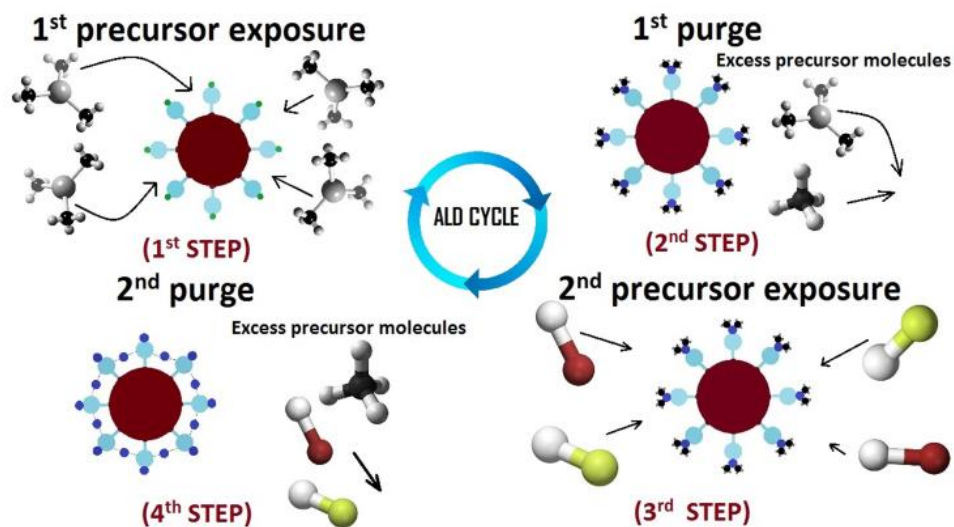


Figure 2.1: Schematic representation of an ALD cycle consisting of four steps.

2.1.2 Factors Causing Saturation and Growth of Less than Monolayer per Cycle

With the completion of one ALD cycle, amount of material deposited is called growth per cycle (GPC). There is a common misconception that ALD deposits one monolayer of material per cycle, however, reality is different i-e amount of material grown per cycle of ALD is less than a monolayer due to an effect known as “steric hindrance”. When a limited number of reactive sites are occupied by the reactants, a part of the surface is shielded by the bulky ligands of precursor molecules making some of the reactive sites unavailable to reactant molecules and resulting in less than monolayer GPC. Another possible reason of sub-monolayer GPC is the limited number of reactive sites in which the number of bonding sites is less than required to achieve a full ligand coverage. [1], [2]

2.1.3 ALD Window

ALD window is the temperature range in which self-limiting growth occurs. In this temperature range, deposition has an ideal constant growth rate with

deposition of one monolayer per cycle. Center line (Fig. 2.2) indicates the ALD window on the growth rate vs. temperature graph. Deviation from ideal self-limiting ALD line corresponds to different mechanisms which prevent ALD to attain the requirement of self-limiting reactions.

There are two possible mechanisms below ALD window which correspond to non-self-terminating reactions. There can be condensation of precursor molecules at low temperatures resulting in high deposition rate. Incomplete reactions at low temperature will lead to low GPC.[1], [2]

On the other hand, at high temperatures, thermal decomposition causes a CVD-like growth mechanism in which gas phase decomposition of precursor molecules occur. In addition, deposition rate may be less at higher temperatures owing to desorption of sub-monolayer's deposited by ALD.[1], [2]

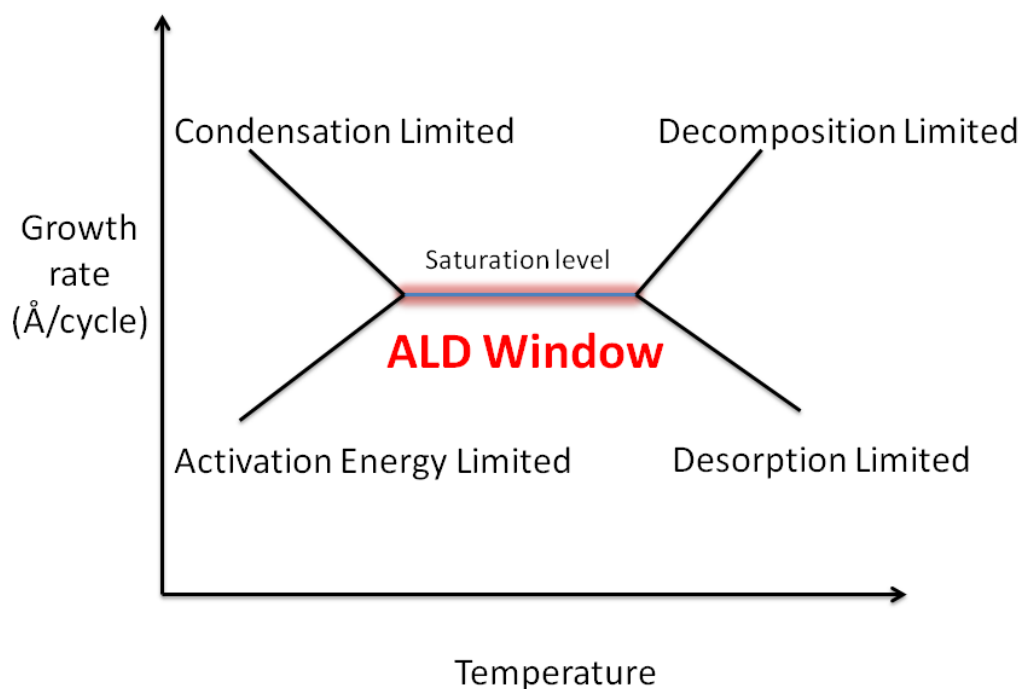


Figure 2.2: Effect of deposition temperature on the ALD growth rate.

2.1.4 Merits and Demerits of ALD and Comparison with Other Deposition Techniques

Table 2.1: Merits and demerits of ALD

Merits	Demerits
Simple and accurate thickness control by changing the number of reaction cycles	Slow growth rate
Excellent conformality and uniformity	Low precursor utilization efficiency
Atomic level control of material composition	
High quality material deposition at low processing temperatures	
No need of reactant flux homogeneity, which enables large area and batch capability	
Good reproducibility and straight forward scale-up	
No gas phase reactions occur, favoring the usage of precursors that are highly reactive towards each other	
Capability to prepare multilayer structures in a continuous process	

Table 2.2: Comparison of ALD with other thin film deposition techniques.

Method	ALD	CVD	MBE	Sputter.	Evapor.	PLD
Thickness Uniformity	Good	Good	Fair	Good	Fair	Fair
Film Density	Good	Good	Good	Good	Good	Good
Step Coverage	Good	Varies	Poor	Poor	Poor	Poor
Interface Quality	Good	Varies	Good	Poor	Fair	Varies
Low Temp. Deposition	Good	Varies	Good	Good	Good	Good
Deposition Rate	Poor	Good	Fair	Good	Good	Good
Lack of Pinholes	Good	Good	Good	Fair	Fair	Fair
Automated Multilayers	Good	Fair	Good	Good	Fair	Fair
Industrial Applicability	Varies	Good	Varies	Good	Good	Poor

MBE= Molecular beam epitaxy, CVD= Chemical vapour deposition, and PLD- Pulsed laser deposition

2.1.5 Plasma vs. Thermal ALD

Exchange reactions between reactant molecules and chemisorbed species can be sufficiently enhanced by using an external source of activation energy. Conventional mode of ALD (Thermal ALD) uses thermal energy to heat the entire reactor chamber of the substrate. One alternative of thermal ALD is plasma-enhanced ALD (PEALD) (also called as plasma-assisted ALD, PA-ALD), in which energetic radicals are generated to accelerate the self-terminating ALD reactions.

PA-ALD offers several merits over thermal ALD such as improved material properties,[31]:[32] reduced growth temperatures,[33], [34] and increased choice of precursors and materials.[35] Mainly, these superior properties are the result of high reactivity provided by energetic radicals. Moreover, better control of stoichiometry, increased growth rate, minimized/eliminated nucleation delay, and increased process versatility have been reported due to higher degree of freedom in processing conditions (operating pressure, plasma power, plasma exposure time, etc.) of PA-ALD.[35] The major limitation of PEALD process is reduced conformality on high aspect ratio structures, which is believed to be due to recombination of radicals in deep trenches of high aspect ratio nanostructures.

2.2 InN and III-Nitride Alloy Thin Film

Deposition Using HCPA-ALD reactor

Among the III-nitride compound semiconductor materials family, InN has attracted much attention due to its largest electron saturation velocity, highest mobility, smallest direct band gap, and smallest electron effective mass. Electronic transport properties of InN reveal exceptionally high peak drift velocity at room temperature which makes it highly attractive potential candidate for high speed electronics.[3], [36], [37] Most thermodynamically favourable and stable phase of InN is hexagonal with wurtzite structure. Small

band gap value of InN has widened the spectral range covered by nitrides, from the ultraviolet for AlN to the near infrared for InN.

Significant progress has been made in the growth of hexagonal InN by different growth methods and among them, the most prominent methods are MBE[38], metal organic vapor phase epitaxy (MOVPE)[39], sputtering[40], and pulsed laser deposition[41].

Hexagonal wurtzite InN and GaN exhibit direct band gaps of 0.7 and 3.4 eV, respectively. Hence, ternary $\text{In}_x\text{Ga}_{1-x}\text{N}$ alloys provide band gap values which can be tuned from near ultraviolet to infrared range.[42] $\text{In}_x\text{Ga}_{1-x}\text{N}$ is a material of prime importance with its applications in $\text{In}_x\text{Ga}_{1-x}\text{N}/\text{GaN}$ based double heterostructure light emitting diodes (LEDs) and potential use in high-efficiency multi-junction thin film solar cells.[43] $\text{In}_x\text{Ga}_{1-x}\text{N}$ alloys are also considered as potential candidates for green LEDs with target wavelength of 525 nm. Green LEDs and deep UV LEDs are conceived as an important challenge in LED technology. Green LEDs with emission wavelength of 525 nm exhibit low efficiency compared to red and blue LEDs and this obstacle is known as the “Green gap”.[44] However, due to the considerable lattice mismatch between GaN and InN, there exists a solid phase miscibility gap in $\text{In}_x\text{Ga}_{1-x}\text{N}$ alloy system which is a significant hurdle in growing particularly In-rich $\text{In}_x\text{Ga}_{1-x}\text{N}$ films with decent crystalline quality.[45] Moreover, difference in formation enthalpies and vapor pressures of InN and GaN can lead to either low solubilities or surface segregation of indium in $\text{In}_x\text{Ga}_{1-x}\text{N}$ alloys.[46], [47]

A number of techniques have been utilized for the growth of $\text{In}_x\text{Ga}_{1-x}\text{N}$ films which include pulsed laser deposition,[48] MOCVD,[49] MBE,[50] sputtering[51], and hydride vapor phase epitaxy.[52] Among them, MOCVD and MBE are the leading epitaxial growth techniques to grow high quality single-crystalline $\text{In}_x\text{Ga}_{1-x}\text{N}$ thin films with very low impurity contents.

Hexagonal boron nitride (*h*BN) thin films have attracted special attention due to their useful properties such as wide band gap, high thermal conductivity, high oxidation resistance, and low surface energy.[53]–[55] On the other hand, GaN has been considered as one of the most important member of the III-nitride

compound semiconductor material family, due to its superior electrical properties in addition to its robustness.[56] Therefore, a hybrid of these superior properties might potentially be achieved via $B_xGa_{1-x}N$ ternary alloys. $B_xGa_{1-x}N$ can provide more degrees of freedom in fabricating optoelectronic device structures operating at shorter wavelengths.[57], [58] $B_xIn_{1-x}N$, a ternary nitride semiconductor alloy that consists of hBN and $hInN$ can be employed in optoelectronic devices which operates in a quite broad spectrum ranging from deep ultraviolet to infrared (200 – 1800 nm).[65]

There are few reports on growth of $B_xGa_{1-x}N$ and $B_xIn_{1-x}N$ which have been grown using high-temperature MBE and MOVPE.[65], [66]

2.3 Template Assisted Fabrication of III-Nitride Nanocylinders

By virtue of significant material properties of III nitrides and wide-spread device applications, nanostructures of III-nitride materials have been thoroughly explored.[8]–[14] As a general classification, either template-assisted or template-free strategies have been used for the fabrication of III-nitride nanostructures. Template-free methods can be further classified into mainly two types: catalyst-assisted and catalyst-free methods. In template-assisted strategy, material growth is carried out on nanostructured templates such as carbon nanotubes, polymers, or anodic AAO.[17], [67], [68] Subsequent to growth, template material might be removed via high-temperature treatment (calcination) or physical/chemical etching to obtain various kinds of nanostructures. On the other hand, catalyst-assisted growth typically occurs via vapor liquid solid growth where nanostructures are fabricated along a supersaturated catalytic liquid metal such as Ni or Au.[67] Catalyst free methods generally utilize selective area growth of preferential growing crystallographic planes over non preferential planes by altering the processing conditions in order to favor growth of material in one dimension.[69], [70]

GaN nanostructures have been prepared in the variety of forms including nanorods[71][72]–[80], nanowires[81], [82], [82]–[103], nanotubes[104], nanoparticles[105], nanopillars[106], [107][108]–[112][113]–[115][111], [113], [114], [116]–[118][8], [107], [119][120]–[125][126]–[128][129], [130][103], [131]–[138], nano-flowers[139], [140], hollow spheres[141], [142], nanowall crystals[8], and nanoplates[143]. The common methods utilized for preparing these nanostructures are arc discharge, laser ablation, MOCVD, MOVPE, and pyrolysis.[104], [140], [142][83], [94], [95], [99] Nanowires and nanorods are obtained via catalyst-assisted MOCVD.[67] The distinction between nanorods and nanowires lies in their aspect ratio; nanowires possess significantly larger aspect ratio. Strong cathodeluminescence and/or photoluminescence from GaN nanopillars has been observed as compared to single crystalline GaN thin films which is attributed to high crystal quality, strain/stress reduction, and improved anti reflection properties of GaN nanopillars.[107], [111], [117], [127], [134], [136] InGaN/GaN multiple quantum well LEDs in the form of nanopillars showed enhanced light extraction efficiencies as compare to their thin film counterparts.[121] Catalyst assisted techniques are preferably used to produce GaN nanowires since catalysts such as Au and Ni provide considerably high growth rates. Au is a preferred catalyst of choice among others, mainly due to two reasons; Au has a high defect formation energy ($\sim 4\text{eV}$) in GaN, and the synthesized final product exhibits lower levels of impurities.[67] Utilizing Fe and Ni materials for catalyst-assisted growth resulted in GaN nanowires with higher impurity concentrations which brings unwanted harms particularly to optical and electrical properties. AlN nanostructures have been fabricated in the form of nanofibers[18][144]–[147], nanorods[144][148]–[155], nanowires[156]–[171], nanoparticles[172]–[174], and nanowhiskers[175][176] mainly using electrospinning, CVD, and MBE methods. InN nanostructures have been synthesized in the form of nanowires[177]–[204], nanoparticles[205]–[212], nanorods[213]–[231] using CVD and MBE techniques.

2.4 Area-Selective ALD of Metal Oxides Using Polymer Growth Inhibition Layers

Micro and nanoscale film patterning is an essential part of modern microelectronics industry, being the essential ingredients of Si-based CMOS transistor technology. As device scaling proceeds towards sub-10 nm era where process tolerances become atomic-scale, the adoption of alternative nanoscale process integration schemes become critical for both Moore's Law (extension of device down-scaling) and beyond Moore (novel device concepts). Nanoscale process integration demands novel nano-patterning techniques in compliance with the requirements of feature generation devices. Conventionally, top-down subtractive (etch) or additive (deposition/lift-off) processes in conjunction with various lithography techniques is employed to achieve film patterning, which become increasingly challenging due to the ever-shrinking alignment requirements.[232]–[234] To reduce the complexity burden of lithographic alignment in future technology nodes, self-aligned processes such as selective deposition and selective etching might provide vital solutions.

Since ALD relies heavily on surface chemistry, it is possible to chemically modify the surface to achieve AS-ALD. Such ALD-enabled nano-patterning approaches have been classified into two categories; (i) area-activated AS-ALD and (ii) area-deactivated AS-ALD. So far, most of the AS-ALD studies have been performed with area deactivation, where part of the substrate is blocked/deactivated by certain coatings allowing film to grow only on the uncovered areas. Surface deactivation has been typically achieved by selectively attaching SAMs on the substrate surface. SAMs are monolayer films which are comprised of relatively long organic chains with reactive groups at both ends. The head group, alkane chain, and a tail group are the main constituents of SAMs. Head group facilitates the adsorption of the molecule on to the substrate surface while tail group terminates the surface and exposes itself directly for ALD reaction. An ordered SAM is formed due to Van der Waals interactions

between the alkane chains. The tail group determines the property of the surface termination either as hydrophilic or hydrophobic which in turn either enhances or blocks the nucleation and growth of ALD grown films.

Certain polymers such as PMMA and PVP have also been used as area deactivating agents to block ALD growth processes.[235]–[237] If ALD grown films start nucleating on these patterned polymer layers, conventional lift-off process is utilized to achieve the desired patterning.[237]–[239][240]

Chapter 3

Experimental Details

This chapter provides experimental details of InN and III-nitride alloy thin film deposition, fabrication of III-nitride nanocylinders, and selective area ALD of metal oxides as well as the materials characterization techniques. All of the deposition and fabrication processes were performed at UNAM Cleanroom Facility (UCF) except AAO (template for III-nitride nano-cylinders fabrication) foil preparation which were prepared in TOBB University of Economics and Technology. UNAM characterization tools were used for materials property evaluation of thin film and nanostructured III-nitride, and metal oxide materials.

3.1 Hollow Cathode Plasma Assisted Atomic Layer Deposition of InN

InN thin films were deposited in a modified Fiji F200-LL remote-plasma ALD reactor (Ultratech/CambridgeNanoTech Inc.), which is backed by an adixen ACP 120G dry scroll vacuum pump. The Fiji is a modular high-vacuum ALD system which is capable of carrying out thermal as well as plasma-enhanced depositions. The details of the system are presented in Fig. 3.1.

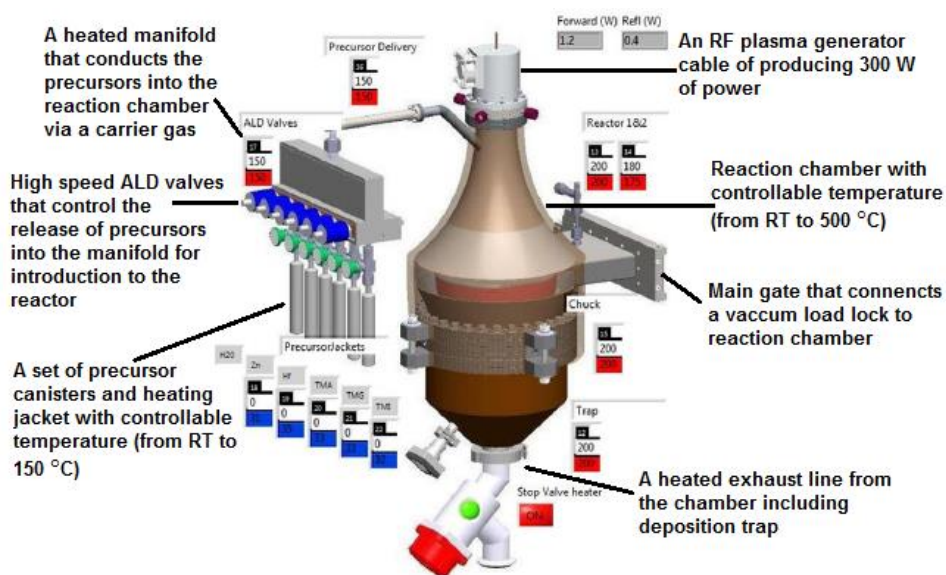


Figure 3.1: Details regarding specific parts and their features of ALD FIJI system

Original system was revamped by replacing the quartz-based ICP source with a stainless steel HCP source (Meaglow Ltd., Thunder Bay, ON, Canada). The original RF power supply (Seren IPS Inc., R301), matching network controller (Seren IPS Inc., MC2), and automatic matching network (Seren IPS Inc., AT-3) units were used to activate the HCP discharge. Si (100) and double-side polished quartz substrates were cleaned by sequential ultrasonic agitation in 2-propanol, acetone, and methanol, followed by rinsing with DI water and drying with N₂. Native oxide layer on Si was removed by submerging the samples into dilute hydrofluoric acid solution for 2 min, followed by rinsing with DI water and drying with N₂. Substrates were kept at deposition temperature for at least 20 min before the growth process was started. The rotation speed of the Adixen ATH 400 M turbo pump was adjusted in order to keep the reactor pressure fixed at ~150 mTorr during growth sessions, whereas the base pressure of the system was lower than 10⁻⁵ Torr.

Trimethylindium (TMI – 99.999%, Dockweiler GmbH.) and N₂ plasma have been used as indium and nitrogen precursors, respectively. Organometallic precursors and N₂ plasma were carried from separate lines using 30 and 100 sccm Ar, respectively. N₂ plasma gas flow rates and plasma power were

constant in all experiments as 50 sccm and 300 W, respectively. Both N₂ and Ar gases were of 99.998% purity which were further purified through Microtorr (MCL-702F) gas purifier units.

3.2 Hollow Cathode Plasma Assisted Atomic Layer Deposition of In_xGa_{1-x}N Thin Films

GaN, InN, and In_xGa_{1-x}N thin films were deposited at 200 °C in the same modified Fiji F200-LL remote-plasma ALD reactor (Ultratech/CambridgeNanoTech Inc.), described in section 3.1. Silicon (Si) and double-side polished quartz substrates were cleaned by sequential ultrasonic agitation in 2-propanol, acetone, and methanol, followed by rinsing with DI water and drying with N₂. Native oxide layer on Si was removed by submerging into dilute hydrofluoric acid solution for 2 min, followed by rinsing with DI water and drying with N₂. Substrates were kept at deposition temperature for at least 20 min before the growth process was started. Triethylgallium (TEG) and TMI were used as gallium and indium metal precursors; whereas N₂/H₂ and N₂ plasma were used as nitrogen precursors for growth of GaN and InN films, respectively. Same nitrogen source was used for respective subcycles of GaN and InN in the main cycle of In_xGa_{1-x}N thin film growth. Organometallic precursors and N₂/H₂ (or N₂) were carried from separate lines using 30 and 100 sccm Ar, respectively. N₂/H₂ (or N₂) gas flow rates and plasma power were constant in all experiments as 50/50 (50) sccm and 300 W, respectively. The system was purged for 10 s after each precursor exposure. Figure 3.2 shows growth process sequence of In_xGa_{1-x}N thin film. A super cycle of In_xGa_{1-x}N is depicted which comprise of a single GaN and InN subcycle. Steps 1 to 11 are repeated in sequence to complete one supercycle of In_xGa_{1-x}N thin film. The recipe starts with 10 s N₂/H₂ plasma exposure followed by 10 s purging time. Carrier gas for the precursors and N₂/H₂ plasma is Ar which is also used for purging to remove excess reactant and byproducts. Step 3 is TEG pulse followed

by 10 s of purge time. After that, N₂/H₂ plasma is introduced as a second reactant followed by purging. Step 7 is 10 s exposure of N₂ plasma followed by purging. The reactor is then subsequently exposed to TMI pulse followed by 10 s of purge time. TMI pulse is marked by a line and is not visible due to low vapour pressure of TMI. The last two steps are 40 s N₂ plasma exposure and 10 sec of purging time.

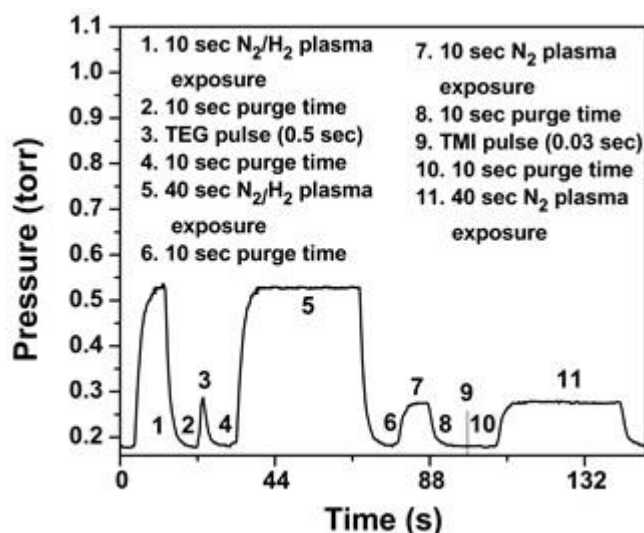


Figure 3.2: A schematic showing growth process sequence of In_xGa_{1-x}N thin film with single sub cycle of InN and GaN

3.3 Sequential Pulsed Chemical Vapor Deposition of Ternary B_xGa_{1-x}N and B_xIn_{1-x}N Thin Film

Alloys

BN, GaN, InN, B_xIn_{1-x}N, and B_xGa_{1-x}N thin films were deposited at 450 °C in a modified Fiji F200-LL remote-plasma ALD reactor (Ultratech/CambridgeNanoTech Inc.). Solvent cleaning of silicon (Si) and double-side polished quartz substrates was performed by sequential ultrasonic agitation in 2-propanol, acetone, and methanol, followed by rinsing with DI water and drying with N₂. Si was submerged into dilute hydrofluoric acid solution for 2 min in order to remove the native oxide layer, followed by rinsing

with DI water and drying with N₂. Substrates were kept at deposition temperature for at least 20 min before the growth process was started.

Triethylboron (TEB), TEG, and TMI were used as boron, gallium and indium metal precursors. N₂/H₂ and N₂ plasma were used as nitrogen precursors for growth of GaN and InN films, respectively. Same nitrogen source was used for respective sub-cycles of GaN and InN in the main cycle of B_xGa_{1-x}N and B_xIn_{1-x}N thin film growth. BN growth with TEB and N₂/H₂ plasma as boron and nitrogen precursors, respectively at 450 °C has been reported elsewhere.[241] For B_xGa_{1-x}N growth, N₂/H₂ plasma has been used as nitrogen source for subcycle of BN. However, as InN subcycle in B_xIn_{1-x}N thin film uses N₂ plasma as nitrogen source, we have used N₂ plasma as nitrogen precursor for BN subcycle in B_xIn_{1-x}N thin film growth in order to match the plasmas in the same growth run. Also, a separate growth run of BN was carried out using N₂ plasma as nitrogen source to compare the material properties of BN with B_xIn_{1-x}N thin film alloys. Organometallic precursors and N₂/H₂ (or N₂) were carried from separate lines using 30 and 100 sccm Ar, respectively. TEG and TMI precursors were 99.999 % pure, while TEB was ≥95 % pure. Initial purity of N₂-H₂ plasma gases and carrier gas, Ar was 99.999 % and these gases were further purified using MicroTorr gas purifiers. N₂/H₂ (or N₂) gas flow rates and plasma power were kept constant in all experiments as 50/50 (50) sccm and 300 W, respectively. The system was purged for 10 s after each precursor exposure.

3.4 Template Assisted Fabrication of III-Nitride Nano-Cylinder Arrays via Plasma-Assisted Atomic Layer Deposition

3.4.1 AAO Foils Preparation

The free standing AAO molds were fabricated by using voltage reduction method.[242] Firstly nanoporous AAO molds were synthesized on both sides of the high purity Al foil by a two-step anodization method.[243] Briefly, Al foil

(99.998%, Alfa Aesar, Germany) was polished with sand paper and cleaned by using a standard electrochemical process. During this process, Al foil was electropolished in a chemical mixture of 95 wt% H₃PO₄ (Sigma, USA), 5 wt% H₂SO₄ (Sigma, USA) and 20 g/l of CrO₃ (Prolabo, Belgium) at 15 V. The first anodization step was then carried out at 50 V at 7 °C in 0.3 M oxalic acid solution for 18 h. A thick and non-uniform AAO layer was removed from Al foil by using 0.2 M chromic acid (Prolabo, Belgium) solution at 75 °C and second anodization step was completed under the same conditions for 20 min. At the end of these steps, anodization voltage was gradually reduced to 14 V by a 5% voltage reduction every 2 min. To obtain free standing AAO mold, this material was immersed in v/v %10 H₃PO₄ solution until bubble layer was formed on AAO molds. The thin molds (5 cm²) were then collected from Al foil using a thin parafilm backing paper.

3.4.2 Vertical III-nitride Hollow Nano-cylinder Array

Fabrication

AAO membrane was attached to the Si(100) surface using triton liquid solution which helped to achieve better adhesion of AAO membrane to the substrate surface and prevent possible membrane detachments during the subsequent fabrication steps. Triton was then removed from the surface using acetone and the surface was dried at conventional air ambient and room temperature.

Si(100) was etched through AAO membrane hard masks in an RIE reactor using Ar (100 sccm)/CHF₃ (5 sccm) etch gas mixture for a total etch time of 70 min. During Si etching, coil and platen power were maintained as 450 and 100 W, respectively. III-nitride materials including GaN, AlN, and InN were deposited in a modified Fiji F200-LL remote-plasma ALD reactor (Ultratech/CambridgeNanoTech Inc.). While the unit growth cycle for GaN consisted of TEG pulse (0.5 s), Ar purge (10 s), N₂/H₂ plasma exposure (60 s), and Ar purge (10 s), one AlN ALD cycle was formed by trimethylaluminum (TMA) pulse (0.06 s), Ar purge (10 s), N₂/H₂ plasma exposure (40 s), and Ar

purge (10 s). For InN on the other hand, unit growth cycle contained TMI pulse (0.07 s), Ar purge (10 s), N₂ plasma exposure (100 s), and Ar purge (10 s). N₂/H₂ or N₂ plasma gas flow rates and plasma power were constant in all experiments as 50/50 sccm and 300 W, respectively. Both N₂ and Ar gases were of 99.998% purity which were further purified through Microtorr (MCL-702F) gas purifier units. All III-nitride growth experiments were performed at a substrate temperature of 200 °C.

III-nitrides deposited on the top of pores were removed in RIE reactor using Ar (100 sccm) etching followed by selective etching of surrounding Si using SF₆ (60 sccm) etch recipe to obtain III-nitride HNCs. During both these etch steps, coil and platen power were maintained as 450 and 100 W, respectively. The schematic step-by-step fabrication of vertically aligned III-nitride HNCs are shown in Fig. 3.3.

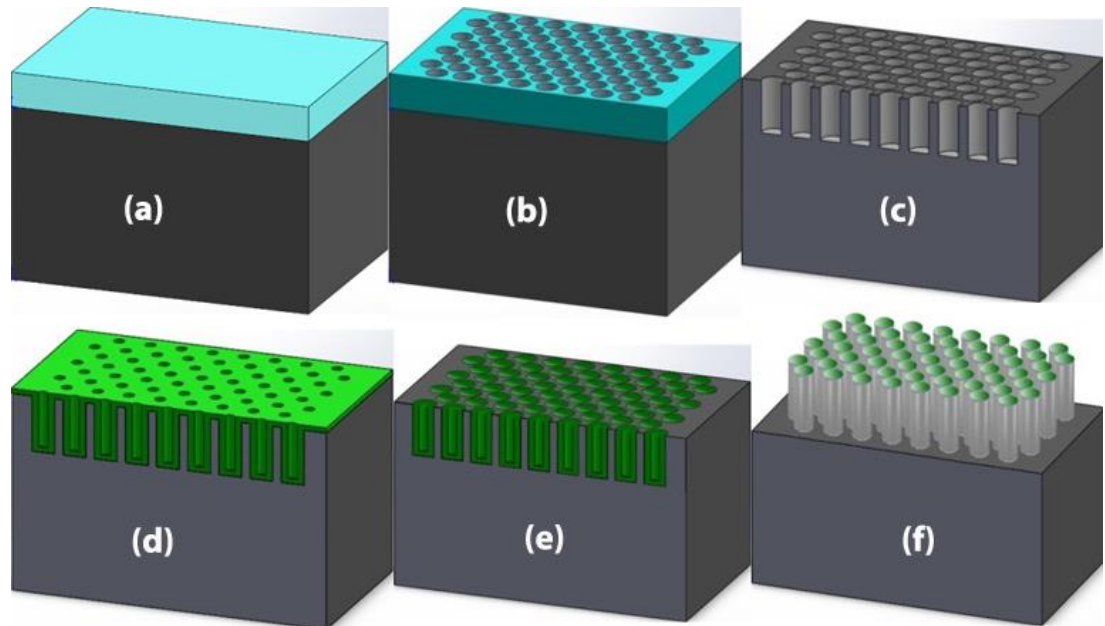


Figure 3.3: The schematic showing step-by-step fabrication of vertically aligned III-nitride HNCs: (a) AAO membrane placement on Si(100), (b and c) Si patterning with Ar/CHF₃ based reactive ion etching (RIE) using AAO membrane as hard mask material to achieve nanoporous Si substrate, (d) conformal coating of III-nitride materials, (e) Ar based RIE of PA-ALD coated III-nitride material from top surface of Si, (f) SF₆ based selective etching of Si to obtain III-nitride HNCs.

3.5 Area Selective Atomic Layer Deposition of Metal Oxides Using Polymer Growth Inhibition Layers

As a proof of concept hydrophobic inhibition layer to demonstrate AS-ALD, CF_x was coated by plasma polymerization using ICP etching reactor with C_4F_8 gas line, normally used to execute deep reactive ion etching (DRIE) recipes for Si etch processes. Deposition of CF_x was performed for 70 sec using C_4F_8 gas flow rate of 70 sccm. A plasma power of 400 W was employed and growth was performed at room temperature. For preparation of reference control samples, Si(100) samples were solvent cleaned and exposed to O_2 plasma for 2 minutes before metal-oxide ALD growth in order to increase the concentration of hydroxyl groups on the substrate. ZnO, HfO_2 , and Al_2O_3 layers were deposited by ALD using Et_2Zn , $\text{Hf}(\text{NMe}_2)_4$, $\text{Al}(\text{CH}_3)_3$, and H_2O as zinc, hafnium, aluminum, and oxygen precursors, respectively. All depositions were carried out at 200 °C in Savannah S100 ALD reactor, (Ultratech/CambridgeNanotech Inc.) using N_2 as the carrier and purge gas. One growth cycle of ZnO consisted of Et_2Zn pulse (0.015 s), N_2 purge (10 s), H_2O pulse (0.015 s), and N_2 purge (10 s). One growth cycle of HfO_2 consisted of $\text{Hf}(\text{NMe}_2)_4$ pulse (0.2 s), N_2 purge (15 s), H_2O pulse (0.015 s), and N_2 purge (10 s). $\text{Hf}(\text{NMe}_2)_4$ was preheated to 75 °C and stabilized at this temperature prior to depositions. One growth cycle of Al_2O_3 consisted of $\text{Al}(\text{CH}_3)_3$ pulse (0.015 s), N_2 purge (8 s), H_2O pulse (0.015 s), and N_2 purge (8 s).

PMMA and PVP polymers films were utilized as growth inhibition layers to demonstrate AS-ALD of TiO_2 . PMMA solution was prepared using 2 % PMMA (Sigma-Aldrich, average Mw 350000) in toluene while PVP solution was prepared using 1 wt % PVP (Sigma-Aldrich, average Mw 1,300,000) in ethanol. PMMA and PVP films were coated on Si(100) substrate using spin coating with a revolution per minute (RPM) value of 4000 and acceleration of 2000 for 40 sec followed by a heat treatment on hot plate for 20 minutes at 110 °C to ensure the complete removal of solvent content. PMMA and PVP film thicknesses were

measured as ~43 and 60 nm, respectively utilizing spectroscopic ellipsometer. As reference control samples, Si(100) samples were solvent-cleaned and exposed to O₂ plasma for 2 minutes before TiO₂ growth in order to increase the concentration of hydroxyl groups on the substrate surface. TiO₂ was deposited using tetrakis(dimethylamido)titanium (TDMAT) and H₂O as titanium and oxygen precursors, respectively with N₂ as carrier gas. ALD experiments were carried out at 150 °C in Savannah S100 ALD reactor (Cambridge Nanotech Inc.) One unit growth cycle of TiO₂ consisted of TDMAT pulse (0.03 s), N₂ purge (20 s), H₂O pulse (0.015 s), and N₂ purge (20 s).

3.6 Characterization Methods

Grazing-incidence X-ray diffraction (GIXRD) patterns were recorded in an X'Pert PRO MRD diffractometer (PANalytical B.V., Almelo, Netherlands) using Cu K α radiation. Data were obtained within the 2 Θ range of 10-90° by the summation of ten scans, which were performed using 0.1° step size and 15 s counting time. Interplanar spacing (d_{hkl}) values were calculated from peak positions using the well-known Bragg's law. Lattice parameters a and/or c were calculated by substituting d_{hkl} values in Eqn. (3.1), which relates the interplanar spacing (d_{hkl}), miller indices (hkl), and lattice parameters (a and c) for hexagonal crystals.

$$\frac{1}{d^2} = \frac{4}{3} \left(\frac{h^2 + hk + k^2}{a^2} \right) + \frac{l^2}{c^2} \quad (3.1)$$

Elemental composition, valence band spectra, and chemical bonding states of the thin films and nanostructures were determined by XPS using Thermo Scientific K-Alpha spectrometer (Thermo Fisher Scientific, Waltham, MA) with a monochromatized Al K α X-ray source. Sputter depth profiling was performed with a beam of Ar ions having an acceleration voltage and spot size of 1 kV and 400 μ m, respectively. Surface morphologies of the thin films and nanostructures were revealed using SEM (FEI, Hillsboro, OR NNL 600i) and an atomic force

microscope (AFM) (XE-100E, PSIA, Suwon, Korea) which was operated in the non-contact mode.

Tecnai G2 F30 TEM (FEI, Hillsboro, OR) was utilized for the high-resolution (HR) imaging and obtaining SAED pattern of the thin film and nanostructured samples. TEM sample for thin films were prepared by a Nova 600i Nanolab focused ion beam (FIB) system (FEI, Hillsboro, OR) with an acceleration voltage of 30 kV using various beam currents ranging from 50 pA to 21 nA. Damage layer was removed by FIB milling at a beam voltage of 5 kV. Elemental mapping was performed in TEM, using an EDX.

Spectral transmission measurements were performed with a UV-VIS spectrophotometer (HR4000CG-UV-NIR, Ocean Optics Inc.) in the wavelength range of 200-1000 nm relative to air, and the optical constants of the films were determined using a variable angle spectroscopic ellipsometer (V-VASE, J.A. Woollam Co. Inc., Lincoln, NE) which is coupled with rotating analyzer and xenon light source. The ellipsometric spectra were collected at three angles of incidence (65°, 70°, and 75°) to yield adequate sensitivity over the full spectral range. Optical constants and film thickness values were extracted by fitting the spectroscopic ellipsometry data. The numerical iteration was performed to minimize the mean-square error function using WVASE32 software (J.A. Woollam Co. Inc., Lincoln, NE). The homogeneous Tauc-Lorentz (TL) function was used as an oscillator. The absorption coefficient,

$$\alpha(\lambda) = \frac{4\pi k(\lambda)}{\lambda} \quad (3.2)$$

was calculated from the $k(\lambda)$ values determined from the ellipsometry data. Optical band gap (E_g) is expressed by the following equation for direct band gap materials, which can be analytically extracted via extrapolation of the linear part of the absorption spectrum to $(\alpha E)^2=0$

$$\alpha E = A(E - E_g)^{1/2} \quad (3.3)$$

PL spectra of the GaN HNCs and thin films was measured at room temperature and at a constant excitation laser intensity of 64 W/cm². The samples were excited by HeCd laser at 325 nm and the PL spectra was recorded by Exemplar Plus BWTek spectrometer.

Chapter 4

InN and III-Nitride Alloy Thin Films Deposition Using HCPA-ALD

This chapter presents the experimental results of HCPA-ALD grown InN, $\text{In}_x\text{Ga}_{1-x}\text{N}$, $\text{B}_x\text{Ga}_{1-x}\text{N}$, and $\text{B}_x\text{In}_{1-x}\text{N}$ thin films. Growth recipe optimization as well as optical, morphological, structural, and compositional characterization results are discussed in detail.

4.1 Hollow Cathode Plasma Assisted Atomic Layer Deposition of InN Thin Films

HCPA-ALD InN thin films were grown using TMI and N_2 plasma as indium and nitrogen precursors, respectively. Several parameters including N_2 plasma exposure time, TMI pulse, purge time, and growth temperature were studied and optimized in order to develop the self-limiting ALD growth recipe for InN. During optimization experiments, N_2 plasma flow rate and plasma power were kept constant as 50 sccm and 300W, respectively.

4.1.1 Optimization of Growth Parameters

Figure 4.1 shows the effect of indium and nitrogen precursor doses on the growth rate of InN. Initially, TMI pulse length, purge time, and growth temperature were kept constant as 0.07 s, 10 s, and 200 °C, respectively. N₂ plasma exposure time was varied to investigate the effect on growth rate. After each growth run using different N₂ plasma exposure time, spectroscopic ellipsometer measurement was carried out subsequently to extract the thickness of the grown film. Growth rate was then evaluated by dividing the measured film thickness with the total number of growth cycles. Growth rate decreases progressively with increase in N₂ plasma exposure time from 40 s to 100 s. It was found as 1.60 Å/cycle with 40 s of plasma exposure time which decreases to 0.64 Å/cycle under 100 s of exposure time. In order to explore the main cause of growth rate decrease, all the samples were examined by XPS and the data is presented as inset of Figure 4.1. Films were etched using Ar⁺ ions before taking XPS data to obtain elemental concentrations from the bulk of the films. XPS measurements revealed a decrease in carbon content of the films with increase in N₂ plasma exposure time. With 40 s N₂ plasma exposure time, 19 at. % carbon was found in the bulk of the film. Carbon content decreases to ~3 at. % with the increase in N₂ plasma exposure time to 100 s. Previously, we have demonstrated HCPA-ALD of AlN, BN, and GaN films using the trimethylaluminum, triethylboron, and trimethylgallium, respectively together with N₂/H₂ plasma.[32], [241], [244] These metal precursors belong to the organometallic precursor family which contains methyl/ethyl groups bonded to metal atoms. Purpose of using H₂ plasma in addition to N₂ plasma was to effectively remove the carbon ligands during the film growth. However, in the case of InN, we had found that addition of H₂ plasma with N₂ plasma as second precursor resulted in InN films with poor crystalline quality showing high level of impurities with significant voids in the films, resulting in low-density films.[245] This profound effect of H₂ plasma was attributed to plasma-related deterioration during the growth. In that context, present results illustrate that N₂-only plasma exposure

time is critical in removing the carbon containing ligands of TMI and results indicate that higher N₂ plasma exposure time is necessary to obtain InN films with minimum amount of carbon incorporation. For the TMI saturation curve (Fig. 4.1), N₂ plasma dose, purge time, and growth temperature were kept constant at 100 s, 10 s, and 200 °C, respectively. Deposition rate increased with increasing TMI dose until 0.07 s, where growth rate became saturated at ~0.67 Å/cycle. Increasing the TMI pulse length above 0.07 s does not affect the amount of species adsorbed. Hence, reaction becomes self-terminating with sufficiently long TMI exposure and GPC shows a decent saturation behaviour.

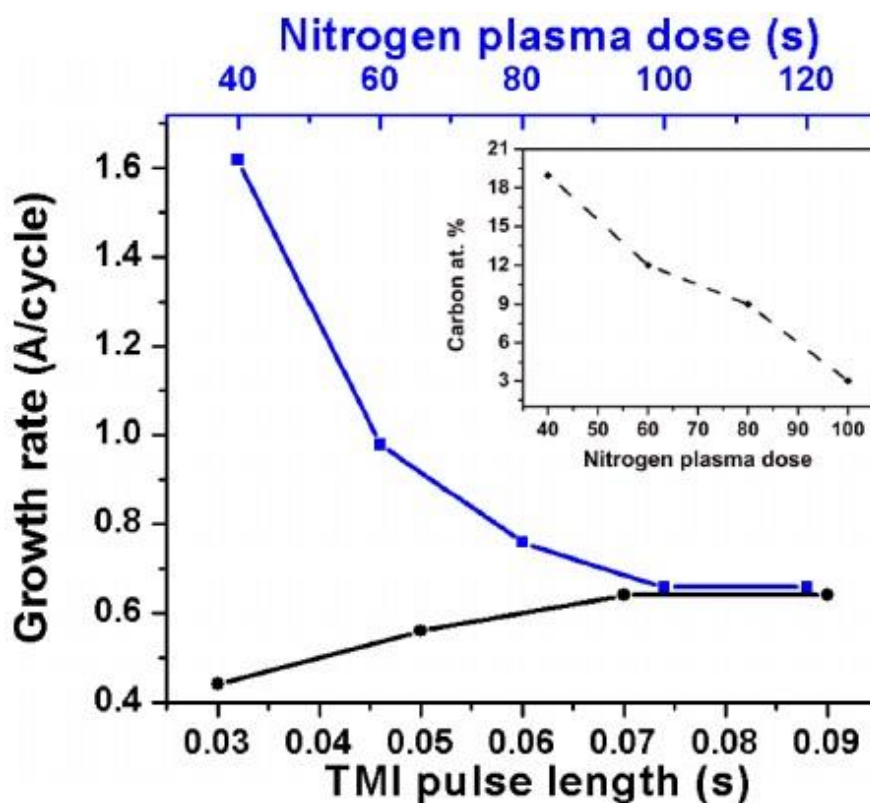


Figure 4.1: Effect of precursor doses on growth rate at 200 °C: TMI pulse length was kept constant at 0.7 s for the N₂ plasma saturation curve, N₂ plasma dose was kept constant at 100 s for the TMI saturation curve. (Inset) N₂ plasma dose vs. carbon at. % present in the bulk of the film.

Film thickness vs. number of deposition cycles is given in Fig. 4.2. The growth can be considered in steady regime where film thickness increases linearly with increasing number of cycles. Linear growth behaviour is an important hall mark of self-limiting ALD due to several reasons: number of cycles does not alter the number of surface reactive sites and steric hindrance of the ligands of the adsorbed species causes saturation. Steric hindrance is a well-known term in ALD where adsorbed ligands in one half reaction can shield/shadow part of the surface from being accessible to the second reactant and surface is considered “fully saturated.”[246] Additionally, these results show that growth of InN begins immediately on the substrate without any incubation period. Indeed, it seems that InN growth exhibits a slight substrate-enhanced behaviour taking into account the non-zero extrapolation of the linear-fitting line. Substrate enhanced growth refers to a growth type in which number of reactive sites on the substrate is higher than on the ALD-grown material, which results in higher GPC in the beginning of the growth than at the steady regime.[246]

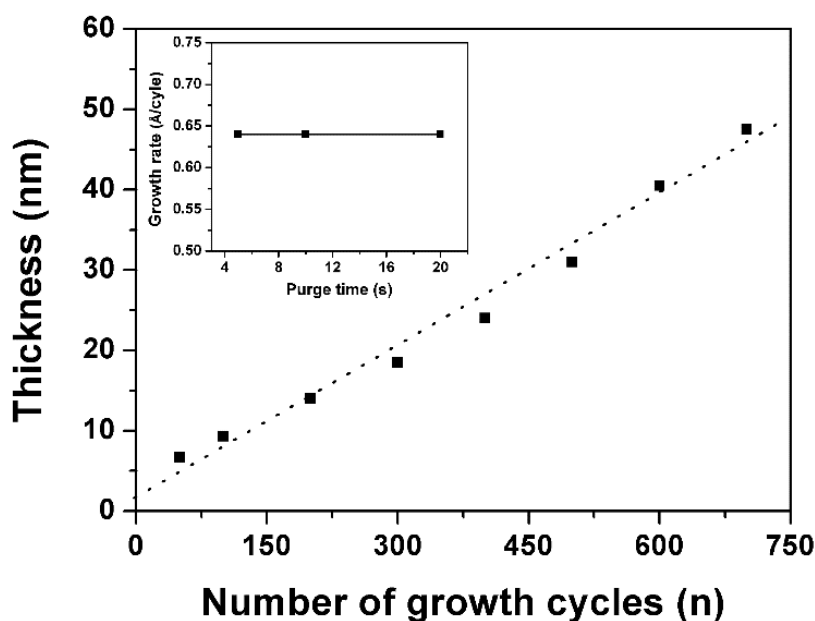


Figure 4.2: InN film thickness vs. number of deposition cycles. (Inset) Deposition rate as a function of purge time: TMI dose and N₂ plasma exposure time were constant at 0.7 and 100 s, respectively.

The purge cycles between the TMI and N₂ plasma exposure steps must also be sufficiently long. If not long enough purged, the GPC increases due to overlapping of metal and nitrogen precursors in gas phase, leading to non-self-limiting chemical vapor deposition (CVD)-type of growth. On the other hand, purge cycles should be short enough so that possible desorption of chemisorbed precursor molecules from the substrate surface can be avoided.[246] The effect of purge time on deposition rate (Inset of Fig. 4.2) was studied at 200 °C by keeping the TMI pulse length (0.07 s) and N₂ plasma exposure time (100 s) at its optimized conditions. Growth rate remained constant as 0.64 Å/cycle for purge times within 5-20 s range, indicating that the studied range of purge time satisfies the necessary conditions for self-limiting ideal ALD. Based on this result, purging time for InN growth cycle was set to 10 s.

Deposition rates of InN thin films and In/N ratio has been obtained at substrate temperatures ranging from 150 to 350 °C (Fig. 4.3). Growth rate decreases sharply from 1.36 to 0.64 Å/cycle with the increase in growth temperature from 150 to 200 °C, respectively. With further increase in substrate temperature, GPC further decreases to ~0.52 Å/cycle and remains saturated around this value within the temperature range of 250-350 °C. XPS measurements from bulk of InN sample grown at 150 °C reveal 25 at. % carbon which suggest the ineffective removal of carbon containing ligands (methyl groups) of TMI in the growing film possibly due to insufficient thermal energy for the completion of TMI-N₂ plasma reaction. These unreacted carbon containing ligands are the main reason for the high growth rate at 150 °C. XPS measurements were conducted on InN samples grown at different temperatures in which data was collected from the surface of the thin films. In/N ratio was computed from the composition of InN thin films and plotted against substrate temperature (Fig. 4.3). At 150 °C, film is found to be N rich with In/N ratio of 0.62 while films are In rich (In/N>1) at temperatures above 200 °C. At 200 °C, film was nearly stoichiometric with In/N ratio of 1.03. A similar trend has been reported for ALE-grown InN films by Nepal *et al.* where they found N rich films for substrate temperatures below 180°C and In rich films above

180°C.[247] Additionally, they reported that N rich InN films were insulating while In rich InN films exhibited lower resistivity. Less resistive In rich films were correlated with nitrogen vacancies (V_N) which is the major contributing source of electrons in InN films. These V_N were believed to form with sufficient thermal energy only at growth temperatures above 200 °C.[247] A summary of the studied growth parameters for HCPA-ALD grown InN thin films and established values are provided in Table 4.1.

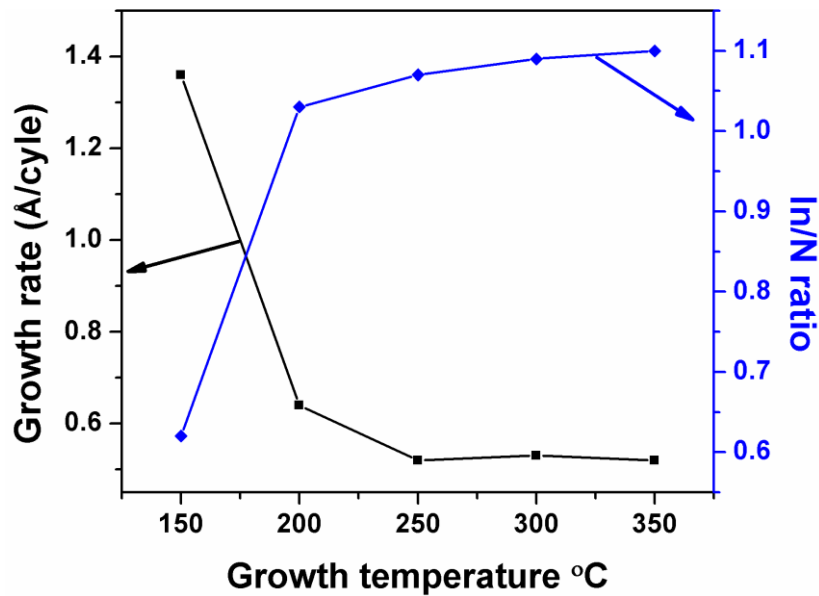


Figure 4.3: Growth rate and In/N ratio (evaluated by XPS) of InN deposited at different substrate temperatures.

Table 4.1: Summary of studied growth parameters range and established value.

Parameters	TMI pulse length (s)	N ₂ plasma exposure time (s)	Purge time	Growth temperature(°C)
Studied range	0.03-0.09	40-100	5-20	150-350
Established value	0.07	100	10	200

4.1.2 Material Characterization of InN Thin Films

After optimization of the main growth parameters, a 700-cycle growth of InN was carried out at 200 °C on Si (100) and double-side polished quartz for

detailed material characterization at optimized conditions listed in Table 4.1. Spectroscopic ellipsometer revealed the thickness of the film as ~48 nm while XRR extracted the thickness of the film as ~43 nm. XRR further reveals film density as 6.30 g/cm³.

XPS measurement was used to analyse the elemental composition, chemical bonding states, and impurity contents of the InN film. Survey spectrum from the surface of the film shows the presence of In 3d, N 1s, C 1s, and O 1s elements. Table 4.2 shows the chemical composition of InN film deposited on Si (100) surface, both on the as deposited surface and in the bulk. Table 4.2 illustrates that In/N ratio is closer to ~1; which indicates that InN deposited at 200 °C possesses near-ideal stoichiometry. Surface of the film showed a highly oxidized and contaminated (21% oxygen and 31% carbon) character. High concentration of adventitious carbon and oxygen found on the surface of the film originates from post deposition atmospheric exposure. InN thin film was etched by Ar⁺ ions for 60 s in order to obtain XPS survey scan from the bulk of the films. Analysis of the bulk InN reveals that In/N ratio is greater than unity and indicates nitrogen deficient films. Similar behaviour has been observed in case of ion beam deposited and reactively sputtered InN films.[248], [249] This observed difference in stoichiometry from surface and bulk of the films have been explained by preferential sputtering of N atoms by Ar⁺ ions used to sputter and depth profile the film of interest. Although Ar⁺ ion etching of InN does not provide information about stoichiometry from the bulk of the film due to limitation of preferential etching, it is a suitable method to estimate impurity concentration within the bulk of the film. ~2 at. % oxygen and ~3 at. % carbon was observed in the bulk of InN sample. Although minimized by the long N₂-plasma exposure cycles, C 1s signals originating from the bulk of the film indicates that carbonaceous ligands from indium precursor have not been removed completely during the reaction of TMI and N₂ plasma. At this point, we are not sure about exact source of oxygen. However, oxygen might come from possible sources such as impurities in plasma gases and organo-metallic precursors as well as from trapped oxygen/water vapor within the relatively

thick, multi-layer coatings on the inner walls of the ALD reactor. Moreover, as films are relatively thin, molecular oxygen and water vapor from atmospheric ambient might diffuse into the InN thin film after the deposition which depends on film characteristics such as grain growth, grain boundaries, stability, defects etc. Either of the above can contribute to the oxygen incorporation in InN thin films.

Table 4.2: Summary of studied growth parameters range and established value.

Position of measurement	Elemental composition (at.%)				In/N ratio
	In	N	O	C	
Surface	24.75	23.96	20.66	30.63	1.03
Bulk	65.02	29.83	2.1	3.05	2.17

Figure 4.4 represents the compositional depth profile of InN film deposited on Si (100) substrate, which reveals the variation in atomic ratios of indium, nitrogen, carbon, oxygen, and silicon along the etching direction from the air/InN interface towards the InN/Si (100) interface. Film stoichiometry was disturbed after the first etching step due to the reason mentioned above. This data reveals that elemental concentration of In and N remains constant in the film along the etching direction. Both oxygen and carbon atomic concentration decays rapidly after the first etching step and becomes nearly constant after second etching step. The high-resolution scans of In3d and N1s are given in Figs. 4.5(a) and (b), respectively, both which refer to the bulk film ($t_{etch} = 60$ s). The In3d spectrum is known to contain the In3d_{5/2} and In3d_{3/2} spin-orbit doublet (separation of 7.6 eV) and an intensity ratio of 3:2.[250] FWHM and asymmetry of the peaks suggest more than one type of bonding scheme for indium and nitrogen. In3d HR spectra (Fig. 4.5a) shows In3d_{5/2} and In3d_{3/2} spin orbit doublet and both of these peaks have been deconvoluted in to two Gaussians. In3d_{5/2} subpeak originating at 443.5 eV corresponds to In-N bond while second subpeak at 444.42 eV is associated with In-O bonds.[250], [251] In3d_{3/2} peak was deconvoluted into two subpeaks located at 451.49 and 451.88 eV, respectively. Former corresponds to In-N bond while later indicates again the presence of In-

O species.[252] The difference between the binding energies of the two In-3d spin orbit doublet peaks is 7.63 eV which is in agreement with previously reported values.[250] N1s spectra is deconvoluted with two Gaussians as shown in the Fig. 4.5b. Literature reports show that N-In bond in nitrogen spectra shows feature at 396.4 eV.[250] Therefore, first subpeak in N1s spectra detected at 396.8 eV can be attributed to the N-In. Bello et al. showed that the most probable formations in InN other than indium-nitride are oxynitrides.[249] Any form of N-O bonding will appear in the spectra at higher binding energy with respect to the main peak (396.4 eV), i.e., the shoulder peak can be attributed to the presence of In-O bond.[250], [251]

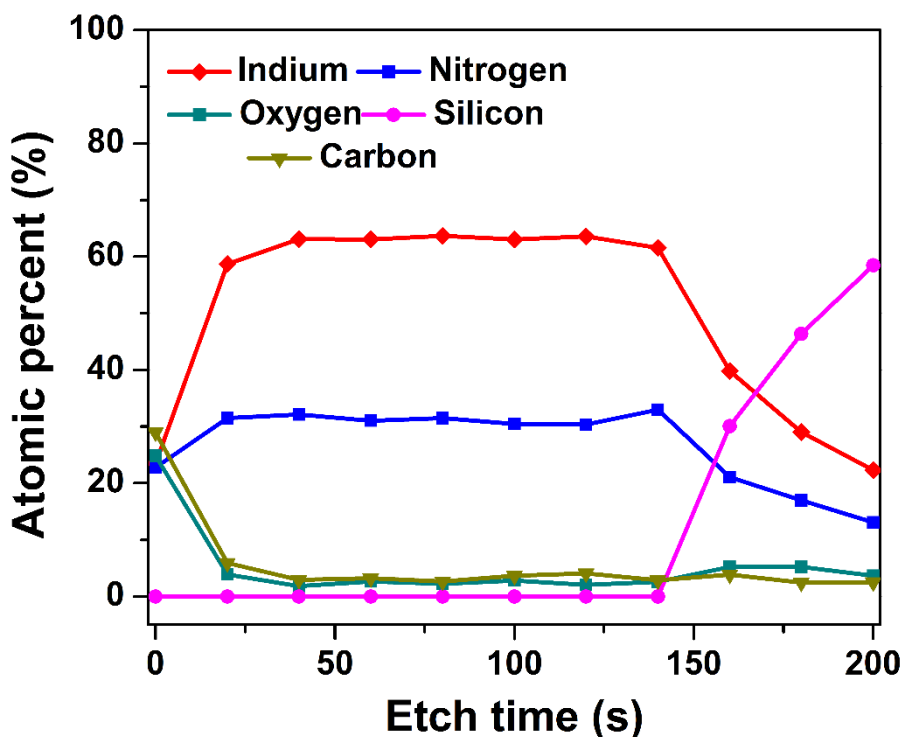


Figure 4.4: Compositional depth profile of InN thin film deposited on Si(100) at 200 °C.

XPS-measured valence band spectrum of HCPA-ALD grown sample was obtained in order to extract information about electronic structure of the InN sample (Fig. 4.6). The position of the valence band maxima has been determined from linear extrapolation of leading edge and base line (inset of Fig. 4.6). It turns out that VBM lies at ~1.7 eV below Fermi level for InN sample. It shows that In4d peaks are by 16.1 eV from VBM of InN. Similar values of VBM has

been reported in literature for InN films grown using different techniques.[251], [253] In our case, we have determined the band gap of InN as ~ 1.9 eV by the help of optical characterization of our sample, which will be discussed later in this section. VBM position reveals that Fermi level is located fairly close to the conduction band and this in turn indicates that the grown InN layers should have n-type conductivity.

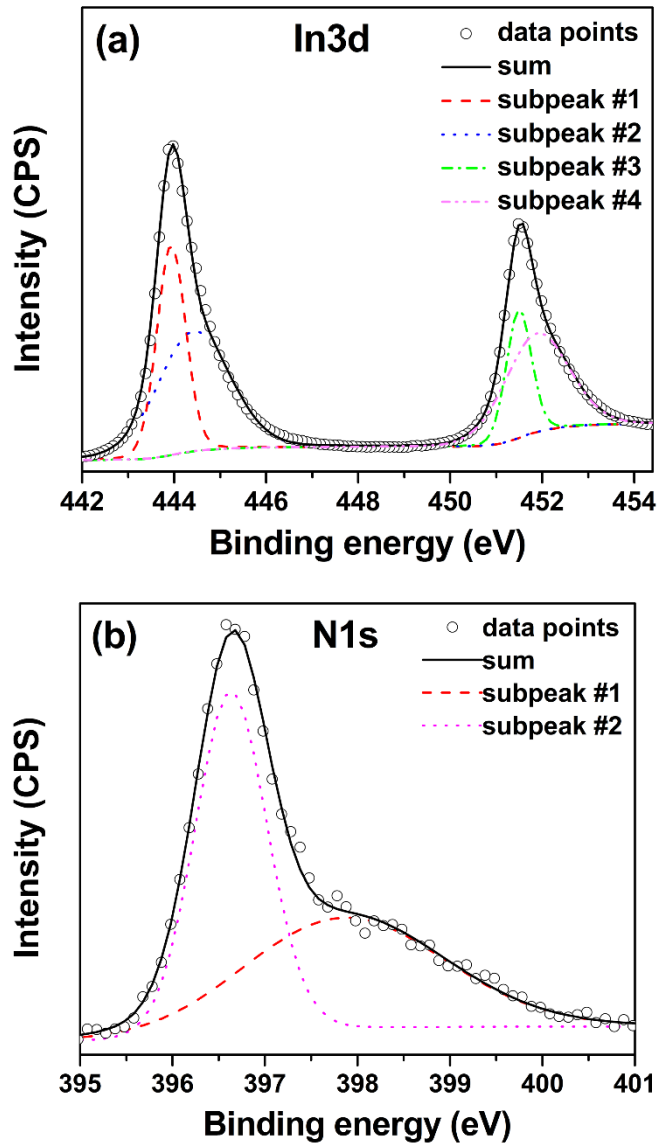


Figure 4.5: High resolution XPS scans of (a) In3d and (b) N1s obtained from InN thin film deposited on Si(100) at 200 °C.

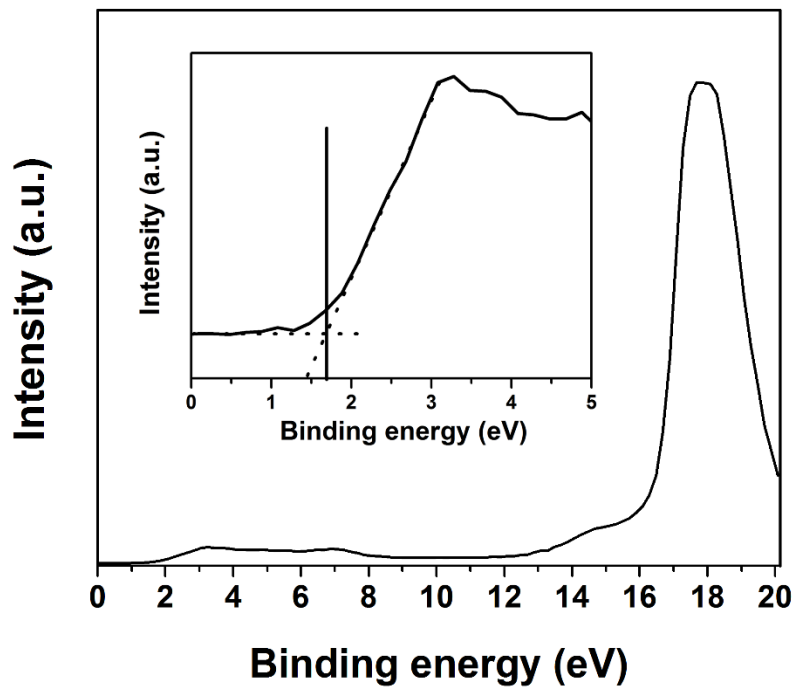


Figure 4.6: Valence band spectra of InN sample deposited on Si(100) at 200 °C. Inset shows the position of spectra near valence band maximum region.

Figure 4.7(a) shows plane view SEM images of InN thin film deposited on Si (100) substrate using optimized parameters. Highly uniform grainy structure is apparent. Spread of grain size is relatively high as some grains grew larger than the others. Average grain size was estimated using Image J image analysis software where grains were marked using the grain boundaries as edges of the grains. Average area of grains was estimated as $3.9 \times 10^{-4} \mu\text{m}^2$ while average diameter was calculated as ~ 22 nm. Surface morphology of the InN thin films was also examined by AFM. Figure 4.7(b) shows the surface scan of InN thin film. Root mean square (Rms) surface roughness of the ~ 48 nm thick InN film was measured as 0.98 nm from a $1 \mu\text{m} \times 1 \mu\text{m}$ scan area.

The structural properties of InN films were studied by GIXRD (Fig. 4.8). Measurement was performed on ~ 48 nm thick InN grown on Si (100) substrate. The polycrystalline wurtzite structure of InN is clearly visible in the recorded GIXRD spectrum. The exhibited pattern was indexed by hexagonal crystal system (ICDD reference code: 00-050-1239). The lattice parameters a and c were calculated using 2θ positions of (002) and (100) reflections. Interplanar

spacing (d_{hkl}) values of (002) and (100) planes were calculated from Bragg's law and it was inserted into Eq. (3.1) to obtain the c and a axis lattice parameters. c-axis lattice parameter was deduced as 5.71 Å which is close to the value of 5.70 Å reported for fully relaxed InN films.[254], [255] a-axis lattice parameter was calculated to be 3.53 Å which matches well with the strain free InN films reported in the literature.[254], [255] We have reported a and c axis lattice parameters of a ~20 nm InN grown using HCPA-ALD as 3.50 and 5.61 Å, respectively.[256] For a thick InN film (~48 nm) reported in the present case, shift of lattice parameters towards the ideal values of stain free InN indicates the relaxation of the film. Strain reduction with the increase in thickness of the polycrystalline InN thin films has been reported in the literature as well.[257]

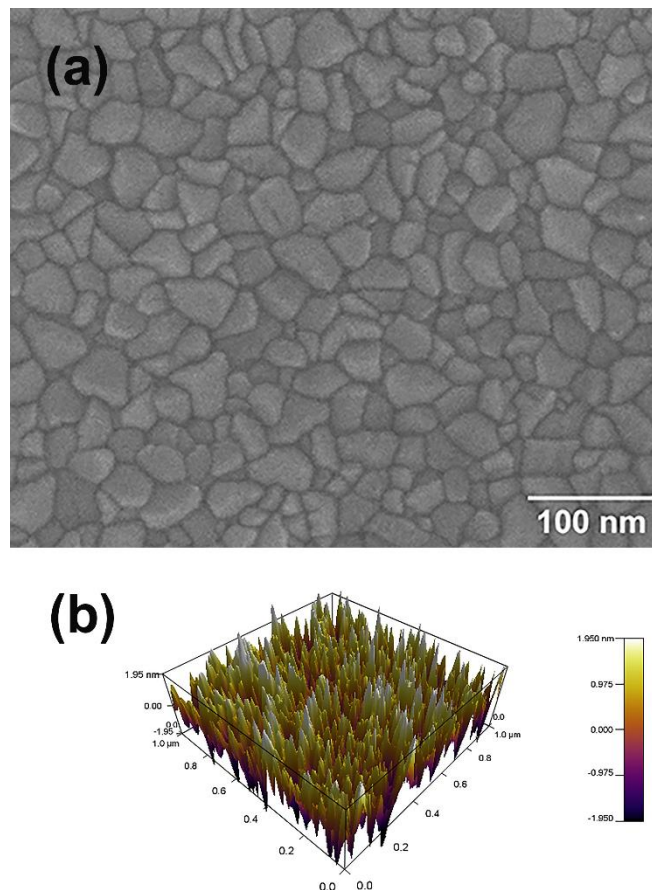


Figure 4.7: (a) SEM images of InN thin film deposited on Si(100) substrate at 200 °C, (b) Surface morphology of same sample revealed by AFM.

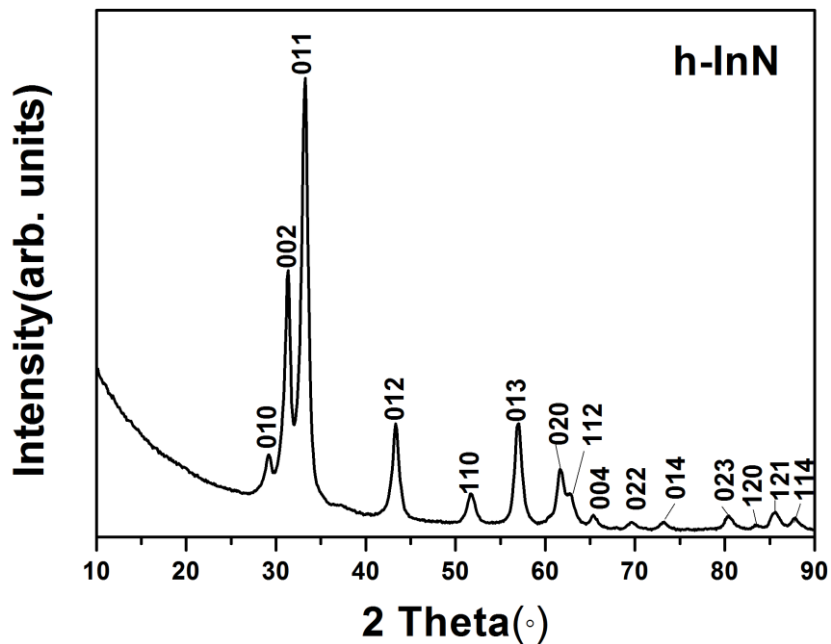


Figure 4.8: GIXRD pattern of InN film deposited on Si(100) substrate at 200 °C.

TEM experiments were carried out on InN sample grown at 200 °C on Si (100) in order to further explore the crystal structure in detail. The sample to be examined was capped with an AlN layer to prevent any possible crystal damage of InN by high energy Ga ions of the FIB system, which is used to prepare the samples to be analysed. The average thickness of InN was measured as ~43 nm from cross-sectional TEM measurements, which is in close agreement with the thickness data obtained from XRR measurements. Fig. 4.9a shows the cross-sectional TEM image of InN sample which depicts the interface of InN with SiO₂/Si. Polycrystalline structure showing several individual crystalline domains of InN with different crystallographic orientations is visible. A ~3 nm thick amorphous SiO₂ layer was observed at the InN/Si interface, which could either form during TEM sample preparation using FIB or it was present as native oxide on the surface of Si before the InN growth. Figure 4.9(b) shows the high resolution cross-sectional TEM image from bulk of InN thin film. It shows several crystalline subsections of InN and in each crystalline subsection, lattice fringes of InN are organized in different orientations which imply the polycrystalline structure of InN.

Inset of Fig 4.9(a) shows EDX elemental maps of In, N, Al and Si obtained from the AlN-capped InN thin film sample deposited on Si (100) at 200 °C. A cross sectional portion of the film is selected and elemental distribution is clarified by exposing the electron beam point by point over the selected portion of interest. Si, In, N, and Al show strong contrast in the colorized maps and they are represented by different colours which show their presence within the scanned area. Presence of Al originates from AlN which was used as capped layer for TEM sample preparation. Interface of AlN and InN is distinct and distribution of In and N is fairly uniform in the scanned InN region. Figure 4.9(c) shows SAED pattern of the same InN sample. Polycrystalline diffraction rings of InN can be seen from this pattern. The interplanar spacing (d_{hkl}) values were calculated from the diffraction rings which have been shown in Table 4.3. The diffraction rings are indexed as (100), (101), (102), and (104) reflections of hexagonal structure of polycrystalline InN, which are supported by GIXRD results (ICDD reference code: 00-050-1239).

Refractive index and extinction coefficient of InN film deposited at 200 °C are shown in Fig. 4.10(a). Refractive index, which is 2.66 at 650 nm, decreases to 2.09 at 1500 nm. These values are in good agreement with the reported values for polycrystalline hexagonal InN thin films.[258] Previously, we had reported refractive index value of 2.55 at 650 nm for a ~20 nm InN thin film grown by HCPA-ALD at the same substrate temperature but non-optimized growth conditions.[245] This shows that, with the increase in thickness of InN from 20 to 48 nm, refractive index increased from 2.55 to 2.66 at 650 nm. This improvement might be attributed to film densification with the increase in thickness of the film. Extinction coefficient (k) of InN film, which is ~0.51 at 600 nm, decreases rapidly within the wavelength range of 600–800 nm. At longer wavelengths, k value further decreases and reaches rather insignificant level.

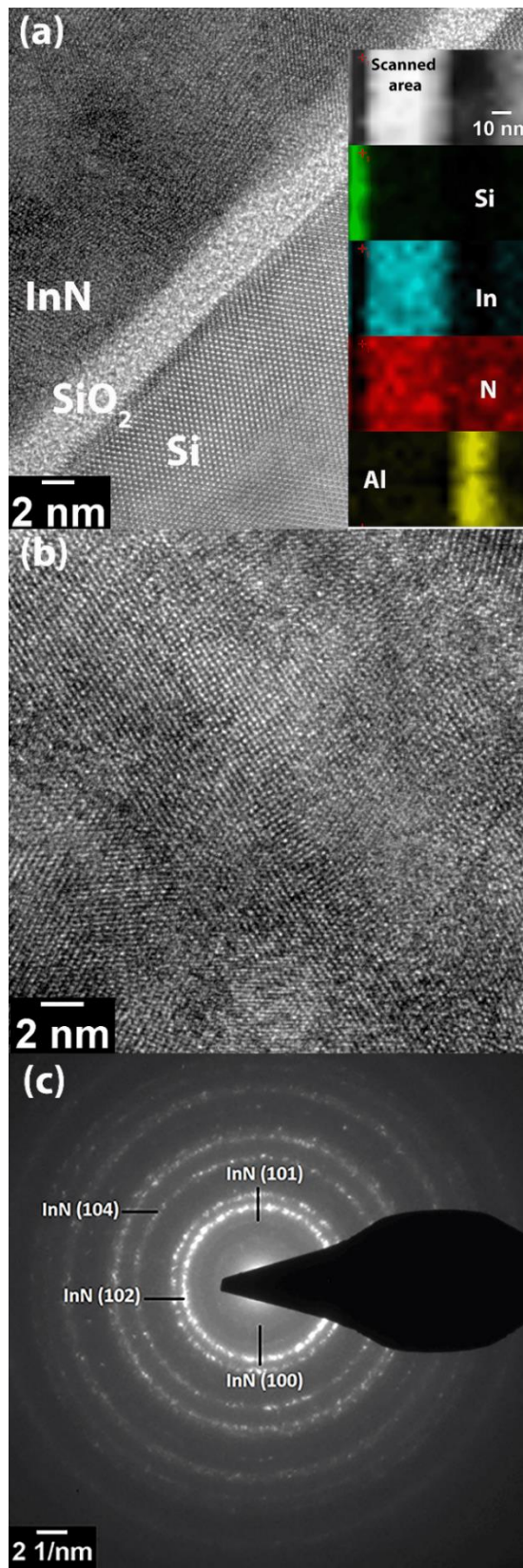


Figure 4.9: (a) Cross-sectional TEM image of AlN capped InN film showing the interface of InN and SiO₂/Si deposited at 200 °C on Si (100) substrate. Inset Colorized elemental map of same sample. (b) Cross-sectional TEM image of same InN sample. (c) SAED pattern of the same sample.

Table 4.3: SAED pattern analysis of InN thin film deposited on Si(100) substrate at 200 °C: comparison between measured and theoretical values of interplanar spacing (d_{hkl}) with corresponding crystallographic planes.

Diameter (nm ⁻¹)	Interplanar spacing, d_{hkl}		Corresponding material	Corresponding plane (hkl)
	Calculated	Theoretical		
6.1910	3.2304	3.0647	InN	100
7.7380	2.5846	2.6998	InN	101
9.751	2.0510	2.0877	InN	102
16.136	1.2394	1.2926	InN	104

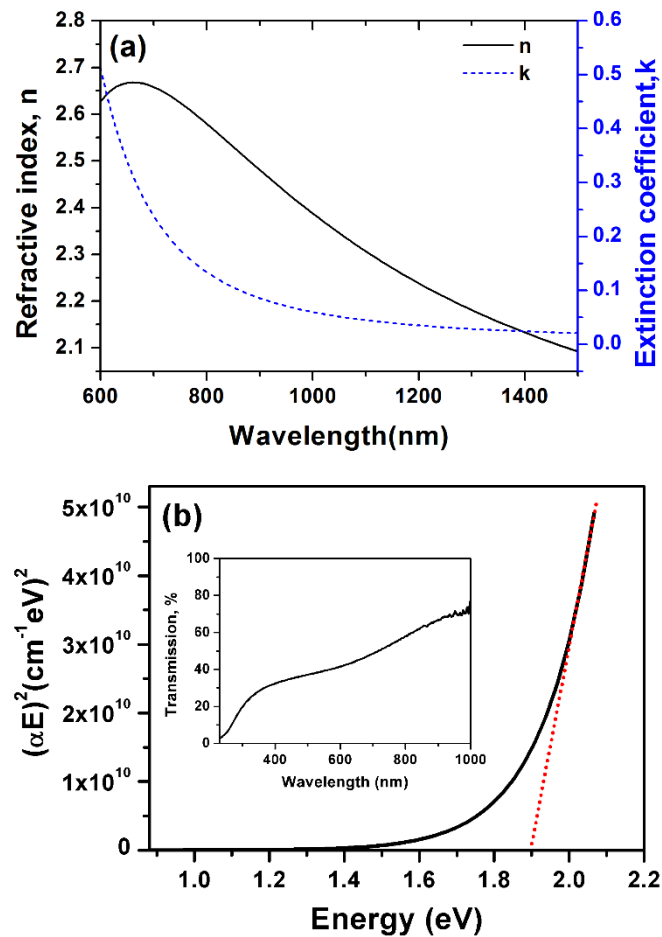


Figure 4.10: (a) Optical constants (refractive index and extinction coefficient) of InN thin film deposited on Si (100) at 200 °C, (b) Absorption spectrum of same InN sample deposited on Si (100). (Inset) Optical transmission spectrum of the InN film deposited on double-side polished quartz.

Figure 4.10(b) shows $(\alpha h\nu)^2$ vs. $h\nu$ plot, which is obtained from spectroscopic ellipsometer measurement and related data analysis as explained in experimental section. Straight line segment of the plot was extrapolated to abscissa which reveals the optical band gap of the material as ~ 1.9 eV. Inset of Fig. 4.10(b) shows optical transmission spectra of InN sample grown on double side polished quartz substrate. Transmission values did not saturate for InN sample, probably due to the high defect density present within the films.[245] InN thin film exhibits 40-50% transmission in the visible regime, which approaches up to 60-70% in the NIR regime. There is a huge controversy in literature for experimental InN thin film band gap values and origin of the observed InN band gap variations between 0.6 and 2.3 eV is not very well understood. This significant discrepancy has been ascribed to several reasons and among them the most prominent ones are the Burstein-Moss shift, defect levels, stoichiometry, and impurity levels. 0.7 eV has been dominantly reported as the optical band gap for MBE-grown single-crystalline InN which became most popular and widely accepted, however there are some doubts as well that this value might originate from a 0.7 eV trapping level. Energy band gap less than 1 eV is mostly obtained from single crystalline InN films, while larger band gap values are reported mostly for polycrystalline InN thin films. From the view point of narrow band gap, larger band gap (1.9 eV) might be due to formation of oxynitrides which have considerable larger band gap than InN. Polycrystalline films can contain a significant level of oxygen incorporation at their grain boundaries which might be the cause of higher band gap in polycrystalline films. There is a growing evidence of 1.1-1.5 eV band gap for InN films in the literature as well. In view of numerous different reports, further investigation will be helpful to reach conclusive evidence for establishing a unanimous InN band gap.[3][37], [259]

4.2 Hollow Cathode Plasma Assisted Atomic Layer Deposition of $\text{In}_x\text{Ga}_{1-x}\text{N}$ Thin Films

$\text{In}_x\text{Ga}_{1-x}\text{N}$ layers with different compositions were deposited at 200 °C on pre-cleaned Si (100) and double-side polished quartz substrates. Prior to that, binary GaN and InN thin films were deposited with 500-cycle recipes at 200 °C on Si and quartz substrates, which were used as reference/calibration samples in order to compare their material properties with ternary $\text{In}_x\text{Ga}_{1-x}\text{N}$ counterparts. Thicknesses of GaN and InN thin films were measured using a spectroscopic ellipsometer and were found to be 21.5 and 20.0 nm, respectively. These thickness values correspond to growth rates of 0.43 and 0.40 Å/cycle for GaN and InN thin films, respectively. In order to adjust the alloy composition, different numbers of GaN and InN subcycles were used in the main cycle; *i.e.*, GaN:InN = 1:1, 1:3, and 1:5. Ratio of subcycles (RS) was calculated by dividing the number of subcycles of InN to total number of subcycles for GaN and InN; *i.e.*, $n_{\text{s InN}}/(n_{\text{s InN}} + n_{\text{s GaN}})$. The term RS will be used throughout the text to specify different $\text{In}_x\text{Ga}_{1-x}\text{N}$ thin films.

Recently, we reported that InN growth using N_2/H_2 plasma as nitrogen source results in a thin film composed of *h*-InN and *t*-InN phases with high percentage of impurities, whereas the film deposited using N_2 plasma is single-phase *h*-InN with low impurity concentrations.[260] Therefore, as mentioned in the experimental section, N_2/H_2 plasma and N_2 plasma were used as nitrogen sources for the growth of GaN and InN films, respectively. Keeping in mind the separate nitrogen precursors used for GaN and InN, 10 s of additional N_2 or N_2/H_2 plasma treatment step (step 1 and 7 in Fig. 3.2) is used to modify/condition the film surface with suitable plasma species in order to make the substrate compatible for the next InN or GaN subcycle. $\text{In}_x\text{Ga}_{1-x}\text{N}$ thin films with RS of 0.5, 0.75, and 0.85 were prepared by the deposition of 500, 300, and 200 supercycles, respectively. Thickness values were theoretically estimated using following Eqn. 4.1,

$$Thickness = n_{GaN(sub)}(Growth\ rate_{GaN})n_{super} + n_{InN(sub)}(Growth\ rate_{InN})n_{super} \quad (4.1)$$

where $n_{GaN(sub)}$, $n_{InN(sub)}$, and n_{super} are the number of subcycles of GaN, number of subcycles of InN, and total number of super cycles, respectively.

Thickness values were determined as 41.5, 48.9, and 60.7 nm for $In_xGa_{1-x}N$ thin films having RS of 0.5, 0.75, and 0.83, respectively. Thickness values experimentally measured using spectroscopic ellipsometry were found to be 31.0, 33.0, and 45.0 nm for the same sequence of $In_xGa_{1-x}N$ samples. Deposition rate of GaN on InN and/or deposition rate of InN on GaN might be different than those of GaN on GaN and InN on InN. So, discrepancy between experimental and theoretical thickness values of $In_xGa_{1-x}N$ thin films might be attributed to the resulting uncertainty in GPC values.

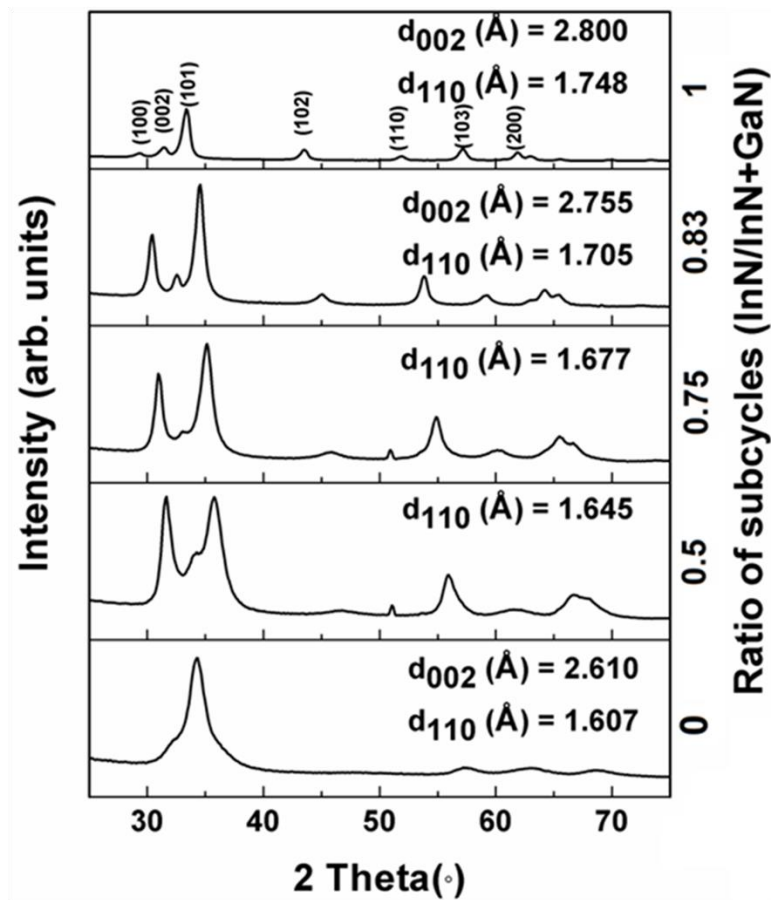


Figure 4.11: GIXRD patterns of GaN, InN, and $In_xGa_{1-x}N$ thin films deposited on Si(100) substrates.

Table 4.4: Lattice parameters and alloy compositions (as determined by Vegard's law) for GaN, $\text{In}_x\text{Ga}_{1-x}\text{N}$, and InN films.

RS ^a	a^b (Å)	c^c (Å)	x_{Veg}^d
0 (GaN)	3.2071	5.2271	0
0.5	3.2895	-	0.28
0.75	3.3508	-	0.49
0.83	3.4089	5.5130	0.70
1 (InN)	3.4915	5.6106	1

^aRS is the ratio of subcycles; *i.e.*, $n_s \text{InN} / (n_s \text{InN} + n_s \text{GaN})$. ^bCalculated using the (110) reflection. ^cCalculated using the (002) reflection. ^d x_{Veg} is the alloy composition calculated from a values using Vegard's law.

GIXRD patterns of GaN, $\text{In}_x\text{Ga}_{1-x}\text{N}$, and InN thin films are shown in Fig. 4.11. GaN and InN thin films were shown to be single-phase as their GIXRD patterns solely exhibited reflections of hexagonal wurtzite GaN (ICDD reference code: 00-050-0792) and hexagonal wurtzite InN (ICDD reference code: 98-015-7515) phases, respectively. The peaks shifted towards lower 2θ values with the increase in InN subcycles. Reflections appeared in the GIXRD patterns of $\text{In}_x\text{Ga}_{1-x}\text{N}$ thin films were indexed according to their shift with respect to those of InN and GaN. The shift in peak positions is attributed to In incorporation into wurtzite GaN lattice. The alloy composition x for each $\text{In}_x\text{Ga}_{1-x}\text{N}$ film has been calculated using Vegard's law (Eqn. 4.2), which states that there is a linear relationship between the lattice parameters of an alloy and concentration of constituent elements.

$$a_{\text{In}_x\text{Ga}_{1-x}\text{N}} = xa_{\text{InN}} + (1 - x)a_{\text{GaN}} \quad (4.2)$$

The interplanar spacing (d_{hkl}) values are indicated in Fig. 4.11 which were calculated from Bragg's law, using the positions of (002) and/or (110) reflections. Lattice parameters a and/or c were calculated by substituting the interplanar spacing (d_{hkl}) values in Eqn. 3.1, which provides a relationship between interplanar spacing (d_{hkl}), miller indices, and lattice parameters for hexagonal crystals.

For $\text{In}_x\text{Ga}_{1-x}\text{N}$ thin films having different RS values, a -axis lattice parameter was calculated and further substituted in Vegard's law to calculate alloy compositions. Table 4.4 shows alloy compositions and lattice parameters (a and/or c) for $\text{In}_x\text{Ga}_{1-x}\text{N}$ thin films having different RS values. The calculated x

values are 0.28, 0.49, and 0.70 for $\text{In}_x\text{Ga}_{1-x}\text{N}$ thin films having RS of 0.5, 0.75, and 0.83, respectively. From 2θ positions of (002) and (110) reflections, a and c lattice parameters of GaN and InN were calculated. a and c values are found to be 3.21 and 5.23 Å for GaN, respectively. a and c values were also determined for InN, which came out as 3.50 and 5.61 Å. The value of a lattice parameters for InN and GaN are in close agreement with the values reported in the literature for strain-free GaN and InN thin films. However, there is a minor variation in c -axis lattice parameters for InN (0.01% lower) and GaN (0.07% higher) layers with respect to the reported values for their nominally strain-free counterparts.[254] The deviation of c lattice parameters from the ideal case indicates that Vegard's law might not be a good-enough approximation in the present case due to presence of strain in the films.

Crystallite sizes (Table 4.5) were roughly estimated from corresponding dominant reflections using the well-known Debye-Scherrer formula (Eqn. 4.3), assuming that observed broadening is only due to the size effects thus neglecting instrumental broadening effects.[261]

$$d = \frac{0.9 \lambda}{B \cos \theta} \quad (4.3)$$

The relatively sharp diffraction peaks obtained from $\text{In}_x\text{Ga}_{1-x}\text{N}$ thin films of higher In content suggest that they are composed of larger crystallites. This is evident from decreasing FWHM values of $\text{In}_x\text{Ga}_{1-x}\text{N}$ thin films with increase in In concentration. The crystallite size for GaN, $\text{In}_x\text{Ga}_{1-x}\text{N}$ (RS=0.5), $\text{In}_x\text{Ga}_{1-x}\text{N}$ (RS=0.75), $\text{In}_x\text{Ga}_{1-x}\text{N}$ (RS=0.83), and InN were found to be 5.5, 7.4, 9.8, 11.3, and 8.1 nm, respectively.

Table 4.5: Crystallite size values estimated using Scherrer formula for GaN, $\text{In}_x\text{Ga}_{1-x}\text{N}$, and InN films.

RS ^a	(<i>hkl</i>)	K	λ (Å)	FWHM β (°)	θ (°)	t (nm)
0(GaN)	(002)	0.94	1.5418	1.56	17.1	5.5
0.5	(100)	0.94	1.5418	1.16	15.7	7.4
0.75	(100)	0.94	1.5418	0.86	15.4	9.8
0.83	(100)	0.94	1.5418	0.76	15.1	11.3
1(InN)	(100)	0.94	1.5418	1.05	14.8	8.1

^aRS is the ratio of subcycles; *i.e.*, $n_s \text{InN} / (n_s \text{InN} + n_s \text{GaN})$.

$\text{In}_x\text{Ga}_{1-x}\text{N}$ samples having various In contents were analyzed for elemental compositions, chemical bonding states, and impurity contents of the films using XPS. All spectra have been charge-corrected by referencing the C 1s peak at 284.8 eV. Survey scans from the surface of $\text{In}_x\text{Ga}_{1-x}\text{N}$ films indicated the presence of gallium, indium, nitrogen, carbon, and oxygen with Ga 3d, In 3d, N 1s, C 1s, and O 1s peaks, respectively. $\text{In}_x\text{Ga}_{1-x}\text{N}$ thin films were etched with Ar^+ ions in order to obtain XPS survey scan from the bulk of the films. Table 4.6 provides a comparison of the elemental compositions of the $\text{In}_x\text{Ga}_{1-x}\text{N}$ films measured from the surface and the bulk. It is apparent that the very surface of all $\text{In}_x\text{Ga}_{1-x}\text{N}$ films were contaminated with oxygen (up to 8 at.%) and carbon (up to 23 at.%). XPS elemental quantification analysis from the bulk of the films revealed no oxygen and carbon in the case of $\text{In}_x\text{Ga}_{1-x}\text{N}$ thin film with RS of 0.5. $\text{In}_x\text{Ga}_{1-x}\text{N}$ thin films with RS of 0.75 and 0.83 showed low oxygen concentrations of 2.53 and 1.57 at.%, respectively. Only $\text{In}_x\text{Ga}_{1-x}\text{N}$ thin film with RS of 0.83 showed bulk carbon contamination of 2.86 at.%, which might be due to partially unreacted methyl and ethyl ligands of TMI and TEG, respectively.

Table 4.6: Elemental composition, Ga/N ratio, and In fractions for $\text{In}_x\text{Ga}_{1-x}\text{N}$ films having different RS values.

RS ^a	Elemental composition (at.%)					Ga/N	In fraction ^b
	Ga	In	N	O	C		
0.5 (surface)	28.42	3.78	46.55	8.67	12.58	0.61	0.11
0.5 (bulk)	36.51	2.93	60.56	-	-	0.60	0.07
0.75 (surface)	30.92	6.17	42.46	8.52	11.93	0.72	0.17
0.75 (bulk)	34.83	3.62	59.02	2.53	-	0.59	0.09
0.83 (surface)	31.08	7.48	29.61	8.94	22.90	1.04	0.19
0.83 (bulk)	38.99	6.05	50.83	1.27	2.86	0.76	0.13

^aRS is the ratio of subcycles; *i.e.*, $n_s \text{InN} / (n_s \text{InN} + n_s \text{GaN})$. ^bIn fraction is obtained using the formula: $\text{In (at.%) / (In (at.%) + Ga (at.%))}$.

Those reactive groups might not have reacted sufficiently with the N_2/H_2 or N_2 plasma, and therefore their carbon-containing ligands possibly remained within the growing film. $In_xGa_{1-x}N$ thin films with RS 0.5, 0.75, and 0.83 exhibited Ga/N ratios of 0.60, 0.59, and 0.76 from the bulk of the films, respectively. Although $In_xGa_{1-x}N$ films exhibit higher N at.% as compared to Ga at.% in the bulk of the films, it is worth mentioning that the N at.% is overestimated due to the significant contribution of Ga Auger peak, which overlaps with the N 1s peak.[32], [262] In concentrations obtained from the surface for $In_xGa_{1-x}N$ thin films with RS of 0.5, 0.75, and 0.83 are calculated to be 0.11, 0.17, and 0.19, respectively, which are significantly lower than the values obtained using Vegard's law. Possible inhomogeneous distribution of In and Ga atoms in the vicinity of the surface of $In_xGa_{1-x}N$ samples might explain the lower In surface concentration.[262], [263] In addition, overestimation of the nitrogen surface contents as explained previously can implicate lowering of In concentration. $In_xGa_{1-x}N$ thin films with RS of 0.5, 0.75, and 0.83 exhibited In concentrations of 0.07, 0.09, and 0.13 from the bulk of the films, respectively. The In content obtained from the bulk of $In_xGa_{1-x}N$ thin films are further reduced in comparison with those obtained from the surface of the films. It indicates the preferential loss of indium with respect to gallium during Ar^+ sputtering, which has been reported in the literature and explained by much lower bond energy of InN (7.7 eV/atom) than GaN (8.9 eV/atom).[264], [265] To clarify the discrepancy in In content of the films obtained via XPS and GIXRD measurements, EDX analysis has been carried out. In concentrations obtained from EDX measurements were found as 0.25, 0.33, and 0.64 for $In_xGa_{1-x}N$ films with RS of 0.5, 0.75, and 0.85, respectively. The resulting In concentration values obtained from EDX, XPS, and GIXRD are plotted against RS for $In_xGa_{1-x}N$ films (Fig. 4.12). EDX analyses reveal closer but still lower In concentration values as compared to the values calculated from Vegard's law. This discrepancy might be attributed to consistent overestimation of Vegard's law assuming the films to be fully relaxed.[266] The difference in In content obtained from XRD and EDX is relatively more reasonable with the downshift

in $\text{In}_x\text{Ga}_{1-x}\text{N}$ film with RS of 0.75, which can be attributed to the presence of higher strain in $\text{In}_x\text{Ga}_{1-x}\text{N}$ film with RS of 0.75.

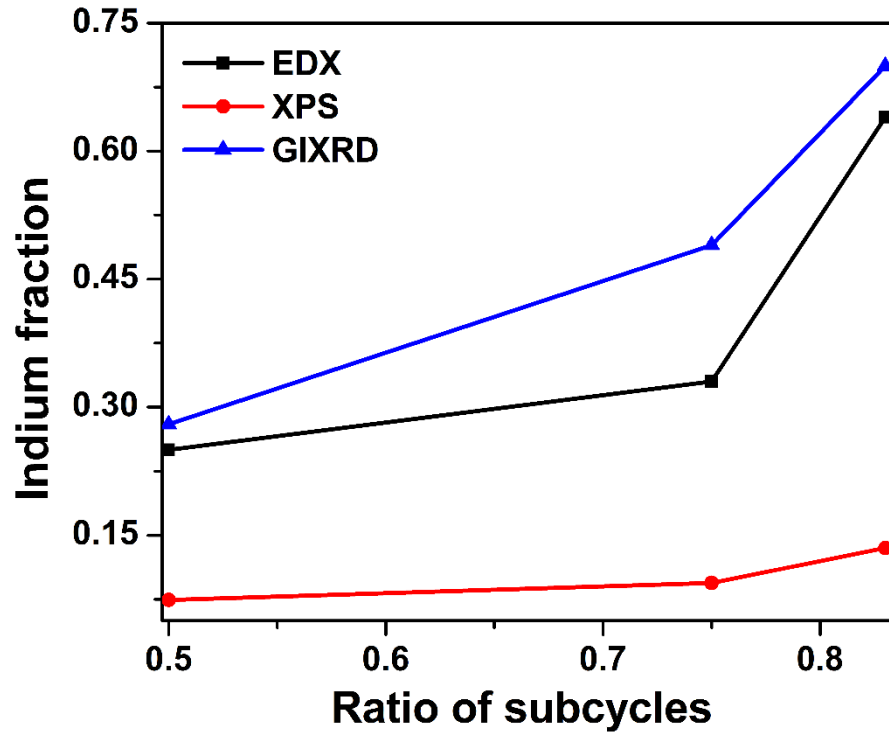


Figure 4.12: Indium concentration values obtained from EDX, XPS, and GIXRD for $\text{In}_x\text{Ga}_{1-x}\text{N}$ films having different RS values.

As a result, EDX appears to be a more appropriate tool for In fraction estimation of $\text{In}_x\text{Ga}_{1-x}\text{N}$ thin films due to shortcomings of GIXRD (presence of strain) and XPS (selective etching) for this specific case as explained in detail above. $\text{In}_x\text{Ga}_{1-x}\text{N}$ thin films will be specified according to their compositions evaluated from EDX in the following text. In order to check the elemental distribution along the film cross-section, XPS depth profiling was employed on $\text{In}_{0.33}\text{Ga}_{0.67}\text{N}$ sample. Figure 4.13 shows the relative atomic concentrations of oxygen, carbon, gallium, indium, and nitrogen through the depth of sample as a function of sputter time. Carbon and oxygen content decreases progressively along the etching direction. Sample was found to be carbon free, while ~2.5 at.% oxygen was found in the bulk of the sample. The results further reveal that $\text{In}_{0.33}\text{Ga}_{0.67}\text{N}$ can be considered homogeneous in terms of elemental (Ga, N, and In) composition within the bulk of the sample.

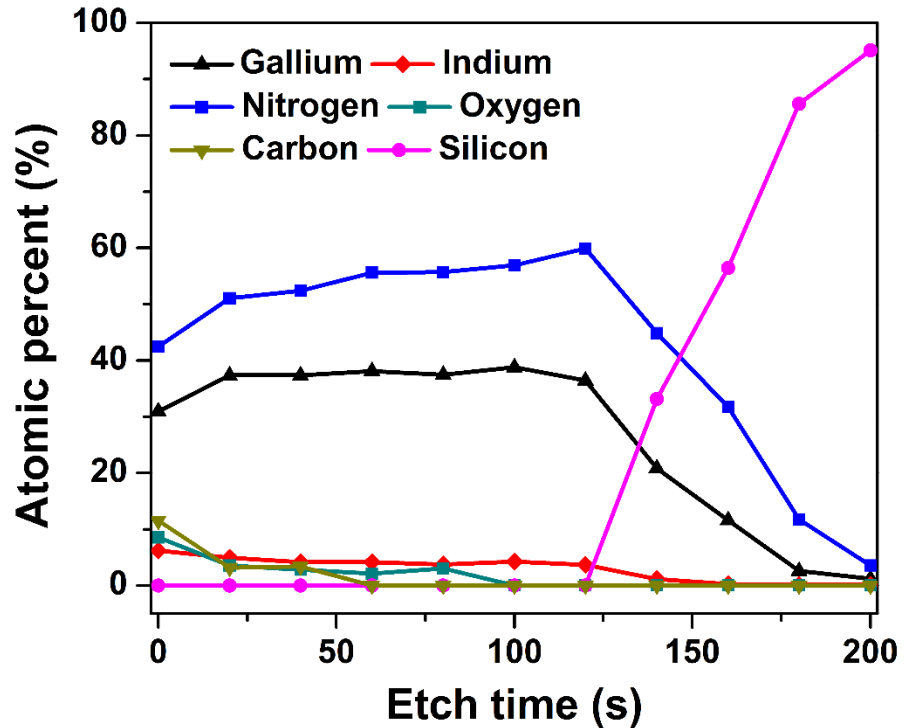


Figure 4.13: Compositional depth profile of ~33 nm thick $\text{In}_{0.33}\text{Ga}_{0.67}\text{N}$ thin film deposited on a Si(100) substrate.

Chemical bonding states from the bulk of $\text{In}_x\text{Ga}_{1-x}\text{N}$ films were studied by the evaluation of their HR-XPS scans and presented in Fig. 4.14. Different subpeaks used to fit HR-XPS scans were assigned to various chemical states of $\text{In}_x\text{Ga}_{1-x}\text{N}$ thin films. Ga 3d HR-XPS (Fig. 4.14a) scan obtained from the bulk of $\text{In}_{0.25}\text{Ga}_{0.75}\text{N}$ has been deconvoluted into two subpeaks located at 19.82 and 18.67 eV, corresponding to Ga-N[267]–[269] and Ga-Ga[267], [269] bonds, respectively. Chang et al.[270] reported that Ar^+ etching has led to rearrangement of $\text{In}_x\text{Ga}_{1-x}\text{N}$ elemental composition accompanied by presence of metallic Ga. In another study, it has been reported that observed Ga-Ga bond in bulk of the GaN films might form during Ar^+ ion etching owing to the accumulation of metallic Ga on the surface of GaN thin film.[271] In 3d HR-XPS scan (Fig. 4.14b) obtained from bulk of $\text{In}_{0.25}\text{Ga}_{0.75}\text{N}$ thin film exhibits In-N[272], [273] bond by showing doublet of indium 3d core levels which are spin-orbit split to the 3d_{5/2} peak at 444.5 eV and 3d_{3/2} peak at 452.1 eV. The N

1s HR-XPS scan (Fig. 4.14c) obtained from the bulk of $\text{In}_{0.25}\text{Ga}_{0.75}\text{N}$ thin film was fitted using three subpeaks, which were assigned to the N–Ga[267], [274] bond (397.0 eV), N–In[272] bond (397.6eV), and Auger Ga[32] peak (395.3 eV). Ga 3d HR-XPS scans (Fig. 4.14d and 4.14g) obtained from the bulk of $\text{In}_{0.33}\text{Ga}_{0.67}\text{N}$ and $\text{In}_{0.64}\text{Ga}_{0.36}\text{N}$ thin films followed the trend of Ga 3d HR-XPS scan of $\text{In}_{0.25}\text{Ga}_{0.75}\text{N}$. Both $\text{In}_{0.33}\text{Ga}_{0.67}\text{N}$ and $\text{In}_{0.64}\text{Ga}_{0.36}\text{N}$ thin films manifested two subpeaks for Ga 3d HR-XPS scan, which have been correlated to presence of Ga–N[267]–[269] (19.5 and 19.3 eV for $\text{In}_{0.33}\text{Ga}_{0.67}\text{N}$ and $\text{In}_{0.64}\text{Ga}_{0.36}\text{N}$, respectively) and Ga–Ga[267], [269] bonds (17.5 and 17.7 for $\text{In}_{0.33}\text{Ga}_{0.67}\text{N}$ and $\text{In}_{0.64}\text{Ga}_{0.36}\text{N}$ thin films, respectively). In 3d HR-XPS scans (Fig. 4.14e and 4.14h) obtained from bulk of $\text{In}_{0.33}\text{Ga}_{0.67}\text{N}$ and $\text{In}_{0.64}\text{Ga}_{0.36}\text{N}$ thin films followed the footprints of In 3d HR scan of $\text{In}_{0.25}\text{Ga}_{0.75}\text{N}$ thin film, and have been fitted with two peaks each which correspond to In–N[272], [273] bond. The N 1s HR-XPS scan (Fig. 4.14f) obtained from the bulk of $\text{In}_{0.33}\text{Ga}_{0.67}\text{N}$ thin film was identical to N1s HR-XPS spectra of $\text{In}_{0.25}\text{Ga}_{0.75}\text{N}$ thin film. On the other hand, N1s HR-XPS scan (Fig. 4.14i) obtained from the bulk of $\text{In}_{0.64}\text{Ga}_{0.36}\text{N}$ thin film was fitted using four subpeaks. The first three peaks belong to N–Ga[267], [274] bond (397.0 eV), N–In[272] bond (397.7eV), and Auger Ga[32] peaks (395.1 eV), while the additional fourth broad subpeak at 398.3 eV shows the presence of nitrogen sub-oxides[275].

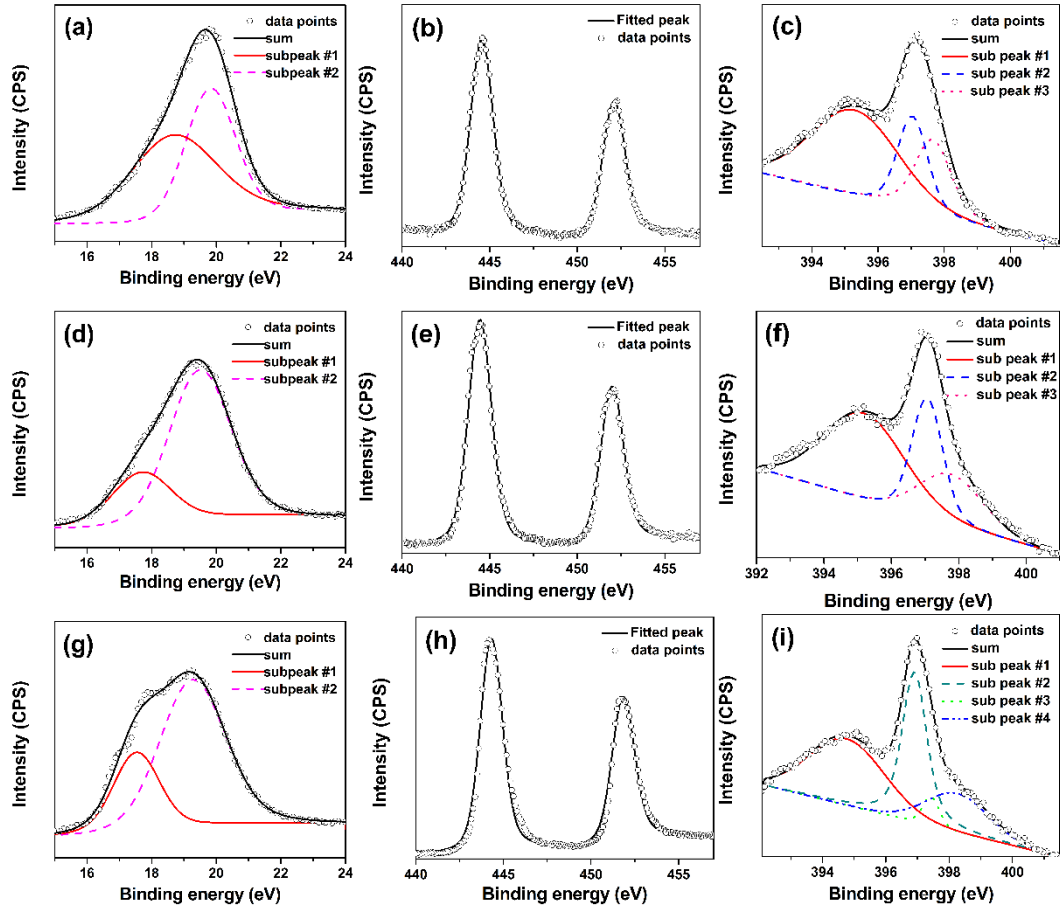


Figure 4.14: Ga 3d, In 3d, and N 1s HR-XPS scans of $\text{In}_{0.25}\text{Ga}_{0.75}\text{N}$ (a, b and c), $\text{In}_{0.33}\text{Ga}_{0.67}\text{N}$ (d, e and f), and $\text{In}_{0.64}\text{Ga}_{0.36}\text{N}$ (g, h and i) thin films deposited on Si(100).

Fig. 4.15a shows optical transmission spectra of GaN, InN, and $\text{In}_x\text{Ga}_{1-x}\text{N}$ thin films deposited on double-side polished quartz wafers. For GaN samples, a significant decrease in the UV transmission was observed at wavelengths <400 nm, which is believed to be caused by the main band-to-band absorption. Transmission values for GaN and $\text{In}_x\text{Ga}_{1-x}\text{N}$ thin films were saturated at wavelengths above their transmission band edge. On the other hand, transmission values did not saturate for InN sample, probably due to the high defect density present within the films.[37] InN thin film exhibits 40-50% transmission in the visible regime, which approaches up to 60-70% in the NIR regime. Optical band edge values of the $\text{In}_x\text{Ga}_{1-x}\text{N}$ layers shifted towards higher

wavelengths with increasing In content as expected, which indicates the tunability of energy band gap by varying In amount.

The optical band gap (E_g) values of $\text{In}_x\text{Ga}_{1-x}\text{N}$ films were determined from spectroscopic ellipsometry measurements and related data analysis. The absorption coefficient (α) values were calculated using Eqn. (3.2). In Fig. 4.15b, $(\alpha E)^2$ plots are presented as a function of energy for GaN, InN, and $\text{In}_x\text{Ga}_{1-x}\text{N}$ thin films. The fundamental absorption edge in the present thin films is formed by the direct allowed transitions. The optical band gap was determined by extrapolating the linear portion of the plot to $(\alpha E)^2=0$. E_g value of GaN thin film was found to be ~3.45 eV, which is relatively close to the widely accepted value of 3.43 eV for GaN thin films.[276] E_g value of InN was extracted as 1.87 eV. MBE grown epitaxial InN films have shown E_g of 0.7 eV,[259] but earlier accepted values around 1.9 eV are still being reported.[277] Optical band gap values of $\text{In}_x\text{Ga}_{1-x}\text{N}$ thin films decreased with In content and E_g values were found to be 2.71, 2.45, and 2.18 for $\text{In}_{0.25}\text{Ga}_{0.75}\text{N}$, $\text{In}_{0.33}\text{Ga}_{0.67}\text{N}$, and $\text{In}_{0.64}\text{Ga}_{0.36}\text{N}$ thin films, respectively. A similar dependency of E_g values of $\text{In}_x\text{Ga}_{1-x}\text{N}$ thin films on In content has been reported in the literature.[266]

The refractive index dispersion curves of $\text{In}_x\text{Ga}_{1-x}\text{N}$ thin films were determined using spectroscopic ellipsometry measurements and the following data analysis. Figure 4.16 shows comparison of refractive index values of GaN, InN, and $\text{In}_x\text{Ga}_{1-x}\text{N}$ layers deposited on Si (100). The wavelength range for spectroscopic ellipsometry measurements was selected on the basis of optical band edge values of GaN, InN, and $\text{In}_x\text{Ga}_{1-x}\text{N}$ samples. Refractive index value of GaN film was measured as 2.10 at 650 nm, which is slightly less than the reported values for polycrystalline GaN thin films.[32] Refractive index value of InN layer was determined as 2.55 at 650 nm, which closely matches with the reported values for polycrystalline InN thin films.[258] As anticipated, refractive index increased from 2.28 to 2.42 as In fraction of $\text{In}_x\text{Ga}_{1-x}\text{N}$ samples increased from 0.25 to 0.64. Refractive index of $\text{In}_{0.25}\text{Ga}_{0.75}\text{N}$, $\text{In}_{0.33}\text{Ga}_{0.67}\text{N}$, and $\text{In}_{0.64}\text{Ga}_{0.36}\text{N}$ samples is measured to be 2.28, 2.31, and 2.42, respectively, at 650 nm. The value determined for the $\text{In}_{0.64}\text{Ga}_{0.36}\text{N}$ was found close to that of InN (n

= 2.55). The results presented here depict that the refractive index values of $\text{In}_x\text{Ga}_{1-x}\text{N}$ thin films change according to alloy composition. XRR measurements revealed mass density of InN, GaN, $\text{In}_{0.25}\text{Ga}_{0.75}\text{N}$, and $\text{In}_{0.64}\text{Ga}_{0.36}\text{N}$ as 5.64, 5.41, 6.23, and 6.57 g/cm^3 , respectively. Fitting of XRR data for $\text{In}_{0.33}\text{Ga}_{0.67}\text{N}$ was not good enough to obtain accurate results for that particular film.

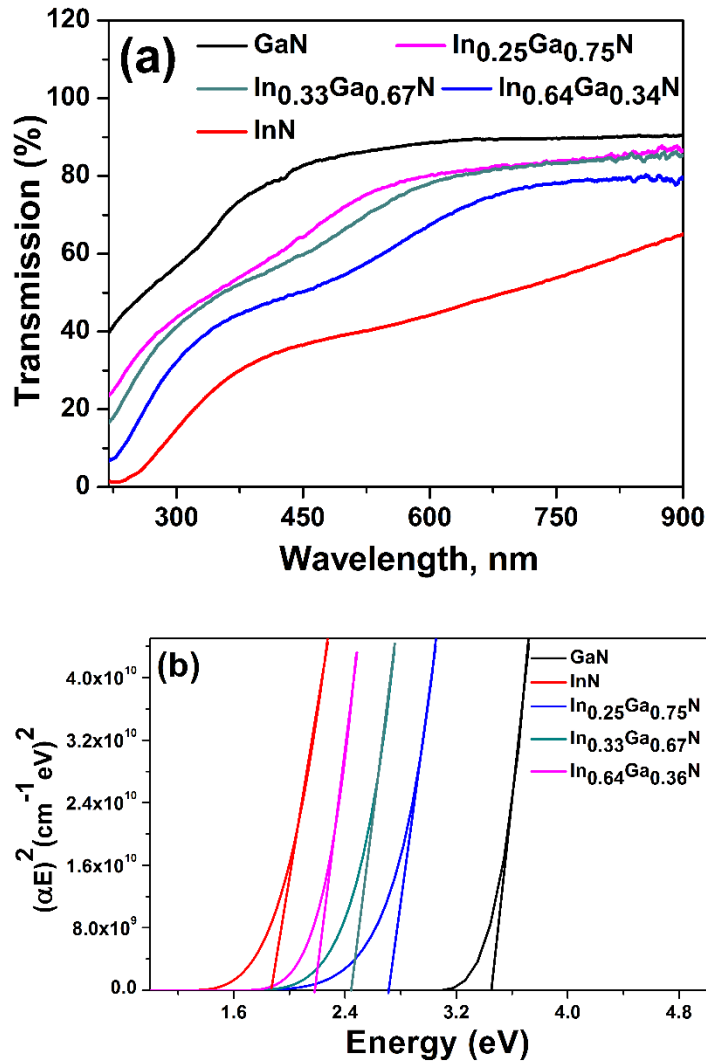


Figure 4.15: (a) Optical transmission spectra of GaN, InN, and $\text{In}_x\text{Ga}_{1-x}\text{N}$ thin films deposited on double-side polished quartz substrates. (b) $(\alpha E)^2$ vs. E plots, indicating the optical band gaps of GaN, InN, and $\text{In}_x\text{Ga}_{1-x}\text{N}$ thin films.

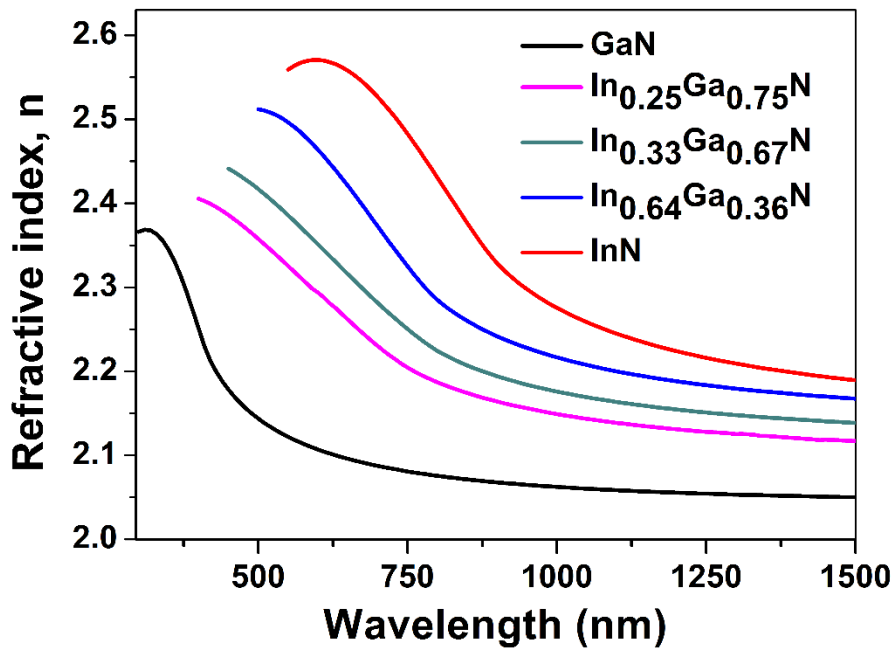


Figure 4.16: Spectral refractive indices of GaN, InN, and $\text{In}_x\text{Ga}_{1-x}\text{N}$ thin films with different In fractions.

TEM experiments were performed on the $\text{In}_{0.33}\text{Ga}_{0.67}\text{N}$ sample. Prior to TEM imaging studies, ~ 20 nm AlN was deposited on top of $\text{In}_{0.33}\text{Ga}_{0.67}\text{N}$ layer in order to provide a shelter to protect its crystal structure from a possible damage of high energy Ga ions of the FIB system, which is used to prepare the samples to be analyzed. Figure 4.17a is the cross-sectional TEM image of $\text{In}_{0.33}\text{Ga}_{0.67}\text{N}$ thin film, where one can observe distinct layers of Pt, AlN, $\text{In}_{0.33}\text{Ga}_{0.67}\text{N}$, and Si. The thickness of $\text{In}_{0.33}\text{Ga}_{0.67}\text{N}$ was measured as ~ 32 nm from cross-sectional TEM measurements, which is in close agreement with the data obtained from spectroscopic ellipsometry. A ~ 3 nm thick amorphous SiO_2 layer was observed at the $\text{In}_{0.33}\text{Ga}_{0.67}\text{N}/\text{Si}$ interface, which is generally named as the “damage layer”, formed during the TEM sample preparation using FIB.[278] Figure 4.17b shows the HR-TEM image where lattice fringes of $\text{In}_{0.33}\text{Ga}_{0.67}\text{N}$ are organized in different orientations implying the polycrystalline structure of $\text{In}_{0.33}\text{Ga}_{0.67}\text{N}$ film.

Figure 4.18 shows EDX elemental maps of Pt, Al, In, Ga, and Si obtained from the AlN-capped $\text{In}_{0.33}\text{Ga}_{0.67}\text{N}$ thin film deposited on Si (100). A cross-sectional portion from specimen was selected and elemental distributions

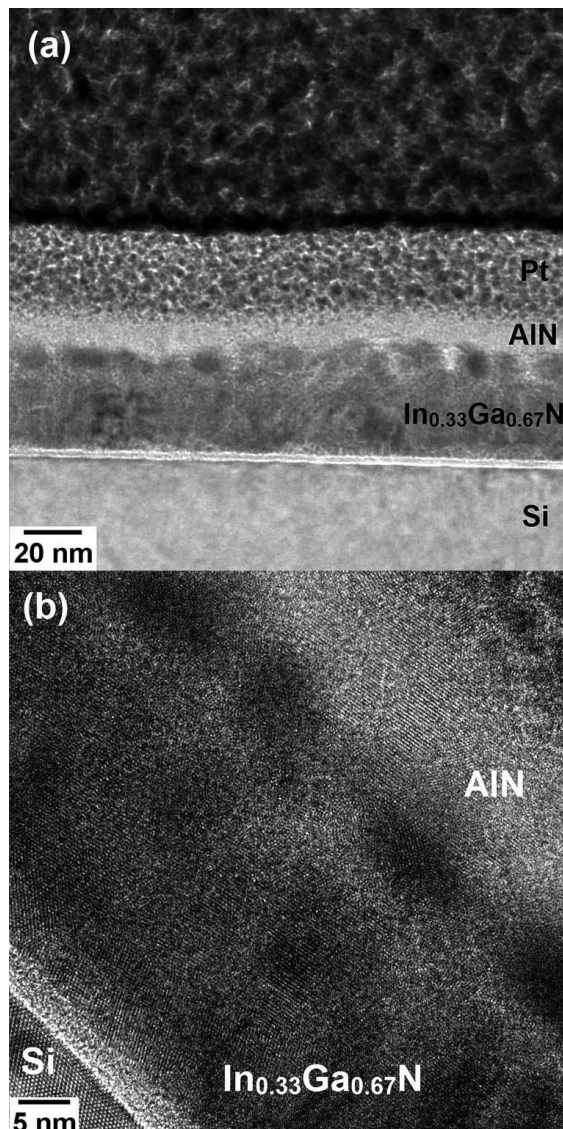


Figure 4.17: (a) Cross-sectional TEM image of the AlN-capped In_{0.33}Ga_{0.67}N thin film deposited on the Si(100) substrate. (b) Cross-sectional HR-TEM image of the same sample.

were analyzed by rastering the electron beam point by point over the selected area. The colorized maps show strong contrast among Pt, Al, In, Ga, and Si, and they reveal the elemental distribution along the scanned area.

The characteristic PL emission spectra of In_{0.25}Ga_{0.75}N, In_{0.33}Ga_{0.67}N, and In_{0.64}Ga_{0.36}N thin films are given in Fig. 4.19a, b, and c, respectively. The excitation wavelength for GaN and In_{0.25}Ga_{0.75}N thin films was 320 and 450 nm, respectively and it was 550 nm for In_{0.33}Ga_{0.67}N and

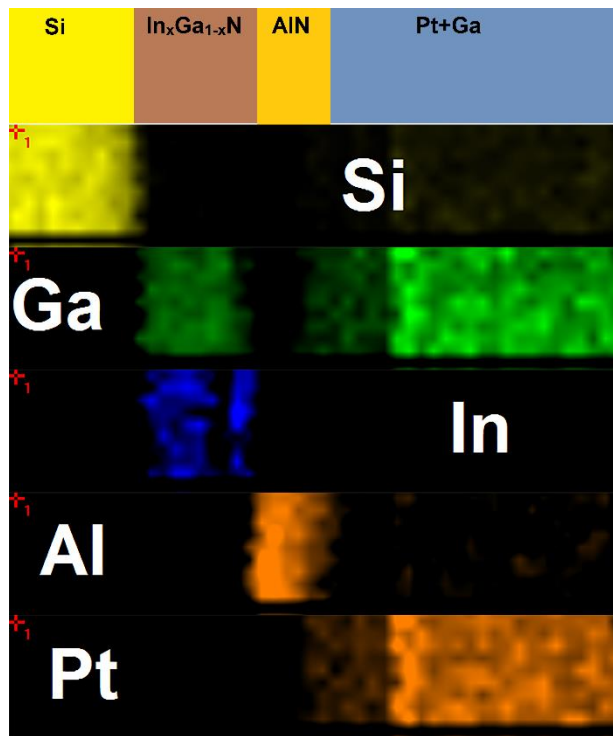


Figure 4.18: (a) Elemental map of the AlN-capped $\text{In}_{0.33}\text{Ga}_{0.67}\text{N}$ thin film deposited on Si(100) substrate

$\text{In}_{0.64}\text{Ga}_{0.36}\text{N}$ thin films. The GaN spectrum (not shown here) exhibited a broad spectral feature centered at ~ 360 nm, which results from the main band gap emission in the GaN thin film.[260] However, PL measurement from InN samples did not exhibit considerable emission. In addition to defect bands at lower wavelength, broad spectral features are visible with peaks centered at 508, 618, and 671 nm for $\text{In}_{0.25}\text{Ga}_{0.75}\text{N}$, $\text{In}_{0.33}\text{Ga}_{0.67}\text{N}$, and $\text{In}_{0.64}\text{Ga}_{0.36}\text{N}$ thin films, respectively. These broad spectral features arise from band gap emission of $\text{In}_x\text{Ga}_{1-x}\text{N}$ thin films and variation of peak position to higher wavelength indicates the lowering of energy band gap of $\text{In}_x\text{Ga}_{1-x}\text{N}$ thin films with increase in In fraction. The broad band emission also points out radiative recombination, which involves structural defects within the films.

Surface morphologies of the $\text{In}_x\text{Ga}_{1-x}\text{N}$ thin films were further examined by AFM. Fig. 4.20 a, b, and c show the surface scans of $\text{In}_{0.25}\text{Ga}_{0.75}\text{N}$, $\text{In}_{0.33}\text{Ga}_{0.67}\text{N}$, and $\text{In}_{0.64}\text{Ga}_{0.36}\text{N}$ thin films, respectively. All $\text{In}_x\text{Ga}_{1-x}\text{N}$ samples revealed island-like granules. Root-mean-square (Rms) surface roughness of the

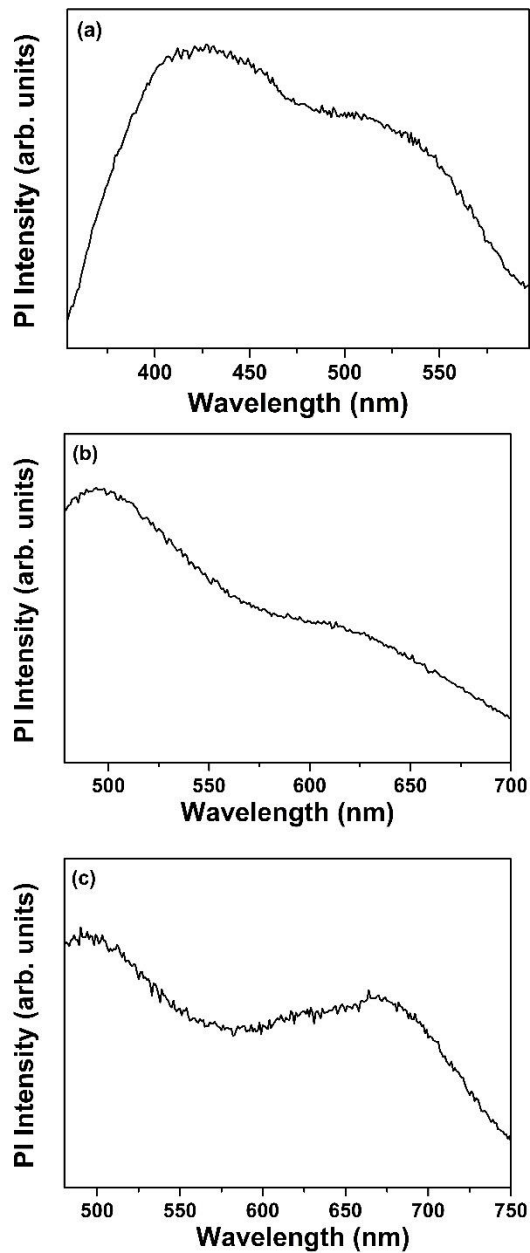


Figure 4.19: Room temperature PL spectra of (a) $\text{In}_{0.25}\text{Ga}_{0.75}\text{N}$, (b) $\text{In}_{0.33}\text{Ga}_{0.67}\text{N}$, and (c) $\text{In}_{0.64}\text{Ga}_{0.36}\text{N}$ thin films deposited on Si(100) substrates.

$\text{In}_x\text{Ga}_{1-x}\text{N}$ layers showed an increasing trend with In concentration: 0.28, 0.42, and 0.65 nm for $\text{In}_{0.25}\text{Ga}_{0.75}\text{N}$, $\text{In}_{0.33}\text{Ga}_{0.67}\text{N}$, and $\text{In}_{0.64}\text{Ga}_{0.36}\text{N}$ thin films, respectively. Similar trend has also been reported in literature where $\text{In}_x\text{Ga}_{1-x}\text{N}$ films grown with plasma-assisted MBE showed increase in surface roughness with In concentration.[279]

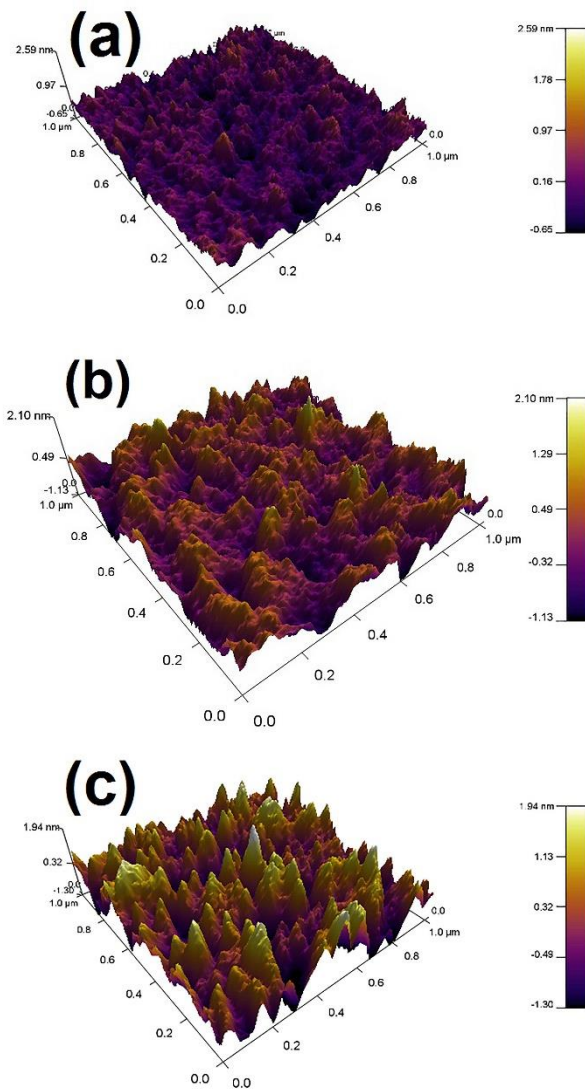


Figure 4.20: Surface morphologies of (a) $\text{In}_{0.25}\text{Ga}_{0.75}\text{N}$, (b) $\text{In}_{0.33}\text{Ga}_{0.67}\text{N}$, and (c) $\text{In}_{0.64}\text{Ga}_{0.36}\text{N}$ thin films deposited on Si(100) substrates.

4.3 Low-temperature Sequential Pulsed Chemical Vapor Deposition of Ternary $B_xGa_{1-x}N$ and $B_xIn_{1-x}N$ Thin Film Alloys

$B_xGa_{1-x}N$ and $B_xIn_{1-x}N$ thin films with different boron compositions were deposited at 450 °C on pre-cleaned Si (100) and double-side polished quartz substrates. In our previous work, we have reported growth of *h*BN thin film on silicon and quartz substrates with low impurities using TEB and N_2/H_2 plasma as boron and nitrogen precursors, respectively in an HCPA-ALD reactor.[31] We were able to grow BN with appreciable GPC values at substrate temperatures of 350 °C and 450 °C. GPC values at 350 °C and 450 °C were 0.15 and 0.47 Å/cycle, respectively. BN thin films deposited in CVD regime at 350 °C and 450 °C were polycrystalline with hexagonal structure as determined by GIXRD and HR-TEM. Films exhibited an optical band edge at ~5.25 eV and high transparency (>90 %) in the visible region of the spectrum. 450 °C was chosen for the growth of $B_xGa_{1-x}N$ and $B_xIn_{1-x}N$ alloys as growth per cycle of BN was substantially higher than the growth rates at lower temperature (<350 °C). However, higher growth temperatures of BN (>250 °C) resulted in thermal decomposition of boron precursor (TEB). Thermal decomposition of precursor leads to CVD type growth at growth temperatures above a possible ALD growth temperature window. Keeping in mind the CVD growth of BN at 450 °C, we have used the term sequential pulsed CVD in present case for growth of $B_xGa_{1-x}N$ and $B_xIn_{1-x}N$. Prior to growth of boron alloys, GaN and InN thin films were deposited at 450 °C on Si (100) and double side polished quartz. GaN and InN thin films were used as reference samples to compare their material properties with $B_xGa_{1-x}N$ and $B_xIn_{1-x}N$ alloys. Recently, we have reported that InN growth at 200 °C using N_2/H_2 plasma as nitrogen source results in a multi-phase thin film composed of *h*-InN and *t*-InN phases with relatively high impurity (21 at.% oxygen) incorporation, whereas the film deposited using N_2 plasma reveals single phase *h*-InN with substantially low impurity (<2 % oxygen) content.[245]

In this work, we have carried out growth of InN at 450 °C with N₂/H₂ plasma as nitrogen source and no film growth was observed. Therefore, N₂ plasma was used as nitrogen source for the growth of InN film while N₂/H₂ plasma was used as nitrogen source for the growth of GaN film at 450 °C.

For B_xIn_{1-x}N growth, as explained in experimental section, in order to keep the nitrogen source fixed as N₂ plasma, nitrogen plasma was used as N-precursor for BN sub-cycle. Additionally, a separate growth of BN thin film was carried out using TEB and N₂ plasma as boron and nitrogen precursors, respectively. Material properties of BN grown with N₂ plasma as nitrogen source were compared with B_xIn_{1-x}N thin film. Thickness values of GaN and InN thin films deposited at 450 °C were measured using spectroscopic ellipsometer and were found to be ~35 (GPC=0.70 Å/cycle) and ~38 nm (GPC=0.76 Å/cycle), respectively. GPC of BN deposited using N₂/H₂ plasma at 450 °C was 0.47 Å/cycle.[241] On the other hand, thickness of BN deposited at 450 °C using N₂ plasma was 80 nm, which corresponds to GPC of 1.6 Å/cycle. Having growth recipes of BN, InN, and GaN in hand, total number of super-cycles were theoretically calculated for depositing ~40 nm of B_xGa_{1-x}N and B_xIn_{1-x}N with different compositions of boron. One super-cycle consisted of several sub-cycles of BN and GaN or InN, while the number of sub-cycles of binary films depends upon the desired concentration of alloy. The number of sub-cycles for a specific desired concentration of alloy was calculated using the following formula.

$$X_B = \frac{n_{BN}GPC_{BN}}{n_{BN}GPC_{BN} + n_{GaN/InN}GPC_{GaN/InN}} \quad (4.4)$$

Where, X_B is concentration of boron, n_{BN} is number of BN sub-cycles, n_{GaN/InN} is number of GaN or InN sub-cycles, and GPC is growth per cycle. Three different concentrations (Table. 4.7 and 4.8) of boron were selected and number of sub-cycles of BN and GaN or InN were calculated. The thickness values of B_xGa_{1-x}N thin films with 10, 30, and 50 % boron extracted from spectroscopic ellipsometer measurements were 30, 37, and 43 nm, respectively. On the other hand, the thickness values of B_xIn_{1-x}N

Table 4.7: Calculation of number of sub-cycles of BN and GaN to deposit ~ 40 nm of $B_xGa_{1-x}N$

	$X_B = 0.1$	$X_B = 0.3$	$X_B = 0.5$
Number of BN sub-cycles	1	2	3
Number of GaN sub-cycles	6	3	2
Thickness of one super cycle (Å)	4.67	3.04	2.81
Number of supercycles required to achieve a target thickness of ~ 40 nm	86	132	143

Table 4.8: Calculation of number of sub-cycles of BN and InN to deposit ~ 40 nm of $B_xIn_{1-x}N$

	$X_B = 0.1$	$X_B = 0.3$	$X_B = 0.5$
Number of BN sub-cycles	1	1	1
Number of InN sub-cycles	18	4	2
Thickness of one super cycle (Å)	15.28	4.64	3.12
Number of supercycles required to achieve a target thickness of ~ 40 nm	26	86	128

thin films extracted from spectroscopic ellipsometer measurements with 10, 30, and 50% boron were 29, 32, and 42 nm, respectively. Thickness values were close to the targeted value of 40 nm that was selected to compute the number of sub-cycles and super-cycles by eqn (4.4). However, it is worth mentioning that the targeted calculation of alloy thickness and composition is not straightforward since the deposition rate of constituents of alloys (BN, GaN or InN) might vary on different materials, i.e., GPC of BN on Si, BN, and GaN or InN might result in different values.

Table 4.9 shows the composition of the B-III-N alloy contents which were revealed by XPS measurements. $B_xIn_{1-x}N$ alloys show boron concentration up to 87% while the minimum concentration of boron in $B_xIn_{1-x}N$ alloys was 32 %. $B_xGa_{1-x}N$ alloys also show increase in boron concentration from 35 to 88 %. Based on XPS evaluation of alloy concentration values, $B_xIn_{1-x}N$ alloys will be mentioned as $B_{0.32}In_{0.67}N$, $B_{0.75}In_{0.25}N$, and $B_{0.87}In_{0.13}N$. While, $B_xGa_{1-x}N$ alloys will be mentioned as $B_{0.35}Ga_{0.65}N$, $B_{0.76}Ga_{0.24}N$, and $B_{0.88}Ga_{0.12}N$. There is a variation between targeted and evaluated composition by XPS. The resulting alloy composition might indicate two possible scenarios:(1) BN growth rate might be faster on GaN and InN layers when compared on Si orBN layer (2)

GaN and InN deposition on BN proceeds slower when compared to their growth on Si or GaN or InN layers.

Table 4.9: $B_xIn_{1-x}N$ and $B_xGa_{1-x}N$ alloy compositions calculated from XPS measurements.

Sample	B concentration	In concentration	Ga concentration
$B_xIn_{1-x}N$ (10 %)	0.32	0.68	---
$B_xIn_{1-x}N$ (30 %)	0.75	0.25	---
$B_xIn_{1-x}N$ (50 %)	0.87	0.13	---
$B_xGa_{1-x}N$ (10 %)	0.35	---	0.65
$B_xGa_{1-x}N$ (30 %)	0.76	---	0.24
$B_xGa_{1-x}N$ (50 %)	0.88	---	0.12

The crystalline structure of $B_xGa_{1-x}N$ and $B_xIn_{1-x}N$ films were characterized by GIXRD (Fig. 4.21). Figure 4.21(a) shows the GIXRD patterns of $B_xGa_{1-x}N$ thin films deposited on Si (100) substrates with different compositions. For comparison, GaN GIXRD pattern is also given. GaN thin film was polycrystalline with hexagonal structure (ICDD reference code: 00-050-0792). There is one dominant reflection of hexagonal (002) crystallographic orientation and two weakly pronounced reflections (101) and (100) appear as shoulders of the main peak. As soon as boron is incorporated in the films, crystallinity of sample is diminished as revealed by a weak shoulder in the case of $B_{0.35}Ga_{0.65}N$ thin film, whereas $B_{0.76}Ga_{0.24}N$, and $B_{0.88}Ga_{0.12}N$ films showed amorphous character without any crystalline feature. Figure 4.21(b) shows the GIXRD patterns of $B_xIn_{1-x}N$ thin films deposited on Si (100) substrates with different compositions. The GIXRD pattern of InN was indexed to reflections from hexagonal wurtzite InN (ICDD reference code: 98-015-7515). Boron incorporation in wurtzite InN lattice destroyed the crystallinity of $B_xIn_{1-x}N$ films as GIXRD measurements of $B_{0.32}In_{0.68}N$, $B_{0.75}In_{0.25}N$, and $B_{0.87}In_{0.13}N$ reveal broad and less intense peaks. Keeping in view the structural dissimilarities of BN and GaN or InN, the results presented here depict that it is quite challenging to grow crystalline $B_xGa_{1-x}N$ and $B_xIn_{1-x}N$ alloys especially at higher boron concentrations.

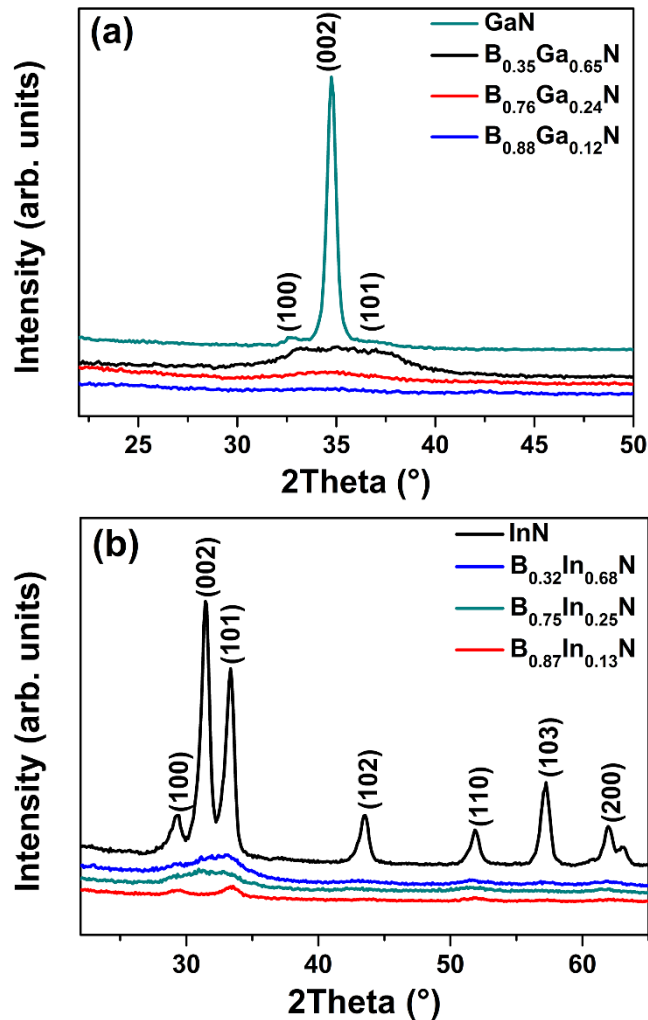


Figure 4.21: GIXRD pattern of (a) GaN and B_xGa_{1-x}N with different compositions, (b) InN and B_xIn_{1-x}N with different compositions.

Figure 4.22(a) shows the spectral refractive index curves of BN, GaN, and B_xGa_{1-x}N films deposited on Si(100). Refractive index value of BN grown at 450 °C using TEB and N₂/H₂ plasma was 1.61 at 550 nm; while for GaN grown at 450 °C, it was measured to be 2.24 at 550 nm. Refractive index values of 1.6-1.7 has been reported in literature for BN thin films grown using plasma enhanced CVD,²⁰⁻²¹ whereas 2.3-2.4

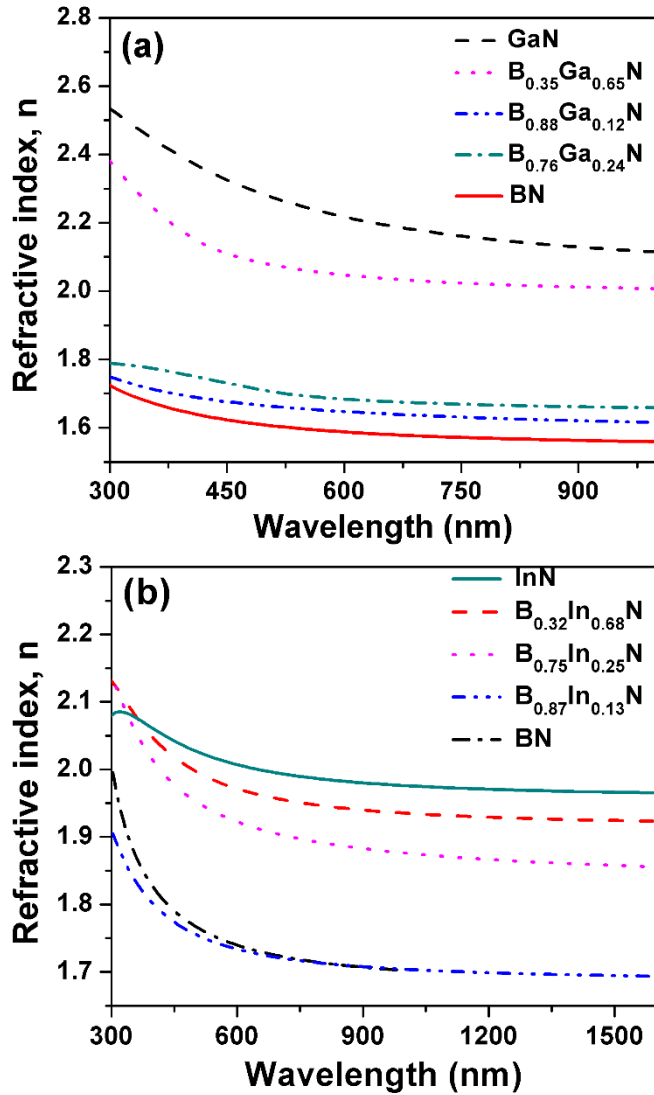


Figure 4.22: Refractive indices of (a) BN, GaN, and $B_xGa_{1-x}N$ with different compositions, (b) BN, InN and $B_xIn_{1-x}N$ with different compositions.

has been reported for GaN deposited using MOCVD.²² Refractive index decreased from 2.24 to 1.65 as the B concentration of $B_xGa_{1-x}N$ increased from 35 to 88 %. Refractive index values of $B_{0.35}Ga_{0.65}N$, $B_{0.76}Ga_{0.24}N$, and $B_{0.87}Ga_{0.13}N$ samples were recorded as 2.06, 1.69, and 1.65, respectively. Figure 4.22(b) shows a comparison of refractive index values of BN, InN, and $B_xIn_{1-x}N$ thin films deposited on Si(100). BN film deposited at 450 °C using TEB and N_2 plasma shows a refractive index value of 1.77 at 550 nm. On the other hand, Refractive index value was measured as 2.01 at 550 nm for InN film deposited

at 450 °C using TMI and N₂ plasma as indium and nitrogen precursors, respectively. Refractive index value of 2.5-2.6 has been reported in literature for InN thin films grown using magnetron sputtering.²³ As anticipated, refractive index decreased from 1.98 to 1.74 as boron concentration was increased from 32 to 87 %. The results presented here shows that the refractive index values of B_xGa_{1-x}N and B_xIn_{1-x}N alloy thin films vary according to alloy composition.

Figure 4.23 shows optical transmission spectra of BN, GaN, InN, B_xGa_{1-x}N, and B_xIn_{1-x}N thin films in UV-Vis and NIR regions deposited on double-side polished quartz substrates. The average transmittance for BN was measured to be 91–93% range within the visible spectrum which is close to bare quartz transmission value. This indicates that BN film is almost fully transparent in visible wavelength region. Decrease in transmission of BN thin film observed at UV wavelengths less than 280 nm was believed to be caused by the main band gap absorption.[241] For GaN thin film (Fig. 4.23a), a significant decrease in the UV transmission was observed at wavelengths < 400 nm, which is most probably due to the main band-to-band absorption. InN thin film (Fig. 4.23b) exhibits 40-50% transmission in the visible regime, which approaches up to 60-70% in the NIR regime. Transmission values did not saturate for InN sample, possibly due to the relatively high impurity content and defect density present within the films.¹⁹ Transmission band edge values of the B_xGa_{1-x}N and B_xIn_{1-x}N thin films shifted to lower wavelengths with increasing boron content, demonstrating the successful tunability of optical band gap by changing alloy composition.

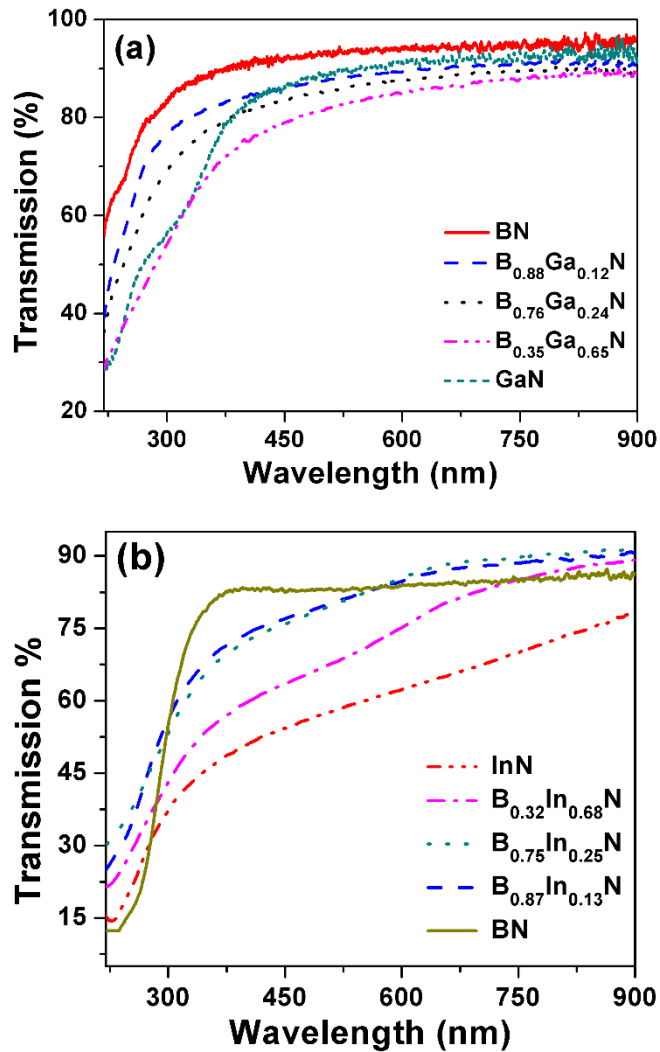


Fig. 4.23: Transmission spectra of (a) BN, GaN, and B_xGa_{1-x}N with different compositions, (b) BN, InN and B_xIn_{1-x}N with different compositions.

Surface morphologies of B_xGa_{1-x}N and B_xIn_{1-x}N samples were examined by AFM. Figures 4.24(a), (b), and (c) show the surface scans of the B_{0.35}Ga_{0.65}N, B_{0.76}Ga_{0.24}N, and B_{0.88}Ga_{0.12}N thin films, respectively. Root-mean-square (Rms) roughness of B_{0.35}Ga_{0.65}N, B_{0.76}Ga_{0.24}N, and B_{0.88}Ga_{0.12}N samples measured from 1 μm×1 μm scan area was 0.75, 3.52, and 4.68 nm, respectively. Previously, we have reported non-uniform, rough, compact, and three-dimensional (3D) curly surface morphology of BN. Rough morphology of BN might be the cause of increased roughness of B_xGa_{1-x}N thin film alloys with increase in boron concentration. Figures 4.24(d), (e), and (f) show the surface

scans of the $B_{0.32}In_{0.67}N$, $B_{0.75}In_{0.25}N$, and $B_{0.87}In_{0.13}N$ thin films, respectively. RMS roughness of $B_{0.32}In_{0.67}N$, $B_{0.75}In_{0.25}N$, and $B_{0.87}In_{0.13}N$ samples was extracted as 5.84, 4.52, and 2.83 nm, respectively. These results imply a totally reverse trend in film surface roughness when compared with $B_xGa_{1-x}N$ samples. The main difference in the growth chemistry between $B_xIn_{1-x}N$ and $B_xGa_{1-x}N$ lies in the choice of nitrogen precursor: N_2 plasma versus N_2/H_2 plasma. Therefore, it can be deduced that this plasma source difference shows a significant impact on the surface roughness of the resulting alloy films.

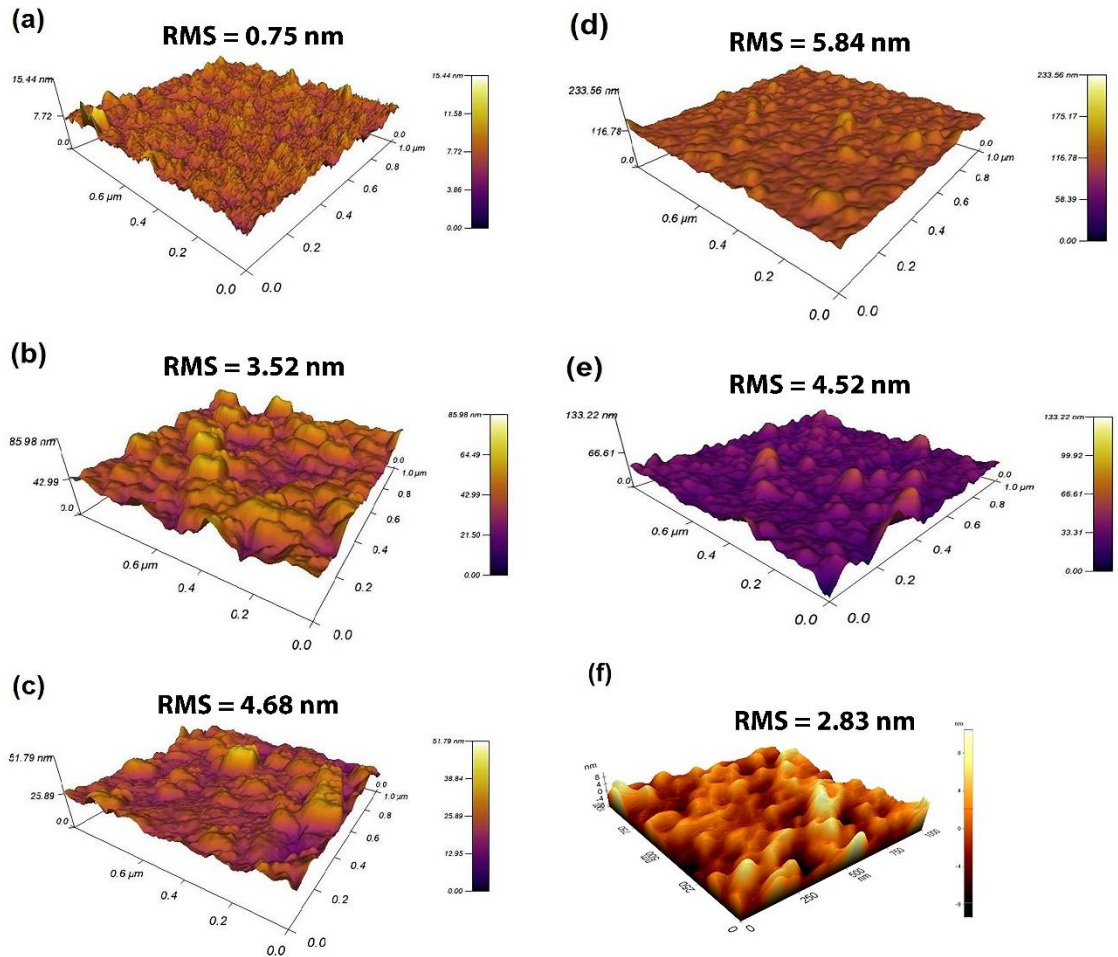


Fig. 4.24: AFM images of (a) $B_{0.35}Ga_{0.65}N$, (b) $B_{0.76}Ga_{0.24}N$, (c) $B_{0.88}Ga_{0.12}N$, (d) $B_{0.32}In_{0.67}N$, (e) $B_{0.75}In_{0.25}N$, and (f) $B_{0.87}In_{0.13}N$.

Chapter 5

Template Assisted Atomic Layer Deposition of III-nitride Nanostructures

This chapter presents the experimental results of GaN, AlN, and InN HNCs integrated to Si(100) substrates using AAO membrane templated PA-ALD. GaN, AlN, and InN HNCs have been characterized using SEM, EDX, TEM, SAED, GIXRD, XPS, and PL measurements. The material properties of nanostructured III-nitride materials have been compared with the thin-film counterparts which were also grown using low-temperature PA-ALD. At first, RIE of Si using AAO membrane as hard mask material was performed to achieve nanoporous Si substrate. Subsequently, PEALD of III nitride materials was performed on nanoporous Si substrate.

Prior to the attachment of AAO hard-mask to the Si substrate, SEM inspection of a free standing AAO membrane revealed that two sides of the membrane have different morphology; one with symmetrical open pores, other with partially open asymmetrical pores with higher surface roughness. Top-view SEM image of the open pores side is shown in Fig. 5.1b which clearly indicates the high density arrays of uniform and aligned nanopores in a honeycomb-like

geometry. Average pore diameter of the as-grown AAO membrane was about 70-80 nm while the average interpore distance was measured as ~130-135 nm. Angled-view SEM image of the AAO membrane (Fig. 5.1c) depicted the height of AAO membrane to be ~2.85 μm , out of which top ~350 nm portion consists of rough and partially blocked pores. Rest of the membrane is composed of relatively uniform pore diameter which extend throughout the entire AAO membrane thickness. AAO membrane is attached to Si with the side having open pores facing Si. In this strategy, RIE etch gases will initially etch the exposed semi-blocked pores of the membrane and hence the rest of etching will proceed smoothly through the open pores. CHF_3 and Ar were used to transfer the AAO honeycomb nano-porous pattern to Si substrate. Ar acts as the physical sputtering agent responsible for vertical anisotropic etch pattern.[280], [281] With the exposure of CHF_3 plasma to exposed Si surface, polymer forming radicals get deposited on the sidewalls forming a barrier layer which prevents undercutting.

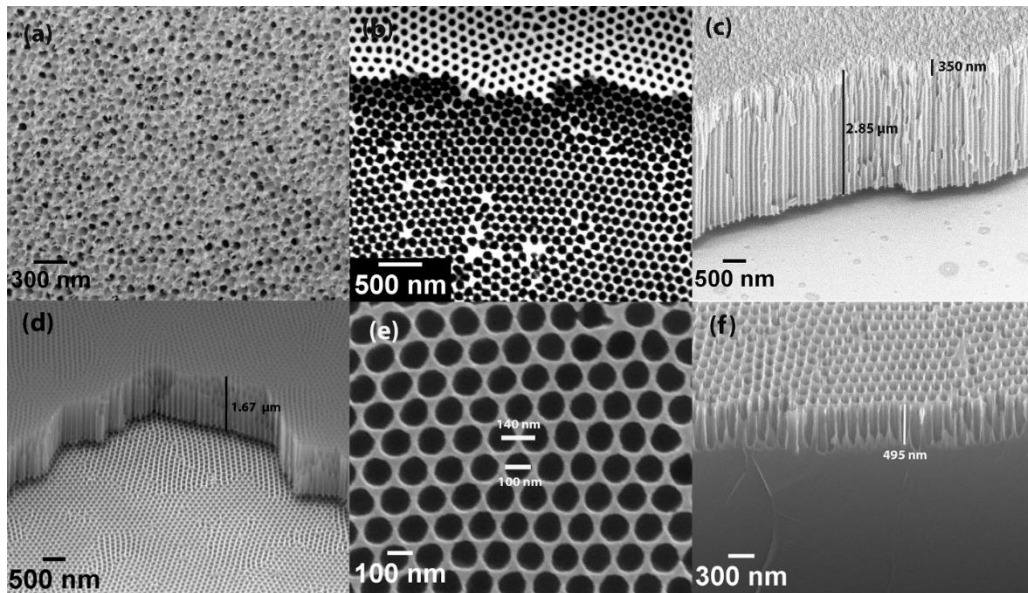


Figure 5.1: SEM image of (a) top side of AAO membrane with partially blocked pores, (b) bottom side of AAO membrane with dominantly open nanopores, (c) cross-section of AAO membrane after substrate attachment showing the total height of AAO membrane and the rough top portion, (d) porous Si surface with AAO membrane on top, (e) nanoporous Si revealing pore-widening effect and uniformly aligned hexagonal pores, and (f) angled-view image of nanoporous Si indicating the depth of etched pores.

Porous Si nano-network was formed by plasma etching through AAO hard mask. A thickness decrease in the AAO membrane (Fig. 5.1d) is observed from $\sim 2.85 \mu\text{m}$ to $\sim 1.67 \mu\text{m}$ after 70 minutes of RIE process, which implies that AAO membrane itself is also being etched simultaneously with the formation of nanopores. Figure 5.1e reveals the highly ordered hexagonal array of nanopores formed on Si surface, confirming the successful pattern transfer. The resulting average diameter of Si nanopores has increased to $\sim 90\text{-}100 \text{ nm}$ due to the non-ideal anisotropic etch which results in a pore-widening effect, while the average pore-to-pore distance remains around $\sim 140\text{-}145 \text{ nm}$. The density and size of nanopores are rather close to the original AAO membrane template, which implies both the success of pattern-transfer process and the ability of tuning simplicity of the pore size and morphology by modifying the initial anodization conditions. An angled-view image of Si nano-porous structure is shown in Fig. 5.1f which shows the depth of pores to be around 500 nm .

III-nitride material growth was carried out on nanoporous Si substrate in a PA-ALD reactor featuring customized hollow-cathode plasma source[32], [147], [282]–[285]. A critical factor in choosing ALD to grow on high aspect ratio porous Si is the superior conformality made possible by its self-limiting characteristic, which allows the surface to get saturated with no more than one layer of chemisorbed precursor molecules. Precursor molecules disperse into deep trench structures with sufficient precursor pulse/exposure time allowing molecules to react with the entire exposed surface. In the subsequent sections of this article, fabrication steps and material characterization details of GaN, AlN, and InN HNCs are provided.

5.1 GaN Hollow Nanocylinder Arrays

1500 cycles of GaN was grown on nanoporous Si substrate via PA-ALD using TEG and N_2/H_2 plasma as gallium and nitrogen precursors, respectively. Figure 5.2a and b shows the top-view and angled-view SEM images after GaN growth on nanoporous Si substrate, respectively. Grainy structure of GaN is visible

from top-view image (Fig. 5.2a) which was also observed in previously reported ~32 nm thick GaN thin films on Si substrates.[286] Porous morphology is still visible after GaN growth on Si nano-pores, however, pore-size is reduced to ~35 nm. Ability of PA-ALD to uniformly coat GaN (thickness ~37.5 nm) on nanoporous Si in a conformal fashion is evident from the angled-view SEM image (Fig. 5.2b). The thickness of GaN observed from inner walls of nanoporous Si substrate is less than the GaN film thickness grown on a planar Si substrate (~37.5 nm vs. 50 nm) in the same growth experiment. The thickness variation of GaN along the Si pore depth is $\pm 24\text{-}25\%$. ALD with its inherent self-limiting growth mechanism is expected to provide highly conformal non-line of sight deposition even on 3D complex nanostructures. However, ideal conformal coating results for ALD-growth on nanostructured templates can only be achieved by carefully optimizing the process parameters such as precursor doses, exposure time, and purging time at a given reaction temperature. A substrate must be exposed to a right amount of precursor as insufficient precursor dose will leave some unreacted surface sites behind resulting in a limited conformality. The most critical parameter in performing ALD on substrates with higher aspect ratio structures is the precursor exposure time. With sufficient precursor exposure time, precursor molecules should be able to reach all the active sites on the 3D substrate surface. Generally, long precursor exposures are relatively less beneficial in plasma-assisted ALD due to the relatively fast plasma radical recombination process. In the present work, we have utilized the PA-ALD growth recipe previously optimized for planar Si surfaces.[286]

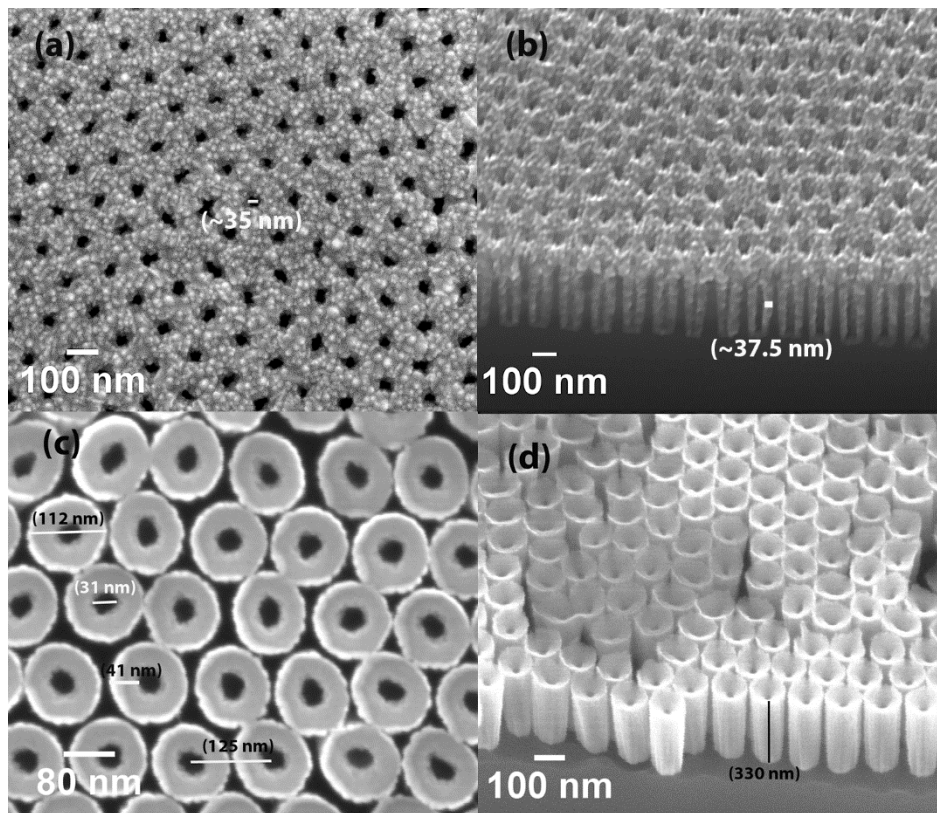


Figure 5.2: (a) Top view SEM image obtained from PA-ALD (1500 cycle) grown GaN on nanoporous Si substrate, (b) Angled-view SEM image of the same sample showing the rather conformal filling of GaN into the Si nanopores, (c) Top-view SEM image of GaN HNCs revealing their morphology and dimensions, and (d) Angled-view SEM image of GaN HNCs showing the total height of nano-cylinders.

As GaN film grows on the horizontal top surface of Si nano-pores as well, those parts must be removed before Si etching can be carried out to obtain free-standing GaN nano-cylindrical arrays on Si surface. Ar plasma was employed to etch GaN from horizontal Si surface followed by SEM imaging. SEM image (Fig. 5.3) showed that 2 minutes of Ar plasma exposure successfully removed GaN from top of nano-pores.

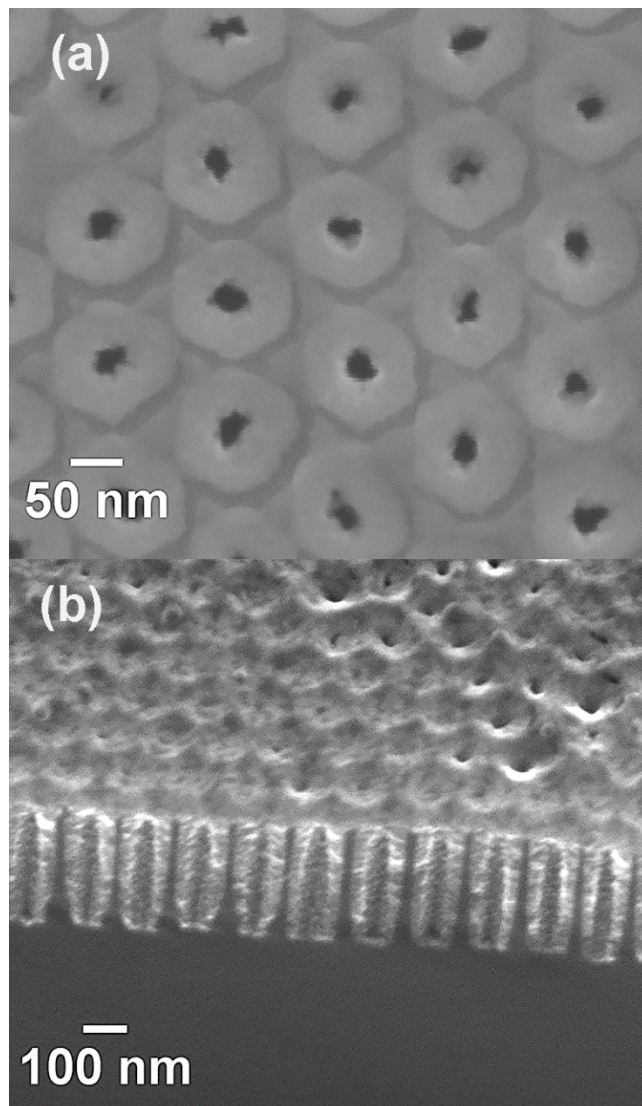


Figure 5.3: (a) Top view and (b) cross-sectional view SEM images obtained after 2 minutes of Ar plasma exposure successfully removed GaN from top of nano-pores leaving GaN integrated inside Si(100).

The last step in fabrication was to selectively etch Si via SF_6 plasma to obtain GaN HNCs. Figure 5.2c and d shows the top-view and angled-view SEM images of GaN HNCs after 6 sec of SF_6 based Si etching, respectively. Width of GaN nano-cylinders is ~ 110 nm, while the pore size within the nanocylinders is about 30 nm. The wall diameter of individual nano-cylinder and inter-cylinders distance were measured as ~ 40 and ~ 125 nm, respectively. Changing the etching time of Si, height of free-standing individual GaN nanocylinders can be varied

as well. After 6 sec of Si etching, the height of GaN HNCs ranged within ~330-360 nm.

TEM characterization was carried out on GaN HNCs to examine their internal morphology and crystalline structure. In order to prepare TEM sample, nanocylinders were scratched by a needle and a TEM grid was gently touched to the top surface of GaN-HNCs/nanoporous-Si samples followed by TEM imaging. Bright field TEM images of GaN HNCs are provided in Fig. 5.4. Finely dispersed hollow nano-cylinders can be seen in Fig. 5.4a. Figure 5.4b confirms the total length of GaN HNCs around ~375 nm and shows that their interior is indeed hollow. It is observed that the outer wall of HNCs is highly uniform along the cylinder axis. However, wall thickness of GaN HNCs along the long axes of individual cylinders shows a degree of non-uniformity. The part where GaN wall is thicker corresponds to the top portion of HNC close to air-HNC interface. This image reveals that GaN wall thickness tend to become thinner along the depth of Si pore. As explained earlier, it might either be due to insufficient precursor exposure and/or N_2/H_2 plasma radicals recombination during HCPA-ALD of GaN. Figure 5.4c shows the high-resolution TEM (HR-TEM) image of HNCs revealing lattice fringes of GaN which are organized in various crystallographic orientations confirming its polycrystalline structure. SAED measurements were performed to further investigate the crystal structure of the GaN HNCs. The SAED pattern (Fig. 5.4d) consists of polycrystalline diffraction rings corresponding to the hexagonal wurtzite GaN (h-GaN) crystal structure. The analysis of SAED pattern has been summarized in Table 5.1, which shows measured ring diameters, the calculated and theoretical inter-planar spacing values, and corresponding crystallographic planes. The first ring from the center is considerably thick and theoretical ring diameters of (101), (100), and (002) crystallographic planes either merge or lie very close to the first thick diffraction ring. Indeed, inner and central diameter of this ring were measured and found to be 7.509 and 8.501 nm⁻¹, corresponding to (100) and (101) planes with a calculated inter-planar spacing (d_{hkl}) values of 2.663 and 2.395 Å, respectively. Other than (100) and (101) crystallographic planes, (102), (101),

(103), and (112) planes corresponding to GaN hexagonal wurtzite crystal structure are also found.

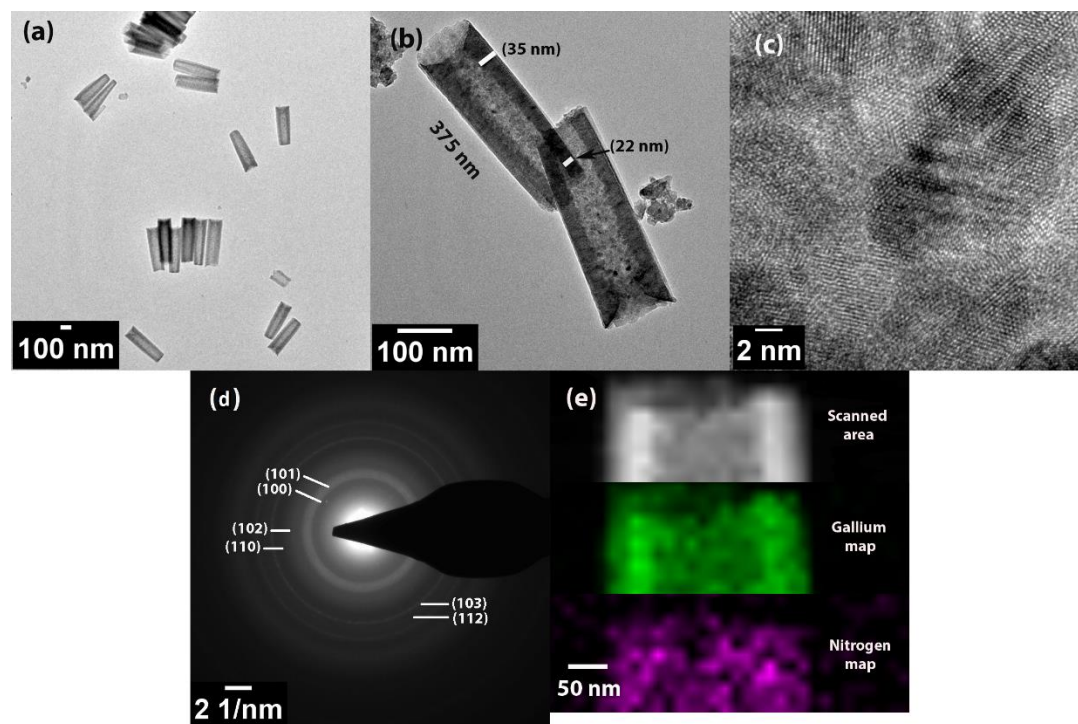


Figure 5.4: (a) TEM image of several individual and bundled GaN HNCs, (b) TEM image of GaN HNCs revealing their wall thickness and total length, (c) HR-TEM image of a GaN HNC displaying the polycrystalline structure of PA-ALD grown GaN, (d) SAED pattern of GaN HNCs, and (e) EDX elemental mapping of the same GaN HNC sample.

Table 5.1: SAED Results, Theoretical Values, and Corresponding Crystallographic Planes

Diameter (nm ⁻¹)	Interplanar spacing, d_{hkl} (Å)		Corresponding plane ^a , hkl
	Calculated	Theoretical ^a	
7.509	2.663	2.7620	100
8.501	2.395	2.4370	101
10.588	1.888	1.8910	102
12.059	1.658	1.5945	110
13.526	1.478	1.4649	103
14.864	1.345	1.3582	112

^aHexagonal GaN, ICDD reference code: 00-025-1133

Figure 5.4e shows EDX elemental mapping of gallium and nitrogen from a part of individual GaN HNC. This measurement reveals the uniform distribution of gallium and nitrogen which confirms the presence of GaN compound structure in the scanned area.

GIXRD patterns of GaN HNCs and GaN thin film deposited on Si are provided in Fig. 5.5a and b, respectively. Patterns obtained from both GaN HNCs and corresponding thin film reveal single-phase polycrystalline hexagonal wurtzite structure. The reflections (100), (002), (101), (101), (103), and (112) of the h-GaN phase appeared in the GIXRD patterns (Hexagonal GaN, ICDD reference code: 00-025-1133). These results are in good agreement with the SAED results given in Fig. 5.4d and Table 5.1. A distinct (002) reflection was not observed in SAED diffraction pattern, however, we believe that it is not distinguishable in SAED pattern due to the merging of three individual diffraction rings in one big thick ring closest from the center. Such a merging of three diffraction rings in one has also been observed previously in a SAED pattern obtained from GaN flexible nanofibers.[17]

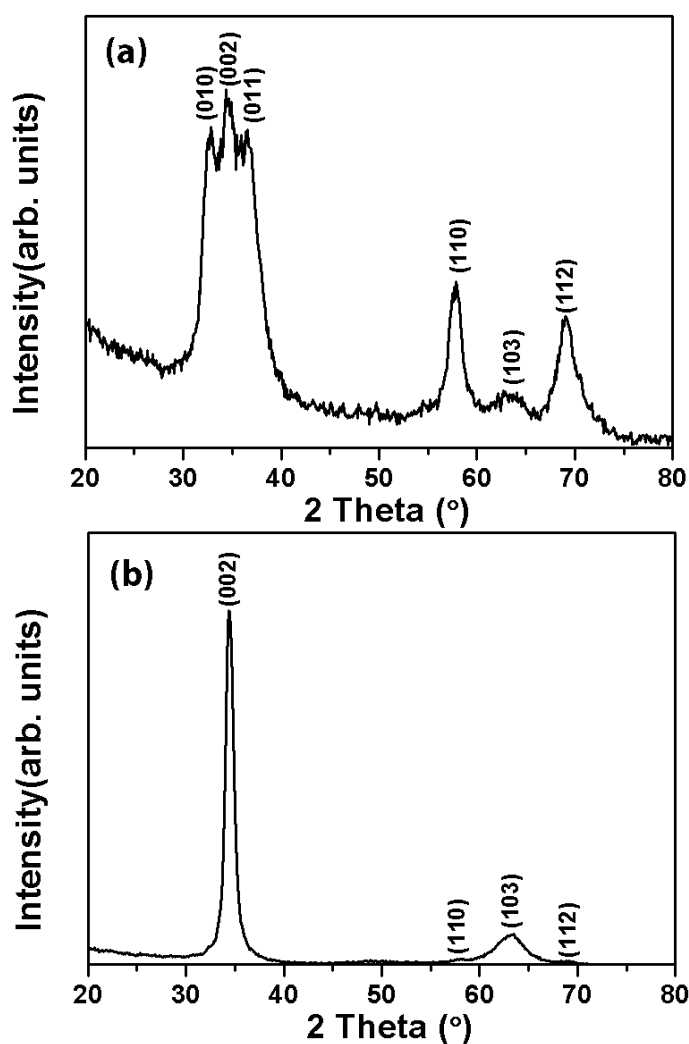


Figure 5.5: GIXRD pattern obtained from (a) GaN HNCs grown on nanoporous Si substrates, (b) ~50 nm thick GaN deposited on planar Si via HCPA-ALD.

Chemical composition and bonding state of GaN HNCs were studied using XPS. XPS survey scan collected from top of ~375 nm long GaN HNCs revealed the presence of gallium, nitrogen, carbon, fluorine, and oxygen elements. Atomic percentages of elements detected from GaN HNCs were as following: 33.21 at. % Ga, 45.08 at. % N, 5.74 at. % C, 5.64 at. % F, and 10.33 at. % O. Although these results suggest N-rich elemental distribution from GaN HNCs, it should be noted that the atomic concentration of N is overestimated due to the significant contribution of Ga Auger peaks, which overlap with the N 1s peak.[17], [32] Previously, we have reported the impurity content from bulk of GaN thin film deposited using the exact same PA-ALD growth recipe parameters utilized for fabrication of GaN HNCs. No carbon was found in the bulk of the film, while oxygen impurities (2–3 at. %) in the bulk of GaN films was detected.[286] Presence of oxygen in the bulk of film was attributed to oxygen and water vapor impurities present in either plasma gases or organometallic precursors and trapped oxygen/water vapor inside the multilayer coatings on the inner walls of the ALD vacuum reactor. XPS gathered data from bulk of the film by in-situ etching first few layers of GaN via Ar⁺ ions. The same technique however, would not be accurate to determine GaN bulk impurity content from GaN HNCs due to possible oxidation of GaN HNCs all along the top surface. Therefore, bulk elemental quantification from the GaN thin film sample can be used as an estimate for the impurity content of GaN HNCs.

The high-resolution XPS (HR-XPS) scans of Ga 3d and N 1s are given in Figs. 5.6a and b, respectively, which were collected from the surface of GaN HNCs. Asymmetry and FWHM of the peaks indicate more than one type of bonding scheme for both gallium and nitrogen. Ga 3d HR-XPS spectrum was fitted using three subpeaks located at 20.30 eV (subpeak#3), 19.38 eV (subpeak#1) and 17.68 eV (subpeak#2). Subpeaks number 1 and 3 were attributed to the Ga-N and Ga-O bonds, respectively, whereas subpeak#2 originates from N2s core level contribution.[17], [32] N 1s HR-XPS spectrum

(Fig. 5.6b) was fitted by three subpeaks located at 397.37 eV (subpeak#1), 395.18 eV (subpeak#2) and 393.08 eV (subpeak#3). Subpeak#1 was assigned to the N-Ga bond, whereas subpeaks#2 and #3 correspond to the Ga Auger peaks.[17], [32]

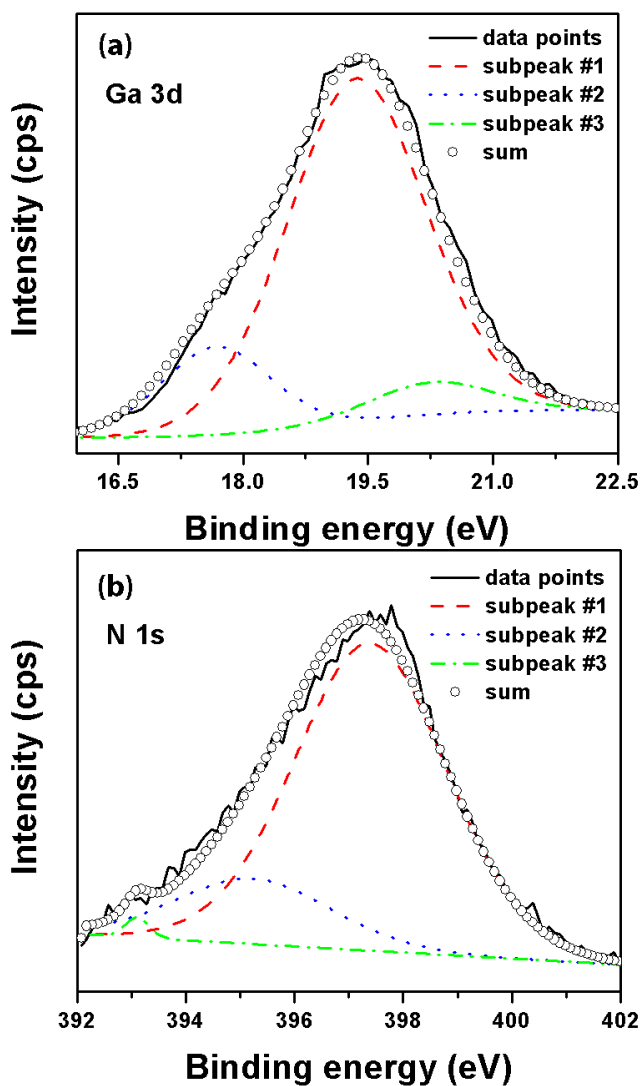


Figure 5.6: HR-XPS scans of (a) Ga 3d and (b) N 1s obtained from GaN HNCs revealing presence of various bonding schemes.

The PL spectra of polycrystalline GaN HNCs and their thin film counterpart was measured in the wavelength range of 350–850 nm at room temperature and is presented in Fig. 5.7. A broad peak at 448 nm “2.76 eV” was observed from GaN HNCs, which represents a defect related emission “blue luminescence

(BL)”. On the other hand, a weak and noisy signal was observed from ~60 nm thick GaN thin films which exhibited two relatively weaker peaks at 371.3 nm “3.34 eV” and 500 nm “2.48 eV”, most probably originating due to a red shifted band-edge-related emission and structural defect sourced “green luminescence (GL)”, respectively.[287], [288] The presence of the “GL” band could be explained by the combination of gallium vacancy clusters and oxygen (or carbon) impurities.[289]–[291] GaN HNCs exhibit a stronger PL signal than their thin-film counterparts possibly due to their higher surface to volume ratio.

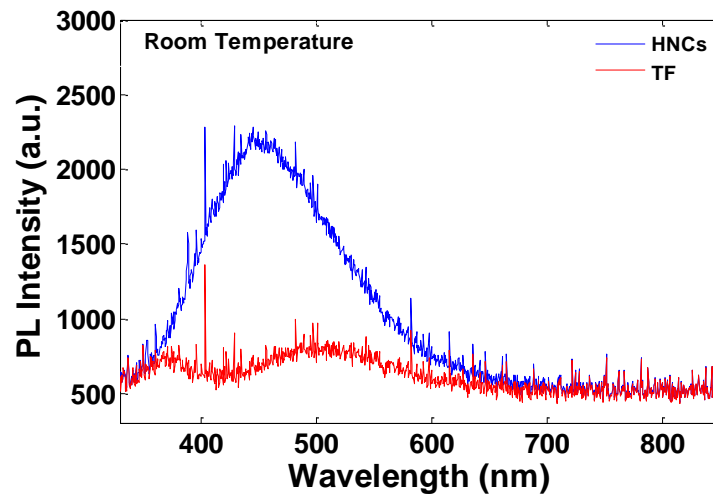


Figure 5.7: PL spectra of GaN HNCs and ~60 nm thick GaN thin film gathered at room temperature.

5.2 AlN Hollow Nanocylinder Arrays

For AlN samples, a total of 500 ALD cycles were used on nanoporous Si substrates. A detailed growth optimization study of AlN on planar Si template has been reported elsewhere.[32] At 200 °C, growth rate of ~1.0 Å/cycle has been reported for AlN deposited with an optimized growth recipe which corresponds to ~50 nm thick film for 500 ALD-cycle growth on planar Si.

Figure 5.8a and b show top and angled-view SEM images of the AlN-coated nanoporous Si template, respectively. AlN covered Si reveals hollow morphology, though the pore size has been reduced to ~30 nm from an initial

pore diameter of ~ 100 nm after nanopore formation. Top-view image also shows nanometer sized grains of AlN observed from the area amid pores. Angled-view SEM image of AlN covered porous Si reveals uniform and conformal growth of AlN inside the nanopores. From the inner cylinder wall, the average wall thickness of AlN was measured as ~ 37 nm. The variation in AlN thickness from top to bottom of pores is about $\pm 15\%$.

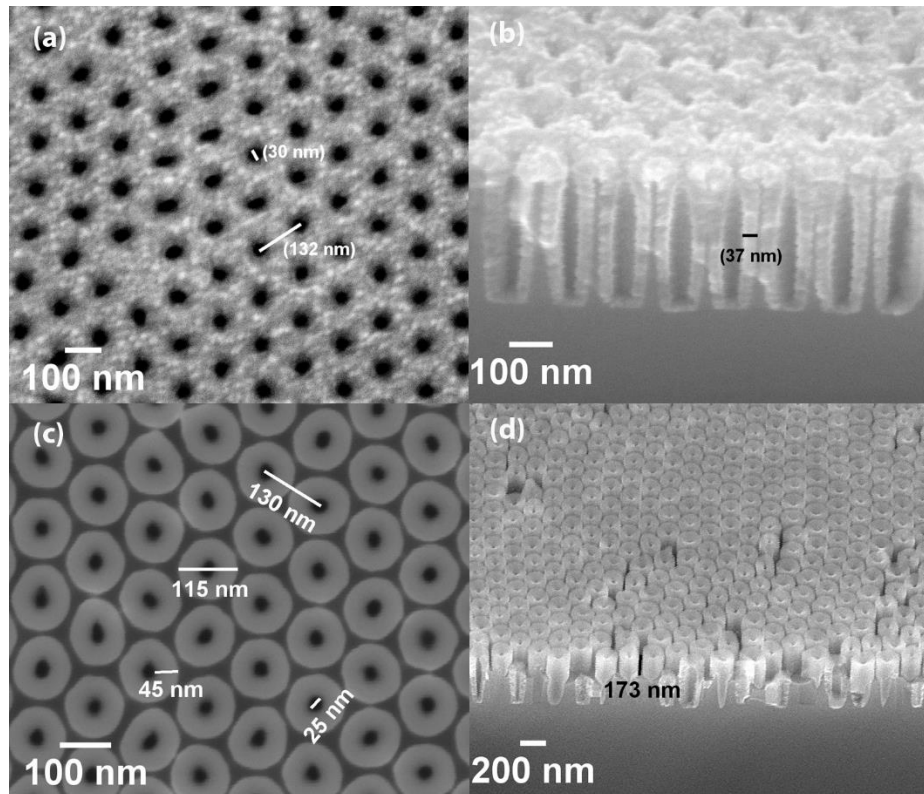


Figure 5.8: (a) Top view SEM image obtained from HCPA-ALD (500-cycle) grown AlN on nanoporous Si substrates, (b) Angled-view SEM image of the same sample, (c) Top-view SEM image of AlN HNCs revealing their morphology and dimensions, (d) angled-view SEM image of AlN HNCs depicting the total height of nanocylinders.

AlN grown on top horizontal surface of nanoporous Si has been etched using Ar plasma. SEM images (Fig. 5.9) obtained after 3 minutes of Ar etching indicates that AlN has been completely removed from top surface.

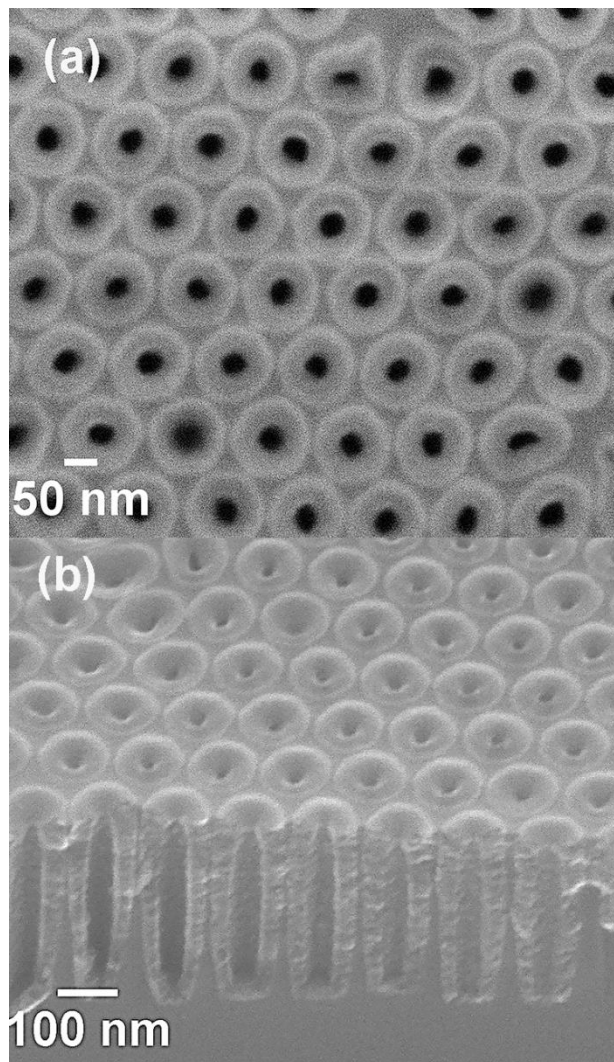


Figure 5.9: (a) Top view and (b) cross-sectional view SEM images obtained after 3 minutes of Ar plasma exposure successfully removed AlN from top of nano-pores leaving AlN integrated inside Si(100).

As a last step in AlN HNCs fabrication, Si was selectively etched by SF_6 gas to obtain free-standing AlN HNCs on Si surface. 5 sec of Si etching yielded ~110 nm long AlN HNCs (Fig. 5.10) with a diameter and internal pore size of ~116 and ~30 nm, respectively. A significant portion of AlN is still embedded inside Si after 5 sec of etching.

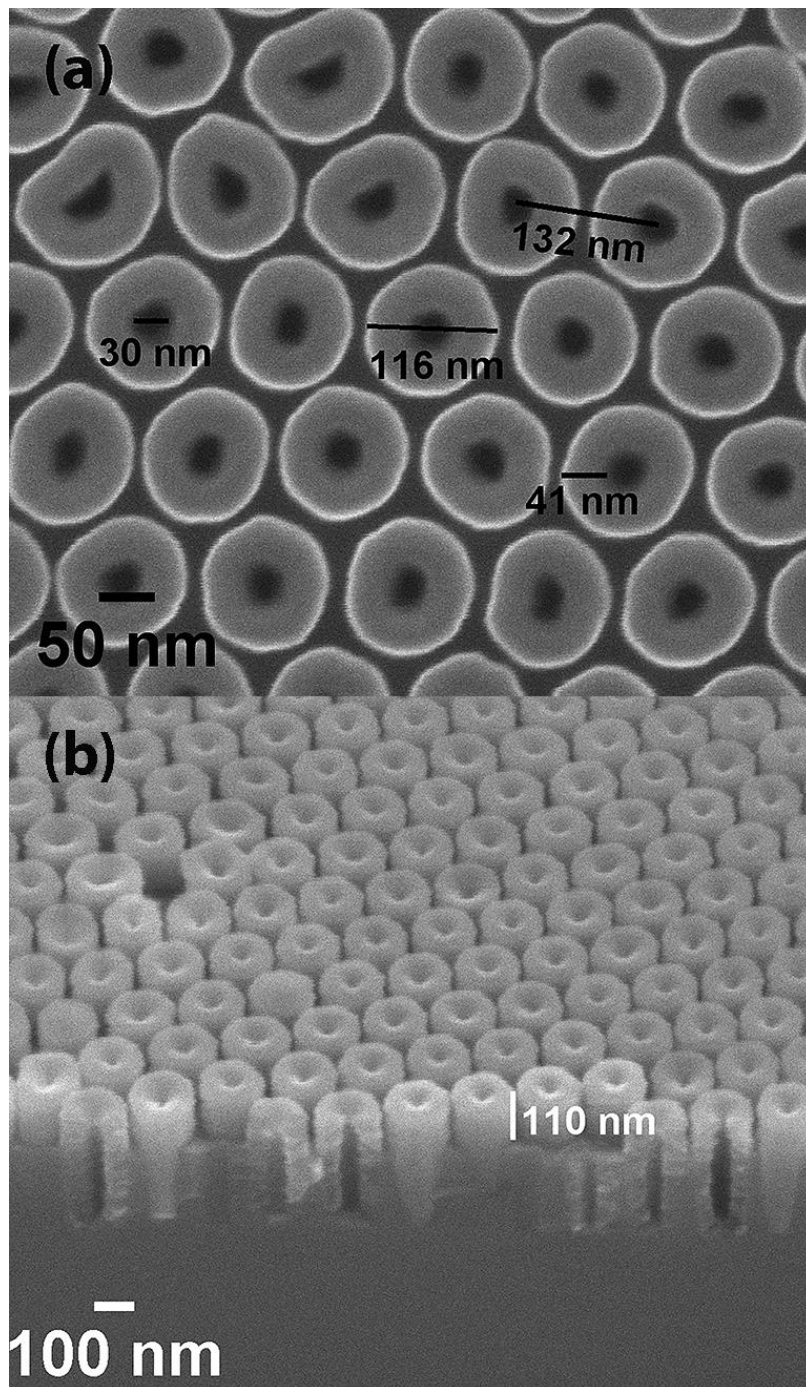


Figure 5.10: (a) Top view SEM image of AlN HNCs obtained after 5 sec of SF₆ based Si(100) etching revealing their morphology and dimensions, (b) cross-sectional image of same AlN HNCs showing the total height of nano-cylinders.

In order to further increase the height of AlN HNCs, a total of 7 sec Si etching was employed on a separate sample. Figure 5.8c and d shows the top-view and angled-view SEM images of AlN HNCs, respectively after 7 sec of SF₆ based Si etching, respectively. Long-range ordered AlN HNCs in well-organized arrays can be observed from top and cross sectional views. Nanocylinder diameter and internal pore size of AlN HNCs is determined to be ~115 nm and ~25 nm, respectively. The AlN wall thickness of individual nanocylinders and inter-pore distance were measured as ~45 and ~130 nm, respectively. The height of AlN HNCs (Fig. 5.8(d)) increased to ~170 nm after 7 sec of Si etching.

Internal morphology and crystalline structure of AlN HNCs are observed with TEM analysis as shown in Fig. 5.11. AlN HNCs exhibited hollow morphology and rather smooth outer walls (Fig. 5.11b). Similar to GaN HNCs, the uniformity degree of AlN HNCs wall thickness is limited. Thickness of AlN measured from two ends of AlN HNF is ~44 nm and ~31 nm which corresponds to a ± 13 % overall thickness non-uniformity. The total length of an individual AlN HNF was measured to be ~172 nm which agrees very well with SEM measurements. Several crystalline compartments of AlN can be observed from HR-TEM image of AlN HNC (Fig. 5.11c), implying polycrystalline structure of AlN, similar to the observations for GaN and InN HNC samples.

EDX elemental maps (Fig. 5.11d and e) were obtained to map the presence of aluminum and nitrogen from AlN HNCs. This colored EDX mapping shows that aluminum and nitrogen are uniformly present only at the place of AlN HNC in the scanned area. SAED pattern (Fig. 5.11f) was extracted from ~172 nm long AlN HNCs which shows multiple diffraction rings confirming the polycrystalline structure of AlN. Diameter of rings and calculated-theoretical interplanar spacing values are tabulated in table 5.2 revealing the presence of (100), (002), (101), (102), (110), (102), and (112) reflections of hexagonal AlN.

Table 5.2: SAED pattern analysis of AlN HNCs: comparison between measured and theoretical values of interplanar spacing (d_{hkl}) with corresponding crystallographic planes.

Diameter (nm^{-1})	Interplanar spacing, d_{hkl} (\AA)		Corresponding plane, hkl
	Calculated	Theoretical ^a	
7.504	2.665	2.6950	100
8.154	2.452	2.490	002
8.625	2.318	2.371	101
11.108	1.800	1.829	102
12.984	1.540	1.555	110
14.242	1.404	1.413	103
15.467	1.293	1.319	112

^aHexagonal AlN, ICDD reference code: 00-025-1133

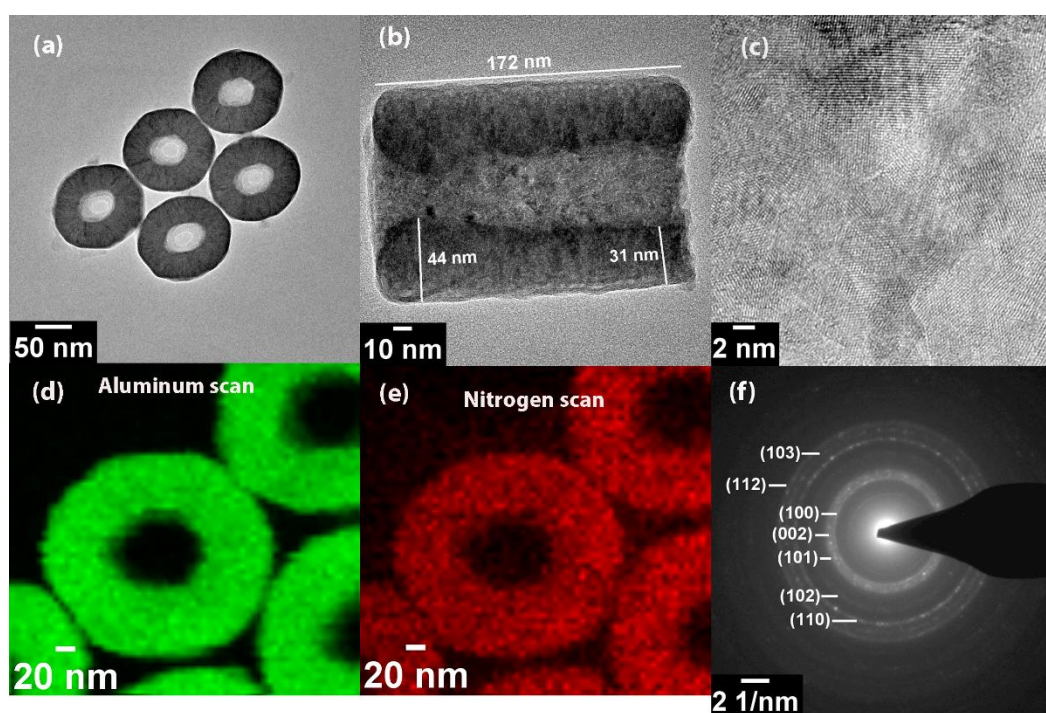


Figure 5.11: (a) TEM image of AlN HNCs, (b) TEM image of an individual AlN HNC revealing thickness and total length, (c) HR-TEM image of AlN HNC displaying internal crystal structure of AlN, (d) EDX elemental map of aluminum, (e) EDX elemental map of nitrogen, and (f) SAED pattern of AlN HNC samples.

The structural and chemical properties of AlN HNCs were studied using GIXRD and XPS. The structural properties of AlN HNCs were also examined by GIXRD (Fig. 5.12 a). Measurement was performed on ~173 nm long AlN HNCs integrated in Si substrate. For comparison, the GIXRD data was also gathered from ~50 nm thick AlN thin film deposited on Si and shown in Fig.

5.12b. Various reflections were observed from GIXRD spectrum of both thin film and HNCs which correspond to polycrystalline wurtzite structure of AlN. The exhibited patterns were indexed by hexagonal crystal system (ICDD reference code: 00-025-1133). The reflections detected from hexagonal wurtzite crystal system in both these spectrum are well supported by SAED diffraction patterns revealed in Fig. 5.11f and table 5.2.

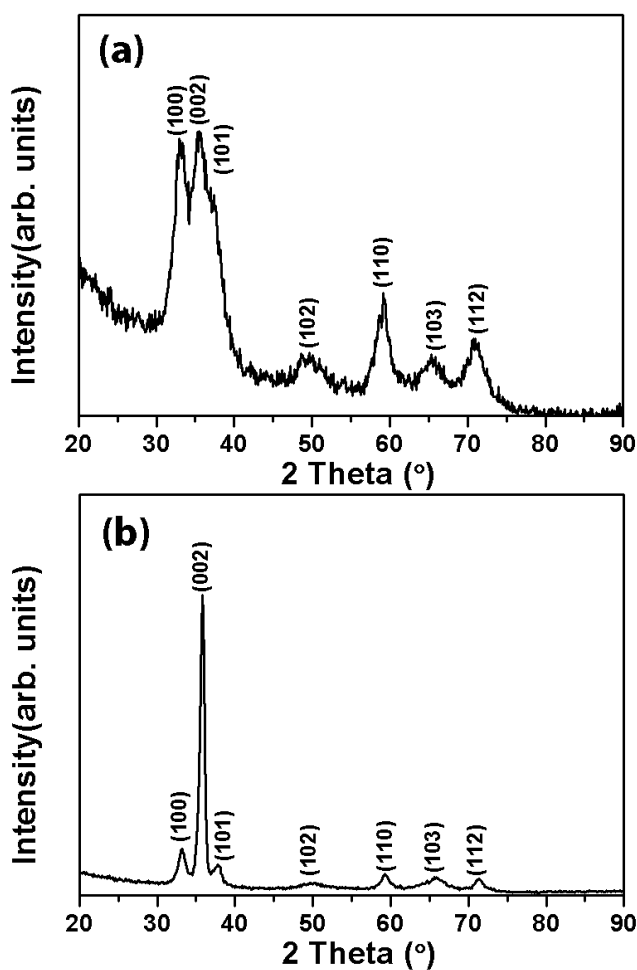


Figure 5.12: GIXRD pattern obtained from (a) ~173 nm long AlN HNCs, (b) ~50 nm thick AlN deposited on Si via HCPA-ALD.

XPS was used to examine the chemical composition and bonding states of AlN HNCs. XPS survey scan collected from top of ~172 nm long AlN HNCs revealed the presence of aluminum, nitrogen, carbon, fluorine, and oxygen elements. Atomic percentages of elements detected were as follows: 19.45 at. %

Al, 14.05 at. % N, 24.42 at. % C, 24.97 at. % F, and 17.12 at. % O. AlN thin film deposited with the same recipe had zero carbon content and 2 at. % O in bulk of the films.

The high-resolution XPS (HR-XPS) scans of Al 2p and N 1s are collected to investigate the bonding schemes of AlN HNCs and are presented in Figs. 5.13 (a) and (b), respectively. Based on asymmetry and FWHM of peaks, more than one type of bonding scheme was observed for both Al and N. Al 2p HR-XPS spectrum was fitted using two subpeaks located at 73.15 eV (subpeak#1) and 74.72 eV (subpeak#2) which were attributed to the Al-N and Al-O bonds, respectively.[32], [292], [293]

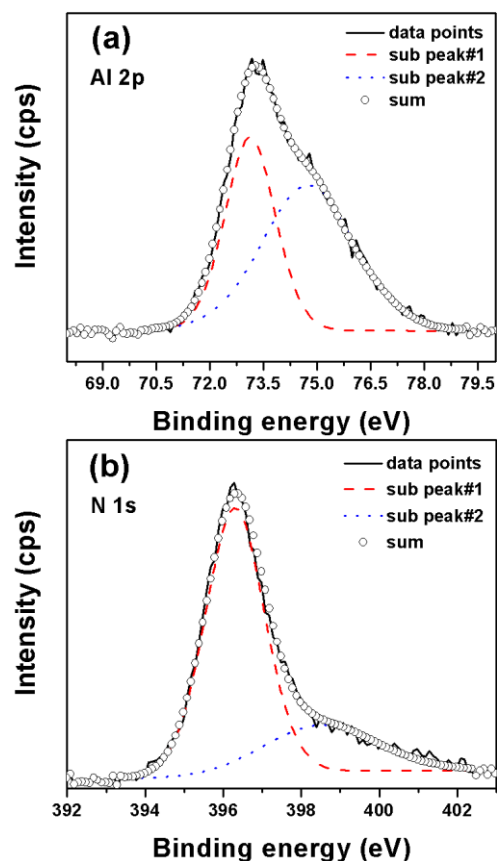


Figure 5.13: HR-XPS scans of (a) Al 2p and (b) N 1s obtained from ~173 nm long AlN HNCs revealing presence of different bonding schemes.

N 1s HR-XPS spectrum (Fig. 5.13 (b)) was fitted by two subpeaks located at 396.28 eV (subpeak#1) and 398.54 eV (subpeak#2) which were assigned to presence of N-Al and oxynitrides bonding species.[32], [292], [293]

5.3 InN Hollow Nanocylinder Arrays

700-cycle PA-ALD growth of InN was carried out on nanoporous Si template using an optimized recipe with TMI and N₂ plasma as indium and nitrogen sources, respectively. InN PA-ALD growth recipe that is utilized in this study was optimized for planar Si substrates and is reported else-where.[284] It was found that InN grown using N₂ plasma only as nitrogen precursor had decent crystalline quality with low impurity content. InN grown with other plasma combinations such as N₂/H₂ plasma as nitrogen precursor resulted in low density films with significant voids and weak surface adherence.

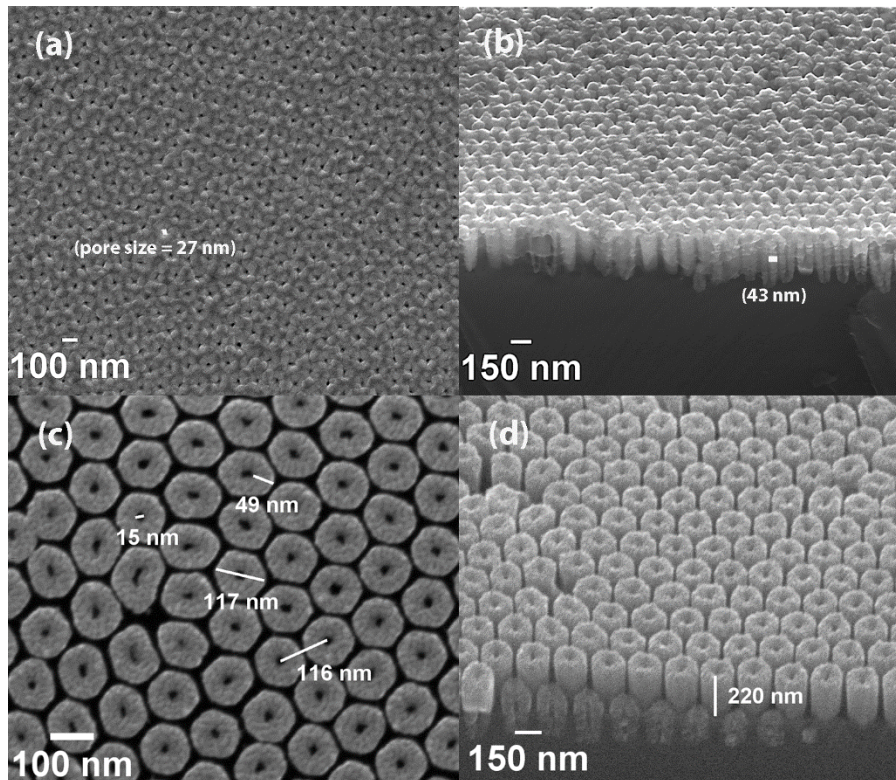


Figure 5.14: (a) Top view SEM image obtained from PA-ALD (700-cycle) grown InN on nanoporous Si substrate, (b) Angled-view SEM image of the same sample, (c) Top view SEM image of InN HNCs revealing their morphology and dimensions, and (d)

Angled-view SEM image of InN HNCs showing the free-standing height of InN nanocylinders.

Figure 5.14a and b show top and angled-view SEM images of InN-coated nanoporous Si templates, respectively. Highly uniform grainy structure of InN (Fig. 5.14a) is visible with relatively smooth surface morphology. The nanopores are still apparent, however pore size is significantly reduced (~25 nm) from original pore size in Si. Angled-view SEM image (Fig. 5.14b) reveals that InN is coated with high conformality along the wall depth of the pores. One can also observe that some of the initially narrower nanopores are indeed completely filled with InN, transforming these structures from hollow nanocylinders to nanopillars/nanorods. Wall thickness of InN nanocylinders was measured to be ~43 nm which is very close to the measured InN film thickness (~47 nm) on planar Si substrate grown during the same ALD experiment. This indicates that conformality of InN deposited on porous Si with a growth recipe optimized for planar Si substrate is substantially better when compared to the conformality performance of GaN.

InN grown on the horizontal Si surface of the nanoporous Si substrate has been etched away using Ar ion milling. Subsequent SEM imaging (Fig. 5.15) revealed complete removal of top InN layer after 3 minutes of Ar plasma exposure.

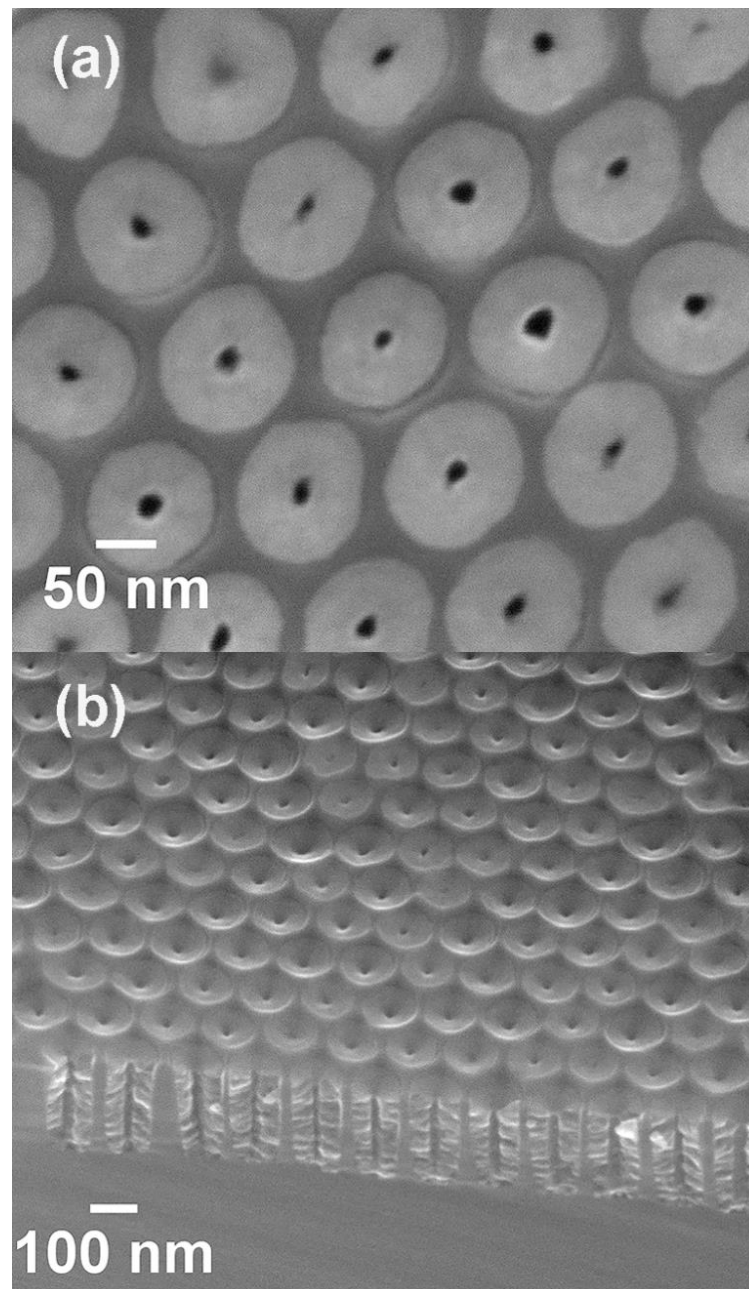


Figure 5.15: (a) Top view and (b) cross-sectional view SEM images obtained after 3 minutes of Ar plasma exposure successfully removed InN from top of nano-pores leaving InN integrated inside Si(100).

Similar to GaN HNCs fabrication strategy, SF₆ was utilized to selectively etch Si to obtain Si-integrated free-standing individual InN HNCs. Figure 5.14c and d show the top-view and angled-view SEM images of InN HNCs after 7 sec of SF₆ etching in RIE reactor, respectively. Both SEM images reveal long-range ordered and well-aligned InN HNC arrays. The wall thickness and pore diameter of individual InN nanocylinder are measured as ~50 and ~15 nm, respectively, while the pore-to-pore distance was found as ~115 nm. After 7 seconds of Si etching, the height of InN HNCs (Fig. 5.14d) was measured as ~220 nm. InN HNCs were also fabricated with 6 sec of Si etching using SF₆ followed by SEM imaging (Fig. 5.16). Nanocylinder diameter, pore size, wall thickness, and pore-to-pore distance (Fig. 5.16) of this set of HNCs were found to be similar with InN HNCs fabricated using 7 sec of Si etching. However, as expected, the height of InN HNCs fabricated using 6 sec of Si etching is reduced to ~170 nm. This result confirms that the final free-standing height of HNCs fabricated using this technique can be varied as desired by adjusting the etch time of Si in the final fabrication step.

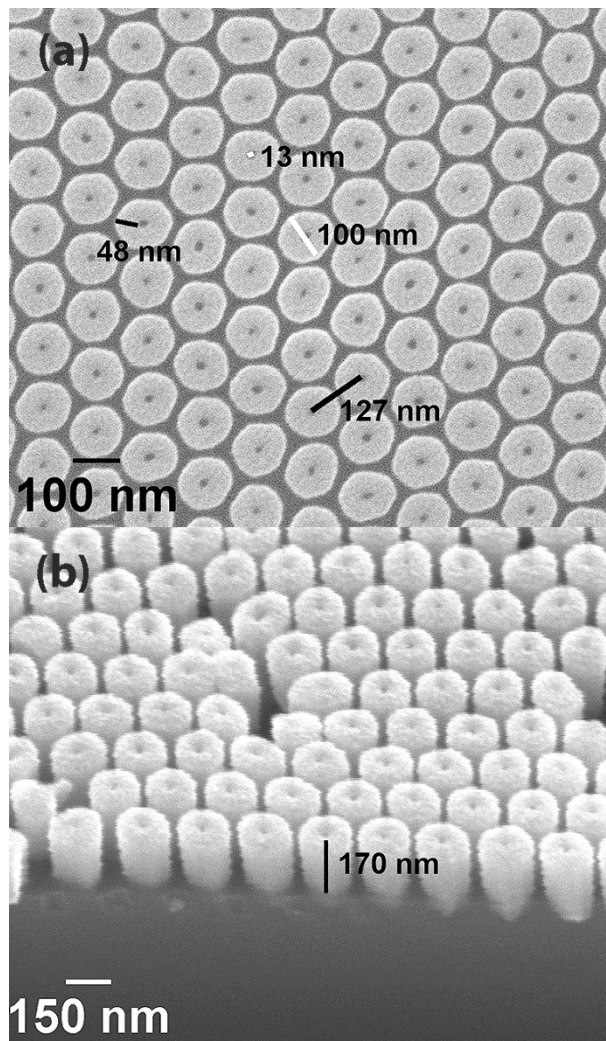


Figure 5.16: (a) Top view SEM image of InN HNCs obtained after 6 sec of SF₆ based Si(100) etching revealing their morphology and dimensions, (b) cross-sectional image of same InN HNCs showing the total height of nano-cylinders.

Internal morphology of InN HNCs can be observed in TEM images provided in Fig. 5.17. Figure 5.17a shows top-view of several InN HNCs with hollow internal morphology. The dimensions of HNCs such as cylinder diameter, pore size, wall thickness, and inter-pore distance seen in this TEM image are similar to observed dimensions in SEM images shown in Fig. 5.17.

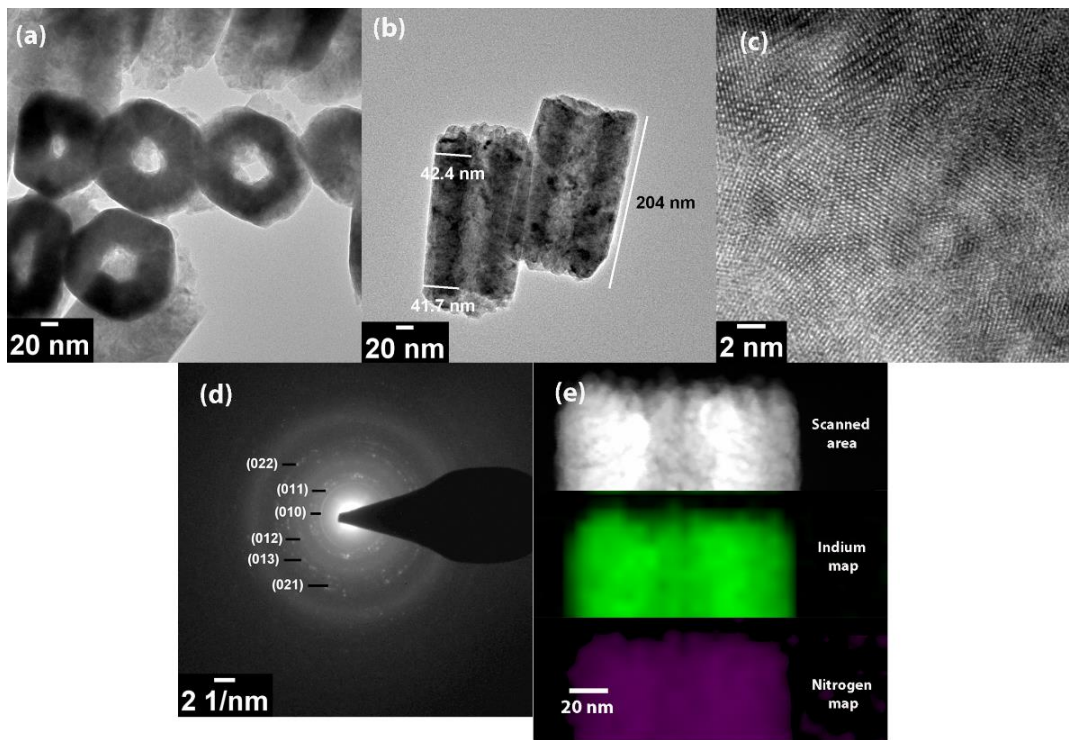


Figure 5.17: (a) TEM image of InN bundled HNCs, (b) TEM image of InN HNCs revealing their wall thickness and total length, (c) HR-TEM image of InN HNC displaying internal crystal structure and confirming the polycrystalline nature, (a) SAED pattern of InN HNCs, and (b) EDX elemental mapping of same sample.

Figure 5.17b shows TEM image of two HNCs. The length of InN HNC measured from this TEM image is ~ 204 nm which is close to the height observed from SEM image. It can be observed that the outer wall of HNCs is quite uniform along the cylinder axes. Contrary to GaN and AlN HNCs, the wall thickness of InN HNCs along the cylinder long axis is decently constant. Wall thickness measured from two ends of HNCs came out to as ~ 41.7 and ~ 42.4 nm which corresponds to less than ± 1.0 % variation in wall thickness along the height of the nanocylinder. This observation confirms the superior InN conformality compared to GaN counterparts. . It has been reported in the literature that recombination loss probability (r) of hydrogen radicals is generally higher than nitrogen radicals on different materials (on Si, 0.0016 vs 0.70 for nitrogen and hydrogen radicals respectively).²⁵⁵⁻²⁵⁷ This means, for instance, a hydrogen radical has higher probability to recombine with a hydrogen atom on the surface to form molecular hydrogen. This hydrogen

molecule will then have no further influence on the ALD surface reactions.²⁵⁷ As nitrogen-only plasma has been used for InN growth compared to N₂/H₂ plasma for GaN and AlN experiments, the observed enhanced conformality of InN can be partly attributed to lower recombination loss probability of nitrogen radicals.²⁵⁷

Figure 5.17c shows the HR-TEM image of a selected InN HNC. Several crystalline subsections of InN can be observed, while in each crystalline subsection, lattice fringes are organized in different orientations implying a polycrystalline structure. Figure 5.17d shows SAED pattern of InN HNCs which exhibit several diffraction rings confirming the polycrystalline structure of InN. The interplanar spacing (d_{hkl}) values of diffraction rings were calculated and compared with theoretical values to identify the associated crystallographic orientations. Table 5.3 shows that (010), (011), (012), (013), (021), and (022) reflections of hexagonal structure of polycrystalline InN are detected. Figure 5.17e shows EDX elemental maps of indium and nitrogen obtained from the InN HNCs sample. Indium and nitrogen show strong contrast in the colored maps which approve their uniform presence within the scanned area.

Table 5.3: SAED pattern analysis of InN HNCs: comparison between measured and theoretical values of interplanar spacing (d_{hkl}) with corresponding crystallographic planes.

Diameter (nm ⁻¹)	Interplanar spacing, d_{hkl} (Å)		Corresponding plane, hkl
	Calculated	Theoretical ^a	
6.501	3.076	3.062	010
7.396	2.704	2.698	011
9.850	2.030	2.088	012
12.455	1.605	1.616	013
13.708	1.459	1.478	021
15.047	1.329	1.349	022

^aHexagonal InN, ICDD reference code: 00-050-1239

The structural and chemical properties of InN HNCs were further investigated by GIXRD and XPS analysis.

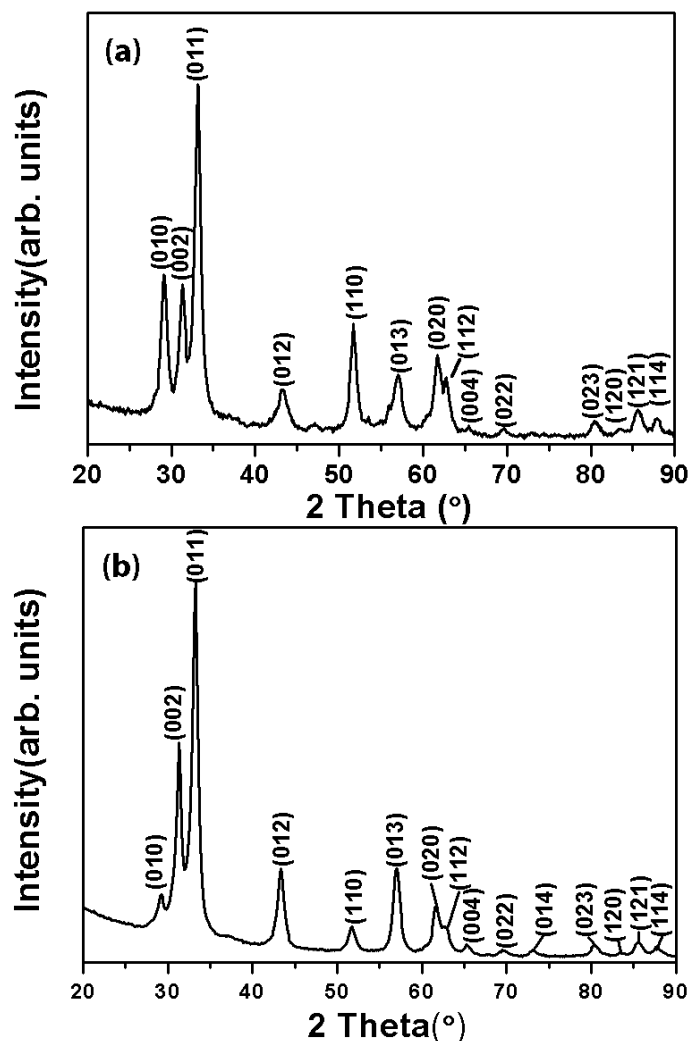


Figure 5.18: GIXRD pattern obtained from (a) ~210 nm long InN HNCs, (b) ~47 nm thick InN deposited on Si via HCPA-ALD.

The structural properties of InN HNCs were further investigated by GIXRD (Fig. 5.18). Measurement was performed on ~210 nm long InN HNCs integrated in Si substrate. For comparison, the GIXRD measurement obtained from ~47 nm thick InN thin film deposited on Si is also provided. Various reflections of polycrystalline wurtzite structure of InN are visible in the recorded GIXRD spectrum for both thin film and HNCs. The exhibited patterns were indexed by hexagonal crystal system (ICDD reference code: 00-050-1239). The reflections detected from hexagonal wurtzite crystal system in both these spectrum are well supported by SAED diffraction patterns.

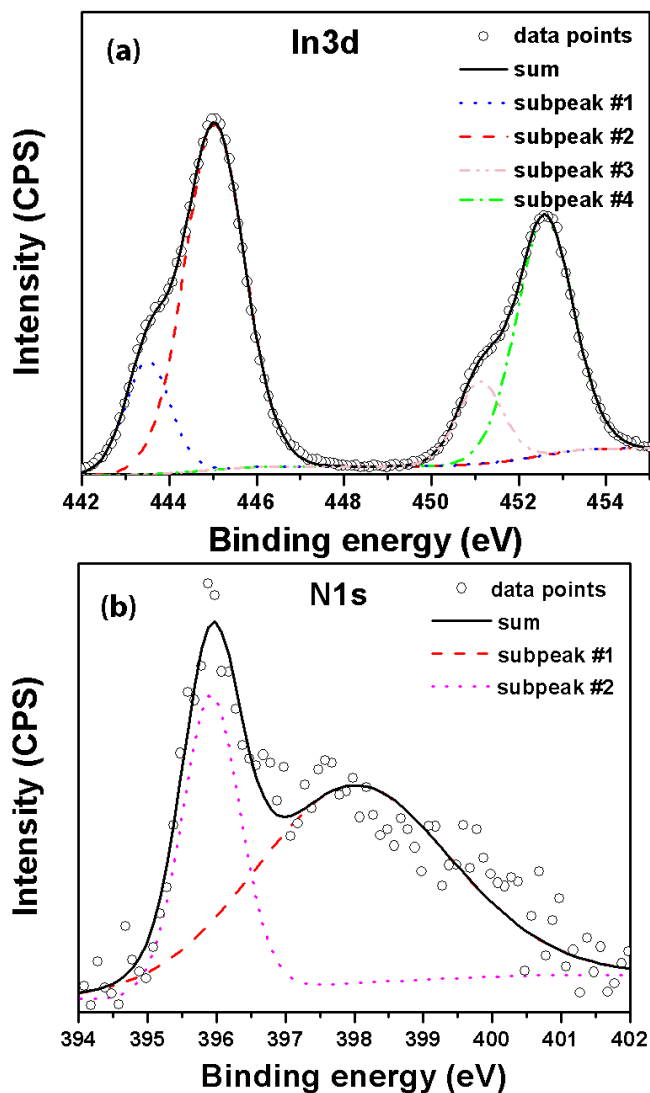


Figure 5.19: HR-XPS scans of (a) In 3d and (b) N 1s obtained from ~210 nm long InN HNCs revealing presence of different bonding schemes.

XPS was conducted to analyze the elemental composition and chemical bonding states of the InN HNCs. Atomic percentages of elements detected from InN HNCs were as following: 11.08 at. % In, 9.34 at. % N, 33.65 at. % C, 10.51 at. % F, and 35.41 at. % O. From the bulk of InN thin film grown with HCPA-ALD using the same growth parameters used in this study, 2.1 % O and 3.05 % C were detected. Figure 5.19 (a) and (b) shows HR-XPS scans of In 3d and N 1s, respectively, both of which were obtained from ~210 nm long InN HNCs. In 3d spectrum reveals In 3d_{5/2} and In 3d_{3/2} spin orbit doublet and considering their unsymmetrical nature, both these peaks have been deconvoluted in to two Gaussians. The first subpeak of In 3d_{5/2} spin orbit located at 443.50 belongs to

In-N bond while the second subpeak originating at 445.04 eV corresponds to In-O bond.[284], [294], [295] In $3d_{3/2}$ spin orbit was deconvoluted into two subpeaks detected at 451.09 and 452.68 eV which are associated with In-N and In-O bonds, respectively. In both these spin orbits, the subpeak having larger area among the two belongs to In-O species. In a previous report, In 3d HR-XPS spectrum obtained from bulk of HCPA-ALD grown InN thin film showed the same In $3d_{5/2}$ and In $3d_{3/2}$ spin orbit doublet which have been deconvoluted in two subpeaks each.[284] In that case, the larger subpeak of these spin orbits belonged to In-N bonding species which showed that In-O bonding content is significantly less than In-N bonding species in the bulk of the InN film. In the present case, In 3d spectrum obtained from surface of InN HNCs reveals that In-O bonding content is greater than In-N in the first few lateral nm of HNCs. N1s HR-XPS spectra obtained from InN HNCs is deconvoluted into two sub-peaks as shown in the Fig. 5.19(b). Based on the reported literature, we conclude that first subpeak in N1s spectra detected at 395.93 eV is attributed to the N-In while shoulder peak located at 397.96 eV is attributed to the presence of oxynitrides.[284], [294], [295]

Chapter 6

Area Selective Atomic Layer Deposition of Metal Oxides Using Polymer Growth Inhibition Layers

This chapter presents the results of AS-ALD of metal oxides using polymers (PMMA, PVP, and fluorocarbons) as growth inhibition layers followed by metal oxide thin films patterning on Si substrates. In first part of the chapter, AS-ALD results of ZnO, HfO₂, and Al₂O₃ using fluorocarbon layers are presented. While, in the second part of the chapter, AS-ALD results of TiO₂ using fluorocarbons, PMMA, and PVP are presented.

6.1 AS-ALD of ZnO, HfO₂, and Al₂O₃ Using Plasma Polymerized Fluorocarbon Growth Inhibition Layer

A ~32 nm thick plasma polymerized fluorocarbon layer was deposited on Si(100) using ICP reactor. The polymer film is believed to be formed by the plasma fragmentation of C₄F₈ monomers into CF_x radicals resulting in the

polymer deposition. Elemental composition and chemical bonding states of plasma polymerized fluorocarbon layer deposited on Si (100) was first investigated by XPS. The spectrum of XPS survey scan and high resolution scans of fluorine and carbon are presented in Fig. 6.1. Survey scan (Fig. 6.1a) revealed the presence of F 1s, C 1s, and O 1s peaks having relative atomic concentrations of 54.51 %, 43.91 %, and 1.57 %, respectively. The fluorine to carbon ratio (F/C) is found to be 1.24. Chemical bonding states in the polymer film were studied by the evaluation of F 1s and C 1s HR-XPS scans and are presented in Fig. 6.1 (b) and (c). HR-XPS Scan of F 1s spectrum shows a single symmetric peak at 689.73 eV which corresponds to C-F covalent bond. HR-XPS scan of C 1s shows various bonding schemes which are assigned to different chemical states (Fig. 6.1c). C 1s HR-XPS spectra has been deconvoluted into four sub peaks, which are assigned to C-CF (288.50 eV), CF (290.77 eV), CF₂ (292.80 eV), and CF₃ (294.60 eV) components.[298] The ability of the plasma polymerized fluorocarbon layer to block deposition against ZnO, HfO₂, and Al₂O₃ ALD was evaluated next by performing contact angle, XPS, spectroscopic ellipsometer, and HR-SEM measurements. As reference control sample, metal oxide films were also grown simultaneously on O₂ plasma treated Si (100). The purpose of pre-deposition O₂ plasma treatment was to impart high concentration of OH groups on Si, which are well-known to prevent nucleation delay at the initial stages of ALD growth.

Figure 6.2 (a) shows the variation in contact angle of Si(100) and fluorocarbon/Si surfaces with the increase in ZnO ALD growth cycles. The contact angle of bare fluorocarbon/Si was measured as 114° which indicates the hydrophobic nature of grown polymer film. On the other hand, contact angle of bare Si (100) was measured as 71°. The contact angle of fluorocarbon/Si film doesn't change noticeably till 136 growth cycles of ZnO. After 102 growth cycles of ZnO on fluorocarbon/Si (100), contact angle was measured as 110.5° which decreases to 104.2° after 136-cycle growth. This slight decrease of contact angle suggests the onset of ZnO nucleation on fluorocarbon/Si after 136 cycles of ZnO growth. With further increase in growth cycles from 136 to 202,

the contact angle decreases remarkably and falls down to 64° . This result shows that ZnO growth initiates around 136 ALD cycles due to degradation of the hydrophobic nature of fluorocarbon polymer layer. On the contrary, the contact angle of Si surface changes from 71° to 49° when exposed to 34 cycles of ZnO growth and remains stable until 202 growth cycles where it exhibits a slight increase. Figure 6.2b shows the change in ZnO thickness with the increase in number of growth cycles on Si(100) and fluorocarbon/Si. Thickness of ZnO increases linearly after nucleation onset with the increase in number of growth cycles which is typically observed for ALD processes. The growth per cycle (GPC) of ZnO on Si(100) is measured as $\sim 1.3\text{-}1.4 \text{ \AA}$. On fluorocarbon/Si, no growth of ZnO is observed until 102 ALD cycles while a very thin layer of $\sim 1.5 \text{ nm}$ ZnO was measured after the 136th cycle. With further increase in growth cycles, the growth rate of ZnO on fluorocarbon/Si becomes similar as on bare Si(100). The ellipsometer measurements are consistent with the contact angle measurements, which confirms ZnO growth inhibition on fluorocarbon/Si(100) up to 102 ALD growth cycles.

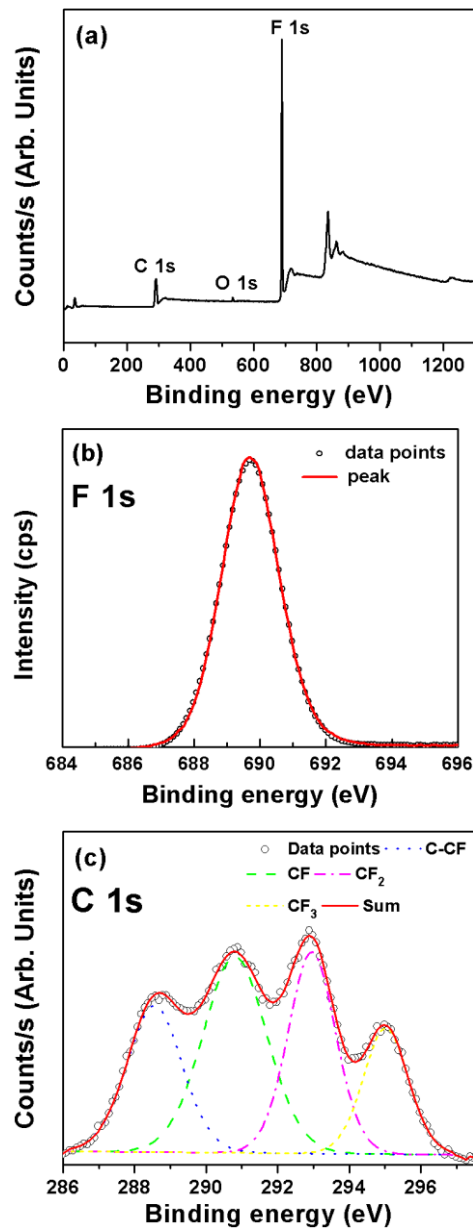


Figure 6.1: (a) XPS survey scan obtained from a ~32 nm thick plasma polymerized fluorocarbon thin film deposited on Si(100). High resolution XPS scans of (b) F 1s and (c) C 1s obtained from the same film.

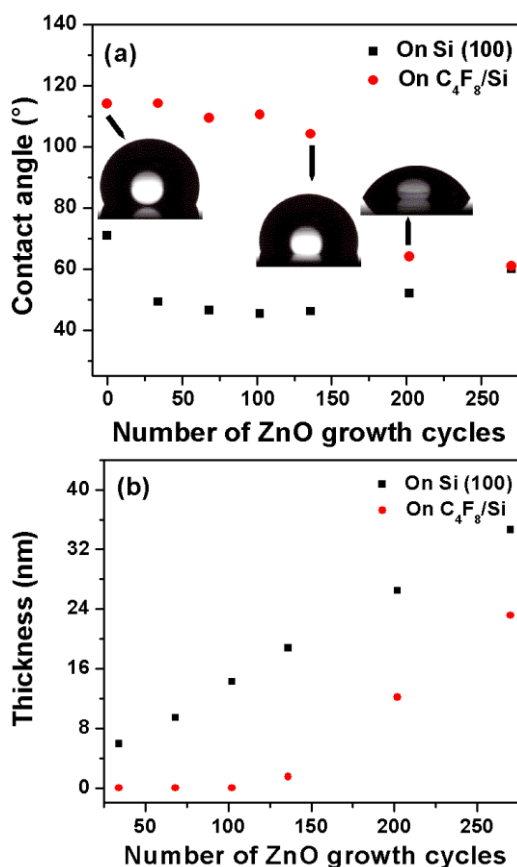


Figure 6.2: Variation in contact angle (a) and thickness (b) of ZnO with the increase in number of growth cycles on Si (100) and fluorocarbon/Si.

To confirm the ZnO blocking ability of plasma polymerized fluorocarbon layer, XPS measurements (Fig. 6.3) were conducted on Si(100) and fluorocarbon/Si substrates exposed with different number of ALD cycles. Survey scans from the surface of ZnO films grown on Si(100) (Fig. 6.3a) indicated the presence of zinc, oxygen, and carbon with Zn 2p₃, O 1s, and C 1s peaks, respectively. ZnO samples with different number of ALD cycles on Si(100) reveal the same peaks of Zn 2p₃, O 1s, and C 1s. Figure 6.3b shows the XPS survey scans obtained from fluorocarbon coated substrates exposed to ALD growth cycles starting from 34 up to 270. Only F 1s and C 1s peaks are observed until 102 growth cycles which are originating from the plasma polymerized fluorocarbon layer. Although no Zn signal was observed up to 102 cycles, a small Zn signal appeared at 136 cycles confirming the initiation of ZnO growth

on fluorocarbon/Si. A meaningful Zn 2p_{3/2} peak begins to appear with 202 ALD cycles and remains stable for further growth cycles. The fact that F 1s peak disappears abruptly after 136 ZnO ALD cycles supports the nucleation onset.

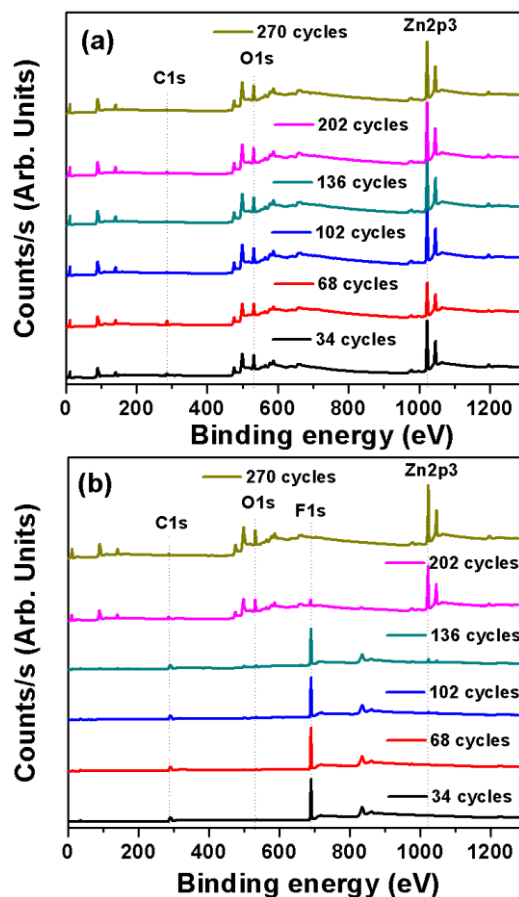


Figure 6.3: XPS survey scans of ZnO grown with different number of ALD cycles on (a) Si(100) and (b) fluorocarbon/Si revealing presence of different elements.

These results further verify the contact angle and ellipsometer measurements and show that ZnO growth initiates around 136 ALD cycles and that plasma polymerized fluorocarbon layer is effectively blocking ZnO growth up to ~130 ALD cycles. Table 6.1 provides a direct comparison of atomic percentages (at. %) of Zn from ZnO grown on Si(100) and fluorocarbon/Si which are evaluated from the quantification of XPS survey scans. A notable rise in Zn at. % is observed only after 136 ZnO ALD growth cycles on fluorocarbon/Si. Zn at. % remains steady at a value around ~36-37 at. % on ZnO/Si with zinc to oxygen ratio (Zn/O) of ~0.86-0.88.

Table 6.1: Variation in Zn at. % with the increase in number of ZnO growth cycles on Si(100) and fluorocarbon/Si.

Number of growth cycles	Zn at. % on fluorocarbon/Si	Zn at. % on Si(100)
34	-	31.28
68	-	24.2
102	-	36.3
136	1.62	37.02
202	24.72	37.54
270	37.58	37.89

High resolution XPS scans of Zn $2p_{3/2}$ state have been acquired to extract the formed bonding configuration and verification of XPS survey scans. Figure 6.4 shows the HR-XPS Zn $2p_{3/2}$ scans obtained from ZnO grown on fluorocarbon/Si with different number of growth cycles. No clear peak is observed for Zn $2p_{3/2}$ scan up to 102 ALD cycles, while a weak and rather broad peak is observed for 136 growth cycles of ZnO on fluorocarbon/Si. There is a drastic increase in Zn $2p_{3/2}$ peak intensity as the number of growth cycles reach 202. Indeed a clear well-established Zn $2p_{3/2}$ peak is observed at 202nd and 270th ALD cycles on fluorocarbon/Si. This peak is observed at a binding energy value of 1022.12 eV and corresponds to the Zn-O bond.[299] These results show excellent correlation with all the characterization results provided so far.

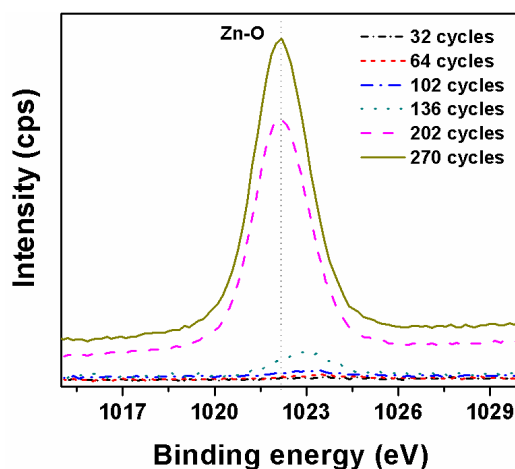


Figure 6.4: HR-XPS scans of Zn $2p_{3/2}$ obtained from ZnO grown on fluorocarbon/Si as a function of ALD growth cycles.

SEM imaging was performed to observe the surface morphology of ZnO grown on Si and fluorocarbon/Si. Figure 6.5a and b show the SEM images of bare fluorocarbon/Si and ZnO grown on fluorocarbon/Si with 68 number of growth cycles, respectively. These SEM images reveal the uniform surface morphology of fluorocarbon layer and illustrate no observable growth of ZnO on fluorocarbon/Si after 68 growth cycles. Figure 6.6a and b show the SEM images of ZnO grown with 102 cycles of growth on fluorocarbon/Si and Si (100), respectively. Very few ZnO nuclei begin to form on fluorocarbon/Si surface after 102 ALD cycles, while the grainy structure of ZnO is clearly visible on Si(100) with the same number of ZnO growth cycles. As XPS didn't detect any ZnO on fluorocarbon/Si up to 102 cycles, the observed ZnO nuclei might possibly be below the detection limit of XPS. Figure 6.6c and d shows the SEM images of 136-cycle ZnO on fluorocarbon/Si and Si. The quantity of ZnO nuclei notably increased after 136 growth cycles on fluorocarbon/Si with significantly larger areal coverage, while relatively larger grains are observed on its counterpart ZnO on Si (100). Based on contact angle, spectroscopic ellipsometer, XPS, and SEM measurements presented above, we conclude that plasma-polymerized fluorocarbon layer is effective in blocking ZnO growth up to more than 100 ALD cycles.

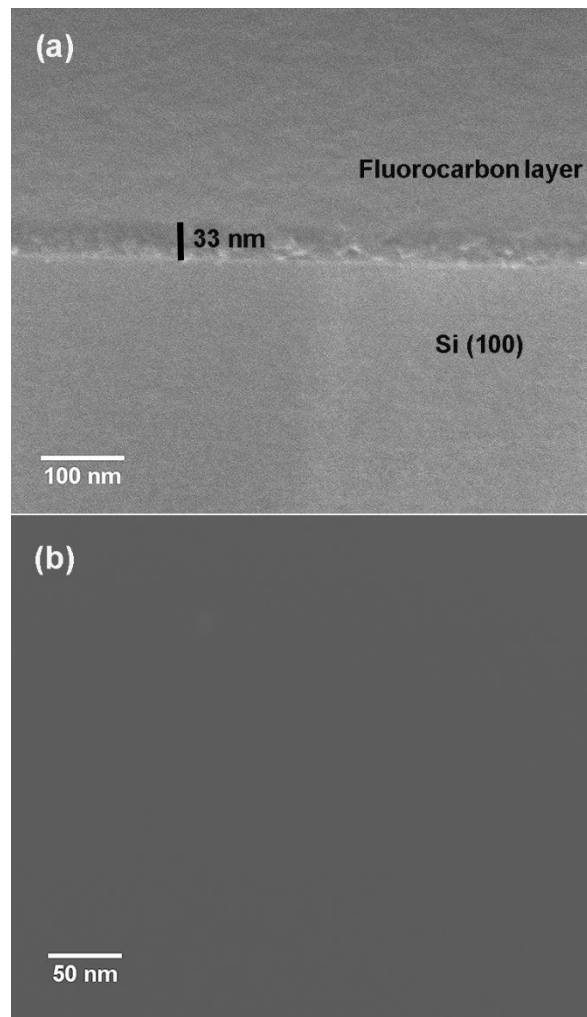


Figure 6.5: SEM images of (a) bare fluorocarbon/Si sample, (b) ZnO coated on fluorocarbon/Si sample with 68 number of growth cycles.

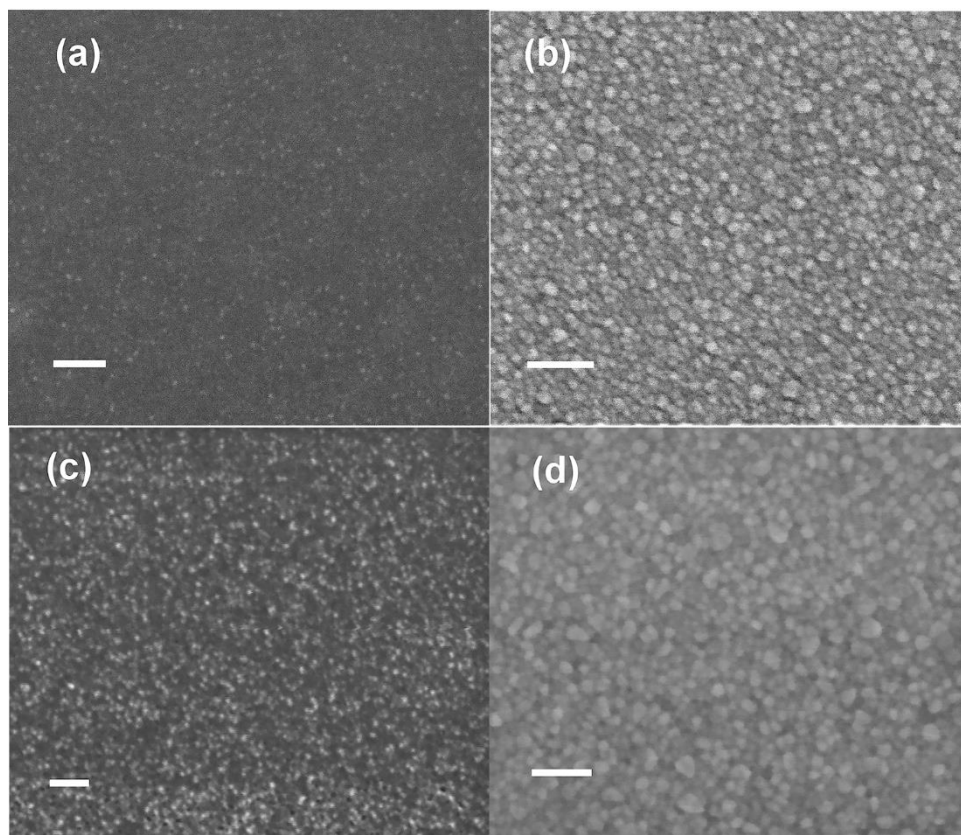


Figure 6.6: Plan view SEM images of 102 cycles ALD grown ZnO on (a) fluorocarbon/Si and (b) Si (100); 136 cycles ALD grown ZnO on (c) fluorocarbon/Si and (d) Si (100) (all scale bars = 50 nm).

We have also investigated the blocking/inhibition ability of plasma-polymerized fluorocarbon layer against other metal oxide materials including HfO_2 and Al_2O_3 . HfO_2 and Al_2O_3 growth have been performed in the same reactor with thermal ALD using various number of ALD cycles on plasma polymerized fluorocarbon layer coated on Si(100) and on bare Si(100) substrates. Contact angle, spectroscopic ellipsometer, and XPS measurements have similarly been performed to investigate the HfO_2 and Al_2O_3 growth selectivity on plasma polymerized fluorocarbon layer. Figure 6.7 shows the contact angle and thickness variation of ALD grown HfO_2 on fluorocarbon/Si(100) and Si(100) as a function of total number of growth cycles. Both Si(100) and fluorocarbon/Si show an abrupt decrease in contact angle (Fig. 6.7a) after 50 cycles of HfO_2 growth. A slight increase in contact angle is

observed for 100 cycles of HfO₂ growth on Si(100) and fluorocarbon/Si and then it becomes nearly constant for both the substrates. Figure 6.7b shows change in thickness of ALD grown HfO₂ on fluorocarbon/Si and Si(100) with the increase in number of growth cycles. The thickness of HfO₂ on Si(100) increases linearly with the increase in number of growth cycles and the GPC is measured as ~0.95-1.00 Å. On the other hand, growth rate of HfO₂ is substantially less on fluorocarbon/Si in the first 100 cycles of growth in contrast with Si(100). With the increase in number of cycles beyond 100, GPC of HfO₂ on fluorocarbon/Si becomes similar as on Si(100). It is evident from Fig. 6.7b that the slope of HfO₂ thickness increase (GPC) on fluorocarbon/Si is less up to 100 cycles while it increases beyond that and becomes same as GPC on Si(100). These results reveal that initial nucleation of HfO₂ is considerably slower on fluorocarbon/Si up to 100 cycles, where GPC equals the GPC on bare Si surface after sufficient coverage of HfO₂ is achieved.

XPS measurements are conducted on HfO₂ grown on Si(100) and fluorocarbon/Si(100) and recorded survey scans are presented in Fig 6.8a and b, which indicate the presence of Hf 4f, C 1s, and O 1s peaks from HfO₂ grown on both substrate surfaces. However, peak intensity of Hf 4f obtained from HfO₂ grown with 50 cycles on fluorocarbon/Si is notably lower than the corresponding peak seen on Si(100) with same number of growth cycles.

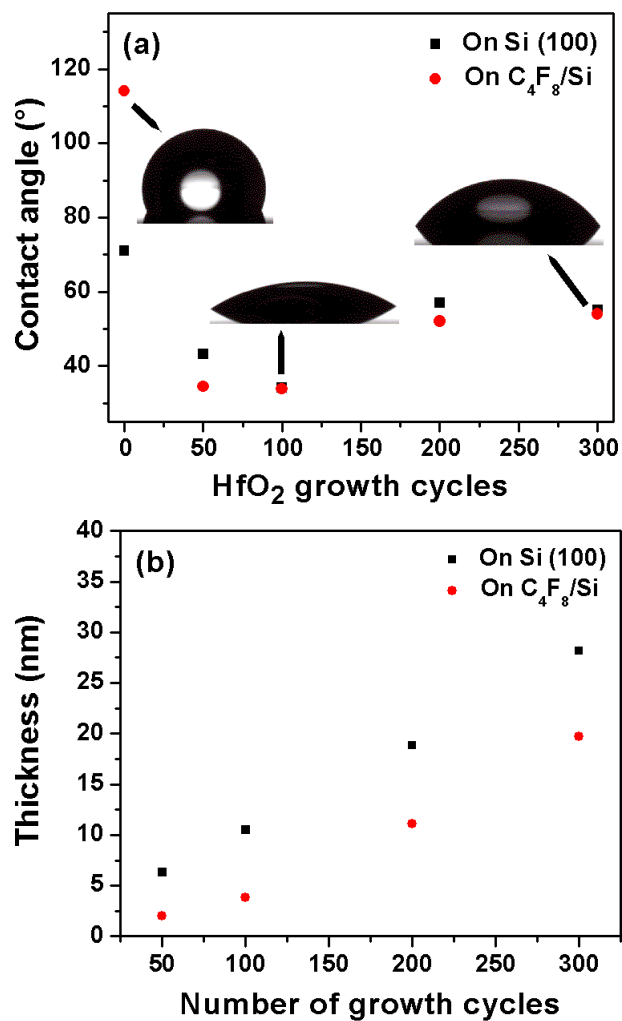


Figure 6.7: Variation in (a) contact angle and (b) thickness of HfO₂ as a function of ALD growth cycles on Si(100) and fluorocarbon/Si.

Atomic percentages obtained from quantification of these survey scans are provided in Table 6.2. These results verify the contact angle and ellipsometer measurements results and confirm that HfO₂ nucleation is relatively slower on fluorocarbon/Si within the initial growth cycles.

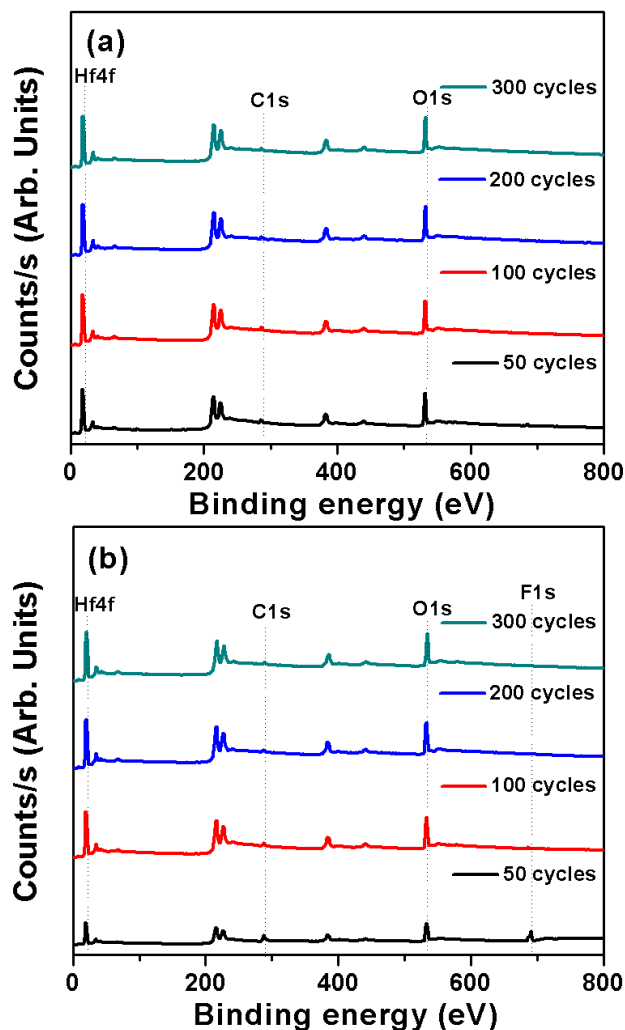


Figure 6.8: XPS survey scans of HfO₂ grown with different number of growth cycles on (a) Si (100) and (b) fluorocarbon/Si revealing presence of different elements.

Table 6.2: Variation in Hf at. % with the increase in number of HfO₂ growth cycles on Si (100) and fluorocarbon/Si

Number of growth cycles	Hf at. % on fluorocarbon/Si	Hf at. % on Si (100)
50	10.53	22.82
100	24.89	26.81
200	27.04	27.12
300	27.6	27.99

A similar set of experiments have been conducted for Al_2O_3 grown on fluorocarbon/Si and Si(100). Figure 6.9 shows the variation of contact angle and thickness with the number of ALD growth cycles on both substrates. In contrary to ZnO and HfO_2 , an immediate sharp decrease in contact angle has been observed for Al_2O_3 on both fluorocarbon/Si and Si(100), stabilizing at a value of $\sim 37\text{-}45^\circ$. A direct relation in alumina thickness and number of ALD cycles can be noticed from Fig. 6.9b with an alumina GPC slightly less on fluorocarbon/Si than on Si(100). XPS measurements have been conducted on Al_2O_3 grown on fluorocarbon/Si and Si(100) and survey scans have been presented in Fig 6.10a and b. Al 2p, C1s, and O1s peaks have been observed from films grown on both substrates. Al quantification from these survey scans have been presented in Table 6.3 which shows the significant presence of Al on all the substrates. These results support the observations of contact angle and spectroscopic ellipsometer measurements and reveal that plasma polymerized fluorocarbon layer is rather ineffective in blocking alumina growth. It has been observed that blocking ability of a particular layer for successful AS-ALD might depend on ALD processing conditions such as precursor employed, working pressure, purge time, and substrate temperature. In addition to ALD processing conditions, blocking capability of the fluorocarbon layer may also depend on plasma polymerization conditions such as plasma energy, working pressure, and flow rate of feed gas. Although plasma polymerized fluorocarbon layer shows superior growth blocking/inhibition feature for ZnO ALD process, it may further be optimized along with ALD process conditions in order to achieve growth selectivity for HfO_2 and Al_2O_3 as well. Moreover, the achieved maximum number of ALD cycles before ZnO nucleation takes over might be further extended with a systematic study in which ICP polymerization and ALD process conditions are optimized.

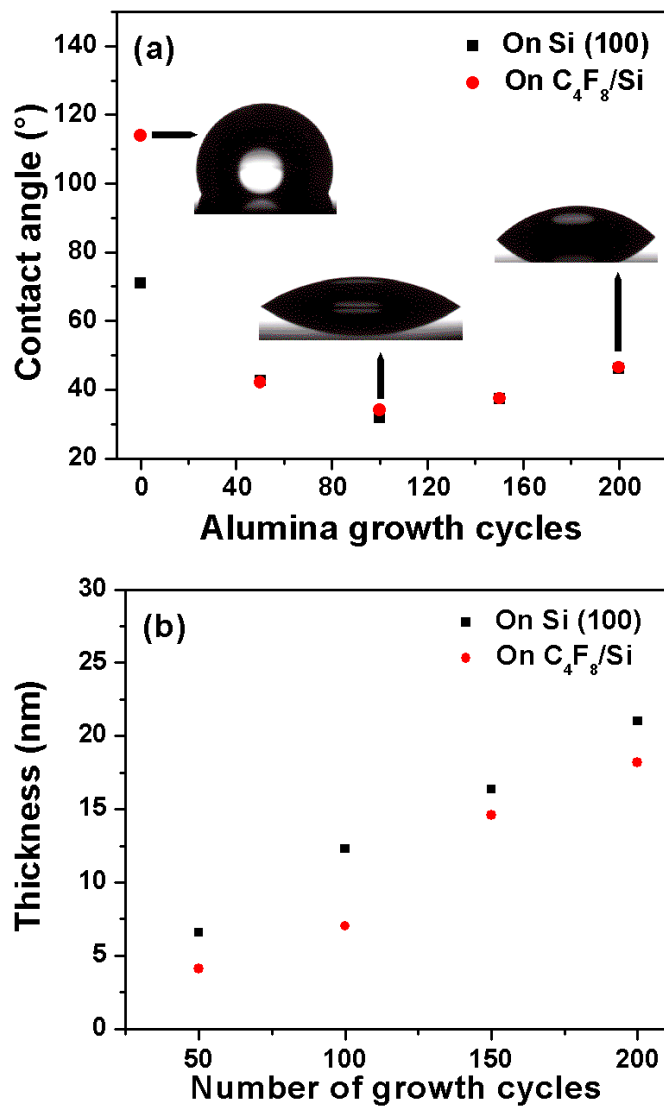


Figure 6.9: Variation in (a) contact angle and (b) thickness of Al₂O₃ with the increase in number of growth cycles on Si(100) and fluorocarbon/Si.

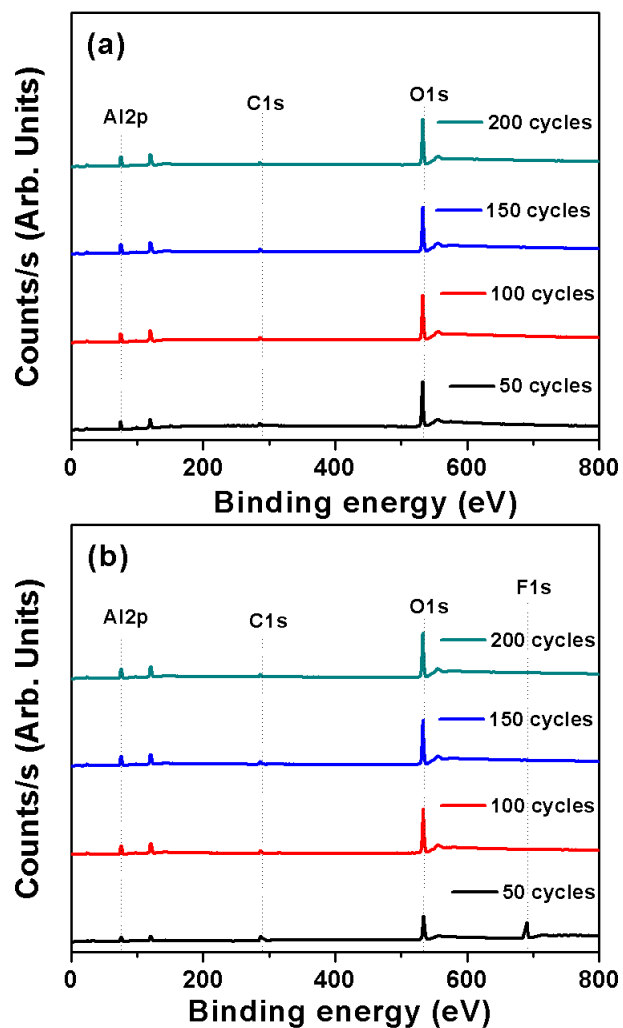


Figure 6.10: XPS survey scans of Al₂O₃ grown with different number of growth cycles on (a) Si (100) and (b) fluorocarbon/Si revealing presence of different elements.

Table 6.3: Variation in Al at. % with the increase in number of Al₂O₃ growth cycles on Si (100) and fluorocarbon/Si

Number of growth cycles	Al at. % on fluorocarbon/Si	Al at. % on Si (100)
50	21.08	32.96
100	38.11	39.66
150	39.43	39.54
200	39.99	40.37

After demonstrating the ability of plasma polymerized fluorocarbon layer to inhibit ZnO ALD growth, the next step was to employ fluorocarbon layer for patterning of ALD grown ZnO. Photolithography was used to prepare bare Si and fluorocarbon/Si checkerboard and line pattern structures in a sequential manner. Figure 6.11a shows a plan-view SEM image of 102 cycle ZnO ALD grown on fluorocarbon layer line patterns. The darker squares represent the areas where fluorocarbon layer is present, while bright areas represent the ZnO grown surface. Inset of Fig. 6.11a shows HR-SEM image from the interface of dark and bright areas, which reveals the grainy structure of ZnO only from fluorocarbon uncoated area while negligible ZnO grains were observed on fluorocarbon layer. Similarly, Fig. 6.11b shows a plan-view SEM image of 102 cycle ZnO ALD grown on fluorocarbon checkerboard patterns. HR-SEM image obtained from the interface of coated and uncoated fluorocarbon regions reveal that grainy structure of ZnO is only present on bare Si region.

XPS line scan was performed on a 2 mm wide ZnO coated patterned fluorocarbon/Si lines. The minimum spot size of X-rays that could be utilized was $\sim 100\ \mu\text{m}$; therefore, patterned lines of 2 mm width were selected for analysis in order to gather the data from various points. A line across an area of interest is selected on the sample and the XPS gathered data along the line at various points. Zn 2p intensity was measured in terms of counts per second vs spatial location along the line and presented in Fig. 6.11c. Clearly, higher intensity of Zn 2p peak is only observed at location of ZnO pattern while intensity at other points was equal to back ground intensity confirming the successful pattern placement of ZnO.

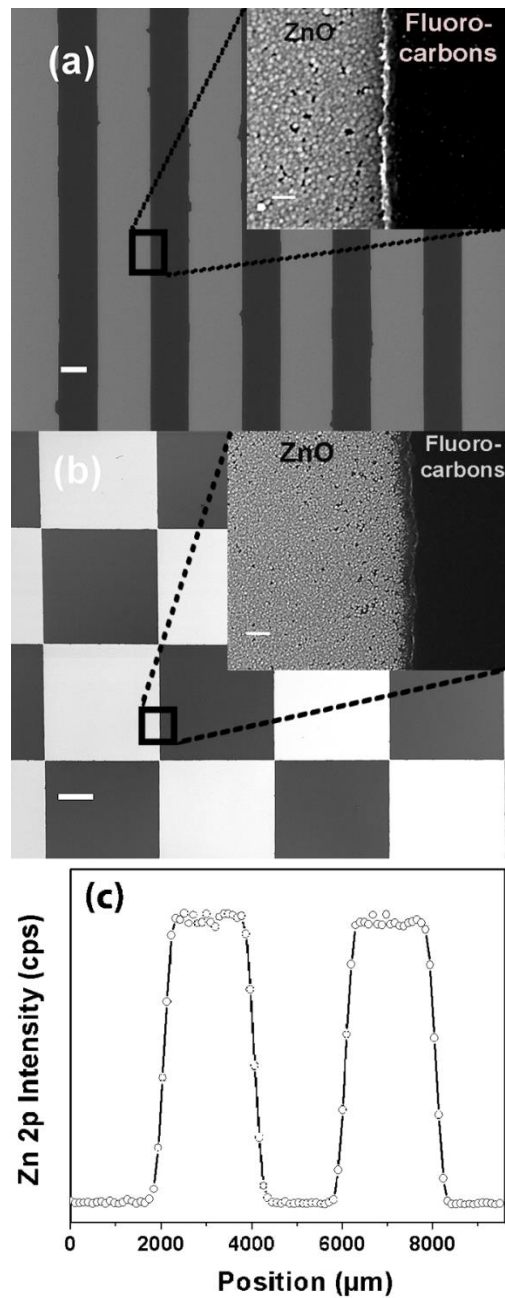


Figure 6.11: (a) Plan-view SEM image of 102 cycle ZnO ALD grown on fluorocarbon line patterns (scale bar = 10 μm) (inset) HR-SEM image from the interface of ZnO and fluorocarbon layer (scale bar = 50 nm). (b) Plan-view SEM image of 102 cycle ZnO ALD grown on fluorocarbon checker board patterns (scale bar = 150 μm) (inset) HR-SEM image from the interface of ZnO and fluorocarbon layer (scale bar = 100 nm). (c) XPS line scan obtained from patterned ZnO substrate.

6.2 Nanoscale Selective Area Atomic Layer Deposition of TiO₂ Using E-beam Patterned Polymers

In order to determine the most efficient surface for nucleation and growth inhibition of TiO₂, deposition was carried out on CF_x, PMMA, and PVP. Contact angle, spectroscopic ellipsometer, XPS, and SEM measurements were performed to investigate the ALD-TiO₂ growth behavior. PMMA and PVP were spin coated while CF_x layer was coated on Si substrates via ICP polymerization using C₄F₈ feed gas.

Figure 6.12 shows the variation in contact angle and thickness of TiO₂ with the increase in number of growth cycles on CF_x, PMMA, PVP, and Si(100). As PVP is soluble in water and other polar solvents, contact angle measurements using water as a solvent would not provide accurate results. Hence, contact angle measurements were only performed on CF_x, PMMA, and Si(100). Initial contact angle of CF_x, PMMA, and Si(100) was measured as 114°, 74°, and 71°, respectively. Contact angle of Si(100) and CF_x samples decreased to ~35° as soon as they were exposed to 100 cycles of TiO₂ growth. With further increase in TiO₂ growth cycles, contact angle rises again and stabilizes around ~62-63° till 1200 cycles. On the other hand, PMMA exhibits quite stable contact angle values around ~73°, almost independent of the number of TiO₂ ALD cycles. The fact that contact angle of PMMA doesn't change with TiO₂ growth cycles suggests that PMMA is efficiently blocking TiO₂ film growth. To confirm this observation, ellipsometric film thickness measurements were carried out. Figure 6.12b shows the evolution of TiO₂ thickness on different surfaces as a function of ALD-growth cycles. As anticipated with conventional ALD growth processes, a linear increase in thickness of TiO₂ is observed on Si(100) with a GPC of ~0.5 Å. TiO₂ thickness increase on CF_x is also linear and nearly matches with the TiO₂ growth rate on Si(100), which indicates that the initially

hydrophobic plasma polymerized CF_x layer is rather ineffective in blocking TiO_2 growth. On the other hand, no growth of TiO_2 is observed on PVP layers up to 300 cycles, while a very thin TiO_2 layer (~ 1.29 nm) is detected at 400 cycles, signaling the nucleation initiation at this growth stage on PVP coatings. With the further increase in ALD cycles beyond 400, TiO_2 eventually nucleates on PVP surface, where after the growth rate becomes similar as on Si(100).

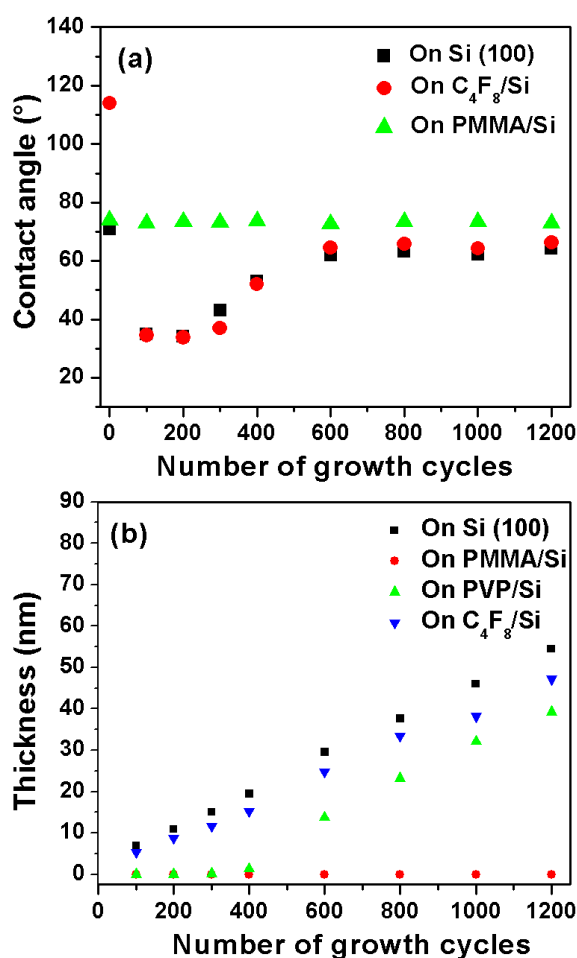


Figure 6.12: Variation in (a) contact angle and (b) thickness of TiO_2 with number of growth cycles on PMMA, PVP, C_4F_8 coatings, and reference Si(100) substrate.

This result suggests that PVP surface is successful in blocking/delaying the TiO_2 growth for more than 300 cycles which corresponds to an effective film thickness of ~ 15 nm on Si surface. For PMMA-coated samples, we have observed that TiO_2 doesn't nucleate on PMMA surface at all, and no film

growth is detected up to 1200 ALD cycles. These results indicate that PMMA is the most effective surface for TiO_2 growth inhibition among the coatings/surfaces studied.

Previous studies on AS-ALD established a direct correlation between surface energy and water contact angle to the growth inhibition ability of SAMs. In a case study of AS-ALD of HfO_2 with SAMs, it has been reported that only ODTs with a sufficiently high water contact angle is effective in blocking nucleation. Short or branched chained SAMs with low water contact angle were not able to inhibit nucleation of HfO_2 . [296] In another study of AS-ALD of TiO_2 with mixed SAM surfaces, it was observed that extent of nucleation increases with decreasing surface energy or water contact angle of SAM surfaces. [297] Higher contact angle of SAM surfaces was only possible for well-packed SAM structures and degree of packing is an important parameter in AS-ALD processes using SAMs. High degree of packing prevents the ALD precursor access to reactive sites on Si substrates while superior hydrophobicity of SAMs prohibits the chemisorption of water which in turn blocks the nucleation of desired material. On the basis of these previous studies, one would expect CF_x to show the highest nucleation delay due to its hydrophobic character and initially high contact angle. However, contact angle and spectroscopic ellipsometer measurements contradicts this prediction and show that TiO_2 nucleates on CF_x with relative ease, showing almost no nucleation delay. PMMA, on the other hand, with a water contact angle significantly smaller than C_4F_8 , is quite effectively blocking TiO_2 growth. Therefore, these results indicate that attaining successful AS-ALD depends on mainly two critical factors: (i) Polymer blocking layer should be able to provide a sufficient barrier for ALD precursors to reach active sites on the surface, (ii) Undesired reactions between inhibition layer and the ALD precursors must be avoided. In order to perform elemental quantification, XPS measurements were conducted on TiO_2 grown on PMMA, PVP, Si(100), and CF_x as a function of ALD cycles up to 1200. Figure 6.13 shows XPS survey scans from TiO_2 grown on PMMA and PVP coatings. Only C1s and O1s peaks are detected from PMMA surface till 1200 cycles of TiO_2

growth. Absence of any Ti peak confirms that PMMA successfully abstain itself from TiO_2 nucleation. Only C1s and O1s peaks are detected on PVP up to 300 cycles of TiO_2 growth, where after Ti2p peak is observed. Figure 6.14 shows XPS survey scans from TiO_2 grown on CF_x and Si(100). C1s, Ti2p, and O1s peaks are observed from TiO_2 grown on CF_x/Si , while F1s peak is observed from the same substrate only with 100 cycles of TiO_2 growth. As anticipated, TiO_2 growth on Si(100) reveals the peaks of C1s, Ti2p, and O1s regardless of number of ALD cycles. These results confirm the rather quick nucleation of TiO_2 and ineffective blocking behavior of both Si and CF_x -coated surfaces.

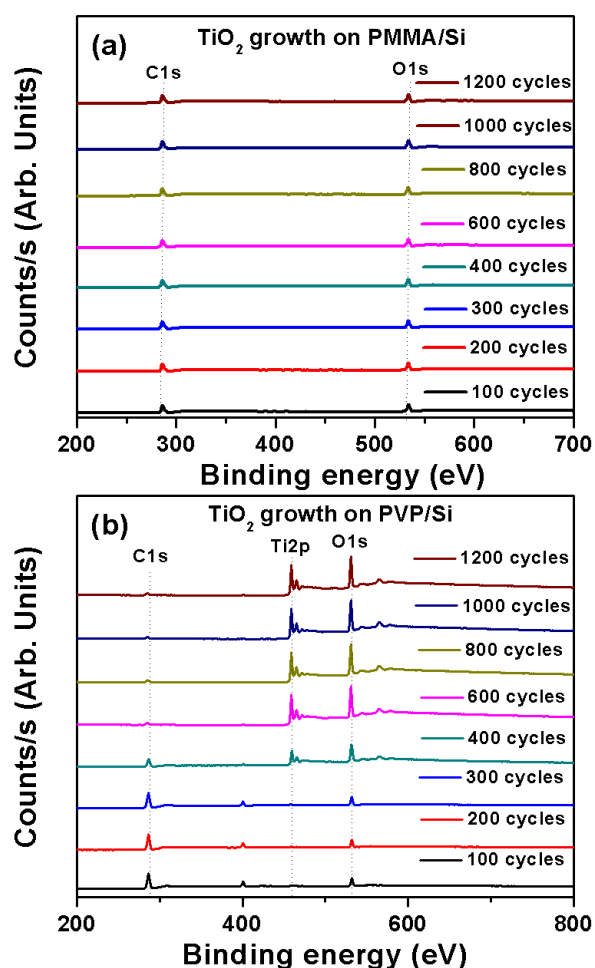


Figure 6.13: XPS survey scans of TiO_2 grown with different number of ALD cycles on (a) PMMA and (b) PVP surface, confirming the effective inhibition/blocking of these layers up to more than 1200 and 300 cycles, respectively.

Table 6.4: Variation in Ti at. % with the increase in number of TiO₂ ALD-growth cycles.

Number of ALD cycles	Ti at. % on C ₄ F ₈ /Si	Ti at. % on Si(100)	Ti at. % on PMMA/Si(100)	Ti at. % on PVP/Si(100)
100	14.06	21.23	0	0
200	21.69	23.95	0	0.92
300	22.73	23.32	0	1.15
400	23.23	23.33	0	17.25
600	22.15	25.32	0	24.93
800	24.82	25.23	0	24.82
1000	23.58	25.21	0	23.52
1200	24.52	24.21	0	24.25

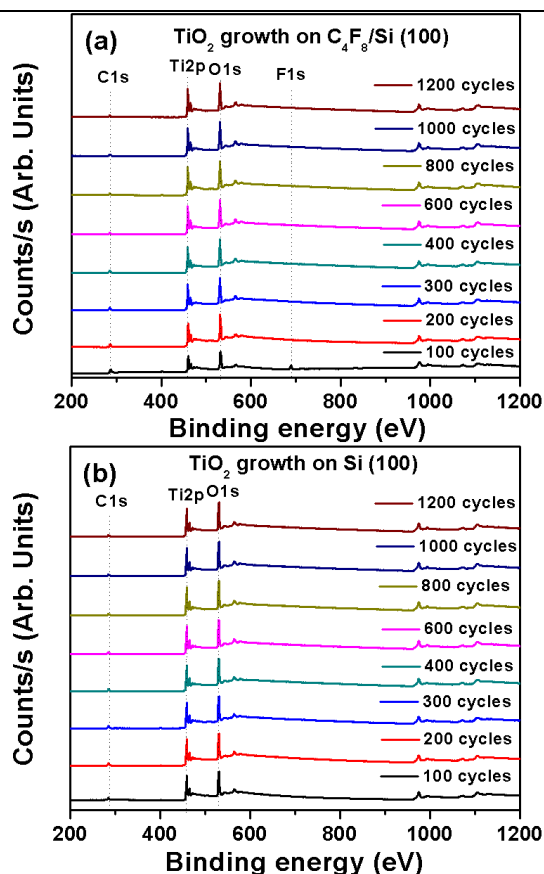


Figure 6.14: XPS survey scans of TiO₂ grown with different number of ALD cycles on (a) CF₈/Si and (b) Si(100) revealing the presence of similar elemental composition almost independent of film growth stage, confirming a non-delayed TiO₂ deposition on both surfaces.

Quantification of Ti in terms of atomic percentages (at. %) from survey scans from all four surfaces studied is summarized in Table 6.4. These XPS survey scan results provide an excellent correlation with contact angle and ellipsometer measurements and approve the following important conclusions: (i) PMMA successfully blocks/inhibits the TiO₂ deposition for at least 1200 growth cycles, which is equivalent to a blocking film thickness of ~55 nm (ii) PVP blocks TiO₂ growth up to 300 ALD cycles and further increase in growth cycles eventually leads to nucleation of TiO₂ on PVP, (iii) CF_x is unable to inhibit TiO₂ nucleation and growth, despite its higher initial contact angle.

Another important observation was the decrease in PMMA film thickness with number of TiO₂ ALD cycles, which is presented in Table 6.5. We had chosen the substrate temperature as 150 °C which is slightly below the glass transition temperature ($T_g = 108-167$ °C) of PMMA. Decrease in PMMA thickness might be partly due to residual solvent removal during excessively long growth periods. In addition to inherent unreactive nature of PMMA, this slight decrease in thickness of PMMA can possibly aid in achieving a better selectivity.

Table 6.5: Decrease in thickness of PMMA with the increase in number of TiO₂ growth cycles.

Number of TiO ₂ cycles	Thickness of PMMA
0	43 nm
100	42.91
200	41.516
300	37.561
400	35.45
600	33.99
800	32.84
1000	27.40
1200	23.96

Figure 6.15 shows the Ti2p high resolution (HR)-XPS scans obtained from TiO₂ grown on PMMA and PVP with various number of ALD cycles. In accordance with the observations made by XPS survey scans, no Ti2p peak is detected from PMMA samples regardless of the number of ALD-growth cycles and on PVP up to 300 ALD cycles. Ti2p_{3/2} and Ti2p_{1/2} peaks are observed at a binding energy of 458.99 and 464.80 eV for 400 and 600-cycle TiO₂ respectively, grown on PVP/Si. These peaks are in agreement with the literature reports where Ti2p_{3/2} and Ti2p_{1/2} peaks are typically observed from TiO₂ at a binding energy value of 458.5 – 458.9 and 463.7 – 464.2 eV, respectively, which are assigned to the distinct Ti⁴⁺ chemical state of Ti in TiO₂.^[300] Same Ti2p peaks are observed for PVP samples with TiO₂ ALD cycle numbers higher than 600.

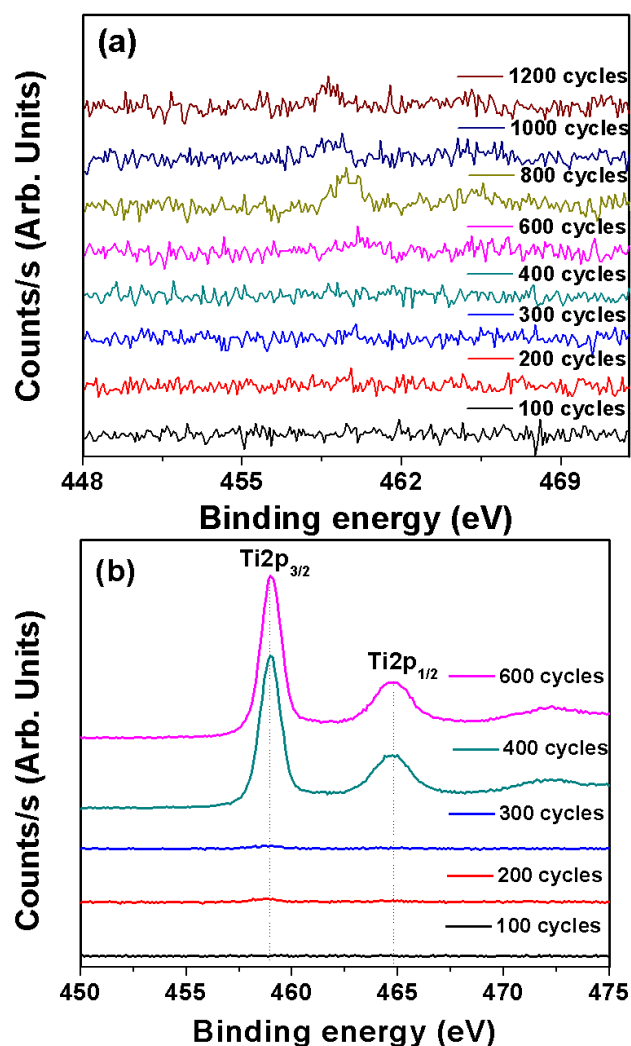


Figure 6.15: HR-XPS survey scans of Ti2p obtained from TiO₂ at different stages of ALD-growth on (a) PMMA/Si(100) and (b) PVP/Si(100).

SEM imaging was performed to observe the surface morphology of TiO₂ grown on Si(100) and PMMA/Si(100) after 1200 ALD cycles. During spin coating of PMMA, a part of Si substrate was deliberately covered by scotch tape, which was taken off before growth to observe the interface of TiO₂/Si and PMMA/Si. Figure 6.16 reveals the surface morphology of TiO₂ (1200 growth cycles) grown on Si(100) and on the interface of TiO₂/Si-PMMA/Si. 1200-cycle TiO₂ grown on Si(100) (Fig. 6.16a) exhibits its grainy surface structure with 5-10 nm sized grains. A boundary (Fig. 6.16b) is clearly visible at the interface of TiO₂/Si and PMMA/Si, where relatively large sized grains are observed at

border on Si(100) side and PMMA surface confirms the absence of TiO₂ film growth.

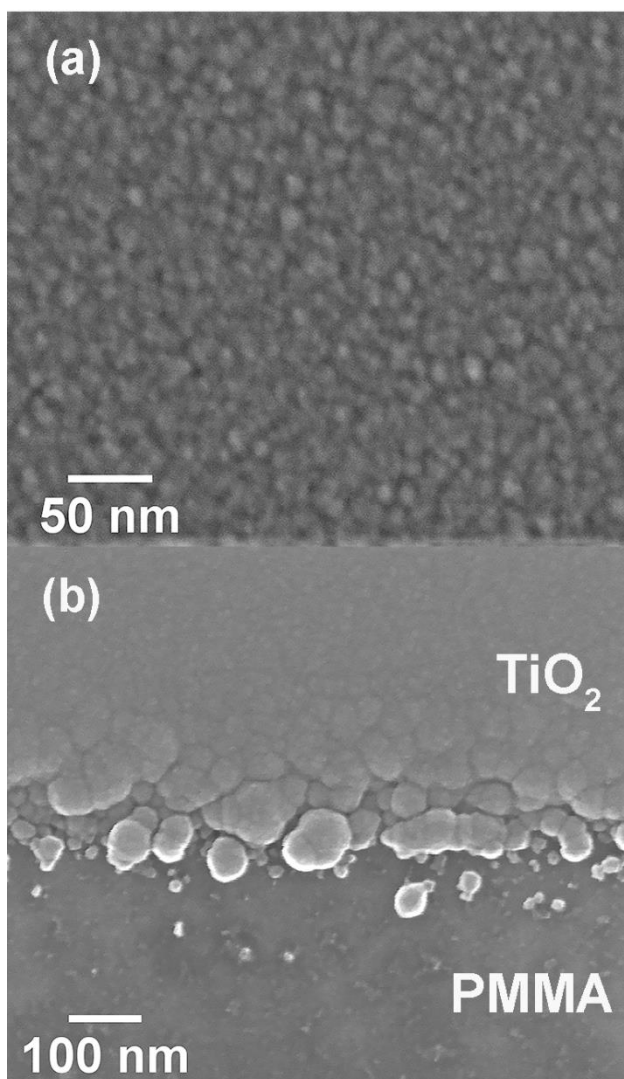


Figure 6.16: SEM images of PMMA/Si surface after 1200-cycle TiO₂ growth (a) Si(100) substrate surface (b) the interface of Si(100) and PMMA showing the effective inhibition at the PMMA side.

Utilization of polymer films for AS-ALD studies brings an extra advantage which is their facile removal after the selective deposition process is completed. PMMA can be easily dissolved in acetone while PVP is soluble in water. After the growth of TiO₂ on PMMA with various number of growth cycles, all the samples were rinsed in acetone for 30 seconds followed by XPS measurements (Fig. 6.17). XPS measurements revealed the presence of O1s, C1s and Si2p

peaks with the similar peak intensity from all samples after PMMA removal. Appearance of Si2p peaks from all samples makes it clear that we were successful in dissolving PMMA. It also signifies the importance of utilization of those precursors for AS-ALD processes that do not react with the polymer masking materials.

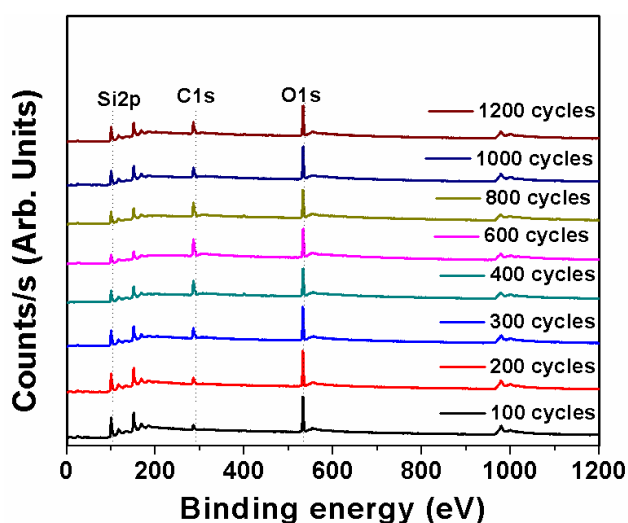


Figure 6.17: XPS survey scans from sample surface after acetone treatment of PMMA layer subsequent to TiO₂ ALD cycles, confirming the facile and complete removal of polymeric blocking layer even for 1200 growth cycles at a substrate temperature of 150 °C.

Otherwise, precursors may diffuse into the polymer masking material and consequently making the removal of PMMA much more difficult and even not possible at all. Precursor exposure time is also very critical in avoiding the diffusion of ALD precursors into polymers and reaching the reactive sites on the substrate. In exposure mode (a trademark of Ultratech/Cambridge Nanotech Inc.), dynamic vacuum was switched to static vacuum just before the precursor and oxidant pulses, and switched back to dynamic vacuum before the purging periods after waiting for some time, i.e., exposure time. Time scale for precursor diffusion can be decreased by decreasing the pulse length or exposure time of precursor, however, this might result in sub-saturation precursor exposure of the surface leading to less than the optimized growth rate. We have also performed TiO₂ growth on PMMA by increasing the exposure time of TDMAT to 40 sec and indeed observed film growth of TiO₂ on PMMA. In the present case,

TDMAT doesn't react with PMMA within the optimized pulse length of TDMAT which makes removal of PMMA with acetone a straightforward job. We also attempted to dissolve PVP in water after TiO₂ growth, however PVP was dissolved in water up to 300 growth cycles, whereas PVP removal beyond 300 ALD cycles were not successful.

Based on contact angle, spectroscopic ellipsometer, XPS, and SEM measurements, we confidently conclude that PMMA is the most suitable blocking layer for AS-ALD of TiO₂ using TDMAT and H₂O as Ti and O precursors, respectively. Hence, we selected PMMA to demonstrate the micron and sub-micron scale patterning of TiO₂ using e-beam lithography.

PMMA is by far the most commonly used e-beam lithography resist as it offers nm-scale high resolution, ease of handling, and wide process latitude. Exposure of e-beam to PMMA results in the breakage of its long chain into smaller soluble fragments, which dramatically renders it soluble in a subsequent development step. Utilization of PMMA as a common e-beam resist presents an inherent advantage to use it as a blocking layer for AS-ALD; i.e., it can be patterned to produce nm scale patterns. E-beam lithography was performed on PMMA coated Si(100) samples to produce mm, μm, and nm scale patterns of TiO₂. Figure 6.18a shows the SEM image of post-developed PMMA after exposure to e-beam revealing patterned PMMA free regions of Si. TiO₂ was grown on this e-beam exposed PMMA using 750 cycles of ALD growth at 150 °C. Samples were dipped in acetone for 30 seconds, rinsed, and dried, where after they were loaded into the SEM chamber for imaging. Figure 6.18b shows the SEM image of patterned TiO₂ after removal of PMMA. Growth only occurred at e-beam exposed PMMA free regions of samples and TiO₂ lines having diameter of ~740-750 nm can be clearly observed. Figure 6.18c shows the TiO₂ lines prepared using the same strategy, however narrower line-widths of ~150-160 nm were produced. The debris observed between the TiO₂ lines in Fig. 6.18c is most probably the residue left after PMMA removal. Figure 6.18d

is the SEM image from the interface of the patterned TiO₂ and Si(100) revealing the grainy structure of TiO₂.

XPS and EDX elemental line scan was performed to study the linear elemental variation along the TiO₂ patterns and presented in Fig. 6.19. XPS line scan was performed on mm-scale TiO₂ patterns due to limitation of X-ray spot size (minimum ~100 μm). A line across an area of interest is selected on the sample and the XPS gathered data periodically along this line. Ti 2p intensity was measured in terms of counts per second vs. spatial location along the line and presented in Fig. 6.19a. A significantly higher intensity of Ti 2p peak is only observed at location of TiO₂ pattern while intensity at other points was equal to the background (noise-floor) intensity confirming the successful patterning of TiO₂. In EDX line-scanning, the electron-beam is aligned to scan across sub-micron scale features and moves along the line at a certain speed depending on the number of data points. The graph (Fig. 6.19b) reveals a Y axis modulated signal, the Y-height of which is an indication of the number of Ti K X-ray quanta being detected along the scan-line.

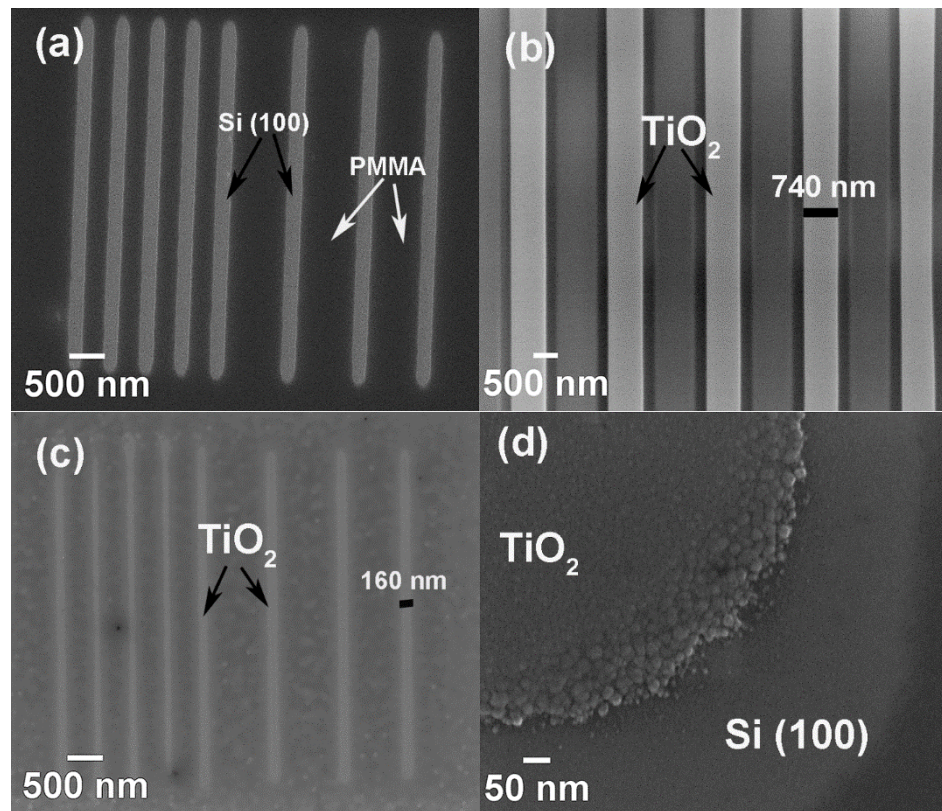


Figure 6.18: SEM images of (a) ebeam exposed and post developed PMMA, (b) and (c) TiO₂ patterns grown on patterned PMMA/Si(100) surface after the removal of PMMA, (d) interface between TiO₂ pattern and Si(100).

Clearly, intensity of Ti K X-ray quanta increases only in TiO₂ lines which reaffirms the successful patterning of TiO₂ line structures. EDX elemental mapping is performed to determine the positions of Ti and O elements at a specific TiO₂ patterned area of the sample. X-ray elemental mapping is a useful technique where elements such as Ti and O emitting characteristic X-rays within the inspection area can be indicated by a unique color. After counting the presence of X-ray signal from a specific element, detector places a bright spot of distinct color on the screen indicating the location of that element in an areal map. Such an EDX elemental map of Ti and O from a patterned TiO₂ area is provided in Fig. 6.20.

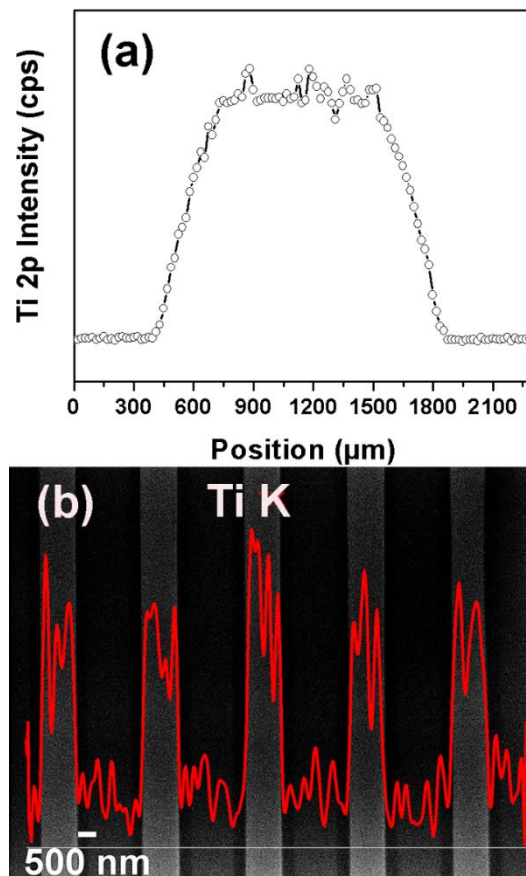


Figure 6.19: (a) XPS Ti2p line scan obtained from mm-scale patterned TiO_2 grown via AS-ALD recipe on PMMA/Si(100) samples, (b) EDX Ti K line scan obtained from nm-scale TiO_2 line features produced via AS-ALD on e-beam lithography patterned samples.

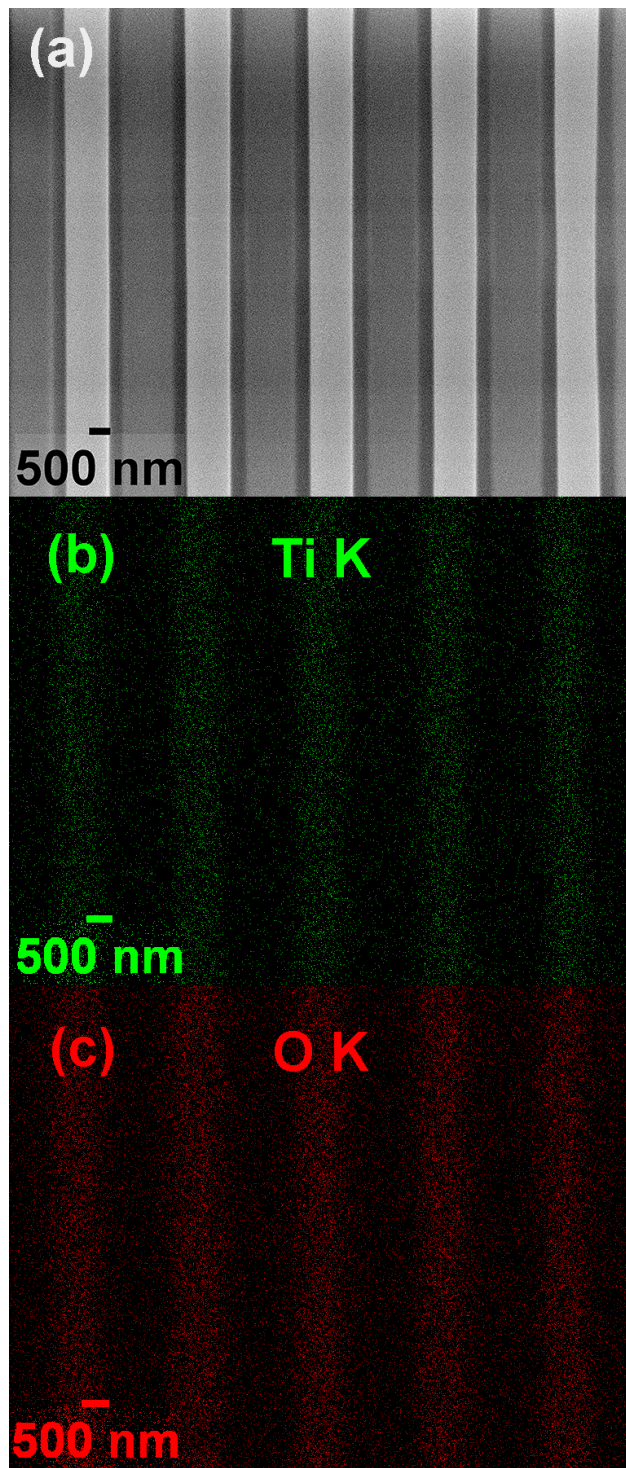


Figure 6.20: SEM image of (a) TiO_2 pattern, (b) Ti K EDX elemental map, (c) O K EDX elemental map.

Figure 6.20 corresponds to the SEM image of patterned TiO_2 line features from which elemental maps of Ti and O are collected. Ti K and O K elemental maps are shown in Fig. 6.20b and c, respectively. The position of Ti is revealed in green color while red color shows O. It is evident from these elemental maps that Ti and O are only present in the line features which coincide with the TiO_2 lines shown in Fig. 6.20a.

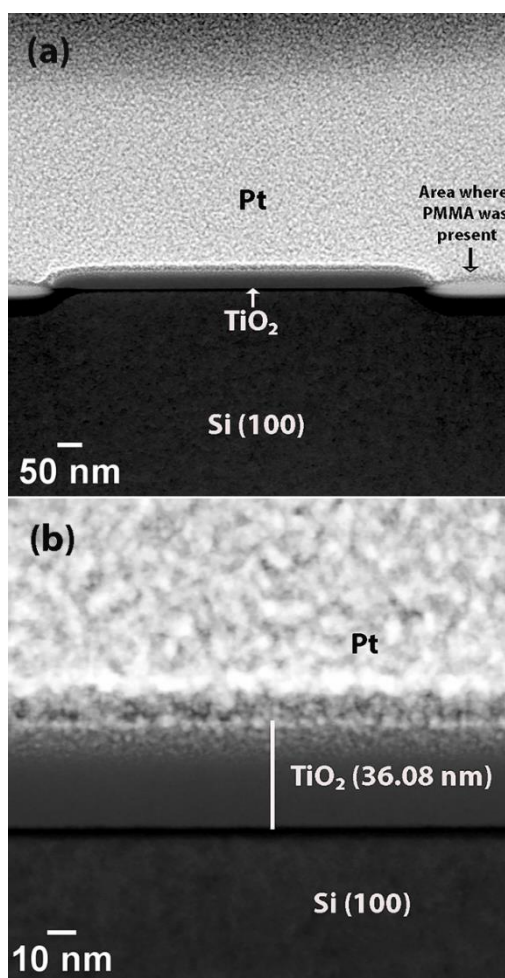


Figure 6.21: TEM image of (a) TiO_2 patterned PMMA free region, (b) patterned TiO_2 region revealing the thickness uniformity of pattern.

Cross-sectional TEM was applied on TiO_2 patterned sample to visualize the area selective deposition. Figure 6.21a and b shows the TEM images obtained after PMMA removal from a single TiO_2 pattern. Figure 6.21a shows different parts of the analyzed area revealing the presence of Si, rectangular pattern of TiO_2 , Pt, and the area where growth was blocked using PMMA. Figure 6.21b

illustrates that TiO_2 was uniformly deposited on PMMA free area with a thickness of 36.1 nm.

Chapter 7

Conclusion and Future Prospects

We have deposited crystalline InN and $\text{In}_x\text{Ga}_{1-x}\text{N}$ thin films on Si(100) and quartz substrates with self-limiting HCPA-ALD at temperatures as low as 200 °C. InN growth rate decreased from 1.60 to 0.64 Å/cycle with increase in N_2 plasma exposure time from 40 s to 100 s. This higher growth rate with 40 s of N_2 plasma exposure was attributed to presence of carbon in InN films which was originating from the partial removal of carbon containing TMI ligands. Longer N_2 plasma exposure time helped in removing carbonaceous ligands more effectively, which decreased the growth rate of InN. InN growth rate at 200 °C was saturated as 0.64 Å/cycle for TMI dose starting from 0.07 s. Individual GaN and InN subcycles have been tailored in the main ALD growth recipe to change the composition of $\text{In}_x\text{Ga}_{1-x}\text{N}$ thin films. Experimental In concentration estimation from EDX analysis turned out to be more accurate as compared to GIXRD and XPS methods due to presence of strain and selective etching of $\text{In}_x\text{Ga}_{1-x}\text{N}$ thin films, respectively. In concentration values obtained from EDX analysis were found to be 0.25, 0.33, and 0.64 for $\text{In}_x\text{Ga}_{1-x}\text{N}$ films with RS of 0.5, 0.75, and 0.85.

InN and $\text{In}_x\text{Ga}_{1-x}\text{N}$ film deposited at 200 °C was polycrystalline with hexagonal wurtzite structure as determined by GIXRD and HR-TEM. XPS survey scans and high resolution XPS measurements confirmed the successful

growth of stoichiometric InN films with relatively low impurity content. AFM measurements performed on InN film revealed smooth films with Rms surface roughness of 0.98 nm while XRR reveals InN film density of 6.30 g/cm³. InN exhibited refractive index of 2.66 at 650 nm and optical band edge at 1.9 eV.

XPS survey scans from surface and bulk of the In_xGa_{1-x}N films exhibited presence of indium, gallium, and nitrogen along with the presence of relatively low impurity contents. Refractive indices of In_xGa_{1-x}N samples increased from 2.28 to 2.42 at 650 nm with increasing In concentration from 0.25 to 0.64. The optical band edge values of In_xGa_{1-x}N thin films decreased with higher In content and band gap values were extracted as 2.71, 2.45, and 2.18 eV for In_xGa_{1-x}N thin films having In concentrations of 0.25, 0.33, and 0.64, respectively. Optical band edge values of the In_xGa_{1-x}N thin films shifted towards higher wavelengths with increasing In content. PL measurements performed on In_xGa_{1-x}N thin films revealed broad spectral features with a wavelength shift depending on In concentration. Root-mean-square (Rms) surface roughnesses of the In_xGa_{1-x}N thin films showed an increasing trend with In content as well.

B_xGa_{1-x}N and B_xIn_{1-x}N thin films have been grown on Si(100) and quartz substrates via sequential pulsed CVD technique in HCPA-ALD reactor at 450 °C. Individual GaN, InN, and BN sub-cycles have been tailored in the main ALD growth recipe to adjust the composition of B_xGa_{1-x}N and B_xIn_{1-x}N thin films. GIXRD measurements revealed that boron incorporation in wurtzite lattice of GaN and InN significantly diminishes the crystallinity in B_xGa_{1-x}N and B_xIn_{1-x}N samples. It is suspected that structural dissimilarities between BN and GaN or InN leads to amorphized B_xGa_{1-x}N and B_xIn_{1-x}N alloys at high boron concentrations. Spectroscopic ellipsometer measurements showed that refractive index varied from 2.24 to 1.65 as the B concentration of B_xGa_{1-x}N increased from 32 to 87%. Similarly, refractive index decreased from 1.98 to 1.74 as the B concentration of B_xIn_{1-x}N increased from 35 to 88%. The shift of optical transmission band edge values of the B_xGa_{1-x}N and B_xIn_{1-x}N films to lower wavelengths with increasing boron contents confirmed the tunability of energy

band gap with alloy composition. AFM measurements revealed an increase in surface roughness with boron content for $B_xGa_{1-x}N$, while an opposite trend was observed for $B_xIn_{1-x}N$ samples. This study not only demonstrate the feasibility of low-temperature ternary alloying of crystalline $In_xGa_{1-x}N$ and amorphous $B_xGa_{1-x}N$ and $B_xIn_{1-x}N$ thin films, but the effective tunability of optical and structural properties of these alloys as well with compositional digital alloying via PA-ALD technique employing a hollow cathode plasma source.

Template-based synthesis of long-range ordered GaN, AlN, and InN vertical hollow nanocylinder arrays was demonstrated via low-temperature PA-ALD and plasma etching processes on Si substrates. In-depth morphological, optical, structural, and chemical characterization was performed to investigate the material properties of the fabricated III-nitride HNCs. SEM images revealed the successful fabrication of long-range ordered arrays of III-nitride HNCs integrated on Si. TEM, GIXRD, and SAED revealed that III-nitride HNCs possess hexagonal wurtzite crystalline structure. Chemical analysis conducted using XPS via survey and HR-scans detected presence of different elements and peaks at specific binding energies which confirmed the successful fabrication of III-nitride HNCs with relatively low impurity content. The unique advantages of the proposed methodology include Si-integration due to low-temperature plasma-assisted growth and nanometer-level precision processing enabling fine control on the targeted nanostructures. Although merely single-material nanostructures are demonstrated in this study, the methodology proposed can be applied for multi-layered heterostructures (GaN/AlN, InN/GaN, etc.) as well as ternary compounds (AlGaN/GaN, InGaN/GaN), potentially resulting in promising alternative quantum-device structures. Such long-range ordered high-surface area III-nitride HNCs might potentially be used in various applications such as nano-(opto)electronics for transistors and LEDs, III-nitride photovoltaic solar cells, plasmonics, piezotronic environmental sensing, and (photo)catalytic surfaces.

Another part of the thesis deals with AS-ALD of metal oxides using polymers as growth inhibition layers followed by self-aligned thin film

patterning of metal oxides. We demonstrate a method for achieving AS-ALD using ICP polymerized CF_x as a hydrophobic blocking layer to inhibit ALD growth. Contact angle, spectroscopic ellipsometry, XPS, and SEM measurements were used to evaluate the capability of plasma polymerized CF_x layer to inhibit metal-oxide ALD growth. Characterizations carried out revealed that effective ZnO blocking on CF_x can be achieved up to more than 100 ALD cycles, resulting in selective growth of ~ 15 nm thick films. Initial nucleation has been observed for 136-cycle ZnO films and additional ALD cycles eventually led to growth on CF_x layer at conventional GPC values. On the other hand, although no complete blocking is observed, a rather slow nucleation has been observed for HfO_2 growth on CF_x coated surfaces up to 100 growth cycles, while the same blocking layer deposited under the present conditions has been found to be ineffective in blocking TiO_2 and Al_2O_3 growth. By exploiting this inhibition feature of CF_x layer, self-aligned ZnO deposition has been performed on lithographically defined patterned $\text{C}_4\text{F}_8/\text{Si}$ sample. High-resolution SEM images and XPS line scans confirmed the successful patterning of ZnO up to a film thickness of ~ 15 nm. The robust albeit rather simple and straightforward technique presented in this work overcomes various challenges associated with previous methods of AS-ALD and provides an alternative route towards nano-patterning using AS-ALD. Moreover, this method is expected to be implemented in achieving AS-ALD of other materials as well including metals and III-V compounds.

Additionally, a systematic investigation on the blocking/inhibition efficacy of different polymeric materials including PMMA, PVP, and CF_x for achieving selective ALD of TiO_2 has been presented. Contact angle and spectroscopic ellipsometer measurements revealed the following results; (i) PMMA successfully blocks the TiO_2 deposition for at least 1200 ALD cycles, (ii) PVP blocks TiO_2 growth up to 300 ALD cycles, (iii) CF_x is unable to inhibit TiO_2 nucleation and growth despite its initial hydrophobic character. Subsequent XPS measurements endorsed the results of contact angle and spectroscopic ellipsometer measurements as no Ti peak is observed for TiO_2 deposition up to

1200 growth cycles on PMMA-coated samples, while Ti peaks became detectable after 400 cycles on PVP and after the first 100 cycles on CF_x . Based on the complete TiO_2 inhibition performance on PMMA up to 1200 cycles, we conclude that PMMA is the most efficient surface to provide effective blocking of TiO_2 growth with an equivalent blocking film thickness of at least ~ 55 nm. SEM measurements on a 1200-cycle grown TiO_2 on Si(100) reveal the grainy structure of TiO_2 . We have also demonstrated that PMMA can be rather easily removed by just 30 seconds dipping into acetone solution, even after 1200 ALD-growth cycles, while PVP can be removed by dissolving in water up to 300 ALD cycles. We have demonstrated micro and nano-scale direct patterned deposition of TiO_2 using PMMA masking layer that has been patterned using e-beam lithography. SEM, EDX line scan, EDX elemental mapping, and XPS elemental mapping revealed successful patterning of μm and nm-scale TiO_2 lines. AS-ALD of TiO_2 demonstrated in the present work offers a novel approach to fabricate closely packed nanopatterns for various device architectures without any additional etching or lift-off processes.

Bibliography

- [1] R. L. Puurunen, "Surface chemistry of atomic layer deposition: A case study for the trimethylaluminum/water process," *J. Appl. Phys.*, vol. 97, no. 12, 2005.
- [2] H. Van Bui, F. Grillo, and J. R. van Ommen, "Atomic and molecular layer deposition: off the beaten track," *Chem. Commun.*, vol. 53, no. 1, pp. 45–71, 2017.
- [3] A. G. Bhuiyan, A. Hashimoto, and A. Yamamoto, "Indium nitride (InN): A review on growth, characterization, and properties," *J. Appl. Phys.*, vol. 94, no. 2003, pp. 2779–2808, 2003.
- [4] V. Y. Davydov, A. A. Klochikhin, V. V. Emtsev, S. V. Ivanov, V. V. Vekshin, F. Bechstedt, J. Furthmüller, H. Harima, a. V. Mudryi, a. Hashimoto, a. Yamamoto, J. Aderhold, J. Graul, and E. E. Haller, "Band Gap of InN and In-Rich In_xGa_{1-x}N alloys (0.36 < x < 1)," *Phys. Status Solidi B*, vol. 230, no. 2, pp. R4–R6, 2002.
- [5] V. Y. Davydov, A. A. Klochikhin, V. V. Emtsev, S. V. Ivanov, V. V. Vekshin, F. Bechstedt, J. Furthmüller, H. Harima, a. V. Mudryi, a. Hashimoto, a. Yamamoto, J. Aderhold, J. Graul, and E. E. Haller, "Band Gap of InN and In-Rich InGa_xN alloys," *Phys. Status Solidi*, vol. 230, no. 3, pp. 4–6, 2002.
- [6] S. Strite, "GaN, AlN, and InN: A review," *J. Vac. Sci. Technol. B Microelectron. Nanom. Struct.*, vol. 10, no. 1992, p. 1237, 1992.
- [7] O. Ambacher, "Growth and applications of Group III-nitrides," *J. Phys. D: Appl. Phys.*, vol. 31, pp. 2653–2710, 1999.
- [8] Y. Tamura and K. Hane, "Optical characteristics of multiple layered InGa_xN quantum wells on GaN nanowalls grown on Si (111) substrate," *Mater. Res. Bull.*, vol. 83, pp. 563–567, 2016.
- [9] G. Suo and J. Li, "One dimensional polar surface dominated GaN nanostructures with zigzag morphology," *J. Alloys Compd.*, vol. 674, pp. 16–20, 2016.
- [10] L. Monteagudo-Lerma, S. Valdueza-Felip, a. Núñez-Cascajero, a. Ruiz, M. González-Herráez, E. Monroy, and F. B. Naranjo, "Morphology and arrangement of InN nanocolumns deposited by radio-frequency

- sputtering: Effect of the buffer layer,” *J. Cryst. Growth*, vol. 434, pp. 13–18, 2016.
- [11] A. T. M. G. Sarwar, F. Yang, B. D. Esser, T. F. Kent, D. W. McComb, and R. C. Myers, “Self-assembled InN micro-mushrooms by upside-down pendeoepitaxy,” *J. Cryst. Growth*, vol. 443, pp. 90–97, 2016.
- [12] H. J.-Y. Chen, D.-L. Yang, T.-W. Huang, and I.-S. Yu, “Formation and Temperature Effect of InN Nanodots by PA-MBE via Droplet Epitaxy Technique,” *Nanoscale Res. Lett.*, vol. 11, no. 1, p. 241, 2016.
- [13] R. Ren, M. S. Faber, and R. Dziedzic, “Epitaxial InN/InGaN quantum dots on Si: Cl⁻ anion selectivity and pseudocapacitor behavior,” 1882.
- [14] Y. Dong, S. Tang, H. Cui, J. Zhang, and Q. Cui, “The synthesis of 3D InN architectures via chemical vapor deposition and their optical properties,” *RSC Adv.*, vol. 6, no. 18, pp. 14958–14963, 2016.
- [15] F. Kayaci, S. Vempati, C. Ozgit-Akgun, I. Donmez, N. Biyikli, and T. Uyar, “Selective isolation of the electron or hole in photocatalysis: ZnO-TiO₂ and TiO₂-ZnO core-shell structured heterojunction nanofibers via electrospinning and atomic layer deposition.,” *Nanoscale*, vol. 6, no. 11, pp. 5735–45, 2014.
- [16] F. Kayaci, C. Ozgit-akgun, I. Donmez, N. Biyikli, and T. Uyar, “Polymer – Inorganic Core – Shell Nano fi bers by Electrospinning and Atomic Layer Deposition: Flexible Nylon – ZnO Core – Shell Nano fi ber Mats and Their Photocatalytic Activity,” *ACS Appl. Mater. Interfaces*, vol. 4, p. 6185–6194, 2012.
- [17] C. Ozgit-Akgun, F. Kayaci, S. Vempati, A. Haider, A. Celebioglu, E. Goldenberg, S. Kizir, T. Uyar, and N. Biyikli, “Fabrication of flexible polymer–GaN core–shell nanofibers by the combination of electrospinning and hollow cathode plasma-assisted atomic layer deposition,” *J. Mater. Chem. C*, vol. 3, no. 20, pp. 5199–5206, 2015.
- [18] A. Haider, C. Ozgit-Akgun, F. Kayaci, A. K. Okyay, T. Uyar, and N. Biyikli, “Fabrication of AlN/BN bishell hollow nanofibers by electrospinning and atomic layer deposition,” *Apl Mater.*, vol. 2, no. 2014, pp. 096109, 2014.
- [19] M. Norek, G. Łuka, M. Godlewski, T. Płociński, M. Michalska-Domańska, and W. J. Stępniewski, “Plasmonic enhancement of blue emission from ZnO nanorods grown on the anodic aluminum oxide (AAO) template,” *Appl. Phys. A Mater. Sci. Process.*, vol. 111, no. 1, pp. 265–271, 2013.

- [20] Y.-H. Chang, C.-M. Liu, C. Chen, H.-E. Cheng, and T.-C. Lu, "The Differences in Optical Characteristics of TiO₂ and TiO₂/AAO Nanotube Arrays Fabricated by Atomic Layer Deposition," *J. Electrochem. Soc.*, vol. 159, no. 5, p. K136, 2012.
- [21] H. W. Lin, Y. H. Chang, and C. Chen, "Facile Fabrication of TiO₂ Nanorod Arrays for Gas Sensing using Double-Layered Anodic Oxidation Method," *J. Electrochem. Soc.*, vol. 159, no. 1, pp. K5–K9, 2012.
- [22] Y.-H. Chang, S.-M. Wang, C.-M. Liu, and C. Chen, "Fabrication and Characteristics of Self-Aligned ZnO Nanotube and Nanorod Arrays on Si Substrates by Atomic Layer Deposition," *J. Electrochem. Soc.*, vol. 157, no. 11, p. K236, 2010.
- [23] C.-J. Yang, S.-M. Wang, S.-W. Liang, Y.-H. Chang, C. Chen, and J.-M. Shieh, "Low-temperature growth of ZnO nanorods in anodic aluminum oxide on Si substrate by atomic layer deposition," *Appl. Phys. Lett.*, vol. 90, no. 3, p. 033104, 2007.
- [24] W.-H. Kim, S.-J. Park, J.-Y. Son, and H. Kim, "Ru nanostructure fabrication using an anodic aluminum oxide nanotemplate and highly conformal Ru atomic layer deposition," *Nanotechnology*, vol. 19, no. 4, p. 045302, 2008.
- [25] H. Robotjazi, S. M. Bahauddin, L. H. Macfarlan, S. Fu, and I. Thomann, "Ultrathin AAO Membrane as a Generic Template for Sub-100 nm Nanostructure Fabrication," *Chem. Mater.*, vol. 28, no. 13, pp. 4546–4553, 2016.
- [26] A. Haider, P. Deminskyi, T. M. Khan, H. Eren, and N. Biyikli, "Area-Selective Atomic Layer Deposition Using an Inductively Coupled Plasma Polymerized Fluorocarbon Layer: A Case Study for Metal Oxides," *J. Phys. Chem. C*, vol. 120, no. 46, pp. 26393–26401, 2016.
- [27] F. S. Minaye Hashemi, C. Prasittichai, and S. F. Bent, "Self-Correcting Process for High Quality Patterning by Atomic Layer Deposition," *ACS Nano*, vol. 9, no. 9, pp. 8710–8717, 2015.
- [28] W. M. . Mackus, A.J.M., Bol, A.A., Kessels, "The use of atomic layer deposition in advanced nanopatterning," *Nanoscale*, vol. 6, no. 2011, pp. 10941–10960, 2014.
- [29] E. Färm, M. Kemell, M. Ritala, and M. Leskelä, "Self-assembled octadecyltrimethoxysilane monolayers enabling selective-area atomic

- layer deposition of iridium,” *Chem. Vap. Depos.*, vol. 12, no. 7, pp. 415–417, 2006.
- [30] E. Färm, M. Kemell, M. Ritala, and M. Leskelä, “Selective-area atomic layer deposition with microcontact printed self-assembled octadecyltrichlorosilane monolayers as mask layers,” *Thin Solid Films*, vol. 517, no. 2, pp. 972–975, 2008.
- [31] A. Haider, C. Ozgit-Akgun, E. Goldenberg, A. K. Okyay, and N. Biyikli, “Low-Temperature Deposition of Hexagonal Boron Nitride Via Sequential Injection of Triethylboron and N_2/H_2 Plasma,” *J. Am. Ceram. Soc.*, vol. 97, no. 12, pp. 4052–4059, 2014.
- [32] C. Ozgit-Akgun, E. Goldenberg, A. K. Okyay, and N. Biyikli, “Hollow cathode plasma-assisted atomic layer deposition of crystalline AlN, GaN and $Al_xGa_{1-x}N$ thin films at low temperatures,” *J. Mater. Chem. C*, vol. 2, no. 12, p. 2123, 2014.
- [33] S. E. Potts, W. Keuning, E. Langereis, G. Dingemans, M. C. M. van de Sanden, and W. M. M. Kessels, “Low Temperature Plasma-Enhanced Atomic Layer Deposition of Metal Oxide Thin Films,” *J. Electrochem. Soc.*, vol. 157, p. P66, 2010.
- [34] M. Caymax, G. Brammertz, A. Delabie, S. Sioncke, D. Lin, M. Scarrozza, G. Pourtois, W. E. Wang, M. Meuris, and M. Heyns, “Interfaces of high-k dielectrics on GaAs: Their common features and the relationship with Fermi level pinning (Invited Paper),” *Microelectron. Eng.*, vol. 86, no. 7–9, pp. 1529–1535, 2009.
- [35] H. B. Profijt, S. E. Potts, M. C. M. van de Sanden, and W. M. M. Kessels, “Plasma-Assisted Atomic Layer Deposition: Basics, Opportunities, and Challenges,” *J. Vac. Sci. Technol. A Vacuum, Surfaces, Film.*, vol. 29, no. 2011, p. 050801, 2011.
- [36] E. Bellotti, B. K. Doshi, K. F. Brennan, J. D. Albrecht, and P. P. Ruden, “Ensemble Monte Carlo study of electron transport in wurtzite InN,” *J. Appl. Phys.*, vol. 85, no. 1999, p. 916, 1999.
- [37] K. S. A Butcher and T. L. Tansley, “InN, latest development and a review of the band-gap controversy,” *Superlattices Microstruct.*, vol. 38, pp. 1–37, 2005.
- [38] Y. Nanishi, Y. Saito, and T. Yamaguchi, “RF-molecular beam epitaxy growth and properties of InN and related alloys,” *Japanese J. Appl. Physics, Part 1 Regul. Pap. Short Notes Rev. Pap.*, vol. 42, pp. 2549–2559, 2003.

- [39] M. C. Johnson, S. L. Konsek, a. Zettl, and E. D. Bourret-Courchesne, "Nucleation and growth of InN thin films using conventional and pulsed MOVPE," *J. Cryst. Growth*, vol. 272, pp. 400–406, 2004.
- [40] Z. G. Qian, W. Z. Shen, H. Ogawa, and Q. X. Guo, "Infrared reflection characteristics in InN thin films grown by magnetron sputtering for the application of plasma filters," *J. Appl. Phys.*, vol. 92, no. 2002, pp. 3683–3687, 2002.
- [41] M. A. Hafez and H. E. Elsayed-Ali, "Low-temperature growth of InN on Si(100) by femtosecond pulsed laser deposition," *J. Vac. Sci. Technol. A Vacuum, Surfaces, Film.*, vol. 27, no. 100, p. 696, 2009.
- [42] J. Wu and W. Walukiewicz, "Band gaps of InN and group III nitride alloys," *Superlattices Microstruct.*, vol. 34, no. 2003, pp. 63–75, 2003.
- [43] H. Search, C. Journals, A. Contact, M. Iopscience, and I. P. Address, "P-GaN / N-InGaN / N-GaN Double-Heterostructure Blue-Light-Emitting Diodes," vol. 8.
- [44] S. J. Chang, W. C. Lai, Y. K. Su, J. F. Chen, C. H. Liu, and U. H. Liaw, "InGaN-GaN multiquantum-well blue and green light-emitting diodes," *IEEE J. Sel. Top. Quantum Electron.*, vol. 8, no. 2, pp. 278–283, 2002.
- [45] G. B. Stringfellow and I. Ho, "Solid phase immiscibility in GaInN," *Appl. Phys. Lett.*, vol. 69, p. 2701, 1996.
- [46] V. Chaly, B. Borisov, D. Demidov, D. Krasovitsky, Y. Pogorelsky, A. Shkurko, I. Sokolov, and S. Y. Karpov, "Indium droplet formation during molecular beam epitaxy of InGaN," *J. Cryst. Growth*, vol. 206, pp. 147–149, 1999.
- [47] H. Lu, M. Thothathiri, Z. Wu, and I. Bhat, "Study of indium droplets formation on the $\text{In}_x\text{Ga}_{1-x}\text{N}$ films by single crystal x-ray diffraction," *J. Electron. Mater.*, vol. 26, no. 3, pp. 281–284, 1997.
- [48] A. Kobayashi, J. Ohta, and H. Fujioka, "Low temperature epitaxial growth of $\text{In}_{0.25}\text{Ga}_{0.75}\text{N}$ on lattice-matched ZnO by pulsed laser deposition," *J. Appl. Phys.*, vol. 99, no. 2006, pp. 1–5, 2006.
- [49] S. Kim, K. Lee, H. Lee, K. Park, C. S. Kim, S. J. Son, and K. W. Yi, "The influence of ammonia pre-heating to InGaN films grown by TPIS-MOCVD," *J. Cryst. Growth*, vol. 247, pp. 55–61, 2003.
- [50] D. N. Nath, E. Gür, S. a. Ringel, and S. Rajan, "Molecular beam epitaxy of N-polar InGaN," *Appl. Phys. Lett.*, vol. 97, no. 2010, pp. 10–13, 2010.

- [51] H. Shinoda and N. Mutsukura, "Structural properties of GaN and related alloys grown by radio-frequency magnetron sputter epitaxy," *Thin Solid Films*, vol. 516, pp. 2837–2842, 2008.
- [52] H.-M. Kim, W. C. Lee, T. W. Kang, K. S. Chung, C. S. Yoon, and C. K. Kim, "InGaN nanorods grown on (111) silicon substrate by hydride vapor phase epitaxy," *Chem. Phys. Lett.*, vol. 380, pp. 181–184, 2003.
- [53] R. Paine and C. Narula, "Synthetic Routes to Boron Nitride," *Chem. Rev.*, vol. 90, pp. 73–91, 1990.
- [54] K. Watanabe, T. Taniguchi, and H. Kanda, "Direct-bandgap properties and evidence for ultraviolet lasing of hexagonal boron nitride single crystal," *Nat. Mater.*, vol. 3, no. June, pp. 404–409, 2004.
- [55] K. Watanabe, T. Taniguchi, T. Niiyama, K. Miya, and M. Taniguchi, "Far-ultraviolet plane-emission handheld device based on hexagonal boron nitride," *Nat. Photonics*, vol. 3, no. October, pp. 591–594, 2009.
- [56] S. C. Jain, M. Willander, J. Narayan, and R. Van Overstraeten, "III-nitrides: Growth, characterization, and properties," *J. Appl. Phys.*, vol. 87, no. 2000, p. 965, 2000.
- [57] C. H. Wei and J. H. Edgar, "Thermodynamic analysis of $GaxB_{1-x}N$ grown by MOVPE," *J. Cryst. Growth*, vol. 217, pp. 109–114, 2000.
- [58] T. Akasaka, Y. Kobayashi, and T. Makimoto, "BGaN micro-islands as novel buffers for growth of high-quality GaN on sapphire," *J. Cryst. Growth*, vol. 298, pp. 320–324, 2007.
- [59] S. F. Chichibu, T. Azuhata, M. Sugiyama, T. Kitamura, Y. Ishida, H. Okumura, H. Nakanishi, T. Sota, and T. Mukai, "Optical and structural studies in InGaN quantum well structure laser diodes," *J. Vac. Sci. Technol. B Microelectron. Nanom. Struct.*, vol. 19, no. 2001, p. 2177, 2001.
- [60] J. J. Wierer, D. a. Steigerwald, M. R. Krames, J. J. O'Shea, M. J. Ludowise, G. Christenson, Y. C. Shen, C. Lowery, P. S. Martin, S. Subramanya, W. Götz, N. F. Gardner, R. S. Kern, and S. a. Stockman, "High-power AlGaInN flip-chip light-emitting diodes," *Appl. Phys. Lett.*, vol. 78, no. 2001, pp. 3379–3381, 2001.
- [61] B.-H. Chu, H.-W. Lin, S. Gwo, Y.-L. Wang, S. J. Pearton, J. W. Johnson, P. Rajagopal, J. C. Roberts, E. L. Piner, K. J. Linthicuni, and F. Ren, "Chloride ion detection by InN gated AlGaInN/GaN high electron mobility

- transistors,” *J. Vac. Sci. Technol. B Microelectron. Nanom. Struct.*, vol. 28, no. 2010, p. L5, 2010.
- [62] Y. Bu, “Laser-assisted chemical vapor deposition of InN on Si(100),” *J. Vac. Sci. Technol. A Vacuum, Surfaces, Film.*, vol. 11, no. 100, p. 2931, 1993.
- [63] T. Matsuoka, H. Okamoto, M. Nakao, H. Harima, and E. Kurimoto, “Optical bandgap energy of wurtzite InN,” *Appl. Phys. Lett.*, vol. 81, no. 2002, pp. 1246–1248, 2002.
- [64] R. Ascázubi, I. Wilke, K. Denniston, H. Lu, and W. J. Schaff, “Terahertz emission by InN,” *Appl. Phys. Lett.*, vol. 84, no. 2004, pp. 4810–4812, 2004.
- [65] L. C. Chen and C. H. Tien, “Growth and characterization of nanocolumnar-structure boron indium nitride alloys deposited on sapphire substrates by solution chemical vapor deposition,” *Jpn. J. Appl. Phys.*, vol. 48, pp. 1010011–1010013, 2009.
- [66] G. Orsal, N. Maloufi, S. Gautier, M. Alnot, a. a. Sirenko, M. Bouchaour, and a. Ougazzaden, “Effect of boron incorporation on growth behavior of B GaN/GaN by MOVPE,” *J. Cryst. Growth*, vol. 310, pp. 5058–5062, 2008.
- [67] T. Kente and S. D. Mhlanga, “Gallium nitride nanostructures: Synthesis, characterization and applications,” *J. Cryst. Growth*, vol. 444, pp. 55–72, 2016.
- [68] A. Haider, C. Ozgit-Akgun, F. Kayaci, A. K. Okyay, T. Uyar, and N. Biyikli, “Fabrication of AlN/BN bishell hollow nanofibers by electrospinning and atomic layer deposition,” *Apl Mater.*, vol. 2, p. 096109, 2014.
- [69] R. Koester, J. S. Hwang, C. Durand, D. L. S. Dang, and J. Eymery, “Self-assembled growth of catalyst-free GaN wires by metal-organic vapour phase epitaxy,” *Nanotechnology*, vol. 21, no. 111, p. 015602, 2010.
- [70] Y. T. Lin, T. W. Yeh, Y. Nakajima, and P. D. Dapkus, “Catalyst-free GaN nanorods synthesized by selective area growth,” *Adv. Funct. Mater.*, vol. 24, no. 21, pp. 3162–3171, 2014.
- [71] J. Martinez, F. Barbagini, A. Bengoechea-Encabo, S. Albert, M. A. Sanchez García, and E. Calleja, “Fabrication of GaN nanorods by focused ion beam,” *Microelectron. Eng.*, vol. 98, pp. 250–253, 2012.

- [72] Y. Wu, C. Xue, H. Zhuang, D. Tian, and Y. Liu, "Synthesis and photoluminescence of single-crystal GaN nanorods prepared by sol-gel method," *Appl. Surf. Sci.*, vol. 253, no. 2, pp. 485–487, 2006.
- [73] J. Y. Li, X. L. Chen, Z. Y. Qiao, Y. G. Cao, and Y. C. Lan, "Formation of GaN nanorods by a sublimation method," *J. Cryst. Growth*, vol. 213, no. 3–4, pp. 408–410, 2000.
- [74] Z. J. Li, X. L. Chen, H. J. Li, and Y. P. Xu, "Regular arrays of GaN nanorods," *J. Cryst. Growth*, vol. 236, no. 1–3, pp. 71–76, 2002.
- [75] F. Yuan, B. Liu, Z. Wang, B. Yang, Y. Yin, B. Dierre, T. Sekiguchi, G. Zhang, and X. Jiang, "Synthesis, microstructure, and cathodoluminescence of [0001]-oriented GaN nanorods grown on conductive graphite substrate," *ACS Appl. Mater. Interfaces*, vol. 5, no. 22, pp. 12066–12072, 2013.
- [76] M. Müller, P. Veit, F. F. Krause, T. Schimpke, S. Metzner, F. Bertram, T. Mehrstens, K. Müller-Caspary, A. Avramescu, M. Strassburg, A. Rosenauer, and J. Christen, "Nanoscopic Insights into InGaN/GaN Core–Shell Nanorods: Structure, Composition, and Luminescence," *Nano Lett.*, no. C1, p. acs.nanolett.6b01062, 2016.
- [77] M. Heilmann, a. M. Munshi, G. Sarau, M. Göbelt, C. Tessarek, V. T. Fauske, A. T. J. Van Helvoort, J. Yang, M. Latzel, B. Hoffmann, G. Conibeer, H. Weman, and S. Christiansen, "Vertically Oriented Growth of GaN Nanorods on Si Using Graphene as an Atomically Thin Buffer Layer," *Nano Lett.*, vol. 16, no. 6, pp. 3524–3532, 2016.
- [78] Z. Yu, Z. Yang, S. Wang, Y. Jin, J. G. Liu, M. Gong, and X. Sun, "Growth of GaN nanorods via Au catalyst-assisted CVD," *Chem. Vap. Depos.*, vol. 11, no. 10, pp. 433–436, 2005.
- [79] M. Reddeppa, B. G. Park, S. T. Lee, M. D. Kim, R. Kuchi, and J. R. Jeong, "Ferromagnetic properties of GaN nanorods: Effect of silicon doping and hydrogenation," *Curr. Appl. Phys.*, vol. 16, no. 8, pp. 886–889, 2016.
- [80] J. Z. Li, Z. Z. Chen, S. F. Li, Q. Q. Jiao, Y. L. Feng, S. X. Jiang, Y. F. Chen, T. J. Yu, B. Shen, and G. Y. Zhang, "The anti-surfactant effect of silane on the facets-controlled growth of GaN nanorods by MOCVD," *Superlattices Microstruct.*, vol. 96, pp. 234–240, 2016.
- [81] D. Tsivion and E. Joselevich, "Guided growth of horizontal GaN nanowires on spinel with orientation-controlled morphologies," *J. Phys. Chem. C*, vol. 118, no. 33, pp. 19158–19164, 2014.

- [82] R. Koester, J. S. Hwang, C. Durand, D. L. S. Dang, and J. Eymery, “Self-assembled growth of catalyst-free GaN wires by metal-organic vapour phase epitaxy,” *Nanotechnology*, vol. 21, no. 110, p. 015602, 2010.
- [83] Ž. Gačević, D. Gómez Sánchez, and E. Calleja, “Formation mechanisms of gan nanowires grown by selective area growth homoepitaxy,” *Nano Lett.*, vol. 15, no. 2, pp. 1117–1121, 2015.
- [84] V. Kumaresan, L. Largeau, F. Oehler, H. Zhang, O. Mauguin, F. Glas, N. Gogneau, M. Tchernycheva, and J.-C. Harmand, “Self-induced growth of vertical GaN nanowires on silica,” *Nanotechnology*, vol. 27, no. 13, p. 135602, 2016.
- [85] H. Liu, Q. Hua, R. Yu, Y. Yang, T. Zhang, Y. Zhang, and C. Pan, “A Bamboo-Like GaN Microwire-Based Piezotronic Memristor,” *Adv. Funct. Mater.*, vol. 26, no. 29, pp. 5307–5314, 2016.
- [86] B. Kuppulingam, G. M. Bhalerao, S. Singh, and K. Baskar, “Growth behavior of GaN nanowires on c-plane sapphire substrate by applying various catalysts,” *Appl. Phys. A*, vol. 122, no. 7, p. 667, 2016.
- [87] B. Yang, F. Yuan, Q. Liu, N. Huang, J. Qiu, T. Staedler, B. Liu, and X. Jiang, “Dislocation-induced nanoparticle decoration on a GaN nanowire,” *ACS Appl. Mater. Interfaces*, vol. 7, no. 4, pp. 2790–2796, 2015.
- [88] V. Kumaresan, L. Largeau, A. Madouri, F. Glas, H. Zhang, F. Oehler, A. Cavanna, A. Babichev, L. Travers, N. Gogneau, M. Tchernycheva, and J. C. Harmand, “Epitaxy of GaN Nanowires on Graphene,” *Nano Lett.*, vol. 16, no. 8, pp. 4895–4902, 2016.
- [89] J. K. Zettler, P. Corfdir, C. Hauswald, E. Luna, U. Jahn, T. Flissikowski, E. Schmidt, C. Ronning, A. Trampert, L. Geelhaar, H. T. Grahn, O. Brandt, and S. Fernández-Garrido, “Observation of Dielectrically Confined Excitons in Ultrathin GaN Nanowires up to Room Temperature,” *Nano Lett.*, vol. 16, no. 2, pp. 973–980, 2016.
- [90] M. Wölz, C. Hauswald, T. Flissikowski, T. Gotschke, S. Fernández-Garrido, O. Brandt, H. T. Grahn, L. Geelhaar, and H. Riechert, “Epitaxial Growth of GaN Nanowires with High Structural Perfection on a Metallic TiN Film,” *Nano Lett.*, vol. 15, no. 6, pp. 3743–3747, 2015.
- [91] M. S. Kang, C. H. Lee, J. B. Park, H. Yoo, and G. C. Yi, “Gallium nitride nanostructures for light-emitting diode applications,” *Nano Energy*, vol. 1, no. 3, pp. 391–400, 2012.

- [92] M. Hetzl, F. Schuster, A. Winnerl, S. Weiszer, and M. Stutzmann, “GaN nanowires on diamond,” *Mater. Sci. Semicond. Process.*, vol. 48, pp. 65–78, 2016.
- [93] E. Li, B. Wu, S. Lv, Z. Cui, D. Ma, and W. Shi, “Field emission properties of Ge-doped GaN nanowires,” *J. Alloys Compd.*, vol. 681, pp. 324–329, 2016.
- [94] Q. N. Abdullah, F. K. Yam, Z. Hassan, and M. Bououdina, “Author’s personal copy Growth and conversion of b-Ga₂O₃ nanobelts into GaN nanowires via catalyst-free chemical vapor deposition technique,” *Superlattices Microstruct.*, vol. 54, pp. 215–224, 2013.
- [95] X. M. Cai, a. B. Djurišić, and M. H. Xie, “GaN nanowires: CVD synthesis and properties,” *Thin Solid Films*, vol. 515, no. 3, pp. 984–989, 2006.
- [96] Y. Wu, C. Xue, H. Zhuang, D. Tian, Y. Liu, J. He, F. Wang, L. Sun, and Y. Ai, “Synthesis of single-crystal GaN nanowires on Si(111) substrate by ammonification technology,” *Mater. Lett.*, vol. 60, no. 25–26, pp. 3076–3078, 2006.
- [97] P. Aseev, Z. Gačević, a. Torres-Pardo, J. M. González-Calbet, and E. Calleja, “Improving optical performance of GaN nanowires grown by selective area growth homoepitaxy: Influence of substrate and nanowire dimensions,” *Appl. Phys. Lett.*, vol. 108, no. 25, 2016.
- [98] F. Yu, D. Rümmler, J. Hartmann, L. Caccamo, T. Schimpke, M. Strassburg, a. E. Gad, a. Bakin, H. H. Wehmann, B. Witzigmann, H. S. Wasisto, and a. Waag, “Vertical architecture for enhancement mode power transistors based on GaN nanowires,” *Appl. Phys. Lett.*, vol. 108, no. 21, pp. 10–15, 2016.
- [99] G. Calabrese, P. Corfdir, G. Gao, C. Pfüller, A. Trampert, O. Brandt, L. Geelhaar, and S. Fernández-Garrido, “Molecular beam epitaxy of single crystalline GaN nanowires on a flexible Ti foil,” *Appl. Phys. Lett.*, vol. 108, no. 20, 2016.
- [100] J. Zhang and C. Wang, “Size-dependent pyroelectric properties of gallium nitride nanowires,” *J. Appl. Phys.*, vol. 119, no. 14, 2016.
- [101] O. Benner, C. Blumberg, K. Arzi, a. Poloczek, W. Prost, and F. J. Tegude, “Erratum: Electrical characterization and transport model of n-gallium nitride nanowires (Appl. Phys. Lett. (2015) 107(082103)),” *Appl. Phys. Lett.*, vol. 108, no. 4, pp. 1–5, 2016.

- [102] P. C. Upadhyaya, J. a. Martinez, Q. Li, G. T. Wang, B. S. Swartzentruber, A. J. Taylor, and R. P. Prasankumar, "Space-and-time-resolved spectroscopy of single GaN nanowires," *CLEO 2011 - Laser Sci. to Photonic Appl.*, vol. 263103, no. 2015, pp. 1–2, 2011.
- [103] G. S. Cheng, L. D. Zhang, Y. Zhu, G. T. Fei, L. Li, C. M. Mo, and Y. Q. Mao, "Large-scale synthesis of single crystalline gallium nitride nanowires," *Appl. Phys. Lett.*, vol. 75, no. 1999, pp. 2455–2457, 1999.
- [104] C. Hemmingsson, G. Pozina, S. Khromov, and B. Monemar, "Growth of GaN nanotubes by halide vapor phase epitaxy.," *Nanotechnology*, vol. 22, no. 8, p. 085602, 2011.
- [105] M. a. Qaeed, K. Ibrahim, K. M. a Saron, M. S. Mukhlif, a. Ismail, N. G. Elfadill, K. M. Chahrour, Q. a. Abdullah, and K. S. a Aldroobi, "New issue of GaN nanoparticles solar cell," *Curr. Appl. Phys.*, vol. 15, no. 4, pp. 499–503, 2015.
- [106] A. Fadil, Y. Ou, T. Zhan, K. Wu, D. Suyatin, W. Lu, P. M. Petersen, Z. Liu, and H. Ou, "Fabrication and improvement of nanopillar InGaN / GaN light-emitting diodes using nanosphere lithography," *J. Nanophotonics*, vol. 9, no. 1, p. 093062, 2015.
- [107] N. P. Reddy, S. Naureen, and S. Mokkaapati, "Enhanced luminescence from GaN nanopillar arrays fabricated using a top-down process," *Nanotechnology*, vol. 27, no. 6, p. 65304, 2015.
- [108] S. Nagarajan, O. Svensk, L. Lehtola, H. Lipsanen, and M. Sopanen, "Stress distribution in GaN nanopillars using confocal Raman mapping technique," *Appl. Phys. Lett.*, vol. 104, no. 15, pp. 0–5, 2014.
- [109] W. H. Choi, G. You, M. Abraham, S. Y. Yu, J. Liu, L. Wang, J. Xu, and S. E. Mohney, "Sidewall passivation for InGaN/GaN nanopillar light emitting diodes," *J. Appl. Phys.*, vol. 116, no. 1, 2014.
- [110] D.-W. Jeon, L.-W. Jang, H.-S. Cho, K.-S. Kwon, M.-J. Dong, a. Y. Polyakov, J.-W. Ju, T.-H. Chung, J. H. Baek, and I.-H. Lee, "Enhanced optical output performance in InGaN/GaN light-emitting diode embedded with SiO₂ nanoparticles," *Opt. Express*, vol. 22, no. 18, p. 21454, 2014.
- [111] Y. Hu, Z. Hao, W. Lai, C. Geng, Y. Luo, and Q. Yan, "Nano-fabrication and related optical properties of InGaN/GaN nanopillars," *Nanotechnology*, vol. 26, no. 7, p. 075302, 2015.
- [112] a. Adikimenakis, a. Lotsari, G. P. Dimitrakopoulos, T. Kehagias, K. E. Aretouli, K. Tsagaraki, M. Androulidaki, P. Komninou, and a.

Georgakilas, "Direct spontaneous growth and interfacial structural properties of inclined GaN nanopillars on r-plane sapphire," *J. Appl. Phys.*, vol. 117, no. 24, 2015.

- [113] T.-T. Wan, Z.-Q. Ye, T. Tao, Z.-L. Xie, R. Zhang, B. Liu, X.-Q. Xiu, Y. Li, P. Han, Y. Shi, and Y.-D. Zheng, "The enhancement of light-emitting efficiency using GaN-based multiple quantum well light-emitting diodes with nanopillar arrays," *Chinese Phys. B*, vol. 22, no. 8, p. 088102, 2013.
- [114] C. B. Soh, C. B. Tay, R. J. N. Tan, a P. Vajpeyi, I. P. Seetoh, K. K. Ansah-Antwi, and S. J. Chua, "Nanopore morphology in porous GaN template and its effect on the LEDs emission," *J. Phys. D. Appl. Phys.*, vol. 46, no. 36, p. 365102, 2013.
- [115] T. Erdem, V. Ibrahimova, D. Jeon, and I. Lee, "Morphology-Dependent Energy Transfer of Poly fl uorene," *J. Phys. Chem. CPhysical Chem.*, vol. 117, pp. 18613–18619, 2013.
- [116] A. Y. Polyakov, D. W. Jeon, a. V. Govorkov, N. B. Smirnov, V. N. Sokolov, E. a. Kozhukhova, E. B. Yakimov, and I. H. Lee, "Properties of nanopillar structures prepared by dry etching of undoped GaN grown by maskless epitaxial overgrowth," *J. Alloys Compd.*, vol. 554, pp. 258–263, 2013.
- [117] W. J. Tseng, M. Gonzalez, L. Dillemans, K. Cheng, S. J. Jiang, P. M. Vereecken, G. Borghs, and R. R. Lieten, "Strain relaxation in GaN nanopillars," *Appl. Phys. Lett.*, vol. 101, no. 25, 2012.
- [118] J. R. Chang, S. P. Chang, Y. J. Li, Y. J. Cheng, K. P. Sou, J. K. Huang, H. C. Kuo, and C. Y. Chang, "Fabrication and luminescent properties of core-shell InGaN/GaN multiple quantum wells on GaN nanopillars," *Appl. Phys. Lett.*, vol. 100, no. 26, 2012.
- [119] K. H. Li, Z. Ma, and H. W. Choi, "Single-mode whispering gallery lasing from metal-clad GaN nanopillars.," *Opt. Lett.*, vol. 37, no. 3, pp. 374–6, 2012.
- [120] M. H. Lo, Y. J. Cheng, H. C. Kuo, and S. C. Wang, "Enhanced electron-hole plasma stimulated emission in optically pumped gallium nitride nanopillars," *Appl. Phys. Lett.*, vol. 98, no. 12, 2011.
- [121] J. Zhu, L. Wang, S. Zhang, H. Wang, D. Zhao, J. Zhu, Z. Liu, D. Jiang, and H. Yang, "Light extraction efficiency improvement and strain relaxation in InGaN/GaN multiple quantum well nanopillars," *J. Appl. Phys.*, vol. 109, no. 8, pp. 1–6, 2011.

- [122] C. H. Chiu, P. M. Tu, C. C. Lin, D. W. Lin, Z. Y. Li, K. L. Chuang, J. R. Chang, T. C. Lu, H. W. Zan, C. Y. Chen, H. C. Kuo, S. C. Wang, and C. Y. Chang, "Highly efficient and bright LEDs overgrown on GaN nanopillar substrates," *IEEE J. Sel. Top. Quantum Electron.*, vol. 17, no. 4, pp. 971–978, 2011.
- [123] A. Ghosh, H. P. Bhasker, a. Mukherjee, T. Kundu, B. P. Singh, S. Dhar, S. De, and a. Chowdhury, "Polarity selective etching: A self-assisted route for fabricating high density of c-axis oriented tapered GaN nanopillars," *J. Appl. Phys.*, vol. 110, no. 3, 2011.
- [124] M.-H. Lo, Y.-J. Cheng, M.-C. Liu, H.-C. Kuo, and S. C. Wang, "Lasing at exciton transition in optically pumped gallium nitride nanopillars.," *Opt. Express*, vol. 19, no. 19, pp. 17960–5, 2011.
- [125] X. H. Wang, J. Q. Ning, S. J. Xu, and H. W. Choi, "Raman and photoluminescence characterization of focused ion beam patterned InGaN/GaN multi-quantum-wells nanopillar array," *J. Appl. Phys.*, vol. 110, no. 9, 2011.
- [126] M. H. Lo, Y. J. Cheng, H. C. Kuo, and S. C. Wang, "Fabrication and lasing characteristics of GaN nanopillars," *Gall. Nitride Mater. Devices Vi*, vol. 7939, p. 6, 2011.
- [127] J. Zhu, L. Wang, S. Zhang, H. Wang, D. Zhao, J. Zhu, Z. Liu, D. Jiang, and H. Yang, "The fabrication of GaN-based nanopillar light-emitting diodes," *J. Appl. Phys.*, vol. 108, no. 7, 2010.
- [128] K. H. Li and H. W. Choi, "Air-spaced GaN nanopillar photonic band gap structures patterned by nanosphere lithography," *J. Appl. Phys.*, vol. 109, no. 2, 2011.
- [129] W. Y. Fu, K. K. Y. Wong, and H. W. Choi, "A novel GaN photonic crystal structure comprising nanopillars with inclined sidewalls," *Phys. Status Solidi Curr. Top. Solid State Phys.*, vol. 6, no. SUPPL. 2, pp. 639–642, 2009.
- [130] W. C. Lai, P. H. Chen, L. C. Chang, C. H. Kuo, J. K. Sheu, C. J. Tun, and S. C. Shei, "GaN-based LEDs with mesh ITO p-contact and nanopillars," *IEEE Photonics Technol. Lett.*, vol. 21, no. 18, pp. 1293–1295, 2009.
- [131] S.-E. Wu, T.-H. Hsueh, and C.-P. Liu, "Fabrication of Nanopillars comprised of InGaN/GaN Multiple Quantum Wells by Focused Ion Beam Milling," *2007 Dig. Pap. Microprocess. Nanotechnol.*, pp. 64–65, 2007.

- [132] C. H. Chiu, P. Yu, H. C. Kuo, C. C. Chen, T. C. Lu, S. C. Wang, S. H. Hsu, Y. J. Cheng, and Y. C. Chang, "Broadband and omnidirectional antireflection employing disordered GaN nanopillars.," *Opt. Express*, vol. 16, no. 12, pp. 8748–8754, 2008.
- [133] Y. Inoue, T. Hoshino, S. Takeda, K. Ishino, a. Ishida, H. Fujiyasu, H. Kominami, H. Mimura, Y. Nakanishi, and S. Sakakibara, "Strong luminescence from dislocation-free GaN nanopillars," *Appl. Phys. Lett.*, vol. 85, no. 12, pp. 2340–2342, 2004.
- [134] Y. D. Wang, S. J. Chua, S. Tripathy, M. S. Sander, P. Chen, and C. G. Fonstad, "High optical quality GaN nanopillar arrays," *Appl. Phys. Lett.*, vol. 86, no. 7, pp. 1–3, 2005.
- [135] N. A. Kouklin and J. Liang, "Ultradense GaN nanopillar and nanopore arrays by self-assembly nanopatterning," *J. Electron. Mater.*, vol. 35, no. 5, pp. 1133–1137, 2006.
- [136] S. Keller, N. a. Fichtenbaum, C. Schaake, C. J. Neufeld, a. David, E. Matioli, Y. Wu, S. P. DenBaars, J. S. Speck, C. Weisbuch, and U. K. Mishra, "Optical properties of GaN nanopillar and nanostripe arrays with embedded InGaN/GaN multi quantum wells," *Phys. Status Solidi Basic Res.*, vol. 244, no. 6, pp. 1797–1801, 2007.
- [137] C. H. Hsieh, I. Lo, M. H. Gau, Y. L. Chen, M. C. Chou, W. Y. Pang, Y. I. Chang, Y. C. Hsu, M. W. Sham, J. C. Chiang, and J. K. Tsai, "Self-assembled c-plane GaN nanopillars on γ -LiAlO₂ substrate grown by plasma-assisted molecular-beam epitaxy," *Jpn. J. Appl. Phys.*, vol. 47, no. 2 PART 1, pp. 891–895, 2008.
- [138] S.-E. Wu, T.-H. Hsueh, C.-P. Liu, J.-K. Sheu, W.-C. Lai, and S.-J. Chang, "Focused Ion Beam Milled InGaN/GaN Multiple Quantum Well Nanopillars," *Jpn. J. Appl. Phys.*, vol. 47, no. 4, pp. 3130–3133, 2008.
- [139] S. Dhamodaran, D. S. Chander, and J. Ramkumar, "Anti-reflective and hydrophobic surface of self-organized GaN nano-flowers," *Appl. Surf. Sci.*, vol. 257, no. 22, pp. 9612–9615, 2011.
- [140] K. Bao, L. Wang, J. Yan, H. Sun, R. Guo, and Y. Wu, "Synthesis of GaN cauliflowers by ammoniating Ga₂O₃," *J. Alloys Compd.*, vol. 552, pp. 26–30, 2013.
- [141] L. W. Yin, Y. Bando, M. Sen Li, and D. Golberg, "Growth of semiconducting GaN hollow spheres and nanotubes with very thin shells via a controllable liquid gallium-gas interface chemical reaction," *Small*, vol. 1, no. 11, pp. 1094–1099, 2005.

- [142] X. Sun and Y. Li, "Ga₂O₃ and GaN semiconductor hollow spheres," *Angew. Chemie - Int. Ed.*, vol. 43, no. 29, pp. 3827–3831, 2004.
- [143] W. Mao, K. Bao, R. Sun, Z. Li, and L. Rong, "Synthesis of hexagonal GaN nanoplates via a convenient solid state reaction," *J. Alloys Compd.*, vol. 620, pp. 5–9, 2015.
- [144] Y. Tang, H. Cong, Z. Wang, and H. M. Cheng, "Synthesis of rectangular cross-section AlN nanofibers by chemical vapor deposition," *Chem. Phys. Lett.*, vol. 416, no. 1–3, pp. 171–175, 2005.
- [145] Y. Sun, J. Y. Li, Y. Tan, and L. Zhang, "Fabrication of aluminum nitride (AlN) hollow fibers by carbothermal reduction and nitridation of electrospun precursor fibers," *J. Alloys Compd.*, vol. 471, no. 1–2, pp. 400–403, 2009.
- [146] C. Ozgit-Akgun, F. Kayaci, I. Donmez, T. Uyar, and N. Biyikli, "Template-based synthesis of aluminum nitride hollow nanofibers via plasma-enhanced atomic layer deposition," *J. Am. Ceram. Soc.*, vol. 96, no. 3, pp. 916–922, 2013.
- [147] N. Biyikli, C. Ozgit-Akgun, E. Goldenberg, A. Haider, S. Kizir, T. Uyar, S. Bolat, B. Tekcan, and A. K. Okyay, "Hollow-cathode plasma-assisted atomic layer deposition: A novel route for low-temperature synthesis of crystalline III-nitride thin films and nanostructures," *2015 IEEE 35th Int. Conf. Electron. Nanotechnology, ELNANO 2015 - Conf. Proc.*, pp. 218–221, 2015.
- [148] M. Conroy, V. Z. Zubialevich, H. Li, N. Petkov, S. O'Donoghue, J. D. Holmes, and P. J. Parbrook, "Ultra-High-Density Arrays of Defect-Free AlN Nanorods: A 'space-Filling' Approach," *ACS Nano*, vol. 10, no. 2, pp. 1988–1994, 2016.
- [149] H. Hu, Z. Wu, W. Zhang, H. Li, R. Zhuo, D. Yan, J. Wang, and P. Yan, "Effect of Mg doping on growth and photoluminescence of AlN hexagonal nanorods," *J. Alloys Compd.*, vol. 624, pp. 241–246, 2015.
- [150] S. Y. Huang, Q. J. Cheng, S. Xu, and K. Ostrikov, "Single-step, catalyst-free plasma-assisted synthesis and growth mechanism of single-crystalline aluminum nitride nanorods," *Appl. Phys. Lett.*, vol. 97, no. 21, pp. 2014–2017, 2010.
- [151] D. Lee, I. S. Shin, L. Jin, D. Kim, Y. Park, and E. Yoon, "Nanoheteroepitaxy of GaN on AlN/Si(111) nanorods fabricated by nanosphere lithography," *J. Cryst. Growth*, vol. 444, pp. 9–13, 2016.

- [152] S. Shetty, J. Ghatak, and S. M. Shivaprasad, "Surface nitridation induced AlN nano-columnar growth on c-sapphire," *Solid State Commun.*, vol. 180, pp. 7–10, 2014.
- [153] S. Kong, H. Wei, S. Yang, H. Li, Y. Feng, Z. Chen, X. Liu, L. Wang, and Z. Wang, "Morphology and structure controlled growth of one-dimensional AlN nanorod arrays by hydride vapor phase epitaxy," *RSC Adv.*, vol. 4, no. 97, pp. 54902–54906, 2014.
- [154] L. Yu, Y. Lv, P. Liu, and X. Yu, "Synthesis of rhombic and triangular cross-sectional AlN nanorods on Si substrate via thermal CVD," *Mater. Lett.*, vol. 65, no. 10, pp. 1499–1502, 2011.
- [155] P. G. Zhang, K. Y. Wang, J. Liang, and S. M. Guo, "Formation of hexagonal AlN nanotowers and layered nanorods by direct nitridation of aluminum," *Phys. E Low-Dimensional Syst. Nanostructures*, vol. 43, no. 4, pp. 934–937, 2011.
- [156] A. Aghdaie, H. Haratizadeh, S. H. Mousavi, S. a. Jafari Mohammadi, and P. W. De Oliveira, "Effect of doping on structural and luminescence properties of AlN nanowires," *Ceram. Int.*, vol. 41, no. 2, pp. 2917–2922, 2015.
- [157] A. T. Connie, S. Zhao, S. M. Sadaf, I. Shih, Z. Mi, X. Du, J. Lin, and H. Jiang, "Optical and electrical properties of Mg-doped AlN nanowires grown by molecular beam epitaxy," *Appl. Phys. Lett.*, vol. 106, no. 21, 2015.
- [158] A. Cros, R. Mata, K. Hestroffer, and B. Daudin, "Ultraviolet Raman spectroscopy of GaN/AlN core-shell nanowires: Core, shell, and interface modes," *Appl. Phys. Lett.*, vol. 102, no. 14, 2013.
- [159] Y. E, Z. Hao, J. Yu, C. Wu, R. Liu, L. Wang, B. Xiong, J. Wang, Y. Han, C. Sun, and Y. Luo, "MBE Growth of AlN Nanowires on Si Substrates by Aluminizing Nucleation," *Nanoscale Res. Lett.*, vol. 10, no. 1, p. 383, 2015.
- [160] Kenry, K. T. Yong, and S. F. Yu, "AlN nanowires: Synthesis, physical properties, and nanoelectronics applications," *J. Mater. Sci.*, vol. 47, no. 14, pp. 5341–5360, 2012.
- [161] O. Landré, V. Fellmann, P. Jaffrennou, C. Bougerol, H. Renevier, a. Cros, and B. Daudin, "Molecular beam epitaxy growth and optical properties of AlN nanowires," *Appl. Phys. Lett.*, vol. 96, no. 6, pp. 061912–061912–3, 2010.

- [162] M. Lei, J. Wang, J. R. Li, Y. G. Wang, H. L. Tang, and W. J. Wang, “Emerging methanol-tolerant AlN nanowire oxygen reduction electrocatalyst for alkaline direct methanol fuel cell,” *Sci. Rep.*, vol. 4, p. 6013, 2014.
- [163] C. Li, “Strong cathodoluminescence of AlN nanowires synthesized by aluminum and nitrogen,” *Mater. Lett.*, vol. 115, no. 08, pp. 212–214, 2014.
- [164] F. Liu, Z. J. Su, F. Y. Mo, L. Li, Z. S. Chen, Q. R. Liu, J. Chen, S. Z. Deng, and N. S. Xu, “Controlled synthesis of ultra-long AlN nanowires in different densities and in situ investigation of the physical properties of an individual AlN nanowire,” *Nanoscale*, vol. 3, no. 2, pp. 610–618, 2011.
- [165] P. A. Mante, Y. C. Wu, Y. T. Lin, C. Y. Ho, L. W. Tu, and C. K. Sun, “Gigahertz coherent guided acoustic phonons in AlN/GaN nanowire superlattices,” *Nano Lett.*, vol. 13, no. 3, pp. 1139–1144, 2013.
- [166] S. Min Kim, H. Kim, Y. Nam, and S. Kim, “Effects of external surface charges on the enhanced piezoelectric potential of ZnO and AlN nanowires and nanotubes,” *AIP Adv.*, vol. 2, no. 4, 2012.
- [167] F. Qian, M. Brewster, S. K. Lim, Y. Ling, C. Greene, O. Laboutin, J. W. Johnson, S. Gradečak, Y. Cao, and Y. Li, “Controlled synthesis of AlN/GaN multiple quantum well nanowire structures and their optical properties,” *Nano Lett.*, vol. 12, no. 6, pp. 3344–3350, 2012.
- [168] H. M. Wu and Y. W. Peng, “Investigation of the growth and properties of single-crystalline aluminum nitride nanowires,” *Ceram. Int.*, vol. 41, no. 3, pp. 4847–4851, 2015.
- [169] Y. Wu, G. Chen, S. H. Wei, M. M. Al-Jassim, and Y. Yan, “Origin of charge separation in III-nitride nanowires under strain,” *Appl. Phys. Lett.*, vol. 99, no. 26, pp. 3–6, 2011.
- [170] S. Zhao, M. Djavid, and Z. Mi, “Surface Emitting, High Efficiency Near-Vacuum Ultraviolet Light Source with Aluminum Nitride Nanowires Monolithically Grown on Silicon,” *Nano Lett.*, vol. 15, no. 10, pp. 7006–7009, 2015.
- [171] W. Zheng, F. Huang, R. Zheng, and H. Wu, “Low-Dimensional Structure Vacuum-Ultraviolet-Sensitive ($\lambda < 200$ nm) Photodetector with Fast-Response Speed Based on High-Quality AlN Micro/Nanowire,” *Adv. Mater.*, vol. 27, no. 26, pp. 3921–3927, 2015.

- [172] S. G. Pandya and M. E. Kordesch, "Erbium doped aluminum nitride nanoparticles for nano-thermometer applications," *Mater. Res. Express*, vol. 2, no. 6, p. 065006, 2015.
- [173] C. Balasubramanian, V. P. Godbole, V. K. Rohatgi, a K. Das, and S. V. Bhoraskar, "Synthesis of nanowires and nanoparticles of cubic aluminium nitride," *Nanotechnology*, vol. 15, no. 3, pp. 370–373, 2004.
- [174] T.-H. Kim, S. Choi, and D.-W. Park, "Effects of NH₃ flow rate on the thermal plasma synthesis of AlN nanoparticles," *J. Korean Phys. Soc.*, vol. 63, no. 10, pp. 1864–1870, 2013.
- [175] Z. Shi, M. Radwan, S. Kirihara, Y. Miyamoto, and Z. Jin, "Morphology-controlled synthesis of quasi-aligned AlN nanowhiskers by combustion method: Effect of NH₄Cl additive," *Ceram. Int.*, vol. 35, no. 7, pp. 2727–2733, 2009.
- [176] Z. Shi, M. Radwan, S. Kirihara, Y. Miyamoto, and Z. Jin, "Formation and evolution of quasi-aligned AlN nanowhiskers by combustion synthesis," *J. Alloys Compd.*, vol. 476, no. 1–2, pp. 360–365, 2009.
- [177] a. T. M. Golam Sarwar, S. D. Carnevale, T. F. Kent, M. R. Laskar, B. J. May, and R. C. Myers, "Molecular beam epitaxy of InN nanowires on Si," *J. Cryst. Growth*, vol. 428, pp. 59–70, 2015.
- [178] S. Rafique, L. Han, and H. Zhao, "Chemical vapor deposition of m-plane and c-plane InN nanowires on Si (100) substrate," *J. Cryst. Growth*, vol. 415, pp. 78–83, 2015.
- [179] J. Ristić, E. Calleja, S. Fernández-Garrido, L. Cerutti, A. Trampert, U. Jahn, and K. H. Ploog, "On the mechanisms of spontaneous growth of III-nitride nanocolumns by plasma-assisted molecular beam epitaxy," *J. Cryst. Growth*, vol. 310, no. 18, pp. 4035–4045, 2008.
- [180] C. W. Wu and Y. R. Wu, "Thermoelectric characteristic of the rough InN/GaN core-shell nanowires," *J. Appl. Phys.*, vol. 116, no. 10, 2014.
- [181] S. Zhao, X. Liu, and Z. Mi, "Photoluminescence properties of Mg-doped InN nanowires," *Appl. Phys. Lett.*, vol. 103, no. 20, 2013.
- [182] S. Zhao, O. Salehzadeh, S. Alagha, K. L. Kavanagh, S. P. Watkins, and Z. Mi, "Probing the electrical transport properties of intrinsic InN nanowires," *Appl. Phys. Lett.*, vol. 102, no. 7, pp. 0–5, 2013.

- [183] G. Cheng, E. Stern, D. Turner-Evans, and M. a. Reed, “Electronic properties of InN nanowires,” *Appl. Phys. Lett.*, vol. 87, no. 25, pp. 1–3, 2005.
- [184] M. C. Johnson, C. J. Lee, E. D. Bourret-Courchesne, S. L. Konsek, S. Aloni, W. Q. Han, and a. Zettl, “Growth and morphology of 0.80 eV photoemitting indium nitride nanowires,” *Appl. Phys. Lett.*, vol. 85, no. 23, pp. 5670–5672, 2004.
- [185] Y. L. Chang, Z. Mi, and F. Li, “Photoluminescence properties of a nearly intrinsic single InN nanowire,” *Adv. Funct. Mater.*, vol. 20, no. 23, pp. 4146–4151, 2010.
- [186] B. K. Barick, C. Rodríguez-Fernández, A. Cantarero, and S. Dhar, “Structural and electronic properties of InN nanowire network grown by vapor-liquid-solid method,” *AIP Adv.*, vol. 5, no. 5, p. 057162, 2015.
- [187] J. Kamimura, P. Bogdanoff, M. Ramsteiner, L. Geelhaar, and H. Riechert, “Photoelectrochemical properties of InN nanowire photoelectrodes for solar water splitting,” *Semicond. Sci. Technol.*, vol. 31, no. 7, p. 074001, 2016.
- [188] H. J. Xiang, S. H. Wei, J. L. F. Da Silva, and J. Li, “Strain relaxation and band-gap tunability in ternary $\text{In}_x\text{Ga}_{1-x}\text{N}$ nanowires,” *Phys. Rev. B - Condens. Matter Mater. Phys.*, vol. 78, no. 19, pp. 4–7, 2008.
- [189] F. Werner, F. Limbach, M. Carsten, C. Denker, J. Malindretos, and A. Rizzi, “Electrical conductivity of InN nanowires and the influence of the native indium oxide formed at their surface,” *Nano Lett.*, vol. 9, no. 4, pp. 1567–1571, 2009.
- [190] S. Zhao, B. H. L. D. P. Liu, X. D. Liu, M. G. Kibria, T. Szkopek, H. Guo, and Z. Mi, “p-Type InN Nanowires,” pp. 2–5, 2013.
- [191] D. Bayerl and E. Kioupakis, “Visible-wavelength polarized-light emission with small-diameter InN nanowires,” *Nano Lett.*, vol. 14, no. 7, pp. 3709–3714, 2014.
- [192] S. K. Lim, S. Crawford, G. Haberfehlner, and S. Gradečak, “Controlled modulation of diameter and composition along individual III-V nitride nanowires,” *Nano Lett.*, vol. 13, no. 2, pp. 331–336, 2013.
- [193] T. Stoica, R. J. Meijers, R. Calarco, T. Richter, E. Sutler, and H. Lüth, “Photoluminescence and intrinsic properties of MBE-Grown InN nanowires,” *Nano Lett.*, vol. 6, no. 7, pp. 1541–1547, 2006.

- [194] T. Richter, H. Lüth, T. Schäpers, R. Meijers, K. Jeganathan, S. Estévez Hernández, R. Calarco, and M. Marso, “Electrical transport properties of single undoped and n-type doped InN nanowires.,” *Nanotechnology*, vol. 20, no. 40, p. 405206, 2009.
- [195] Y.-L. Chang, F. Li, A. Fatehi, and Z. Mi, “Molecular beam epitaxial growth and characterization of non-tapered InN nanowires on Si(111).,” *Nanotechnology*, vol. 20, no. 34, p. 345203, 2009.
- [196] Z. Mi and S. Zhao, “Extending group-III nitrides to the infrared: Recent advances in InN,” *Phys. Status Solidi Basic Res.*, vol. 252, no. 5, pp. 1050–1062, 2015.
- [197] G. Liu, S. Zhao, R. D. E. Henderson, Z. Leonenko, E. Abdel-Rahman, Z. Mi, and D. Ban, “Nanogenerators based on vertically aligned InN nanowires,” *Nanoscale*, pp. 2097–2106, 2016.
- [198] E. B. Quddus, A. Wilson, R. a Webb, and G. Koley, “Oxygen mediated synthesis of high quality InN nanowires above their decomposition temperature.,” *Nanoscale*, pp. 1166–1172, 2013.
- [199] Y. Yang, Y. Ling, G. Wang, X. Lu, Y. Tong, and Y. Li, “Growth of gallium nitride and indium nitride nanowires on conductive and flexible carbon cloth substrates.,” *Nanoscale*, vol. 5, no. 5, pp. 1820–4, 2013.
- [200] Z. Chen, Y. Li, J. Jiang, C. Cao, T. Xu, Q. Chen, X. Xu, and H. Zhu, “Template-assisted synthesis of ordered single crystal InN nanowires,” *RSC Adv.*, vol. 2, no. 17, p. 6806, 2012.
- [201] J. Zhang, F. Jiang, and T. Sun, “Fabrication, morphologies and structural characterization of InN nanowire arrays,” *Appl. Phys. A Mater. Sci. Process.*, vol. 116, no. 1, pp. 207–211, 2014.
- [202] V. Parameshwaran, X. Xu, and B. Clemens, “Crystallinity, Surface Morphology, and Photoelectrochemical Effects in Conical InP and InN Nanowires Grown on Silicon,” *ACS Appl. Mater. Interfaces*, vol. 8, no. 33, pp. 21454–21464, 2016.
- [203] C. Bagavath, L. Nasi, and J. Kumar, “Investigations on the nanostructures of GaN, InN and In_xGa_{1-x}N,” *Mater. Sci. Semicond. Process.*, vol. 49, pp. 61–67, 2016.
- [204] K. Wang, T. Araki, T. Yamaguchi, Y. T. Chen, E. Yoon, and Y. Nanishi, “InN nanocolumns grown by molecular beam epitaxy and their luminescence properties,” *J. Cryst. Growth*, vol. 430, pp. 93–97, 2015.

- [205] N. S. Karan, Y. Chen, Z. Liu, and R. Beaulac, "Solution-Liquid-Solid Approach to Colloidal Indium Nitride Nanoparticles from Simple Alkylamide Precursors," *Chem. Mater.*, vol. 28, no. 16, pp. 5601–5605, 2016.
- [206] K. K. Madapu, a. K. Prasad, a. K. Tyagi, and S. Dhara, "Investigation of gas sensing properties of InN nanoparticles," vol. 050089, no. 2015, p. 050089, 2015.
- [207] S. Alkis, M. Alevli, S. Burzhuev, H. A. Vural, A. K. Okyay, and B. Ortaç, "Generation of InN nanocrystals in organic solution through laser ablation of high pressure chemical vapor deposition-grown InN thin film," *J. Nanoparticle Res.*, vol. 14, no. 8, 2012.
- [208] K. K. Madapu, S. R. Polaki, and S. Dhara, "Excitation dependent Raman studies of self-seeded grown InN nanoparticles with different carrier concentration," *Phys. Chem. Chem. Phys.*, vol. 18, no. 27, pp. 18584–18589, 2016.
- [209] K. S. Khashan and S. F. Abbas, "Characterization of InN nanoparticles prepared by laser as photodetector," *Int. J. Mod. Phys. B*, vol. 30, no. 14, p. 1650080, 2016.
- [210] M. a. Qaeed, K. Ibrahim, K. M. a Saron, Q. N. Abdullah, N. G. Elfadill, S. H. Abud, and K. M. Chahrour, "The effective role of time in synthesising InN by chemical method at low temperature," *J. Mater. Sci. Mater. Electron.*, vol. 25, no. 3, pp. 1376–1380, 2014.
- [211] F. I. Chowdhury, A. Alnuaimi, S. Alkis, B. Ortaç, S. Aktürk, M. Alevli, N. Dietz, A. K. Okyay, A. Nayfeh, and N. J, "Enhancement in c-Si solar cells using 16 nm InN nanoparticles," *Mater. Res. Express*, vol. 3, no. 5, p. 056202, 2016.
- [212] A. Gautam and F. C. J. M. Van Veggel, "Devices," no. C1, 2012.
- [213] Y. Pan, T. Wang, K. Shen, T. Peng, K. Wu, W. Zhang, and C. Liu, "Rapid growth and characterization of InN nanocolumns on InGaN buffer layers at a low ratio of N/In," *J. Cryst. Growth*, vol. 313, no. 1, pp. 16–19, 2010.
- [214] P. T. Terziyska, K. S. A. Butcher, D. Gogova, D. Alexandrov, P. Binsted, and G. Wu, "InN nanopillars grown from In-rich conditions by migration enhanced afterglow technique," *Mater. Lett.*, vol. 106, pp. 155–157, 2013.

- [215] H. Yang, J. Yin, W. Li, F. Gao, Y. Zhao, G. Wu, B. Zhang, and G. Du, “In-assisted growth of InN nanocolumn on Si(111) substrate by molecular beam epitaxy,” *Vacuum*, vol. 128, pp. 133–136, 2016.
- [216] C. H. Shen, H. Y. Chen, H. W. Lin, S. Gwo, a. a. Klochikhin, and V. Y. Davydov, “Near-infrared photoluminescence from vertical InN nanorod arrays grown on silicon: Effects of surface electron accumulation layer,” *Appl. Phys. Lett.*, vol. 88, no. 25, pp. 2004–2007, 2006.
- [217] M. a. Sánchez-García, J. Grandal, E. Calleja, S. Lazic, J. M. Calleja, and a. Trampert, “Epitaxial growth and characterization of InN nanorods and compact layers on silicon substrates,” *Phys. Status Solidi Basic Res.*, vol. 243, no. 7, pp. 1490–1493, 2006.
- [218] N. J. Ku, J. H. Huang, C. H. Wang, H. C. Fang, and C. P. Liu, “Crystal face-dependent nanopiezotronics of an obliquely aligned InN nanorod Array,” *Nano Lett.*, vol. 12, no. 2, pp. 562–568, 2012.
- [219] M. H. Kim, D. Y. Moon, J. Park, Y. Nanishi, G. C. Yi, and E. Yoon, “Catalyst-free growth of InN nanorods by metal-organic chemical vapor deposition,” *Phys. Status Solidi Appl. Mater. Sci.*, vol. 209, no. 1, pp. 50–55, 2012.
- [220] H. Song, A. Yang, R. Zhang, Y. Guo, H. Wei, G. Zheng, S. Yang, X. Liu, Q. Zhu, and Z. Wang, “Well-aligned Zn-doped InN nanorods grown by metal-organic chemical vapor deposition and the dopant distribution,” *Cryst. Growth Des.*, vol. 9, no. 7, pp. 3292–3295, 2009.
- [221] K. K. Madapu, S. Dhara, S. Polaki, S. Amirthapandian, and a. K. Tyagi, “Growth of InN quantum dots to nanorods: a competition between nucleation and growth rates,” *CrystEngComm*, vol. 17, no. 16, pp. 3139–3147, 2015.
- [222] H. Li, G. Zhao, H. Wei, L. Wang, Z. Chen, and S. Yang, “Growth of Well-Aligned InN Nanorods on Amorphous Glass Substrates,” *Nanoscale Res. Lett.*, vol. 11, no. 1, p. 270, 2016.
- [223] W.-C. Chen, S.-Y. Kuo, W.-L. Wang, J.-S. Tian, W.-T. Lin, F.-I. Lai, and L. Chang, “Study of InN epitaxial films and nanorods grown on GaN template by RF-MOMBE,” *Nanoscale Res. Lett.*, vol. 7, no. 1, p. 468, 2012.
- [224] K.-W. Liu, S.-J. Chang, S.-J. Young, T.-H. Hsueh, H. Hung, Y.-C. Mai, S.-M. Wang, K.-J. Chen, Y.-L. Wu, and Y.-Z. Chen, “InN nanorods prepared with CrN nanoislands by plasma-assisted molecular beam epitaxy,” *Nanoscale Res. Lett.*, vol. 6, no. 1, p. 442, 2011.

- [225] K. Y. Chang, Y. S. Liu, S. Gwo, and H. Ahn, "Photoluminescence from InN nanorod arrays with a critical size," *Pacific Rim Conf. Lasers Electro-Optics, CLEO - Tech. Dig.*, 2013.
- [226] I. Shalish, G. Seryogin, W. Yi, J. M. Bao, M. a. Zimmler, E. Likovich, D. C. Bell, F. Capasso, and V. Narayanamurti, "Epitaxial catalyst-free growth of InN nanorods on c-plane sapphire," *Nanoscale Res. Lett.*, vol. 4, no. 6, pp. 532–537, 2009.
- [227] S. Feng, J. Tan, B. Li, H. Song, Z. Wu, and X. Chen, "Nitridation effects of Si(111) substrate surface on InN nanorods grown by plasma-assisted molecular beam epitaxy," *J. Alloys Compd.*, vol. 621, no. 2015, pp. 232–237, 2015.
- [228] P. T. Terziyska, K. S. a Butcher, P. Rafailov, and D. Alexandrov, "Growth of vertically oriented InN nanorods from In-rich conditions on unintentionally patterned sapphire substrates," *Appl. Surf. Sci.*, vol. 353, pp. 103–105, 2015.
- [229] F. Zhang, Q. Wu, Y. Zhang, J. Zhu, N. Liu, J. Yang, X. Wang, and Z. Hu, "Chemical vapor deposition growth of InN nanostructures: Morphology regulation and field emission properties," *Appl. Surf. Sci.*, vol. 258, no. 24, pp. 9701–9705, 2012.
- [230] L. E. Goff, R. E. L. Powell, a. J. Kent, C. T. Foxon, S. V. Novikov, R. Webster, and D. Cherns, "Molecular beam epitaxy of InN nanorods on Si- and C-faces of SiC substrates," *J. Cryst. Growth*, vol. 386, pp. 135–138, 2014.
- [231] K. W. Liu, S. J. Young, S. J. Chang, T. H. Hsueh, Y. Z. Chen, K. J. Chen, H. Hung, S. M. Wang, and Y. L. Wu, "Growth of InN nanorods prepared by plasma-assisted molecular beam epitaxy with varying Cr thicknesses," *J. Cryst. Growth*, vol. 347, no. 1, pp. 113–118, 2012.
- [232] P. Zhang, T. S. Mayer, and T. N. Jackson, "2007 IEEE Device Research Conference : Metal Oxide Semiconductor Field-Effect Transistors and Their Application," vol. 1, no. 1, pp. 6–9, 2007.
- [233] M. J. Biercuk, D. J. Monsma, C. M. Marcus, J. S. Becker, R. G. Gordon, M. J. Biercuk, D. J. Monsma, and C. M. Marcus, "Low-temperature atomic-layer-deposition lift-off method for microelectronic and nanoelectronic applications Low-temperature atomic-layer-deposition lift-off method for microelectronic and nanoelectronic applications," vol. 2405, no. 2003, pp. 20–23, 2007.

- [234] J. Goldberger, A. I. Hochbaum, R. Fan, and P. Yang, "Silicon Vertically Integrated Nanowire Field Effect Transistors," 2006.
- [235] A. Sinha, D. W. Hess, and C. L. Henderson, "Area selective atomic layer deposition of titanium dioxide: Effect of precursor chemistry," *J. Vac. Sci. Technol. B Microelectron. Nanom. Struct.*, vol. 24, no. 6, p. 2523, 2006.
- [236] Y. Hua, W. P. King, and C. L. Henderson, "Nanopatterning materials using area selective atomic layer deposition in conjunction with thermochemical surface modification via heated AFM cantilever probe lithography," *Microelectron. Eng.*, vol. 85, no. 5–6, pp. 934–936, 2008.
- [237] A. Haider, M. Yilmaz, P. Deminskyi, H. Eren, and N. Biyikli, "Nanoscale selective area atomic layer deposition of TiO₂ using e-beam patterned polymers," *RSC Adv.*, vol. 6, no. 108, pp. 106109–106119, 2016
- [238] M. J. Biercuk, D. J. Monsma, C. M. Marcus, J. S. Backer, and R. G. Gordon, "Low-temperature atomic-layer-deposition lift-off method for microelectronic and nanoelectronic applications," *Appl. Phys. Lett.*, vol. 83, no. 12, pp. 2405–2407, 2003.
- [239] E. Färm, M. Kemell, E. Santala, M. Ritala, and M. Leskelä, "Selective-Area Atomic Layer Deposition Using Poly(vinyl pyrrolidone) as a Passivation Layer," *J. Electrochem. Soc.*, vol. 157, p. K10, 2010.
- [240] A. Sinha, D. W. Hess, and C. L. Henderson, "Area-Selective ALD of Titanium Dioxide Using Lithographically Defined Poly(methyl methacrylate) Films," *J. Electrochem. Soc.*, vol. 153, no. 5, p. G465, 2006.
- [241] A. Haider, C. Ozgit-Akgun, E. Goldenberg, A. K. Okyay, and N. Biyikli, "Low-Temperature Deposition of Hexagonal Boron Nitride via Sequential Injection of Triethylboron and N₂/H₂ Plasma," *J. Am. Ceram. Soc.*, vol. 97, no. 10, pp. 4052–4059, 2014.
- [242] A. P. Furneaux, R.C., Rigby, W.R., Davidson, "The formation of controlled-porosity membranes from anodically oxidized aluminum," *Nature*, vol. 337, no. 12. p. 147, 1989.
- [243] S. Altuntas and F. Buyukserin, "Fabrication and characterization of conductive anodic aluminum oxide substrates," *Appl. Surf. Sci.*, vol. 318, pp. 290–296, 2014.
- [244] A. Haider, C. Ozgit-Akgun, F. Kayaci, A. K. Okyay, T. Uyar, and N. Biyikli, "Fabrication of AlN/BN bishell hollow nanofibers by

electrospinning and atomic layer deposition,” *Apl Mater.*, vol. 2, no. 9, p. 096109, 2014.

- [245] C. Ozgit-Akgun, E. Goldenberg, S. Bolat, B. Tekcan, F. Kayaci, T. Uyar, A. K. Okyay, and N. Biyikli, “Low-temperature hollow cathode plasma-assisted atomic layer deposition of crystalline III-nitride thin films and nanostructures,” *Phys. Status Solidi*, vol. 398, no. 4, p. n/a–n/a, 2015.
- [246] R. L. Puurunen, “Surface chemistry of atomic layer deposition: A case study for the trimethylaluminum/water process,” *J. Appl. Phys.*, vol. 97, no. 2005, 2005.
- [247] N. Nepal, N. a. Mahadik, L. O. Nyakiti, S. B. Qadri, M. J. Mehl, J. K. Hite, and C. R. Eddy, “Epitaxial growth of cubic and hexagonal InN thin films via plasma-assisted atomic layer epitaxy,” *Cryst. Growth Des.*, vol. 13, pp. 1485–1490, 2013.
- [248] S. Kumar, L. Mo, M. Motlan, and T. L. Tansley, “Elemental Composition of Reactively Sputtered Indium Nitride Thin Films,” *Jpn. J. Appl. Phys.*, vol. 35, pp. 2261–2265, 1996.
- [249] I. Bello, “Deposition of indium nitride by low energy modulated indium and nitrogen ion beams,” *J. Vac. Sci. Technol. A Vacuum, Surfaces, Film.*, vol. 10, no. 1992, p. 1642, 1992.
- [250] I. J. Lee and C. Yu, “Observation of Complete Oxidation of InN to In₂O₃ in Air at Elevated Temperatures by Using X-ray Photoemission Spectroscopy,” vol. 49, no. 5, pp. 2176–2179, 2006.
- [251] V. Lebedev, V. Cimalla, J. Pezoldt, M. Himmerlich, S. Krischok, J. a. Schaefer, O. Ambacher, F. M. Morales, J. G. Lozano, and D. González, “Effect of dislocations on electrical and electron transport properties of InN thin films. I. Strain relief and formation of a dislocation network,” *J. Appl. Phys.*, vol. 100, no. 2006, 2006.
- [252] M. K. Indika Senevirathna, S. Gamage, R. Atalay, A. R. Acharya, a. G. Unil Perera, N. Dietz, M. Buegler, A. Hoffmann, L. Su, A. Melton, and I. Ferguson, “Effect of reactor pressure on the electrical and structural properties of InN epilayers grown by high-pressure chemical vapor deposition,” *J. Vac. Sci. Technol. A Vacuum, Surfaces, Film.*, vol. 30, p. 031511, 2012.
- [253] C. F. Shih, N. C. Chen, and C. Y. Tseng, “Photoelectron spectroscopic investigation of InN and InN/GaN heterostructures,” *Thin Solid Films*, vol. 516, pp. 5016–5019, 2008.

- [254] M. A. Moram and M. E. Vickers, "X-ray diffraction of III-nitrides," *Reports Prog. Phys.*, vol. 72, p. 036502, 2009.
- [255] M. F. Wu, S. Q. Zhou, a. Vantomme, Y. Huang, H. Wang, and H. Yang, "High-precision determination of lattice constants and structural characterization of InN thin films," *J. Vac. Sci. Technol. A Vacuum, Surfaces, Film.*, vol. 24, p. 275, 2006.
- [256] A. Haider, S. Kizir, C. Ozgit, E. Goldenberg, S. A. Leghari, A. K. Okyay, and N. Biyikli, "Low-temperature grown wurtzite $\text{In}_x\text{Ga}_{1-x}\text{N}$ thin films via hollow cathode plasma-assisted atomic layer deposition," *J. Mater. Chem. C*, vol. 3, pp. 9620-9630, 2015.
- [257] M. V. S. da Silva, D. G. F. David, I. Pepe, a. Ferreira da Silva, J. S. de Almeida, a. L. Gazoto, a. O. dos Santos, L. P. Cardoso, E. a. Meneses, D. L. Graybill, and K. M. Mertes, "Structural, optical and electrical properties of indium nitride polycrystalline films," *Thin Solid Films*, vol. 520, no. 15, pp. 4848-4852, 2012.
- [258] L. F. Jiang, W. Z. Shen, H. F. Yang, H. Ogawa, and Q. X. Guo, "Temperature effects on optical properties of InN thin films," *Appl. Phys. A Mater. Sci. Process.*, vol. 78, pp. 89-93, 2004.
- [259] V. Y. Davydov, A. A. Klochikhin, R. P. Seisyan, V. V. Emtsev, S. V. Ivanov, F. Bechstedt, J. Furthmüller, H. Harima, a. V. Mudryi, J. Aderhold, O. Semchinova, and J. Graul, "Absorption and emission of hexagonal InN. Evidence of narrow fundamental band gap," *Phys. Status Solidi Basic Res.*, vol. 229, no. 3, pp. 1972-1974, 2002.
- [260] C. Ozgit-Akgun, E. Goldenberg, S. Bolat, B. Tekcan, F. Kayaci, T. Uyar, A. K. Okyay, and N. Biyikli, "Low-temperature hollow cathode plasma-assisted atomic layer deposition of crystalline III-nitride thin films and nanostructures," *Phys. Status Solidi*, vol. 5, p. n/a-n/a, 2015.
- [261] B. D. Cullity, "Stress measurement," *Elements X-ray Diffr.*, pp. 431-453, 1956.
- [262] M. Krawczyk, W. Lisowski, J. W. Sobczak, A. Kosiński, A. Jablonski, C. Skierbiszewski, M. Siekacz, and S. Wiązkowska, "Surface and in-depth characterization of InGaN compounds synthesized by plasma-assisted molecular beam epitaxy," *J. Alloys Compd.*, vol. 509, pp. 9565-9571, 2011.
- [263] H. Chen, R. Feenstra, J. Northrup, T. Zywietz, and J. Neugebauer, "Spontaneous Formation of Indium-Rich Nanostructures on InGaN(0001) Surfaces," *Phys. Rev. Lett.*, vol. 85, no. 0001, pp. 1902-1905, 2000.

- [264] S. Kizir, A. Haider, and N. Biyikli, "Substrate impact on the low-temperature growth of GaN thin films by plasma-assisted atomic layer deposition," *J. Vac. Sci. Technol. A*, vol. 34, no. 4, p. 041511, 2016.
- [265] J. E. Northrup, L. T. Romano, and J. Neugebauer, "Surface energetics, pit formation, and chemical ordering in InGaN alloys," *Appl. Phys. Lett.*, vol. 74, no. 1999, p. 2319, 1999.
- [266] S. R. Meher, a. Subrahmanyam, and M. K. Jain, "Composition-dependent structural, optical and electrical properties of in x Ga_{1-x} N (0.5 \leq x \leq 0.93) thin films grown by modified activated reactive evaporation," *J. Mater. Sci.*, vol. 48, pp. 1196–1204, 2013.
- [267] M. Kumar, A. Kumar, S. B. Thapa, S. Christiansen, and R. Singh, "XPS study of triangular GaN nano/micro-needles grown by MOCVD technique," *Mater. Sci. Eng. B Solid-State Mater. Adv. Technol.*, vol. 186, pp. 89–93, 2014.
- [268] P. Kumar, M. Kumar, Govind, B. R. Mehta, and S. M. Shivaprasad, "XPS investigation of ion beam induced conversion of GaAs(0 0 1) surface into GaN overlayer," *Appl. Surf. Sci.*, vol. 256, pp. 517–520, 2009.
- [269] H. Xiao, R. Liu, H. Ma, Z. Lin, J. Ma, F. Zong, and L. Mei, "Thermal stability of GaN powders investigated by XRD, XPS, PL, TEM, and FT-IR," *J. Alloys Compd.*, vol. 465, pp. 340–343, 2008.
- [270] C.-A. Chang, C.-F. Shih, N.-C. Chen, T. Y. Lin, and K.-S. Liu, "In-rich In_{1-x}Ga_xN films by metalorganic vapor phase epitaxy," *Appl. Phys. Lett.*, vol. 85, no. 2004, p. 6131, 2004.
- [271] K. S. A Butcher, Afifuddin, T. L. Tansley, N. Brack, P. J. Pigram, H. Timmers, K. E. Prince, and R. G. Elliman, "Gallium and oxygen accumulations on gallium nitride surfaces following argon ion milling in ultra-high vacuum conditions," *Appl. Surf. Sci.*, vol. 230, pp. 18–23, 2004.
- [272] H. Parala, A. Devi, F. Hipler, E. Maile, A. Birkner, H. W. Becker, and R. a. Fischer, "Investigations on InN whiskers grown by chemical vapour deposition," *J. Cryst. Growth*, vol. 231, pp. 68–74, 2001.
- [273] Y. Huang, H. Wang, Q. Sun, J. Chen, J. F. Wang, Y. T. Wang, and H. Yang, "Study on the thermal stability of InN by in-situ laser reflectance system," *J. Cryst. Growth*, vol. 281, pp. 310–317, 2005.

- [274] Z. Majlinger, a. Bozanic, M. Petrvacic, K. J. Kim, B. Kim, and Y. W. Yang, "NEXAFS and XPS study of GaN formation on ion-bombarded GaAs surfaces," *Vacuum*, vol. 84, no. 1, pp. 41–44, 2009.
- [275] H. Shinoda and N. Mutsukura, "Deposition of an InN thin film by a r.f. plasma-assisted reactive ion-beam sputtering deposition (R-IBSD) technique," *Diam. Relat. Mater.*, vol. 11, pp. 896–900, 2002.
- [276] M. M. El-Nahass and a. a. M. Farag, "Structural, optical and dispersion characteristics of nanocrystalline GaN films prepared by MOVPE," *Opt. Laser Technol.*, vol. 44, no. 2, pp. 497–503, 2012.
- [277] A. K. Mann, D. Varandani, B. R. Mehta, and L. K. Malhotra, "Conducting atomic force microscopy studies of InN nanocomposite layers having conducting and nonconducting phases," *J. Appl. Phys.*, vol. 101, no. 2007, 2007.
- [278] J. Mayer, L. a Giannuzzi, T. Kamino, and J. Michael, "TEM Sample Preparation and Damage," *MRS Bull.*, vol. 32, no. May, pp. 400–407, 2007.
- [279] E. J. Shin, S. H. Lim, M. Jeong, D. S. Lim, S. K. Han, H. S. Lee, S. K. Hong, J. Y. Lee, and T. Yao, "Growth and structural characterization of InGa_xN layers with controlled In content prepared by plasma-assisted molecular beam epitaxy," *Thin Solid Films*, vol. 546, pp. 42–47, 2013.
- [280] C. Gatzert, a. W. Blakers, P. N. K. Deenapanray, D. Macdonald, and F. D. Auret, "Investigation of reactive ion etching of dielectrics and Si in CHF₃/O₂ or CHF₃/Ar for photovoltaic applications," *J. Vac. Sci. Technol. A Vacuum, Surfaces, Film.*, vol. 24, no. 5, p. 1857, 2006.
- [281] R. Legtenberg, H. Jansen, M. Deboer, and M. Elwenspoek, "Anisotropic Reactive Ion Etching of Silicon Using SF₆/O₂/CHF₃ Gas Mixtures," *J. Electrochem. Soc.*, vol. 142, no. 6, pp. 2020–2028, 1995.
- [282] M. Alevli, A. Haider, S. Kizir, S. A. Leghari, and N. Biyikli, "Comparison of trimethylgallium and triethylgallium as 'Ga' source materials for the growth of ultrathin GaN films on Si (100) substrates via hollow-cathode plasma-assisted atomic layer deposition," *J. Vac. Sci. Technol. A*, vol. 34, no. 1, pp. 01A137, 2016.
- [283] H. Altuntas, T. Bayrak, S. Kizir, A. Haider, and N. Biyikli, "Electrical conduction and dielectric relaxation properties of AlN thin films grown by hollow-cathode plasma-assisted atomic layer deposition," *Semicond. Sci. Technol.*, vol. 31, no. 7, pp. 075003, 2016.

- [284] A. Haider, S. Kizir, and N. Biyikli, “Low-temperature self-limiting atomic layer deposition of wurtzite InN on Si(100),” *AIP Adv.*, vol. 6, pp. 045203, 2016.
- [285] A. Haider, S. Kizir, C. Ozgit-Akgun, A. K. Okyay, and N. Biyikli, “Low-temperature sequential pulsed chemical vapor deposition of ternary $B_xGa_{1-x}N$ and $B_xIn_{1-x}N$ thin film alloys,” *J. Vac. Sci. Technol. A*, vol. 34, no. 1, p. 01A123, 2016.
- [286] S. Ali, “No Title,” *J. Vac. Sci. Technol. A Vacuum, Surfaces, Film.*, vol. 34, p. 041511, 2016.
- [287] L. Qin, C. Xue, Y. Duan, and L. Shi, “Fabrication and photoluminescence of GaN nanorods by ammoniating Ga₂O₃ films deposited on Co-coated Si(1 1 1) substrates,” *Phys. B Condens. Matter*, vol. 404, no. 2, pp. 190–193, 2009.
- [288] H. Di Xiao, R. Liu, J. Q. Liu, Z. J. Lin, and L. M. Mei, “Growth process from amorphous GaN to polycrystalline GaN on Si (111) substrates,” *Vacuum*, vol. 83, no. 11, pp. 1393–1396, 2009.
- [289] A. H. Chin, T. S. Ahn, H. Li, S. Vaddiraju, C. J. Bardeen, C. Z. Ning, and M. K. Sunkara, “Photoluminescence of GaN nanowires of different crystallographic orientations,” *Nano Lett.*, vol. 7, no. 3, pp. 626–631, 2007.
- [290] M. Alevli, N. Gungor, A. Haider, S. Kizir, S. A. Leghari, and N. Biyikli, “Substrate temperature influence on the properties of GaN thin films grown by hollow-cathode plasma-assisted atomic layer deposition,” *J. Vac. Sci. Technol. A*, vol. 34, no. 1, p. 01A125, 2016.
- [291] G. Santana, O. de Melo, J. Aguilar-Hernández, R. Mendoza-Pérez, B. Marel Monroy, A. Escamilla-Esquivel, M. López-Sópez, F. de Moure, L. a. Hernández, and G. Contreras-Puente, “Photoluminescence study of gallium nitride thin films obtained by infrared close space vapor transport,” *Materials (Basel)*, vol. 6, no. 3, pp. 1050–1060, 2013.
- [292] A. Haider, H. Cansizoglu, M. F. Cansizoglu, T. Karabacak, A. K. Okyay, and N. Biyikli, “Enhanced photoresponse of conformal TiO₂/Ag nanorod array-based Schottky photodiodes fabricated via successive glancing angle and atomic layer deposition,” *J. Vac. Sci. Technol. A*, vol. 33, no. 1, p. 01A110, 2015.
- [293] C. Ozgit, I. Donmez, M. Alevli, and N. Biyikli, “Self-limiting low-temperature growth of crystalline AlN thin films by plasma-enhanced

atomic layer deposition,” *Thin Solid Films*, vol. 520, no. 7, pp. 2750–2755, 2012.

- [294] B. K. Barick and S. Dhar, “Surface and bulk electronic properties of low temperature synthesized InN microcrystals,” *J. Cryst. Growth*, vol. 416, pp. 154–158, 2015.
- [295] A. K. S. Chauhan, M. Kumar, and G. Gupta, “Catalyst free self-assembled growth of InN nanorings on stepped Si (553) surface,” *Appl. Surf. Sci.*, vol. 345, no. 553, pp. 156–161, 2015.
- [296] R. Chen, H. Kim, P. C. McIntyre, and S. F. Bent, “Investigation of self-assembled monolayer resists for hafnium dioxide atomic layer deposition,” *Chem. Mater.*, vol. 17, no. 3, pp. 536–544, 2005.
- [297] J. P. Lee, Y. J. Jang, and M. M. Sung, “Atomic layer deposition of TiO₂ thin films on mixed self-assembled monolayers studied as a function of surface free energy,” *Adv. Funct. Mater.*, vol. 13, no. 11, pp. 873–876, 2003.
- [298] X. Li, X. Hua, L. Ling, G. S. Oehrlein, M. Barela, and H. M. Anderson, “Fluorocarbon-based plasma etching of SiO₂: Comparison of C₄F₆/Ar and C₄F₈/Ar discharges,” *J. Vac. Sci. Technol. A Vacuum, Surfaces, Film.*, vol. 20, no. 6, pp. 2052–2061, 2002.
- [299] S. N. Q. A. Abd Aziz, S.-Y. Pung, N. N. Ramli, and Z. Lockman, “Growth of ZnO nanorods on stainless steel wire using chemical vapour deposition and their photocatalytic activity,” *Sci. World J.*, vol. 2014, p. 252851, 2014.
- [300] H. Lin, A. K. Rumaiz, M. Schulz, D. Wang, R. Rock, C. P. Huang, and S. I. Shah, “Photocatalytic activity of pulsed laser deposited TiO₂ thin films,” *Mater. Sci. Eng. B*, vol. 151, no. 2, pp. 133–139, 2008.